Optical Waveguides and Devices in Lithium Niobate by the Proton Exchange Process

by

Loi Kwok Kwong

(雷 國 光)

A Master Thesis

Submitted in partial fulfilment of the requirement

for the Degree of Master of Philosophy

in

Department of Electronic Engineering

The Chinese University of Hong Kong

June, 1992

Acknowledgements

I am deeply indebted to Dr. E.Y.B. Pun for his guidance and encouragement throughout the course of my work. The continuing support and encouragement of Prof. P.S. Chung and Dr. A.H.P. Chan is gratefully acknowledged.

I am grateful to Dr. K.Y. Tong for access to the facilities of the Microelectronics Laboratory at Hong Kong Polytechnic. With respect to the structural characterization measurements of proton-exchanged waveguides, I am most grateful to Prof. M.N. Armenise of Politecnico di Bari, Dr. L.M.L. Leung of Hong Kong Baptist College, and Dr. H.K. Wong of Physics Department, CUHK. I acknowledge K.K.F. Leung of Hua Ko Electronics Co Ltd. for supplying the photoresist used in the fabrication of channel waveguides.

I would like to thank S.A. Zhao of Jinan University and Emil Jelenković of Hong Kong Polytechnic for help in waveguide fabrication. I also thank W.C. Chu, C.K. Pun and L.Y. Pi for their technical support. Special thanks are due to J.Y.L. Lu for her technical support and help in preparation of the thesis figures. My sincere thanks go to K.W. Choi of Information Engineering Department for help in taking the photographs of the experimental arrangements.

Finally I would like to express my gratitude to my parents who gave me the faith and strength in the course of my work.

Abstract

Optical waveguides in z-cut lithium niobate have been fabricated by the proton exchange technique using four different proton sources: phosphoric, toluic, stearic and cinnamic acids. The optical properties of these waveguides were characterized using the prism-coupling technique. The diffusion constant D_o and activation energy Q of the proton-exchange process were obtained for these proton sources. The relationship between waveguide depth and fabrication conditions were established. It is shown that diffusion rate increases with the acidity of the proton source.

The structural properties of the proton-exchanged waveguiding layer were characterized using several methods, viz. Raman spectroscopy, infrared spectrometry, double-crystal x-ray diffractometry and thermogravimetric analysis. There is a positive strain of 0.4% along the crystallographic z-axis in the waveguiding layer.

Proton-exchanged waveguides fabricated using toluic and stearic acids exhibit a step-index profile similar to that of the popular benzoic acid. The refractive index profile of proton-exchanged waveguides using phosphoric acid is not a simple step function, but is a graded function. The graded index profile could be modelled accurately by a polynomial expression with a maximum surface index increase of 0.145. The value obtained is the largest reported using an acidic medium. Proton-exchanged waveguides using cinnamic acid also exhibit a graded-index profile which could be modelled accurately by a truncated parabolic junction. The maximum surface index change is 0.141 measured at 0.633μm wavelength, and is larger than

those obtained using other organic acids.

The effects of post-exchange annealing on these proton-exchanged waveguides have been studied systematically. Annealing reduces the waveguide propagation loss, increases the number of waveguide modes, and changes the refractive index profile to a Gaussian-like function. Both the surface index change and waveguide depth increase were found to follow a power-law relationship with annealing time.

Contents

Chapter 1

INTRODUCTION

1.1 An Overview of Integrated Optics

Fuelled by the invention of semiconductor laser [1.1] and concurrently with the development of low-loss optical fiber for communications [1.2], vigorous research efforts began in the late 1960s focusing on the application of thin-film and microfabrication technologies to the development of miniaturized optical circuits and devices [1.3-1.5]. The name *integrated optics* was coined by S.E. Miller of Bell Laboratories who envisaged a new form of 'laser beam circuitry' [1.6]. The main idea of integrated optics is to process and manipulate light which is confined in optical waveguides. Research in integrated optics has evolved in two main directions [1.7,1.8]: (i) exploration of guided-wave techniques to fabricate new or improved optical components, and (ii) integration of a number of optical components on a single substrate to form integrated optical circuits (IOC). The various optical components in IOC are interconnected by optical waveguides which play a role similar to that of copper conductors in electronic integrated circuits.

Integrated optics technology [1.8,1.9] provides key advantages and unique capabilities in accomplishing compact, miniaturized, and rugged optical devices which are insensitive to external thermal and mechanical variations. These devices are also immune to electromagnetic interference from surrounding electric fields. Using lightwave as the signal carrier with an optical frequency of 10^{14} - 10^{15}Hz, potentially large usable bandwidth could be achieved. In addition, integration of several guided-wave devices may well eliminate the alignment problem that is

crucial in optical systems. At the same time it reduces the power requirement. Higher reliability and small size would be attainable through application of batch fabrication technology.

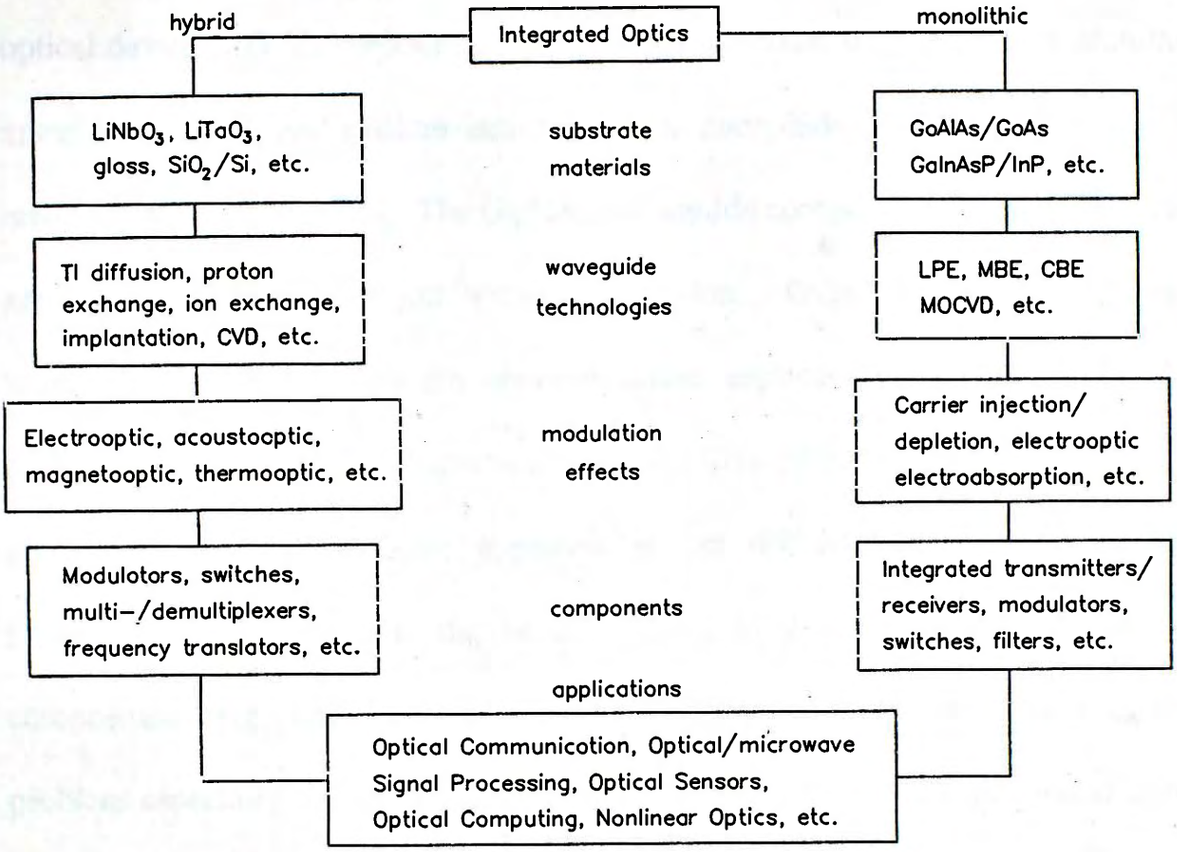

Fig. 1.1 Monolithic and hybrid approaches to integrated optics

Progress in integrated optics is driven largely by the enormous development in the areas of optical fiber communications, optical signal processing and optical sensors [1.10-1.13]. In particular, it is the rapid growth in the use of optical communication systems in the past decade that has stimulated worldwide research and development activities in integrated optics. Integrated optics devices have been investigated and demonstrated in the last two decades. Two separate approaches to the realization of integrated optical circuits are pursued (Fig.1.1): a monolithic approach, where all devices were fabricated on a common substrate, and a hybrid

approach, where several devices were fabricated on different substrates and subsequently bonded together [1.8,1.14]. Key features of these two approaches are distinguished by their substrate materials and waveguide fabrication technologies. In order to integrate monolithically the sources, detectors as well as guided-wave optical devices, III-V compound semiconductor materials such as gallium-aluminum arsenide (GaAlAs) and gallium-indium arsenide phosphide (GaInAsP) have attracted much attention [1.15,1.16]. The GaAlAs waveguide components on GaAs substrates are used for the 0.7-0.9 μm wavelength region. GaInAsP materials are more important for long-wavelength communication applications where optical fibers exhibit very low loss and dispersion in the vicinity of 1.55 μm wavelength. The main problem of monolithic approach is the different technologies involved [1.14-1.16]. In particular the lateral control in growing devices of different composition (e.g. laser diodes, waveguides, detectors, etc.) remains a difficult problem especially for *in-situ* processes. Therefore, monolithic integrated optical devices are still in an early stage of research and development.

The hybrid approach to IOC uses different substrate materials to optimize the performances of individual components, and the components are assembled together in a single working unit or in an overall fiber-pigtailed package. Ferroelectric crystals, particularly lithium niobate ($LiNbO_3$) and lithium tantalate ($LiTaO_3$), are promising substrate materials for the hybrid approach [1.15,1.16]. In particular, $LiNbO_3$ is the premier material for many integrated optics components by virtue of its excellent optical properties and well-established fabrication technologies for low-loss waveguides. At present the status of development of $LiNbO_3$ devices is higher than that of semiconductor waveguide components [1.17,1.18]. A large variety of

$LiNbO_3$ single components and the integration of several components on a single substrate have been demonstrated. Some significant examples of application of $LiNbO_3$ IOC are described in the following subsection.

1.2 Application of Lithium Niobate Integrated Optical Circuit

$LiNbO_3$ integrated optical circuits have a variety of applications from optical communications [1.17-1.20], coherent optical fiber systems [1.21,1.22], microwave applications [1.23] to optical signal processing and sensing [1.24], etc. This progress has been achieved by improvements made in the quality of the substrate material (homogeneity, control of stoichiometry, impurity content), in the waveguide fabrication technology, and in the tools for device modelling. The high status of $LiNbO_3$ IOC is highlighted by the following nonexhaustive listing of applications:

(a) High-speed intensity and phase modulators [1.25-1.28];

(b) Complex optical switch matrices [1.29-1.33];

(c) Wavelength multiplexers and demultiplexers [1.34,1.35];

(d) Optical sensors for temperature [1.36], humidity [1.37], displacement [1.38], electric field [1.39] and wavefront angle measurements [1.40];

(e) Optical signal processing chips for fiber optic gyroscopes [1.41,1.42];

(f) Coherent optical heterodyne detectors [1.43];

(g) Optical frequency translators [1.44-1.47];

(h) Picosecond pulse generators [1.48,1.49].

Further examples of $LiNbO_3$ IOC for different applications can be found in a number of general references [1.50-1.52] and some recent excellent review papers [1.53-1.59].

$LiNbO_3$ IOC are currently offered commercially by at least half a dozen manufacturers in the US, Europe and Japan [1.60]. These include Crystal Technology Inc., United Technologies Photonics, GEC-Marconi and Ericsson Telecom. Several are setting up pilot production lines for a wide range of components. The components emerging in the market target a very wide range of applications, including telecommunications, sensors, and instrumentation. Although there have been many demonstrations of the performance advantages of $LiNbO_3$ IOC, these components are mainly for niche applications and are available commercially in small quantities because the technological processes required to produce these components have not yet reached an economical stage [1.13,1.16].

1.3 Summary

A brief overview on the evolution of integrated optics has been given. The two main approaches to the realization of integrated optical circuits, viz. the hybrid and the monolithic approach, are described. An illustration is given on recent applications of lithium niobate integrated optics devices. $LiNbO_3$ as well as semiconductor-based IOC may be used for a wide range of applications in the future.

Since optical waveguides play an important role in integrated optics devices, the theory of optical waveguides is discussed firstly in Chapter 2, including numerical methods to calculate propagation constants for both planar and channel optical waveguides. The fabrication of optical waveguides with a review of the substrate materials and fabrication techniques is discussed in Chapter 3. The fabrication process of proton-exchanged $LiNbO_3$ waveguides are described in Chapter 4, together with the measurements of waveguide parameters. In this work,

$LiNbO_3$ planar and channel waveguides have been fabricated using the proton-exchange process with different proton sources: phosphoric, toluic, stearic and cinnamic acids. The results of our systematic studies are discussed in Chapter 5, which includes the diffusion parameters, annealing properties and structural characteristics of these waveguides. Finally, conclusions are given in Chapter 6.

Chapter 2

Optical Waveguide Theory

2.1 Introduction

This chapter is devoted to the basic theory of thin-film optical waveguides. Dielectric slabs are the simplest optical waveguides. The study of planar (or slab) waveguides and their properties is useful in gaining an understanding of the waveguiding properties of more complicated structures. In Section 2.2, the principles of propagation of two-dimensional planar waveguides are discussed using the ray optics approach. The propagation characteristics of both step-index and graded-index planar waveguides are described. Since most waveguide devices require three-dimensional waveguide structures, approximation methods for quantitative analysis of these 3D channel waveguides are discussed in Section 2.3, followed by a summary in Section 2.4.

2.2 Ray Optics Treatment of Planar Waveguide

Ray (or geometric) optics [2.1,2.2] describes the propagation of light by defining rays as the lines that cross the planes of constant phase of the light at right angles. Light rays have intuitive appeal because a narrow beam of light is a good approximation to the more abstract notion of light waves. In the ray optics picture, light rays in a homogeneous medium follow a straight path. To explain the guidance of light in a planar waveguide, one needs only Snell's law of refraction [2.3] and the related phenomenon of total internal reflection. With the definition of the angles shown in Fig.2.1, Snell's law can be expressed in the form:

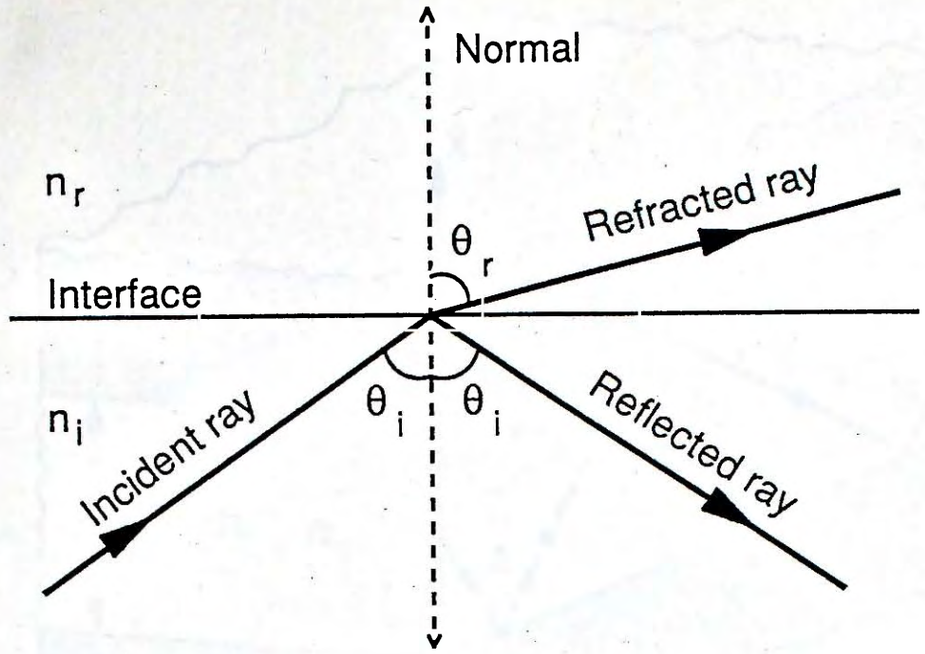

Fig.2.1 Refraction and reflection of a plane wave at a dielectric interface

$$n_i \sin\theta_i = n_r \sin\theta_r \tag{2.1}$$

If $n_i > n_r$, it is apparent from Eq.2.1 that there is no real angle θ_r for $n_i\sin\theta_i > n_r$. In this case no refraction is possible and the light ray is totally reflected inside medium i. The critical angle θ_c associated with the onset of total internal reflection is defined as

$$\theta_c = \arcsin(n_r/n_i) \tag{2.2}$$

We shall assume throughout this chapter that the guided light is coherent and monochromatic and the waveguides consist of dielectric media that are lossless, isotropic and homogeneous.

2.2.1 Step-index Waveguide

The basic planar waveguide with a step-index profile is illustrated in Fig.2.2, where a uniform isotropic planar film of refractive index n_1 and thickness d is sandwiched between two semi-infinite substrate and cover layers of index n_2 and n_3, respectively. In order to confine the light in the film, it is necessary that n_1 is larger

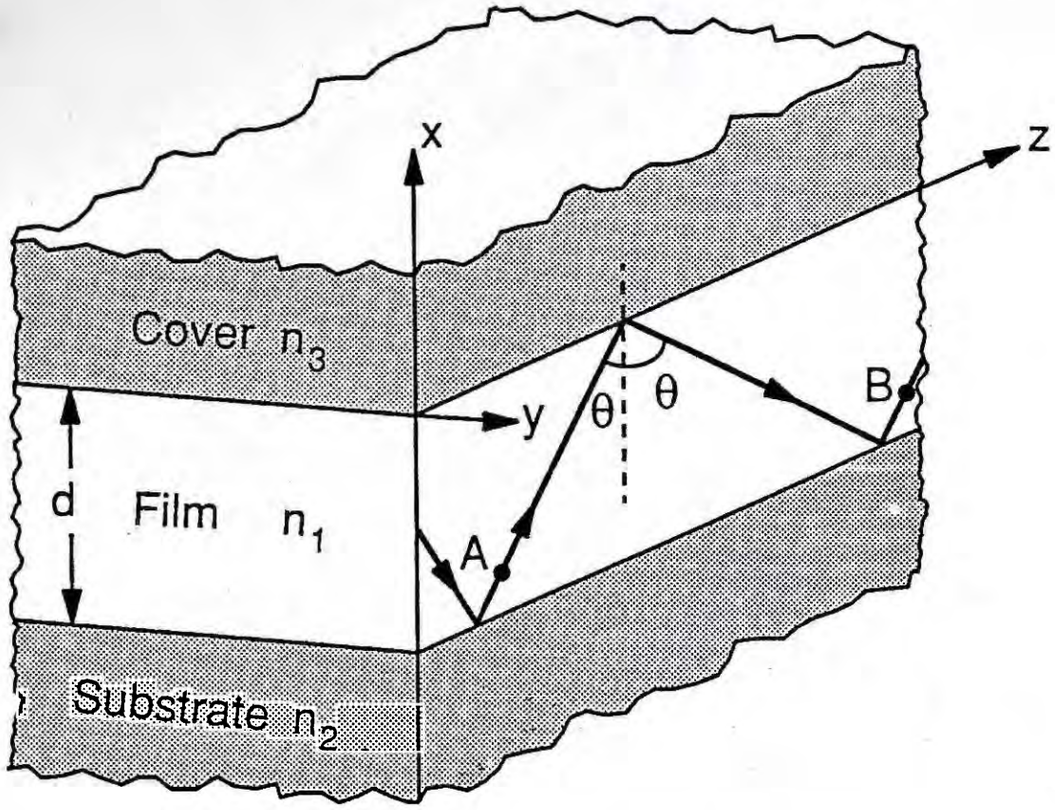

(a)

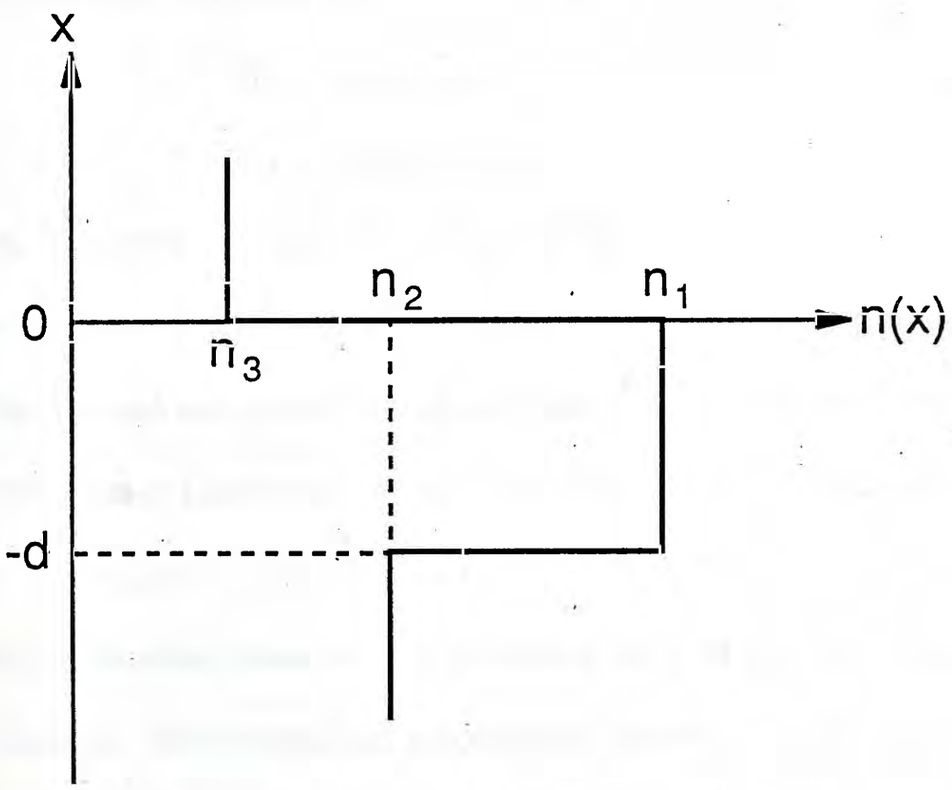

(b)

Fig.2.2 Ray propagation in an optical planar waveguide. (a) Configuration of the waveguide showing the zig-zag path of a guided mode; (b) Refractive index profile of the three layers.

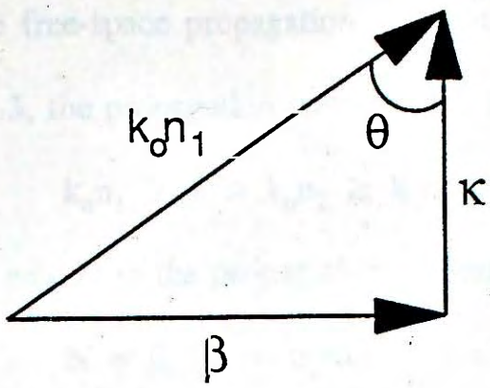

Fig.2.3 Geometric relationship between the propagation constants

than n_2 and n_3, and the thickness d of the film is above the critical thickness. Usually the cover medium is air (i.e. $n_3 = 1$) so that we have $n_1 > n_2 \geq n_3$.

Consider now the light ray travels at an angle of incidence θ (Fig.2.2). The two critical angles θ_{12} and θ_{13} for total internal reflection occurring at the film-substrate and film-cover interfaces are:

$$\theta_{12} = \arcsin(n_2/n_1)$$

$$\theta_{13} = \arcsin(n_3/n_1) \qquad (2.3)$$

Since $n_2 \geq n_3$ in general, we have $\theta_{12} \geq \theta_{13}$. If the condition $\theta > \theta_{12}, \theta_{13}$ is satisfied, total internal reflection occurs at both interfaces. Then the light is confined in the film and propagates in a zig-zag path (Fig.2.2). In this case, light confinement takes place transversely in the x direction and this corresponds to a guided mode of propagation supported by the planar waveguide.

In Fig.2.3, the local plane wave vector $k_o n_1$ is resolved into two orthogonal components β and κ. The longitudinal propagation constant β and the transverse propagation constant κ is related to the incident angle θ by

$$\beta = k_o n_1 \sin\theta$$

$$\kappa = k_o n_1 \cos\theta = [k_o^2 n_1^2 - \beta^2]^{1/2} \qquad (2.4)$$

where k_o ($=2\pi/\lambda$) is the free-space propagation constant and λ is the free-space wavelength. From Eq.2.3, the propagation constant β is bounded by

$$k_o n_1 > \beta > k_o n_2 \geq k_o n_3 \tag{2.5}$$

The effective index N is related to the propagation constant β by

$$N = \beta / k_o = n_1 \sin\theta \tag{2.6}$$

Therefore the value of N is in the range of the film and substrate indices, i.e.

$$n_1 > N > n_2 \geq n_3 \tag{2.7}$$

To avoid decay of optical energy due to destructive interference as the light travels along the waveguide, the condition of transverse phase resonance must be satisfied [2.1,2.2]. This requires that the total transverse phase change for a point on a wavefront that travels one complete zig-zag path between the film-cover interface to the film-substrate interface and back again (e.g. from point A to B in Fig.2.2) must add up to an integral multiple of 2π. The phase resonance condition can be expressed as

$$2k_o n_1 d \cos\theta - 2\phi_{12} - 2\phi_{13} = 2m\pi \tag{2.8}$$

where m is an positive integer which identifies the mode number, ϕ_{12} and ϕ_{13} are the phase changes suffered upon total internal reflection at the film-substrate and film-cover interfaces, respectively. The values of $-2\phi_{12}$ and $-2\phi_{13}$ represent the Goos-Hänchen shifts [2.1-2.5]. These phase shifts can be interpreted as penetration of the light ray into the substrate and cover layers before it is reflected, and their values depend on the polarization of the light. For a wave with transverse electric (TE) polarization, i.e. the electric field is perpendicular to the plane of incidence, the phase changes ϕ_{12} and ϕ_{13} are given by

$$\phi_{12} = \arctan\sqrt{\frac{\beta^2 - k_o^2 n_2^2}{k_o^2 n_1^2 - \beta^2}} = \arctan\sqrt{\frac{N^2 - n_2^2}{n_1^2 - N^2}} \tag{2.9}$$

$$\phi_{13} = \arctan\sqrt{\frac{\beta^2 - k_o^2 n_3^2}{k_o^2 n_1^2 - \beta^2}} = \arctan\sqrt{\frac{N^2 - n_3^2}{n_1^2 - N^2}} \tag{2.10}$$

For a wave polarized in the plane of incidence, i.e. transverse magnetic (TM) polarization, the phase shifts can be expressed as

$$\Phi_{12} = \arctan\frac{n_1^2\sqrt{\beta^2 - k_o^2 n_2^2}}{n_2^2\sqrt{k_o^2 n_1^2 - \beta^2}} = \arctan\frac{n_1^2\sqrt{N^2 - n_2^2}}{n_2^2\sqrt{n_1^2 - N^2}} \tag{2.11}$$

$$\phi_{13} = \arctan\frac{n_1^2\sqrt{\beta^2 - k_o^2 n_3^2}}{n_3^2\sqrt{k_o^2 n_1^2 - \beta^2}} = \arctan\frac{n_1^2\sqrt{N^2 - n_3^2}}{n_3^2\sqrt{n_1^2 - N^2}} \tag{2.12}$$

It can be seen that substitution of either Eqs.2.9-2.10 or Eqs.2.11-2.12 into Eq.2.8 results in a transcendental equation of only one variable (i.e. β or N). The transverse decay constants γ_2 and γ_3 are defined as

$$\gamma_2^2 = \beta^2 - k_o^2 n_2^2$$

$$\gamma_3^2 = \beta^2 - k_o^2 n_3^2 \tag{2.13}$$

Hence the eigenvalue equation for TE waves [2.1-2.5] can be expressed as

$$\tan(\kappa d) = \frac{\kappa(\gamma_2 + \gamma_3)}{\kappa^2 - \gamma_2\gamma_3} \tag{2.14}$$

Similarly, the eigenvalue equation for TM waves can be expressed as

$$\tan(\kappa d) = \frac{n_1^2\kappa(n_3^2\gamma_2 + n_2^2\gamma_3)}{n_2^2 n_3^2\kappa^2 - n_1^4\gamma_2\gamma_3} \tag{2.15}$$

Note that the mode number m defined in Eq.2.8 is implicit in these two eigenvalue equations. Each value of m corresponds to a distinct propagation constant and electric field distribution in the waveguide. The modal electric and magnetic field properties can be derived using the rigorous electromagnetic theory. For TE modes the only nonzero field components are E_y, H_x, and H_z. The transverse electric field $E_y(x)$ can be expressed in terms of a single constant C,

$$\begin{aligned} E_y &= C \exp(-\gamma_3 x) && x \geq 0 \\ E_y &= C [\cos(\kappa x) - (\gamma_3/\kappa) \sin(\kappa x)] && -d \leq x < 0 \\ E_y &= C [\cos(\kappa d) + (\gamma_3/\kappa) \sin(\kappa d)] \exp[\gamma_2(x+d)] && x < -d \end{aligned} \qquad (2.16)$$

For the case of TM modes, the nonzero field components are H_y, E_x, and E_z. The transverse magnetic component $H_y(x)$ is given by

$$\begin{aligned} H_y &= D\Gamma \exp(-\gamma_3 x) && x \geq 0 \\ H_y &= D [\Gamma\cos(\kappa x) - \sin(\kappa x)] && -d \leq x < 0 \\ H_y &= D [\Gamma\cos(\kappa d) + \sin(\kappa d)] \exp[\gamma_2(x+d)] && x < -d \end{aligned} \qquad (2.17)$$

where $\Gamma = n_3^2 \kappa / n_1^2 \gamma_3$. The constants C and D can be arbitrary chosen so that the field components are normalized in the y direction.

When the waveguide parameters n_1, n_2, n_3 and d are given, the effective indices N and the field distributions of the guided TE and TM modes can be obtained by solving the transcendental equations Eqs.2.14 to 2.17. Fig.2.4 shows an example of the theoretical dispersion characteristics together with the electric field distributions for the first three modes of a step-index planar waveguide.

2.2.2 Graded-index Waveguide

Common waveguide fabrication processes such as thermal diffusion and ion exchange produce optical waveguides with graded-index profiles, i.e. the refractive

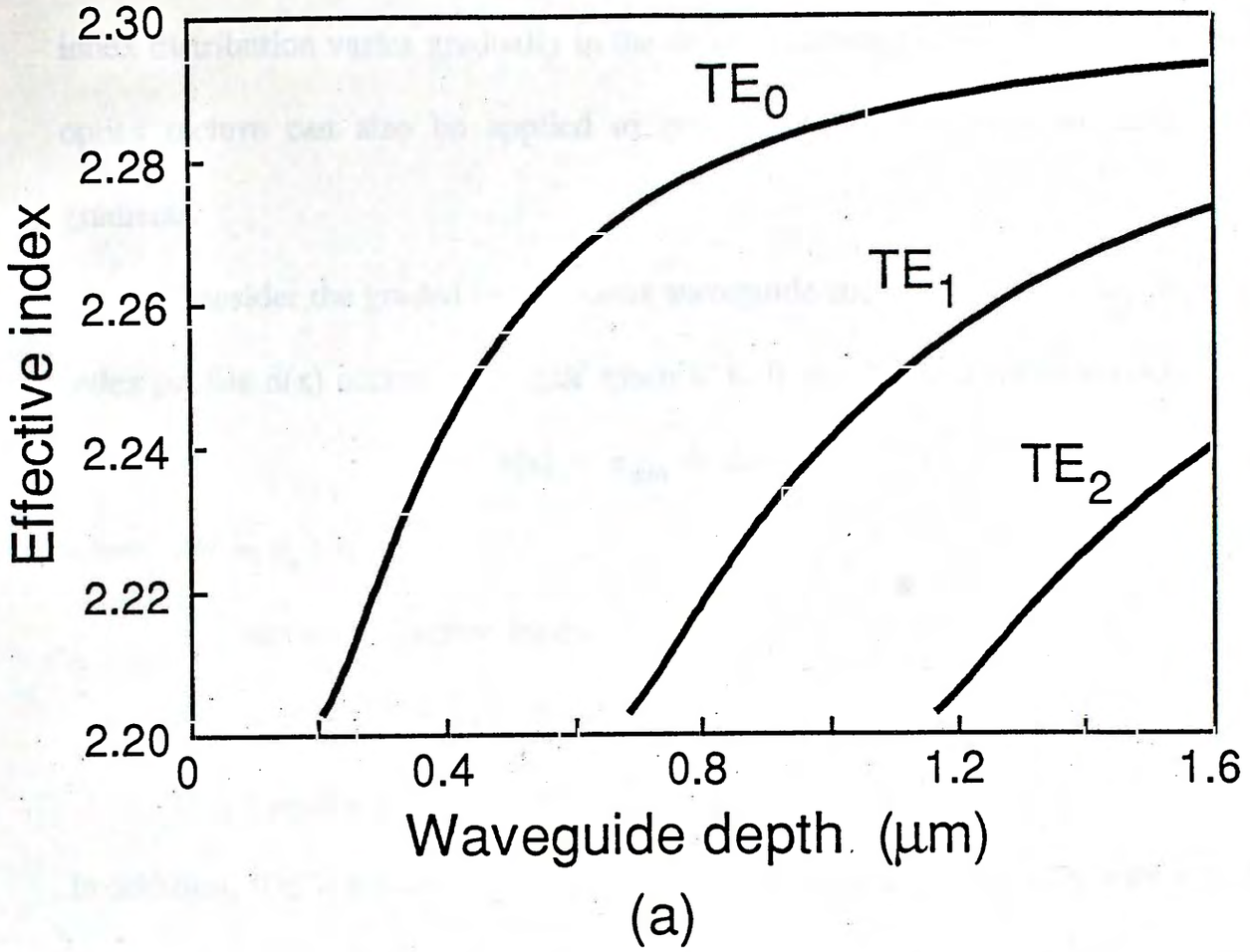

(a)

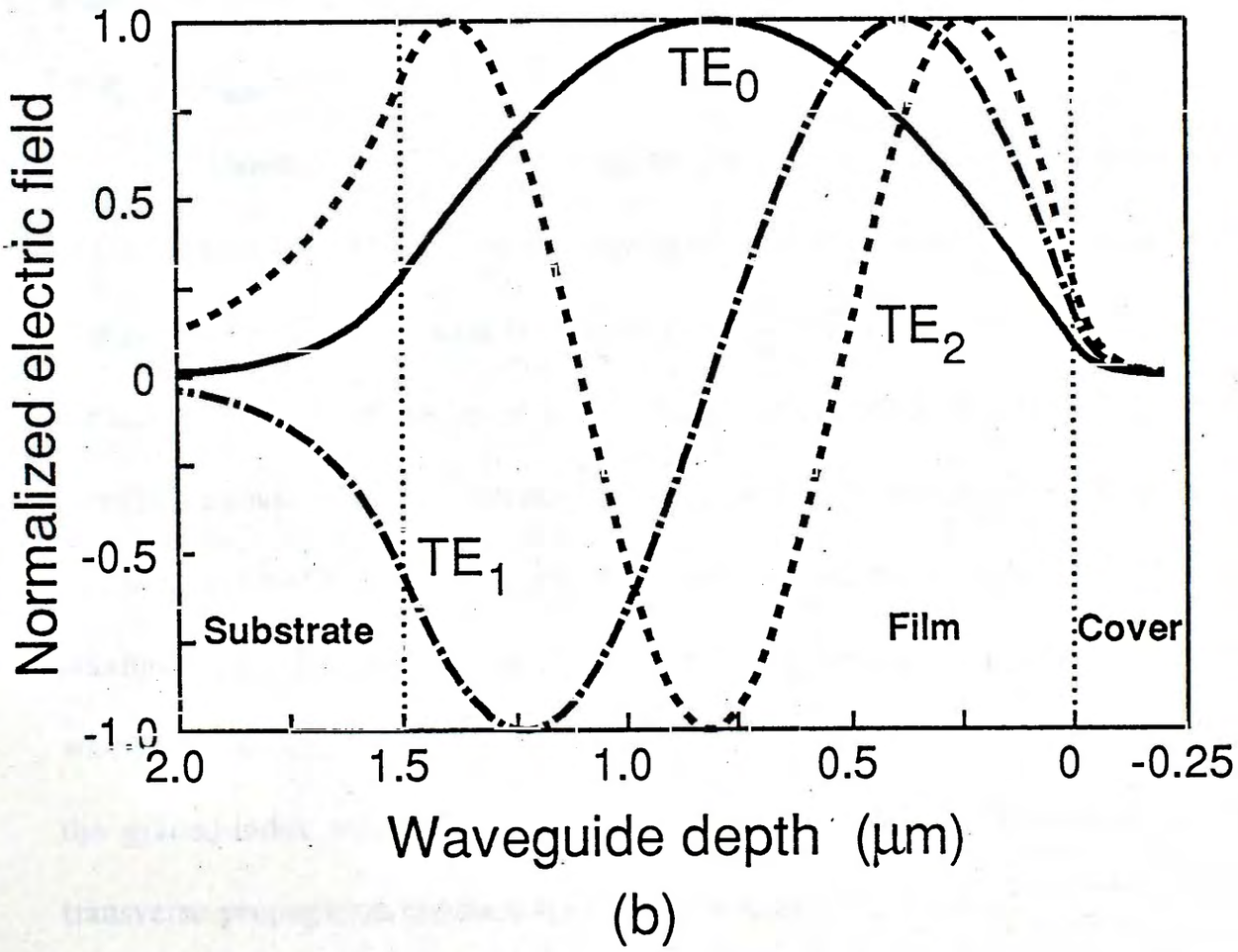

(b)

Fig.2.4 Propagation characteristics of step-index planar waveguides. (a) Theoretical dispersion curves (n_1=2.3, n_2=2.202, n_3=1, λ=0.6328μm); (b) Transverse electric field distributions (d=1.5μm).

index distribution varies gradually in the depth direction [2.5-2.7]. The simple ray optics picture can also be applied to graded-index waveguides of small index gradients.

Consider the graded-index planar waveguide shown in Fig.2.5, the refractive index profile n(x) occupies the half space $x < 0$ and has a distribution defined as

$$n(x) = n_{sub} + \Delta n\, f(x) \tag{2.18}$$

where $\Delta n = n_s - n_{sub}$

n_s : surface refractive index

n_{sub} : substrate refractive index

f(x) : profile function describing the variation of n(x) with x

In addition, f(x) is assumed to be a function decreasing monotonically with x so that it takes on values between 0 and 1. The index function n(x) is therefore bounded by n_s and n_{sub}.

As shown in Fig.2.5, the waveguide depth is denoted by d at which the value of f(-d) equals 1/e. The curved ray trajectories make an angle $\theta(x)$ with the x-axis. The angle $\theta(x)$ at $x = 0$ must be greater than the critical angle $\arcsin(n_c/n_s)$ (n_c is the refractive index of the cover layer) so that total internal reflection occurs at the waveguide/cover interface. Because of the graded-index distribution, the angle $\theta(x)$ increases gradually as the ray penetrates into the substrate region and reaches a maximum of $\pi/2$ at the turning point $-x_t$ at which the ray turns back towards the waveguide surface. The maximum penetration depth x_t is the *effective* thickness of the graded-index waveguide. The longitudinal propagation constant β and the transverse propagation constant $\kappa(x)$ are defined as

$$\beta = k_o n(x) \sin\theta(x)$$

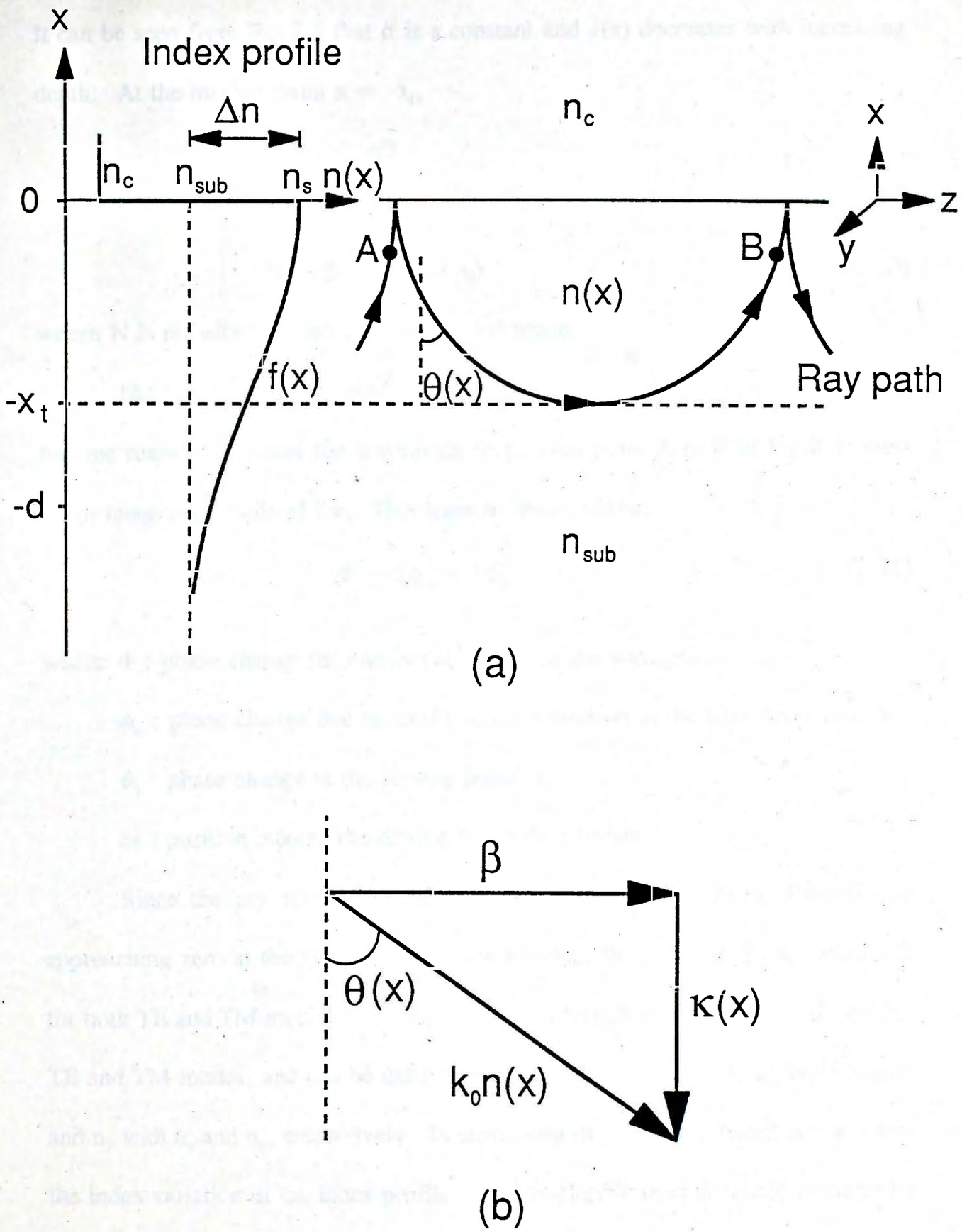

Fig.2.5 (a) Index profile and ray trajectories of a graded-index planar waveguide; (b) Components of the wave vector.

$$\kappa(x) = k_o n(x) \cos\theta(x) = [k_o^2 n(x)^2 - \beta^2]^{1/2} \qquad (2.19)$$

It can be seen from Fig.2.5 that β is a constant and $\kappa(x)$ decreases with increasing depth. At the turning point $x = -x_t$,

$$\theta(-x_t) = \pi/2$$

$$\kappa(-x_t) = 0$$

$$N = \beta / k_o = n(-x_t) \qquad (2.20)$$

where N is the effective index of the guided mode.

The condition of light guidance requires that the total transverse phase change for one round trip across the waveguide (e.g. from point A to B in Fig.2.5) must be an integral multiple of 2π. This leads to the condition

$$\Phi - 2\phi_c - 2\phi_t = 2m\pi \qquad (2.21)$$

where Φ : phase change for one passage through the waveguide

ϕ_c : phase change due to total internal reflection at the film-cover interface

ϕ_t : phase change at the turning point $-x_t$

m : positive integer identifying the mode number

Since the ray approaches grazing incidence with the index discontinuity approaching zero at the fictitious boundary $x = -x_t$, the phase shift $2\phi_t$ equals $\pi/2$ for both TE and TM modes [2.5-2.9]. The Goos-Hänchen shift $-2\phi_c$ is different for TE and TM modes, and can be calculated using Eqs.2.10 and 2.12 by replacing n_1 and n_3 with n_s and n_c, respectively. In most cases of practical interest, $\Delta n \ll 1$ and the index variation of the index profile n(x) is negligible over distances in the order of a wavelength. As a consequence, the well-known Wentzel-Kramers-Brillouin (WKB) condition [2.6-2.9], i.e. $\lambda dn(x)/dx \ll 1$, is satisfied. Hence the phase change Φ can be expressed in terms of the WKB integral:

$$\Phi = 2\int_{-x_t}^{0} \sqrt{k_o^2 n(x)^2 - \beta^2}\, dx = 2k_o \int_{-x_t}^{0} \sqrt{n(x)^2 - N^2}\, dx \qquad (2.22)$$

The integrand vanishes at the turning point $-x_t$ which serves as a fictitious boundary separating regions of oscillatory and evanescent fields.

By substituting Eq.2.22 into Eq.2.21, the eigenvalue equation for a graded-index planar waveguide can be expressed as

$$2k_o \int_{-x_t}^{0} \sqrt{n(x)^2 - N^2}\, dx = (2m + \frac{1}{2})\pi + 2\phi_c \qquad (2.23)$$

An exact analytical solution to this eigenvalue equation does not exist because of its complicated nature. Moreover, the WKB integral involves an integration limit $-x_t$ which depends on the value of the integrand itself. As a result, numerical methods are usually employed to solve this eigenvalue equation. Hocker and Burns [2.10] have described a simple approximation method for calculating the WKB integral. In their algorithm, piecewise-linear segments are used to approximate the ray trajectories in the waveguide layer. The WKB integral can thus be calculated by summing the incremental transverse phase change along the ray paths. By combining the WKB integral with the Goos-Hänchen shift at the waveguide/cover interface, the eigenvalue equation can be solved numerically and yields the dispersion characteristics for an arbitrary refractive index profile. Fig.2.6 shows the theoretical dispersion curves for a Gaussian and a complementary error function index profile using this method.

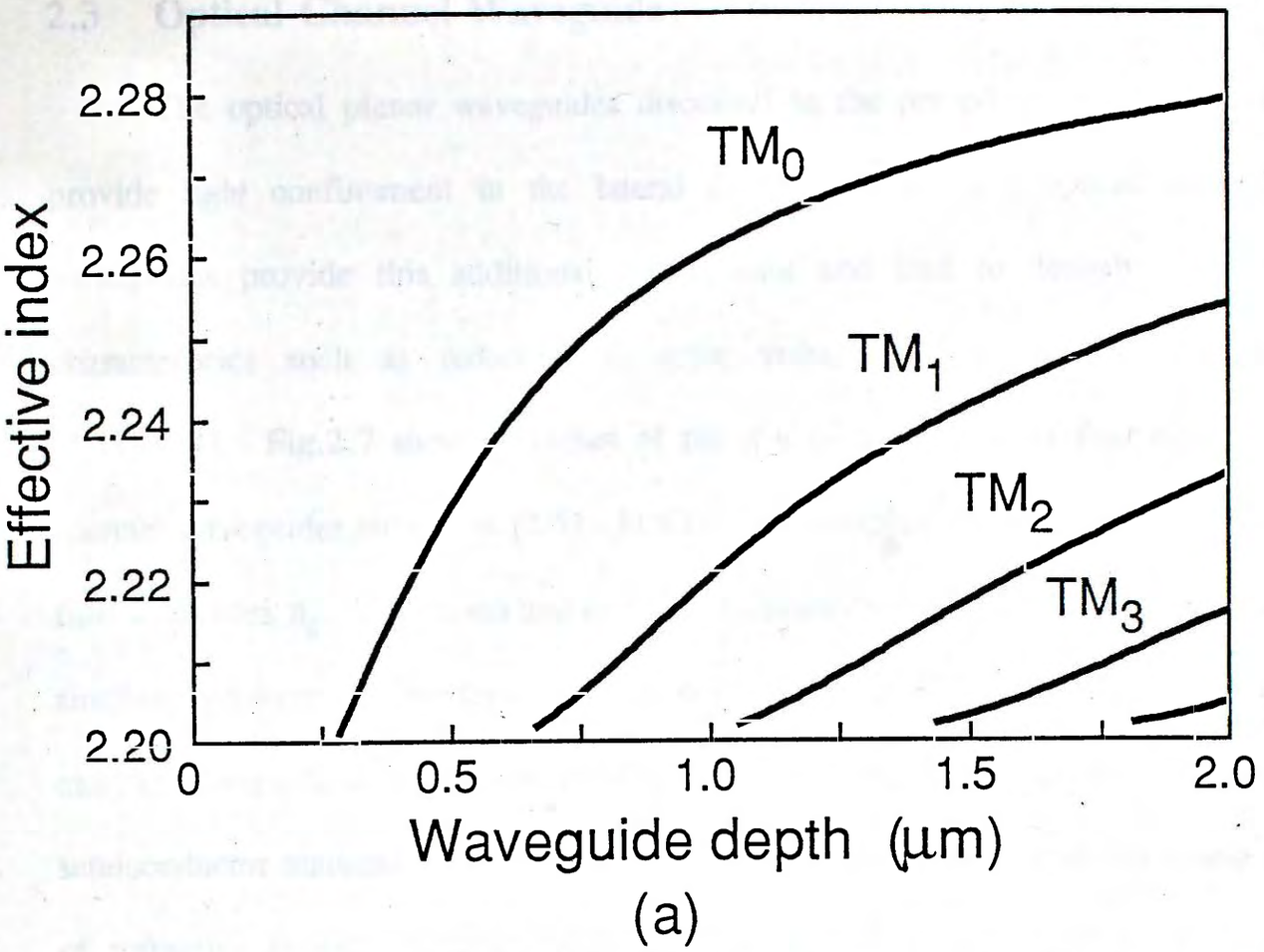

(a)

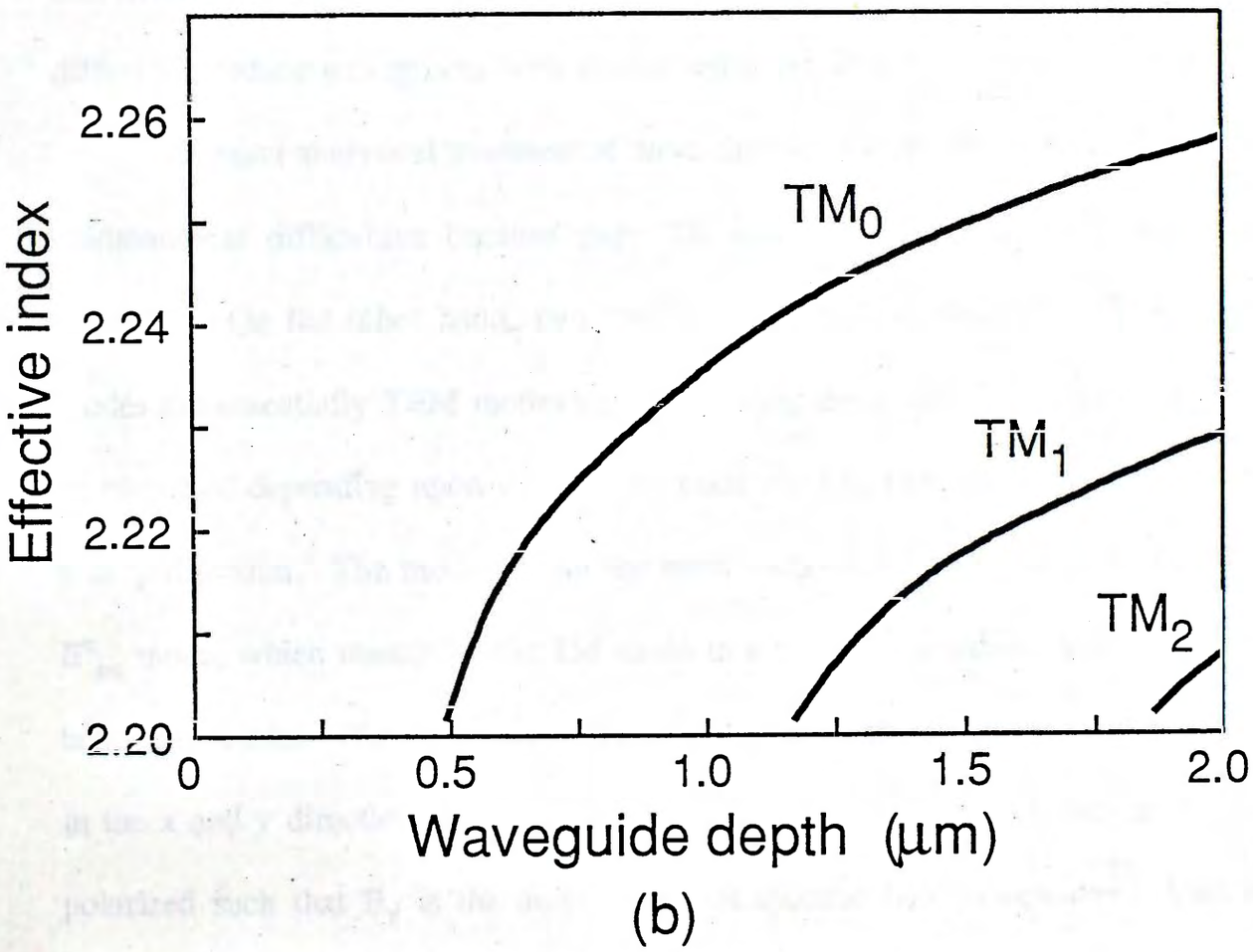

(b)

Fig.2.6 Theoretical dispersion curves for graded-index planar waveguides with $\Delta n = 0.1$, $n_{sub} = 2.202$, $n_c = 1$, $\lambda = 0.6328\mu m$. (a) Gaussian profile: $f(x) = \exp(-x^2)$; (b) Complementary error function: $f(x) = \text{erfc}(x)$.

2.3 Optical Channel Waveguide

The optical planar waveguides discussed in the preceding section do not provide light confinement in the lateral direction (y-axis). Optical channel waveguides provide this additional confinement and lead to desirable device characteristics such as reduction in drive voltage and power consumption [2.11-2.14]. Fig.2.7 shows sketches of the x-y cross-sections of four common channel waveguides structures [2.5]. In all these examples, light is confined in the film with index n_g. The raised and embedded channel waveguide structures are the simplest and most popular for waveguide devices, while the ridge and strip-loaded channel waveguide structures are usually adopted for integrated optics devices using semiconductor materials. For reasons of simplicity Fig.2.7 shows abrupt changes of refractive index. Common waveguide fabrication process such as thermal diffusion produce waveguides with graded index profiles.

An exact analytical treatment of these channel waveguides is accompanied by mathematical difficulties because pure TE and TM modes are not supported [2.1,2.2]. On the other hand, two families of hybrid modes exist. The hybrid modes are essentially TEM modes polarized along the x and y directions, and can be classified depending upon whether the main electric field component lies in the x or y direction. The mode having the main transverse electric field E_x is called E^x_{pq} mode, which resembles the TM mode in a planar waveguide, with E_y and E_z being negligible. The suffixes p and q correspond to the number of field maxima in the x and y directions, respectively. Similarly, E^y_{pq} mode (TE-like mode) are polarized such that E_y is the only significant electric field component. Various approximation methods have been proposed for analyzing optical channel waveguide.

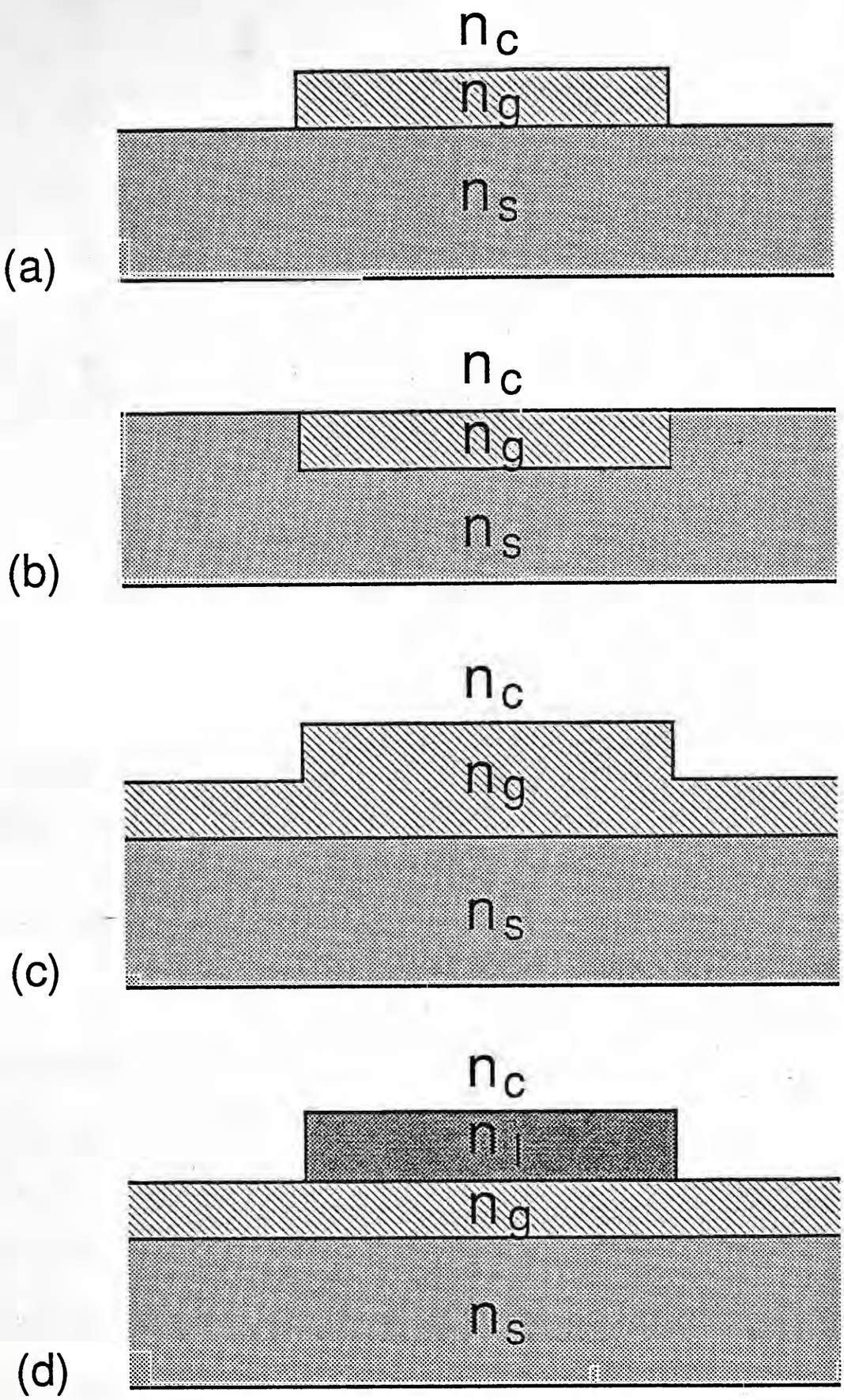

Fig.2.7 Schematic cross-sections of optical channel waveguide structures. (a) Raised, (b) Embedded, (c) Ridge, (d) Strip-loaded waveguide.

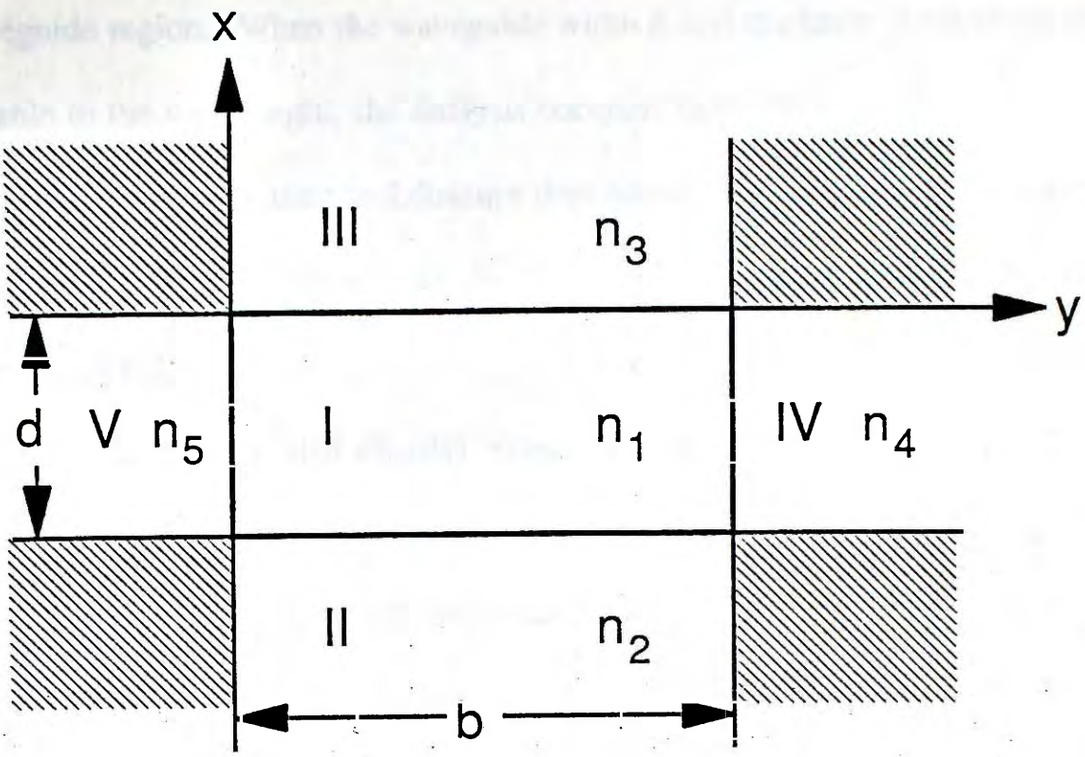

Fig.2.8 Cross-section of a rectangular channel waveguide

Two popular approximate analyses, viz. Marcatili's method [2.15] and the effective index method [2.16], will be discussed in the following subsections.

2.3.1 Marcatili's Method

Fig.2.8 shows the cross-section of a rectangular channel waveguide of dimensions $b \times d$ with core refractive index n_1 surrounded on four sides by media of indices n_2, n_3, n_4 and n_5. Marcatili's approximation method [2.15] considers the case that the modes are guided sufficiently strongly and hence most of the optical power is confined in region I with only a small portion of power travels to the four cladding regions II, III, IV and V, where the electromagnetic fields decay exponentially. It is then reasonable to assume that the magnitudes of the fields in the four shaded corner regions are small enough to be neglected. Clearly this method works well for modes far from cutoff and whose energy is well confined in

the waveguide region. When the waveguide width b and thickness d are small and comparable to the wavelength, the analysis becomes inaccurate.

Assuming that the time and distance dependence of the field is exp[j(ωt-βz)], the transverse field components can be expressed in terms of the longitudinal components [2.1,2.15]:

$$E_x = -(j/\kappa_i^2)[(\beta\, \partial E_z/\partial x) + (\omega\mu_o\, \partial H_z/\partial y)] \tag{2.24}$$

$$E_y = -(j/\kappa_i^2)[(\beta\, \partial E_z/\partial y) - (\omega\mu_o\, \partial H_z/\partial x)] \tag{2.25}$$

$$H_x = -(j/\kappa_i^2)[(\beta\, \partial H_z/\partial x) - (\omega n_i^2 \varepsilon_o\, \partial E_z/\partial y)] \tag{2.26}$$

$$H_y = -(j/\kappa_i^2)[(\beta\, \partial H_z/\partial y) + (\omega n_i^2 \varepsilon_o\, \partial E_z/\partial x)] \tag{2.27}$$

where $\kappa_i^2 = k_o^2 n_i^2 - \beta^2$. The refractive index n_i assumes the values of n_1, n_2, n_3, n_4 and n_5 for fields in the five regions of the waveguide. The longitudinal components of the electric and magnetic fields satisfy the wave equation:

$$\frac{\partial^2}{\partial x^2}\begin{pmatrix}E_z\\H_z\end{pmatrix} + \frac{\partial^2}{\partial y^2}\begin{pmatrix}E_z\\H_z\end{pmatrix} + \kappa_i^2\begin{pmatrix}E_z\\H_z\end{pmatrix} = 0 \tag{2.28}$$

Let us consider first the case of E^x_{pq} modes. Suppressing the time- and z-dependence factor exp[j(ωt-βz)], the following field components satisfy Eqs.2.24 to 2.28 in region I:

$$E_z = A \cos \kappa_x(x+\xi) \cos \kappa_y(y+\eta) \tag{2.29}$$

$$H_z = -A\, (\varepsilon_o/\mu_o)^{1/2} n_1^2 (\kappa_y/\kappa_x)\, (k_o/\beta) \sin \kappa_x(x+\xi) \sin \kappa_y(y+\eta) \tag{2.30}$$

$$E_x = (jA/\kappa_x\beta)\, (k_o^2 n_1^2 - \kappa_x^2) \sin \kappa_x(x+\xi) \cos \kappa_y(y+\eta) \tag{2.31}$$

$$E_y = -jA\, (\kappa_y/\beta) \cos \kappa_x(x+\xi) \sin \kappa_y(y+\eta) \tag{2.32}$$

$$H_x = 0 \tag{2.33}$$

$$H_y = jA\, (\varepsilon_o/\mu_o)^{1/2} n_1^2 (k_o/\kappa_x) \sin \kappa_x(x+\xi) \cos \kappa_y(y+\eta) \tag{2.34}$$

where $\kappa_1^2 = k_o^2 n_1^2 - \beta^2 = \kappa_x^2 + \kappa_y^2$. In these equations, ξ and η are phase

constants to be determined later.

The electromagnetic fields in regions II, III, IV and V are given by relations Eqs.2.29 to 2.34 multiplied by exponentially decaying factors with decay constants γ_2, γ_3, γ_4 and γ_5. In these regions, the principle electric field component E_x is given by:

Region II: $$E_x = jA\,[(\gamma_2^2+k_o^2n_2^2)/\gamma_2\beta]\cos\kappa_x(\xi - d) \times \cos\kappa_y(y+\eta)\exp[\gamma_2(x+d)] \quad (2.35)$$

Region III: $$E_x = -jA\,[(\gamma_3^2+k_o^2n_3^2)/\gamma_3\beta]\cos\kappa_x\xi\cos\kappa_y(y+\eta)\exp(-\gamma_3 x) \quad (2.36)$$

Region IV: $$E_x = jA\,(n_1^2/n_4^2)\,[(k_o^2n_4^2 - \kappa_x^2)/\kappa_x\beta]\cos\kappa_y(b+\eta) \times \sin\kappa_x(x+\xi)\exp[-\gamma_4(y-b)] \quad (2.37)$$

Region V: $$E_x = jA\,(n_1^2/n_5^2)\,[(k_o^2n_5^2 - \kappa_x^2)/\kappa_x\beta]\cos\kappa_y\eta \times \sin\kappa_x(x+\xi)\exp(\gamma_5 y) \quad (2.38)$$

The decay constants γ_i are given by

$$\gamma_i^2 = k_o^2(n_1^2 - n_i^2) - \kappa_x^2 \qquad i = 2, 3 \quad (2.39)$$

$$\gamma_i^2 = k_o^2(n_1^2 - n_i^2) - \kappa_y^2 \qquad i = 4, 5 \quad (2.40)$$

Using boundary conditions that tangential components of the electric and magnetic fields are continuous, we obtain eigenvalue equations to determine the propagation constants in the x and y directions:

$$\tan(\kappa_x d) = n_1^2\kappa_x\frac{n_3^2\gamma_2 + n_2^2\gamma_3}{n_3^2n_2^2\kappa_x^2 - n_1^4\gamma_2\gamma_3} \quad (2.41)$$

$$\tan(\kappa_y b) = \frac{\kappa_y(\gamma_4 + \gamma_5)}{\kappa_y^2 - \gamma_4\gamma_5} \quad (2.42)$$

The phase constants ξ and η are defined as

$$\tan(\kappa_x \xi) = -(n_3^2/n_1^2)(\kappa_x/\gamma_3) \tag{2.43}$$

$$\tan(\kappa_y \eta) = -\gamma_5/\kappa_y \tag{2.44}$$

The propagation constant β is given by the relation

$$\beta^2 = k_o^2 n_1^2 - (\kappa_x^2 + \kappa_y^2) \tag{2.45}$$

Eqs.2.41 and 2.42 are identical to the eigenvalue equations Eqs.2.15 and 2.14 for TM and TE modes of a planar waveguide. The eigenvalue problem now depends on the solutions of the two transcendental equations for κ_x and κ_y, and once κ_x and κ_y are obtained, the propagation constants and electromagnetic field distributions can be determined.

The E^y_{pq} hybrid modes and field distributions can be obtained in close analogy to those of E^x_{pq} modes merely by changing E to H and μ_o to $-\varepsilon_o$. The eigenvalue equations are given by:

$$\tan(\kappa_x d) = \frac{\kappa_x(\gamma_2 + \gamma_3)}{\kappa_x^2 - \gamma_2\gamma_3} \tag{2.46}$$

$$\tan(\kappa_y b) = n_1^2 \kappa_y \frac{n_5^2\gamma_4 + n_4^2\gamma_5}{n_4^2 n_5^2 \kappa_y^2 - n_1^4 \gamma_4\gamma_5} \tag{2.47}$$

where γ_i can be expressed in terms of κ_x and κ_y as before. The phase constants ξ and η for E^y_{pq} modes are defined as

$$\tan(\kappa_x \xi) = \gamma_3/\kappa_x \tag{2.48}$$

$$\tan(\kappa_y \eta) = (n_5^2/n_1^2)(\kappa_y/\gamma_5) \tag{2.49}$$

Similarly, the two eigenvalue equations Eqs.2.46 and 2.47 are again used to determine κ_x and κ_y for E^y_{pq} modes. The propagation constant β is finally obtained from Eq.2.45.

Fig.2.9 shows the theoretical effective indices N ($=\beta/k_o$) as a function of the channel width b using the method outlined above. The transverse field distributions $E_x(x,y)$ of the fundamental mode E^x_{11} and the first-order mode E^x_{12} are illustrated in Fig.2.10.

2.3.2 Effective Index Method

The effective index method (EIM) [2.16,2.17] is a modification of the above analysis which includes the effects of the four corner regions. In this method, the channel waveguide is divided into equivalent planar waveguide I with light confinement in one direction and planar waveguide II with light confinement at right angles to that of waveguide I. The planar waveguide I is solved first and the effective index n_{eff} of the TE (TM) mode is calculated. This effective index n_{eff} is used as the core refractive index of the planar waveguide II and the propagation constant for the TM (TE) mode of this second slab is taken to represent that of the original channel waveguide.

To illustrate the application of EIM, consider the step-index rectangular channel waveguide shown in Fig.2.11(a), where b and d are the width and thickness of the core, n_1, n_2, n_3, and n_4 are the refractive indices of the core and surrounding claddings, respectively. For the case of E^x_{pq} (E^y_{pq}) modes, the effective index n_{eff} for TM_{p-1} (TE_{p-1}) mode of the slab of thickness d shown in Fig.2.11(b) is first calculated using eigenvalue equation Eq.2.15 (Eq.2.14). Then n_{eff} is used to define the core refractive index of the second slab of thickness b as shown in Fig.2.11(c). The solution for TE_{q-1} (TM_{q-1}) mode of the second slab represents the propagation constant of the original channel waveguide.

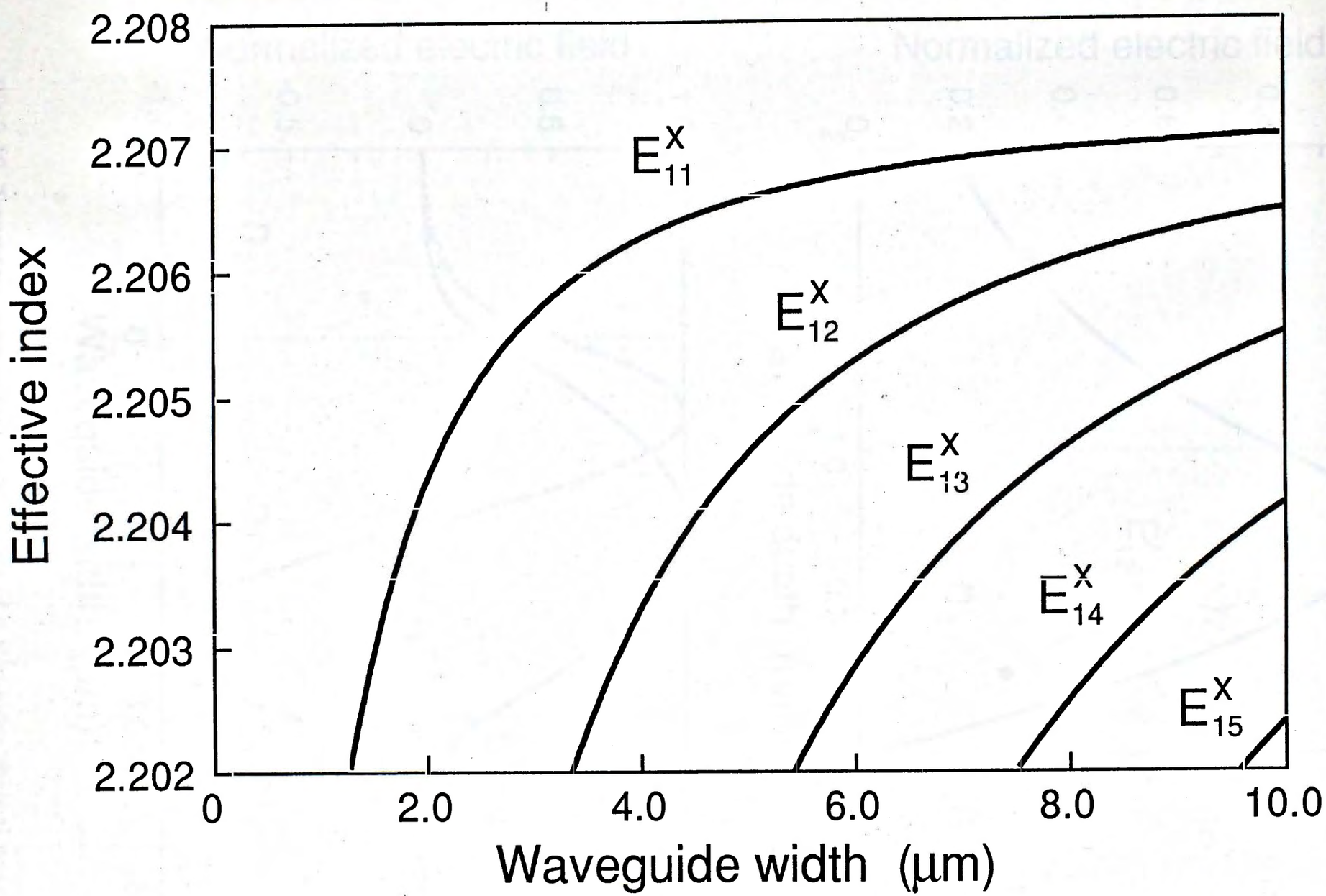

Fig.2.9 Mode effective index as a function of waveguide width b for step-index channel waveguides using Marcatili's method (n_1=2.218, n_2=n_4=n_5=2.202, n_3=1, d=1 μm, λ= 0.6328 μm).

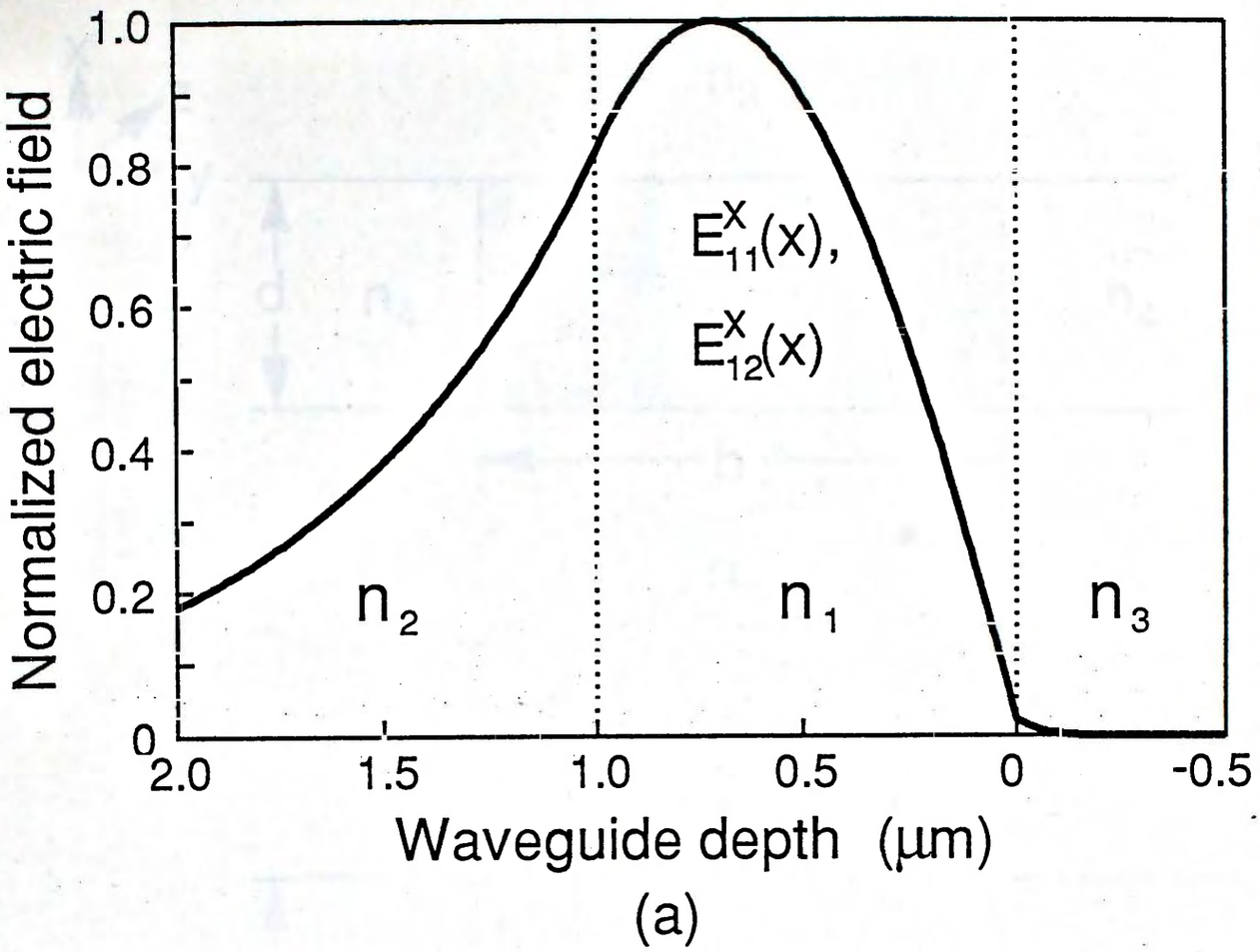

(a)

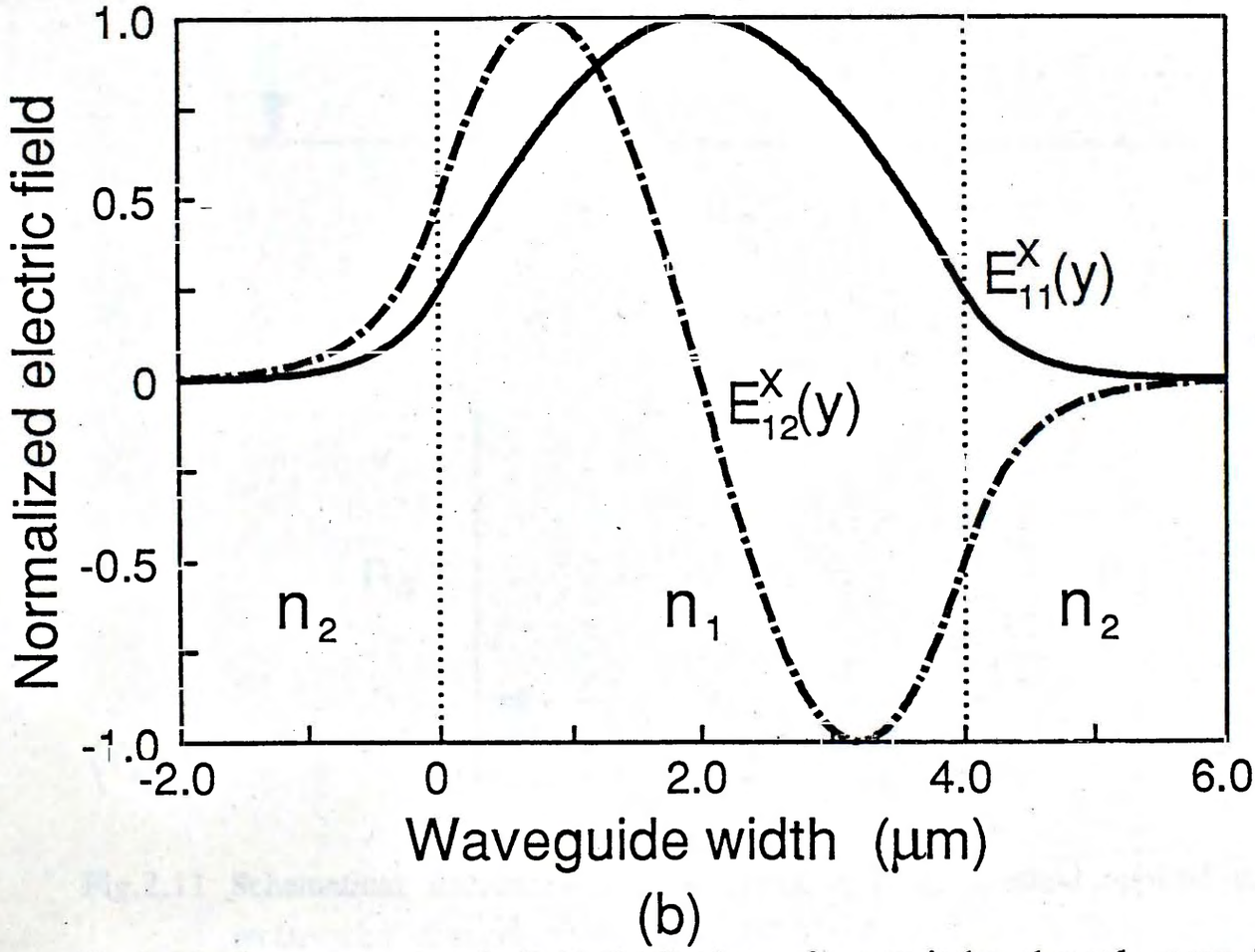

(b)

Fig.2.10 Transverse electric field distributions of a step-index channel waveguide (b=4μm, d=1μm, n_1=2.218, n_2=n_4=n_5=2.202, n_3=1, λ= 0.6328μm).

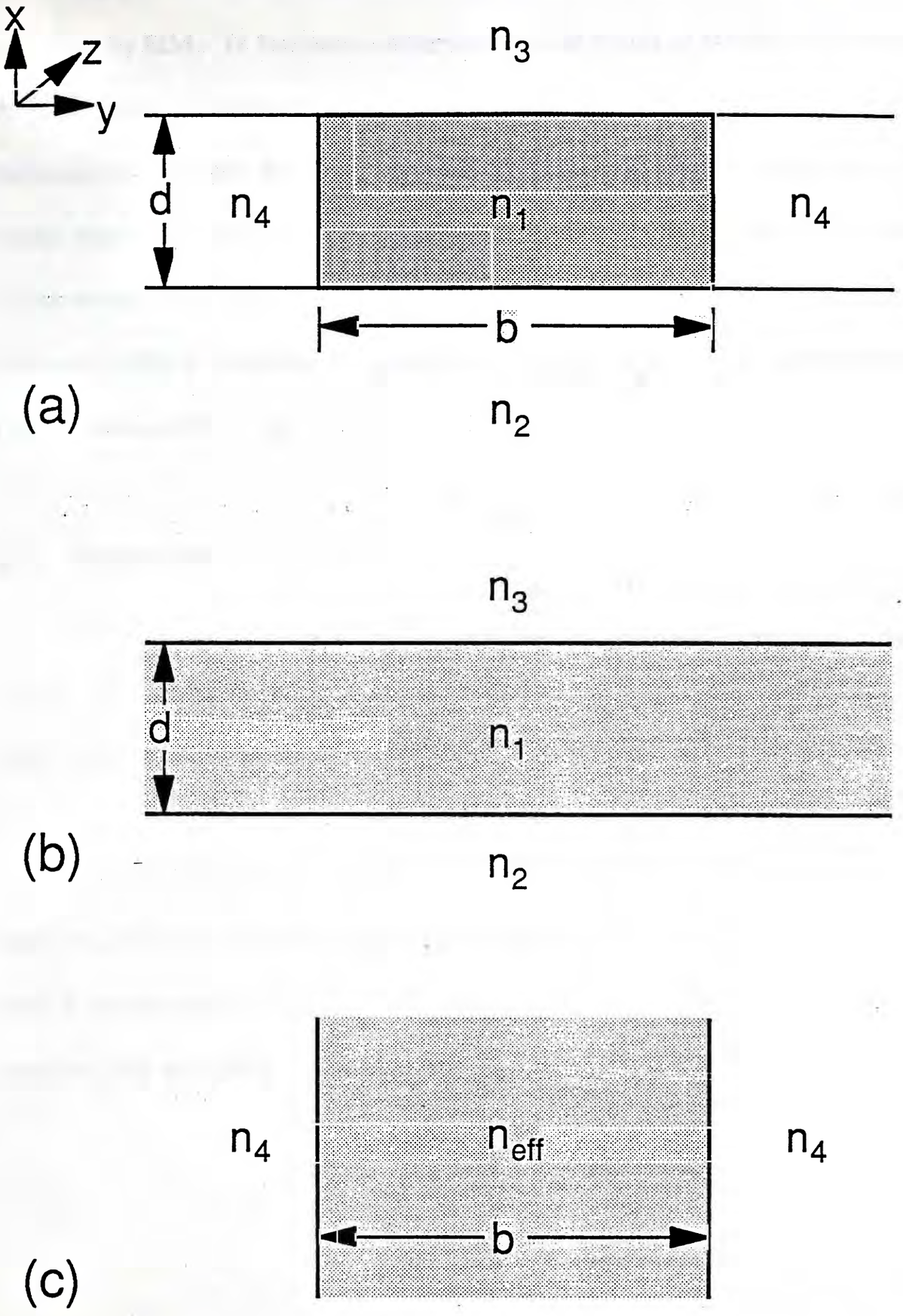

Fig.2.11 Schematical illustration of the effective index method applied to a rectangular channel waveguide. (a) Configuration of the waveguide; (b) Equivalent planar waveguide with confinement in x direction; (c) Equivalent planar waveguide with confinement in y direction.

Fig.2.12 shows the dispersion curves for an embedded channel waveguide calculated by EIM. To facilitate comparison with the results of Marcatili's method, the parameters chosen for Fig.2.12 are the same as those for Fig.2.9. In general the results of EIM give better accuracy and are valid over a larger range, even for modes reasonably close to cutoff [2.18-2.20]. It is because the solutions of the two planar waveguides are coupled in EIM, which is not the case in Marcatili's method. Moreover, EIM is computationally simple and can also be applied for graded-index channel waveguides [2.21].

2.4 Summary

A brief description of the theories of planar and channel waveguides are given. The zig-zag model is employed to explain the condition of propagation of light in planar waveguides. The eigenvalue equations are derived and solved for step-index and graded-index planar waveguides. Approximation methods for calculating the propagation constants of channel waveguides are also discussed. The analyses are useful in designing planar and channel waveguides that are commonly used in integrated optics devices. In the next chapter, the most important waveguide materials and waveguide fabrication methods will be described.

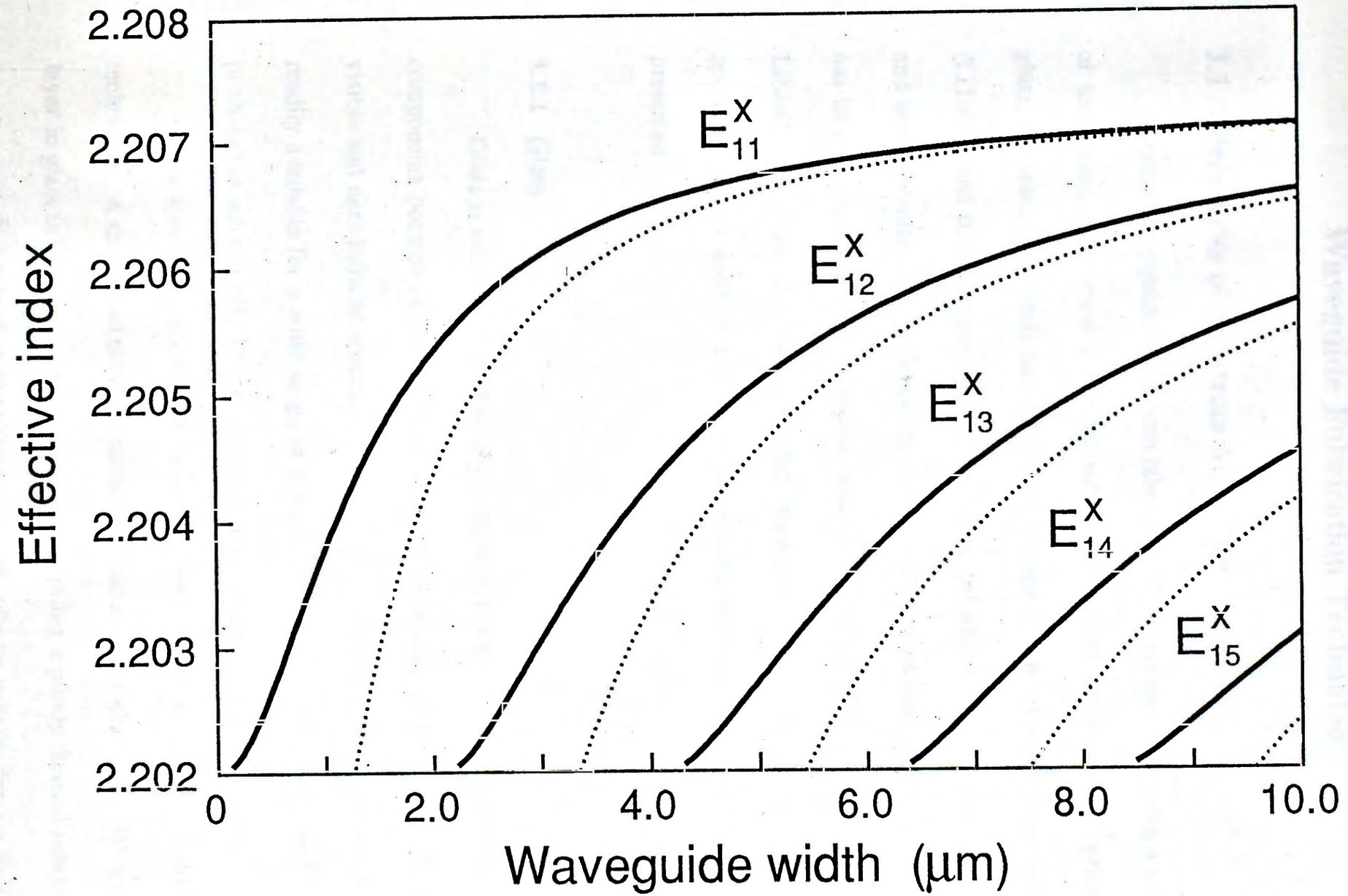

Fig.2.12 Theoretical dispersion curves for step-index channel waveguides using effective index method (solid curves) and Marcatili's method (dotted curves). The parameters used are $n_1=2.218$, $n_2=n_4=n_5=2.202$, $n_3=1$, $d=1$ μm, $\lambda=0.6328$ μm.

Chapter 3

Waveguide Fabrication Technology

3.1 Properties of Substrate Materials

Optical waveguides have been fabricated in various materials using a variety of techniques. The most important substrate materials for integrated optics are glass, ferroelectric crystals such as lithium niobate ($LiNbO_3$) and lithium tantalate ($LiTaO_3$), and III-V compound semiconductors, primarily gallium arsenide (GaAs) and more recently indium phosphide (InP). Each one of these substrate materials has its own strengths and weaknesses, and will be discussed in this chapter. Since $LiNbO_3$ is by far the most popular substrate material for integrated optics applications and used in this work, a detailed discussion on $LiNbO_3$ will be presented.

3.1.1 Glass

Glass is one of the most widely used materials for passive integrated optics components because of its low cost, high optical quality and transparency in the visible and near-infrared spectral region [3.1-3.3]. Moreover, glass substrates are readily available for a wide range of refractive indices ($\sim$1.4 to 2.0), and can be produced in substantially larger sizes than other single-crystal substrates.

Low-loss glass waveguides can be fabricated by a number of different techniques. A simple and effective method of producing a higher index waveguiding layer in glass is by *ion exchange*, which can be either a purely thermal process, or together with an assisted electric field [3.4-3.6]. To be suitable for ion exchange

the glass substrates must fulfil the following requirements [3.1]:

(i) Sufficiently high content of mobile ions (alkali ions such as Na^+ and K^+);

(ii) Chemically stable in the presence of strongly reactive melts, e.g. molten nitrates of alkali metals;

(iii) Transition temperature compatible with processing temperatures, which are in the temperature range of 250 to 500°C.

The properties of several types of glass suitable for ion exchange are summarized in Table 3.1 [3.2]:

Glass	Type	Refractive index n_d	Exchangeable ions
Window-/ microscope slide	Soda lime	1.51	Na^+
TiF6	Phosphate	1.62	Na^+/K^+
BK7	Borosilicate	1.52	Na^+/K^+
Pyrex	Borosilicate	1.47	Na^+
BGG31	Borosilicate	1.48	Na^+

Table 3.1 Properties of commonly used glass substrates for optical waveguide fabrication.

By a suitable selection of diffusion temperatures and times, low-loss glass optical waveguides with desired characteristics can be fabricated. Recently, fiber-compatible single-mode glass waveguides with coupling loss and propagation loss as low as 0.3dB/facet and 0.4dBcm^{-1} at 1.3μm wavelength have been demonstrated [3.5].

Unlike its electrooptic and semiconducting counterparts (e.g. $LiNbO_3$, GaAs,

etc.), the refractive index of glass cannot be changed by application of an external electric field. Therefore, glass has been considered only as a passive substrate material. The recent development of rare-earth-doped glass materials, viz. neodymium-doped [3.7] and erbium-doped glasses [3.8], offers the possibility of active integrated optics devices. The development of waveguide lasers and waveguide amplifiers using rare-earth-doped glasses have attracted much attention. Several laboratories have reported laser oscillations and amplifications in Nd^{3+}-doped glass waveguides fabricated using the ion exchange technique [3.9-3.11].

3.1.2 Semiconductor

III-V compound semiconductors offer the possibility of monolithic integration of light sources, detectors, optical waveguide components and electronic circuitry in the same substrate. The most commonly used materials for semiconductor integrated optics are gallium arsenide (GaAs), indium phosphide (InP) and their related compounds such as aluminum gallium arsenide (AlGaAs) and indium gallium arsenide phosphide (InGaAsP) [3.12,3.13]. In these III-V compound semiconductor material systems, the bandgap energy, transparency range (0.6-12μm) and refractive indices ($\sim$3.0 to 3.4) are functions of the alloy composition. Compounds with different bandgap energies - that can be translated to devices operating at different wavelengths ($\sim$0.65 to 1.7μm) - can be prepared with binary, ternary, and quaternary alloy systems. For waveguiding to take place, index differences can be induced by changing the electrical properties (i.e. free-carrier concentration) and/or alloy composition of the semiconductor. Strain and electric fields can also be used

to locally alter the refractive index.

Semiconductor optical waveguides [3.1-3.3] are generally fabricated by sophisticated epitaxial growth techniques such as liquid phase epitaxy (LPE), molecular beam epitaxy (MBE), metalorganic chemical vapor deposition (MOCVD), and chemical beam epitaxy (CBE). LPE has been the major production technology, and is being replaced by MBE or MOCVD because of ever-demanding higher uniformity and complexity. The rapid advances of epitaxial growth technologies over the last decade have reduced the propagation losses of semiconductor waveguides to the range of 0.2 to 1 $dBcm^{-1}$ [3.13]. Heterostructure, quantum-well and superlattice waveguides have been made in both GaAs- and InP-based material systems. Waveguide devices using the electrooptic and electroabsorption effects have also been demonstrated [3.12,3.13]. Owing to their intrinsically high refractive index, semiconductor optical waveguides present higher coupling losses to optical fibers when compared to glass or $LiNbO_3$ waveguides.

3.1.3 Ferroelectric Material

Lithium niobate ($LiNbO_3$), lithium tantalate ($LiTaO_3$) and potassium niobate ($KNbO_3$) are important ferroelectric and electrooptic crystals [3.1-3.3]. Among these, $LiNbO_3$ is the most popular and thoroughly studied ferroelectric crystal in integrated optics. Before being applied to optical waveguides, $LiNbO_3$ was used for surface acoustic wave applications. As a consequence, the growth technology has been already well-developed. Nowadays, high quality integrated optics grade single crystals of lithium niobate, at up to four inches diameter with uniform properties, and in a range of crystal cuts, are commercially available.

$LiNbO_3$ has a rhombohedral crystalline structure and its symmetry is that of the 3m crystallographic point group [3.14-3.16]. It is a birefringent crystal with the c-axis being the extraordinary axis. It is also a negative uniaxial material with an ordinary index of refraction $n_o = 2.2869$ and an extraordinary index of refraction $n_e = 2.2022$ at $0.6328\mu m$ wavelength. It is transparent in the visible and near-infrared spectral region (i.e. from $0.4\mu m$ to $4.5\mu m$). Its Curie temperature and birefringence vary according to crystal composition, which can be produced with different stoichiometry. The stoichiometry commonly used for integrated optics applications is the so-called congruent composition (i.e. the composition where the solid and liquid in contact are in equilibrium), which corresponds to a Li_2O mole content of 48.45%. The Curie temperature for the congruent composition is around 1150°C, and the melting point is 1253°C. Because of high Curie temperature, $LiNbO_3$ can withstand the high temperature for diffusion (e.g. $\geq$1000°C) without domain reversal. Some other important properties of $LiNbO_3$ are summarized in Table 3.2.

The $LiNbO_3$ structure [3.17] consists of oxygen layers perpendicular to the crystallographic c-axis (Fig.3.1). Along the c-axis oxygen octahedral units are formed which are occupied in sequence by Li^+ and Nb^{5+}, followed by a structural vacancy. In a poled $LiNbO_3$ crystal, there is an ordered sequence of Li-Nb-vacancy-Li-Nb-vacancy sites and the reverse direction of poling is the Li-vacancy-Nb-Li-vacancy-Nb sequence [3.18].

$LiNbO_3$ is the most popular substrate material for integrated optics devices because of its good electrooptic, acoustooptic, piezoelectric, pyroelectric and photoelastic properties [3.12]. The basis of these useful properties is an asymmetry

Crystal Class	Rhombohedral
Space Group	R3c
Point Group	3m or C_{3v}
Lattice Constants Rhombohedral Equivalent Hexagonal	 a_{Rh} = 5.4944Å α_{Rh} = 55°52' a_H = 5.1483Å c_H = 13.8631Å
Density	4.64 gcm^{-3}
Molecular Weight	147.85
Refractive Index (λ = 0.6328μm)	n_o = 2.2869 n_e = 2.2022
Birefringence	-0.0847
Melting Point	1253°C
Curie Temperature	1150°C
Electrical Resistivity (400°C)	5×10^8 Ω-cm
Moh Hardness	5
Condition of Poling	600°C, 10Vcm^{-1}
Pyroelectric Coefficient	0.0083 $\mu Ccm^{-2}°C^{-1}$
Electrooptic Coefficients (λ = 0.6328μm) r_{33} r_{13} r_{22} r_{51}	 30.8 pmV^{-1} 8.6 pmV^{-1} 3.4 pmV^{-1} 28.0 pmV^{-1}
Nonlinear Optical Coefficients (λ = 1.06μm) d_{33} d_{31} d_{22}	 40.68 pmV^{-1} 5.82 pmV^{-1} 3.07 pmV^{-1}

Table 3.2 Properties of lithium niobate

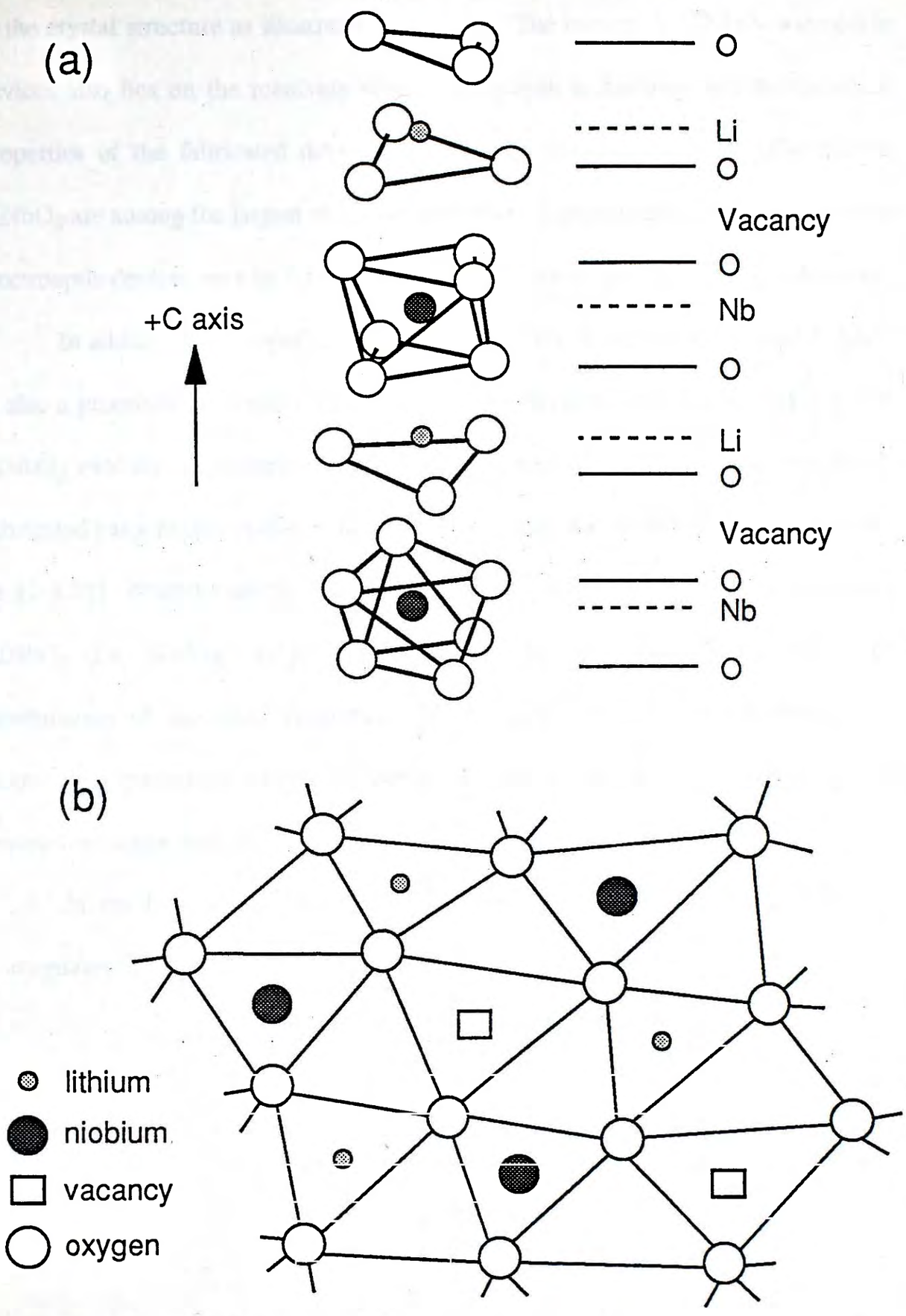

Fig.3.1 Structure of lithium niobate. (a) Atomic arrangement in the ferroelectric phase; (b) Rhombohedral structure with Li, Nb and vacancy sites projected onto the crystallographic a,b-plane (after ref.[3.17]).

in the crystal structure as illustrated in Fig.3.1. The interest in $LiNbO_3$ waveguide devices also lies on the relatively simple fabrication technology and the excellent properties of the fabricated devices. Above all, the electrooptic coefficients of $LiNbO_3$ are among the largest of known materials. Consequently, high performance electrooptic devices may be fabricated in different crystal cuts of $LiNbO_3$ substrates.

In addition to undoped single crystal, $LiNbO_3$ doped with 4.5 mole% MgO is also a promising material for integrated optics devices [3.19,3.20]. MgO doped $LiNbO_3$ exhibits a hundredfold reduced photorefractive response and waveguide fabricated has a higher optical damage threshold than that of its undoped counterpart [3.21-3.23]. With the advent of MgO:$LiNbO_3$, magnesium and neodymium codoped $LiNbO_3$ (i.e. Nd:MgO:$LiNbO_3$) has been available recently [3.24-3.26]. The combination of the laser properties of Nd^{3+} with the excellent nonlinear and electrooptic properties of MgO:$LiNbO_3$ has led to the successful realization of waveguide lasers and amplifiers in Nd:MgO:$LiNbO_3$ [3.27-3.29].

In the following section, the common fabrication techniques for $LiNbO_3$ waveguides are discussed.

3.2 Waveguide Fabrication Techniques

In order of both development and popularity, the most common fabrication techniques for high quality $LiNbO_3$ waveguides are titanium indiffusion, proton exchange and ion implantation [3.30-3.32]. The advantages and disadvantages of these techniques are discussed in the following subsections.

3.2.1 Ion Implantation

In this process, the $LiNbO_3$ substrate is bombarded by ions accelerated in high vacuum with energy up to 2MeV [3.33]. As the impinging ions penetrate into the substrate surface, they lose energy through electronic and nuclear stopping. The effect of ion implantation on $LiNbO_3$ due to nuclear stopping is a decrease in both the ordinary and extraordinary refractive indices in the ion-damaged region [3.34]. Electronic stopping also induces index change but the effect is substantially smaller than that of nuclear stopping. The magnitude of reduction of the refractive indices, which may be up to 7%, is determined by the crystal orientation, implantation temperature and ion dose. Energetic helium ions (He^+) are used usually with doses of 10^{16} to $10^{17} cm^{-2}$.

Good quality $LiNbO_3$ waveguides are fabricated by forming a buried damaged layer, whose refractive index is lower than that of the bulk substrate, to constitute the low-index boundaries of the waveguides [3.33-3.36]. Since n_o and n_e are decreased in the damaged layer, ion implanted waveguides support both TE and TM propagation modes. By using different implantation energies, the depth distribution of the implanted ions can be profiled and hence the waveguide depth can be varied. The only post-implantation process is a low-temperature ($\sim 200°C$)

annealing, which is required to remove ion-induced damage in the waveguiding layer as well as to reduce the waveguide propagation losses. After annealing, propagation losses less than 1 $dBcm^{-1}$ are usually obtained for He^+ implanted $LiNbO_3$ waveguides [3.34].

To summarize, ion implantation has the following advantages:

(i) Small lateral spreading of the implanted species, i.e. better guide definition;

(ii) Control of the concentration profile of the implanted ions;

(iii) Accurate dose measurements and reproducibility;

(iv) Freedom in the choice of implanted species.

The main disadvantages of ion implantation are high cost and complexity of the required machinery. In addition, the electrooptic effect is reduced by $\sim 20\%$ due to the induced radiation damage (i.e. displacement of the original atoms from their sites) in the waveguiding layer [3.30].

3.2.2 Titanium Indiffusion

Since the first demonstration by Schmidt and Kaminow [3.37] that low-loss optical waveguides in $LiNbO_3$ can be fabricated by diffusing a deposited film of titanium (Ti) into the substrate, this technology has been studied extensively. Nowadays Ti indiffusion is the standard waveguide fabrication technique for $LiNbO_3$ integrated optics components [3.30-3.32].

The fabrication process is relatively simple: a thin Ti film (20-150nm) are sputtered or evaporated and photographically delineated onto the $LiNbO_3$ surface (Fig.3.2). The film is then diffused into the crystal at an elevated temperature ($\sim 1000°C$) for several hours (3-15 h). This results in a transparent Ti:$LiNbO_3$

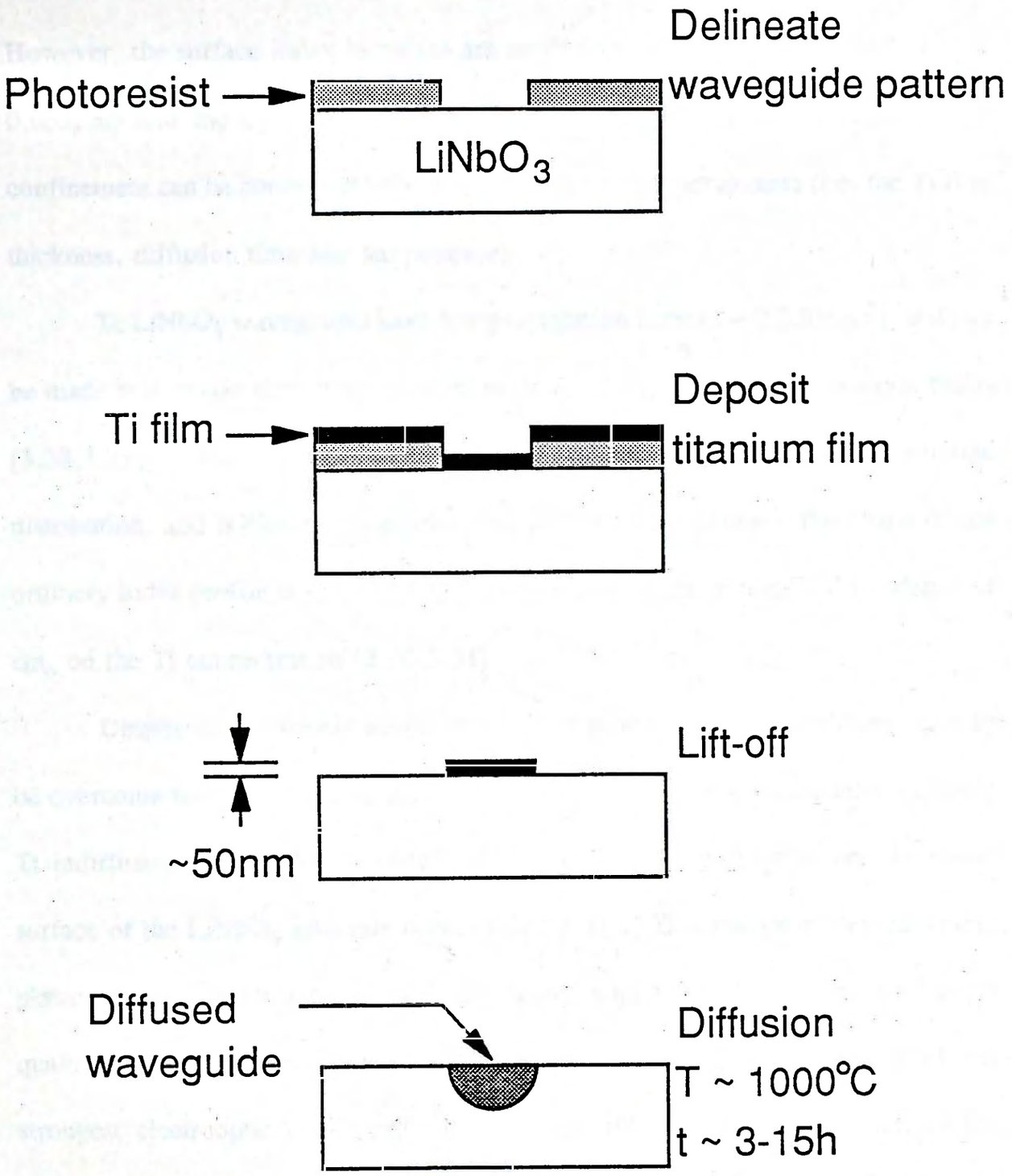

Fig.3.2 Processing steps for Ti:$LiNbO_3$ waveguide fabrication using the lift-off technique.

layer with increased refractive indices for the ordinary (n_o) and extraordinary (n_e) axes. Hence Ti:$LiNbO_3$ waveguides support both TE and TM propagation modes. However, the surface index increases are small ($\Delta n_e \leq 0.04$, $\Delta n_o \leq 0.02$ at $\lambda = 0.633\mu m$) and the optical confinement is weak [3.30]. The degree of optical confinement can be controlled by varying the fabricating parameters (i.e. the Ti film thickness, diffusion time and temperature).

Ti:$LiNbO_3$ waveguides have low propagation losses ($\sim 0.2 dBcm^{-1}$), and can be made with mode sizes well matched to those of conventional single-mode fibers [3.38,3.39]. The extraordinary refractive index profile follows a Gaussian distribution, and is directly proportional to the Ti concentration. The shape of the ordinary index profile is somewhat different because of the nonlinear dependence of Δn_o on the Ti concentration [3.30,3.31].

Despite the relatively simple fabrication process, several problems have to be overcome for reproducible production of stable Ti:$LiNbO_3$ waveguides. During Ti indiffusion, simultaneous outdiffusion of lithium oxide (Li_2O) from the entire surface of the $LiNbO_3$ substrate occurs [3.40,3.41]. This results in an undesirable planar waveguide for the extraordinary wave, which deteriorates the waveguide quality at shorter wavelength (e.g. $0.633\mu m$) and precludes utilization of the strongest electrooptic coefficient r_{33}. Besides, lithium outdiffusion changes the stoichiometry of the substrate in the surface region, and has a considerable influence on the Ti indiffusion rate. Different remedial methods have been proposed to suppress the outdiffusion phenomenon [3.30-3.32]. For example, by placing a powdered source of Li_2O in the diffusion furnace, the Li_2O partial pressure surrounding the $LiNbO_3$ samples is increased so that net outdiffusion can be reduced

substantially to eliminate the unwanted surface guiding. Another method is to perform the diffusion process in a water-vapour enriched atmosphere or in a closed box of pure platinum. Nevertheless, the effectiveness and the reproducibility of these methods are not yet satisfactory.

Like bulk $LiNbO_3$, Ti diffused waveguides are susceptible to optical damage, particulary in the visible spectral region [3.30-3.32]. Optical damage degrades the waveguide properties, which range from slow variations of the waveguide refractive indices to excessive losses due to induced waveguide cutoff. The degree of the optical damage depends mainly on wavelength and optical power. Therefore, the usability of Ti:$LiNbO_3$ waveguide devices has to be compromised by the photo-refractive effect.

3.2.3 Proton Exchange

It is well-known from glass technology that low-loss glass waveguides can be produced at relatively low temperature by means of the ion exchange process [3.4-3.6]. In this process, a glass containing exchangeable ions (e.g. Na^+ in soda-lime glass) is submerged in a salt melt containing suitable mobile ions (e.g. Ag^+ from a silver nitrate melt). Exchange of ions between the glass and the melt occurs due to concentration gradient, resulting in an ion-exchanged surface layer of a different refractive index due to the difference in electronic polarizability of the exchanged ions. A similar fabrication process can be applied to $LiNbO_3$ by using a suitable proton source (e.g. a weak acid or hydrate melt) instead of a salt melt [3.42,3.43]. This so-called *proton exchange* process is first demonstrated by Jackel and Rice [3.42] with benzoic acid (C_6H_5COOH) as the proton source. A variety of

proton sources may be used, the main requirement being an equilibrium in which a significant concentration of solvated protons is present in the exchange medium. The processing steps for fabricating proton-exchanged (PE) waveguides are illustrated in Fig.3.3.

The proton exchange process involves a chemical reaction between the $LiNbO_3$ substrate and the proton source, and also involves the outdiffusion of lithium ions from, and the diffusion of protons into, bulk substrate. The two factors affecting the proton exchange process are the temperature of the acid melt and the acidity of the proton source. Only partial exchange is necessary for waveguide formation, and the process can be represented by the following reaction [3.44]:

$$LiNbO_3 + xH^+ \longrightarrow Li_{1-x}H_xNbO_3 + xLi^+ \qquad (3.1)$$

The change in the refractive indices or the waveguiding effect is attributed to the formation of the $Li_{1-x}H_xNbO_3$ layer. The value of x represents the extent of the reaction, and is determined by the time and temperature of exchange.

PE waveguides are characterized by a large increase of the extraordinary index ($\Delta n_e = 0.12$ at $\lambda = 0.633\mu m$) and by a significant but smaller decrease in the ordinary index ($\Delta n_o = -0.04$) [3.42-3.45]. Because of this inherent anisotropy, PE waveguides only support TM modes in z-cut substrates, and TE modes in x-cut and y-cut substrates. The waveguide propagation losses are dependent on the orientation of the substrate, typical values being 2 $dBcm^{-1}$ for z-cut waveguides and 5 $dBcm^{-1}$ for x-cut waveguides at $0.6328\mu m$ wavelength [3.46-3.48].

The proton exchange process has many distinct advantages which make it attractive as an alternative to the standard technique of titanium indiffusion. The main advantages of the proton exchange process are its simplicity, large index

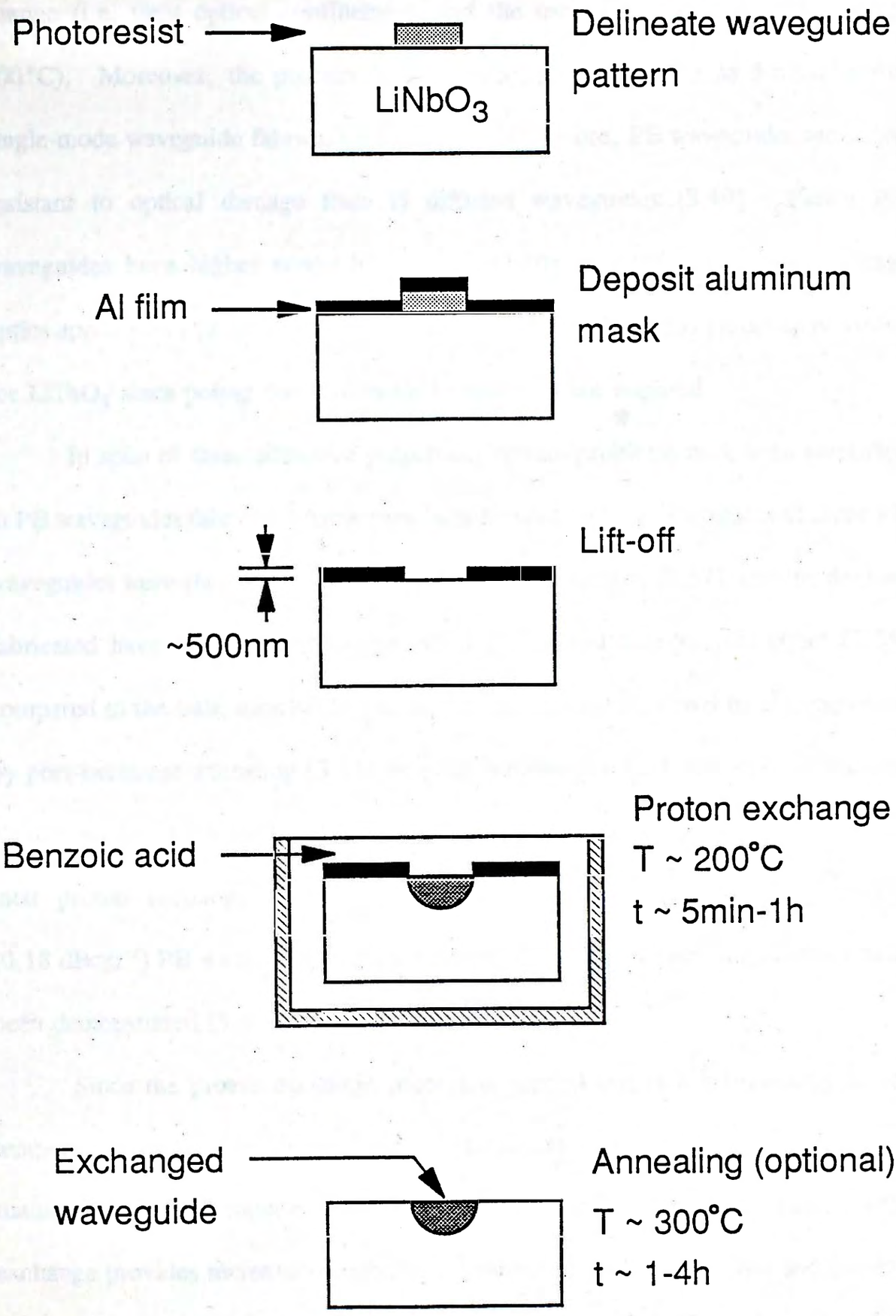

Fig.3.3 Steps for fabricating proton-exchanged $LiNbO_3$ waveguide.

change (i.e. tight optical confinement) and the use of low temperature (~150-300°C). Moreover, the process is quick and may be as little as 5 minutes for single-mode waveguide fabrication [3.42]. Furthermore, PE waveguides are more resistant to optical damage than Ti diffused waveguides [3.49]. Hence PE waveguides have higher power-handling capability and are useful for nonlinear optics applications [3.50,3.51]. This low-temperature process is particularly useful for $LiTaO_3$ since poling due to domain inversion is not required.

In spite of these attractive properties, certain problems have been identified in PE waveguides fabricated using pure benzoic acid. The mode indices of these PE waveguides were shown to suffer from short-term instability [3.52], and the devices fabricated have reduced electrooptic effect [3.53] and acoustooptic effect [3.54] compared to the bulk substrate. These problems, however, could be circumvented by post-exchange annealing [3.55] or using lithium-rich buffered melts containing small amounts of lithium benzoate as the proton source, the latter is known as dilute melt proton exchange [3.44,3.47]. By using these methods, very low-loss (0.18 $dBcm^{-1}$) PE waveguides with a substantially restored electrooptic effect have been demonstrated [3.56].

Since the proton exchange process is carried out at a substantially lower temperature than Ti indiffusion, the two processes can be combined to fabricate titanium-indiffused proton-exchanged waveguides [3.57-3.59]. In this case, proton exchange provides increased flexibility in controlling the birefringence and shaping the refractive index profile of Ti diffused waveguides. Proton exchange has also been employed in conjunction with ion implantation to produce waveguides with complicated index profiles [3.60].

3.3 Summary

In this chapter we have briefly reviewed the characteristics of important substrate materials and waveguide fabrication techniques for integrated optics devices. Of the three main waveguide fabrication methods, Ti indiffusion is in the most advanced status of development. On the other hand, proton exchange offers advantages for some applications where improved power-handling capability is desired.

The selection of a substrate material and waveguide fabrication technique, besides being influenced by the specific device requirements, is also governed by material availability, optical quality, related fabrication technology and system cost. In our work, $LiNbO_3$ is chosen as the substrate material because it provides the possibility for formation of active devices, and the related equipment for waveguide fabrication is readily available. Since proton exchange is currently the only reliable technique to achieve highly confined waveguides in $LiNbO_3$, it is adopted in our work.

Chapter 4

Fabrication and Measurement of Optical Waveguides

4.1 Fabrication of Optical Waveguides

Integrated optics grade z-cut lithium niobate ($LiNbO_3$) wafers of congruent composition (from Barr & Stroud Ltd.) were used throughout our experiments. The wafers were readily in the size of $45(X)\times47(Y)\times1(Z)$ mm^3 and were one-face polished (perpendicular to crystallographic z axis). The procedures for fabricating proton-exchanged planar and channel waveguides are described as follows.

4.1.1 Planar Waveguides

4.1.1.1 Substrate Cutting

The $LiNbO_3$ wafer was cut into substrates of suitable size by a diamond-wire saw (Logitech model-15). Typical substrate size was $5(X)\times15(Y)\times1(Z)mm^3$. The waveguides then fabricated were z-cut y-propagating.

4.1.1.2 Substrate Cleaning

The cleaning procedure consists of ultrasonic agitation of the substrate in several analar grade organic solvents, followed by rinsing in deionized water. The processing steps are outlined below:

(i) Immerse in 1,1,1-trichloroethane (TCA) for 10 minutes to remove wax, grease and oil;

(ii) Immerse in acetone for 10 minutes to remove TCA and other organic substances;

(iii) Immerse in isopropyl-alcohol (IPA) for 10 minutes to remove residual acetone;

(iv) Rinse in running deionized water for 5 minutes to remove IPA drying stains;

(v) Blow dry with a jet of nitrogen.

The cleaning procedure plays an important role in waveguide fabrication since the optical wave propagation will be directly affected by any surface contamination. This procedure was also applied to the containers used in the subsequent proton exchange process.

4.1.1.3 Proton Exchange

A fresh proton source (e.g. phosphoric acid) was contained in a cleaned quartz crucible and maintained at the exchange temperature in a furnace (Memmert U10) controlled to $\pm 2°C$. The crucible was covered to maintain a temperature equilibrium in the proton source. The substrates were preheated and submerged into the proton source with the polished surface facing upwards. The exchange temperature was monitored by a thermocouple and a temperature indicator. The thermocouple was placed close to the crucible to obtain reliable readings. The exchange temperature ranged from 170°C to 260°C, and the exchange time was from 5 minutes to 24 hours. The exchange time is defined as the time taken between immersion of the substrate into the proton source and its subsequent removal.

After the exchange process, the waveguides were removed from the acid melt and were allowed to cool in air to room temperature. Any acid left on the substrate surface was rinsed away thoroughly with acetone. Then the waveguides were stored at room temperature for a week to reduce the refractive index instability [4.1] before

measurements were carried out.

4.1.1.4 Post-exchange Annealing

For fabrication of annealed proton-exchanged waveguides, the as-exchanged waveguides were baked in a quartz tube inside a horizontal furnace controlled to ±0.5°C. The annealing temperature was 350°C (or 300°C), and annealing time ranged from 5 minutes to 7 hours. The annealing time was defined as the interval between the sample reaching the furnace hot spot and its subsequent removal. Dry oxygen with a flow rate of $500cm^3min^{-1}$ (or $50cm^3min^{-1}$) was used to prevent deoxidization of the substrate surface that may affect the optical properties of the waveguides.

4.1.2 Channel Waveguides

The procedures of fabricating proton-exchanged channel waveguides are similar to those of planar waveguides. The $LiNbO_3$ wafer was cut into substrates with a size of $20(X)\times20(Y)\times1(Z)mm^3$ and cleaned thoroughly as before. Then the waveguide pattern was delineated onto the substrate surface by standard photolithographic and lift-off techniques, followed by proton exchange and post-exchange annealing.

4.1.2.1 Patterning Technique : Photolithography and Lift-off

The processing steps for fabricating proton-exchanged channel waveguides are shown in Fig.4.1. A small amount ($\sim0.2cm^3$) of positive photoresist (OSF PR-800) was dispensed onto the polished surface of the substrate by a dropper. Then the substrate was rotated in a high-acceleration spin-coater (Integrated

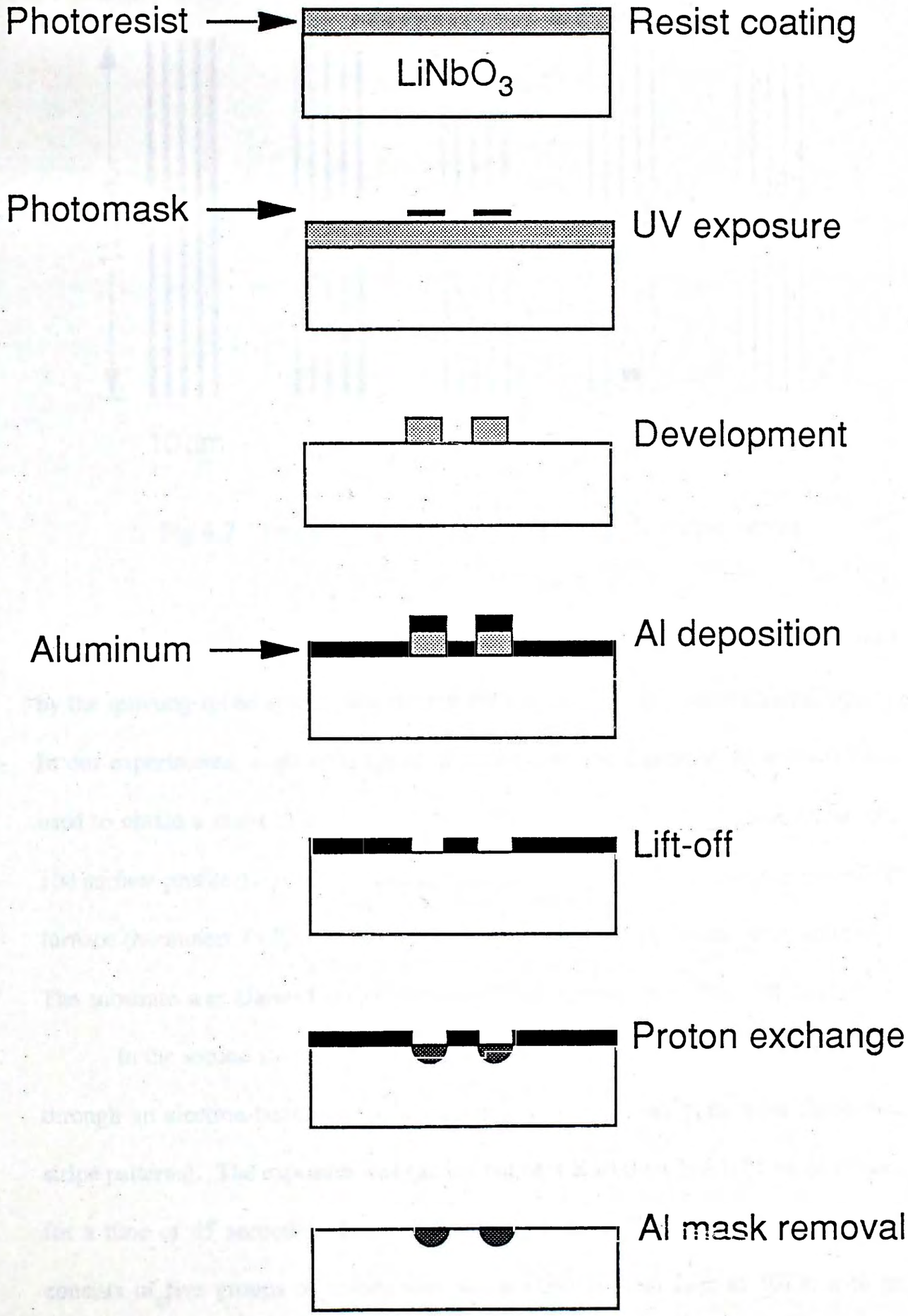

Fig.4.1 Processing steps for fabricating proton-exchanged channel waveguides

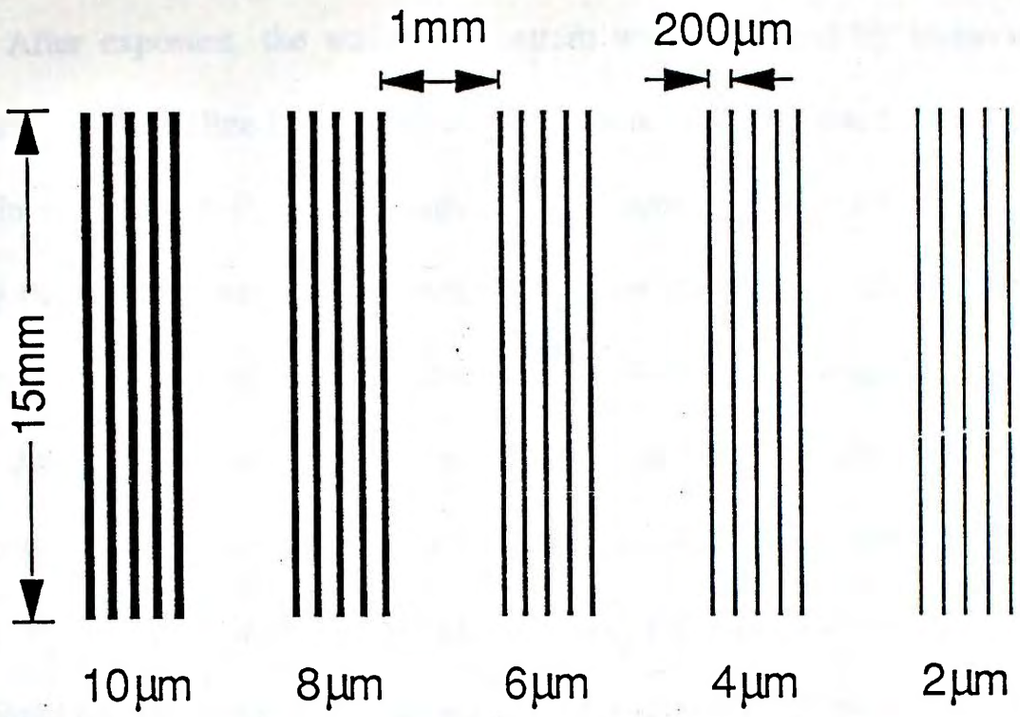

Fig.4.2 Design of the photomask showing the stripe pattern

Technologies P-6000). The thickness of the deposited photoresist was determined by the spinning speed and the viscosity of the photoresist (=30cps without dilution). In our experiments, a spinning speed of 3500r.p.m and a time of 40 seconds were used to obtain a resist thickness of 8000±300Å (measured by a Tencor alpha-step 100 surface profiler). After the coating step, the substrate was baked in a forced-air furnace (Memmert Tv30L) at 105°C for 30 minutes to improve the resist adhesion. The substrate was allowed to cool in air to room temperature after soft-baking.

In the second step, the resist-coated substrate was exposed to ultraviolet light through an electron-beam-generated photomask (i.e. a glass plate with chromium stripe patterns). The exposure was carried out on a Karl Suss MA56M mask aligner for a time of 35 seconds. The design of the photomask is shown in Fig.4.2. It consists of five groups of stripes with width varying from 2μm to 10μm with an increment of 2μm.

After exposure, the waveguide pattern was developed by immersing the substrate in an alkaline-based solution (AZ606 developer diluted with deionized water in a ratio of 1:4) for 60 seconds. The exposed photoresist was dissolved, leaving the original mask pattern in the remaining photoresist. The substrate was then rinsed in deionized water and blown dry with filtered nitrogen.

After development, a 1000Å thick aluminum (Al) film was deposited on the patterned substrate surface by a vacuum evaporator (Edwards model 306). The Al-coated substrate was immediately submerged in acetone to lift off the remaining photoresist together with the Al film on top of the resist. The remaining Al film had a complementary stripe pattern to that of the original photomask, and formed a diffusion barrier for subsequent proton exchange process. A photomicrograph of the Al mask with 4μm wide stripe openings is shown in Fig.4.3. The Al mask opening widths were measured by a micrometer eyepiece (Olympus OSM-4) through an optical microscope, and the results for two samples are shown in Table 4.1.

Sample	Photomask stripe width (μm)	Al mask opening width (μm)
1	2	2.76
	4	5.29
	6	7.11
	8	9.31
	10	11.28
2	2	2.53
	4	4.98
	6	6.87
	8	9.04
	10	11.12

Table 4.1 Typical measurement results of Al mask opening widths

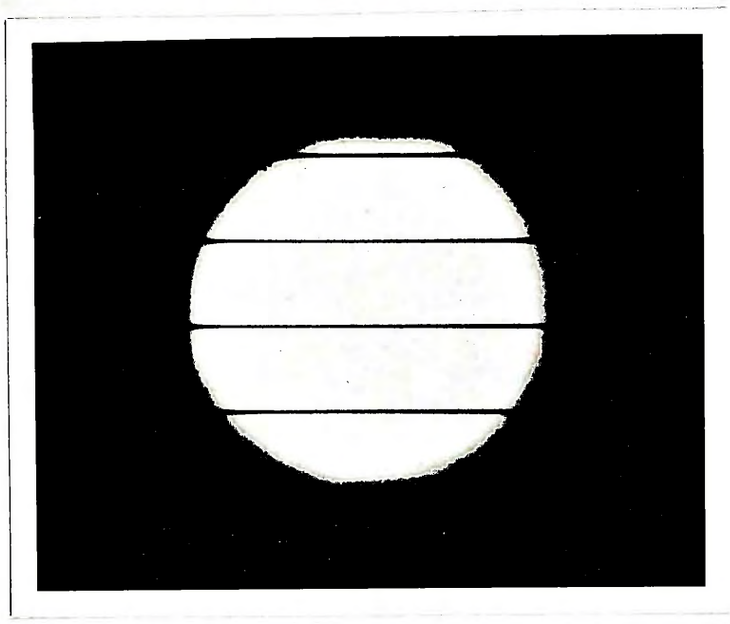

(a)

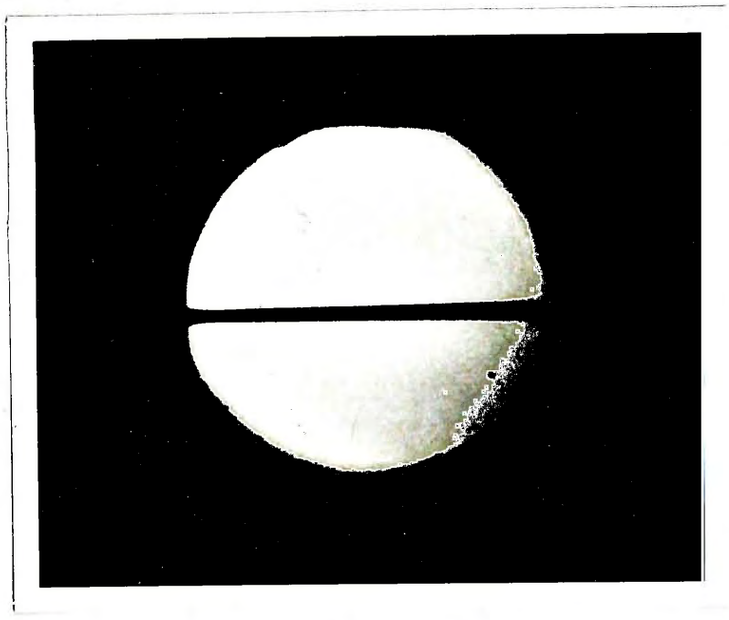

(b)

Fig.4.3 Photomicrograph of the deposited aluminum film with 4μm wide stripe openings. (a) Magnification = 50; (b) Magnification = 500

4.1.2.2 Proton Exchange and Annealing

Single-mode channel waveguides were fabricated by the annealed proton-exchange process. In the first step, proton-lithium exchange in the unmasked region was carried out using organic acids as the proton source. Inorganic acids (e.g. phosphoric acid) could not be used because the Al mask film would be completely etched away by these strong acids. The exchange temperature was 200°C and exchange times ranged from 25 minutes to 1 hour. After the proton exchange process, the Al film was removed by immersing the substrates in a room-temperature wet chemical etchant ($16H_3PO_4$:HNO_3:$4H_2O$) for 5 minutes. Single-mode channel waveguides were formed after annealing the substrates at 350°C for 15 to 30 minutes. In order to estimate the effective index of the channel waveguide by subsequent prism-coupling measurement, a planar waveguide was fabricated using the same exchange and annealing conditions.

4.1.2.3 Lapping and Polishing

The two orthogonal end-faces of a channel waveguide must be optically flat to enable efficient end-fire coupling. Good quality end-faces were prepared by lapping and polishing the waveguide using the Logitech PM2A machine. The waveguide was mounted on a precision polishing jig (PP5) for correct alignment of the end-faces with respect to the lapping plate. Then the polishing jig was placed on top of a cast-iron lapping plate, rotating as the plate went round. The waveguide was lapped by calcined aluminum oxide powder which was dispersed in water to form a slurry. Different grades of powder were used, i.e. from 30μm, 12μm down to 3μm. The time spent on each grade of powder was about 10 to 15 minutes. Before using the next grade of powder, it is necessary to carefully clean the

waveguide (still mounted on the polishing jig) and the lapping plate by running water. Syton polishing was performed after the end-face had been lapped to a pit- and scratch-free surface. The cast-iron lapping plate was replaced by a polyurethane polishing plate, over which syton solution (a polishing suspension with particle size of 0.125μm) was dropped at a rate of 5 to 10$cm^3 min^{-1}$. The time necessary to obtain a mirror-like surface was about 2 hours. After completion of syton polishing, the waveguide was kept immediately under running water for 5 minutes to thoroughly remove residual syton from the polished end-face. Then the waveguide was cleaned following the procedures outlined in Section 4.1.1.2.

4.2 Measurement of Waveguide Parameters

Complete characterization of optical waveguides includes evaluation of the effective index, refractive index profile, waveguide depth, propagation loss and near-field intensity profile. The measurement methods for each one of these waveguide characteristics will be discussed in the following subsections. Before measurement can be made, a suitable light coupling technique should be used to introduce the optical energy into the waveguide. The operation of optical input/output couplers is discussed firstly in Section 4.2.1.

4.2.1 Coupling of Light into Optical Waveguide

Optical input/output couplers are essential elements in integrated optics because they provide an efficient means for launching light into and out of an optical waveguide. The most convenient and commonly used techniques are prism coupling and end-fire coupling.

4.2.1.1 Prism Coupling

The schematic and experimental arrangement of an input and output prism coupler are shown in Fig.4.4. The right angle prisms of a high refractive index n_p are pressed against the waveguide surface, leaving a narrow gap S between the waveguide and base of the prism [4.2,4.3]. The incident light is totally reflected at the input prism base, setting up a standing wave in the prism and its evanescent fields penetrate into the gap. The waveguide can support a number of modes propagating along the y direction, and each mode associates with a mode number m and a propagation constant β_m. For coupling to take place, it is necessary that the component of the wave vector parallel to the prism base surface is equal for the wave in the prism and that in the waveguide, i.e.

$$\beta_m = k_o n_p \sin \phi \tag{4.1}$$

where $k_o=2\pi/\lambda$. In addition, the gap S should be sufficiently small (typically S is in the order of half of a wavelength) so that the evanescent fields of the standing wave overlap that of the waveguide mode. If these conditions are satisfied, coupling becomes effective and optical energy can be transferred from the input prism to the waveguide and back from the waveguide to the output-prism. In this case, the direction of the incident light is called a synchronous direction, and the incident angle θ_m a synchronous angle. The effective index N_{eff} ($= \beta_m/k_o$) can be expressed as [4.4,4.5]

$$N_{eff} = n_p \sin\left[\alpha + \arcsin\left(\frac{\sin\theta_m}{n_p}\right)\right] \tag{4.2}$$

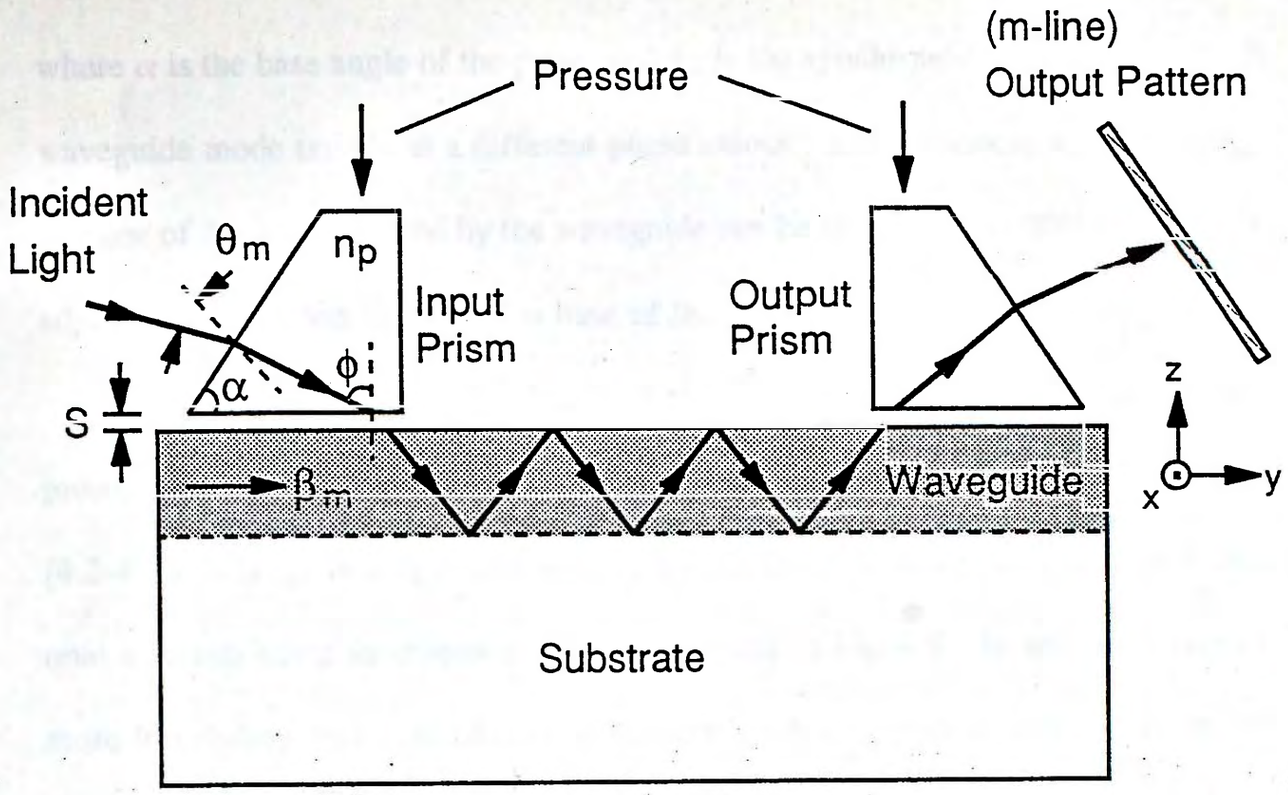

(a)

(b)

Fig.4.4 (a) Schematic of input and output prism couplers;
(b) Actual experimental arrangement.

where α is the base angle of the prism and θ_m is the synchronous angle. Since each waveguide mode travels at a different phase velocity and associates a different θ_m, any one of modes supported by the waveguide can be selectively excited by properly adjusting the incident angle to the base of the prism.

The optical energy in the excited mode is scattered and cross-coupled to other propagation modes due to surface roughness and waveguide inhomogeneities [4.2-4.5]. The guided light can be coupled out from the waveguide and projected onto a screen using an output prism as illustrated in Fig.4.4. In this way, one or more (depending on the number of waveguide modes supported) bright lines called *m* lines will be observed on the screen. Typical *m* lines for glass and $LiNbO_3$ waveguides are shown in Fig.4.5. Each line represents a mode of different order *m*, and the whole is a display of the spectrum of the waveguide modes. With increasing coupling (i.e. by varying θ_m) the *m* lines become brighter. Then they broaden and their positions shift as the phase-matching condition is violated. The synchronous angles θ_m can be easily determined from the positions where the intensity of the *m* lines become maximum.

4.2.1.2 End-fire Coupling

In the end-fire coupling method, microscope objective lenses are used to focus the incident light into, and extract the guided light from, the polished waveguide end-faces (Fig.4.6a) [4.4,4.5]. To achieve high coupling efficiency, the optical flatness of the waveguide end-faces should be within a quarter of a wavelength. The lenses and the waveguide (typically of a few micrometers width and depth) must be separately mounted on high-precision micropositioners and

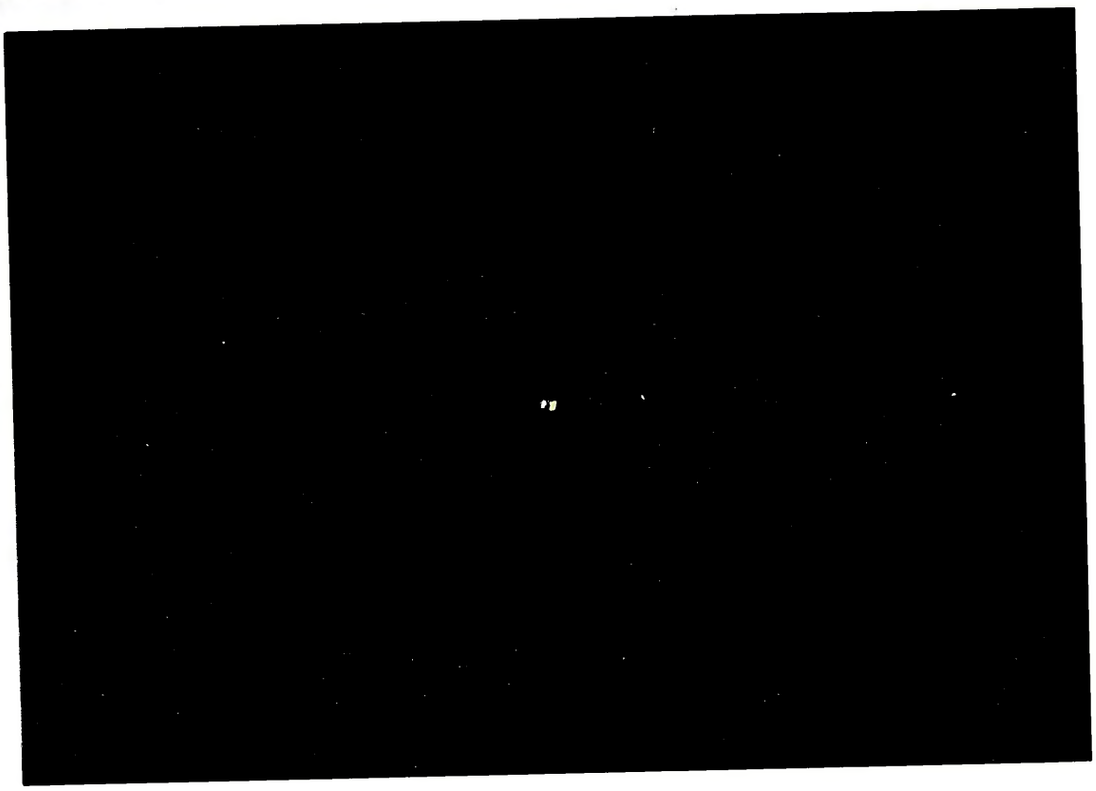

(a)

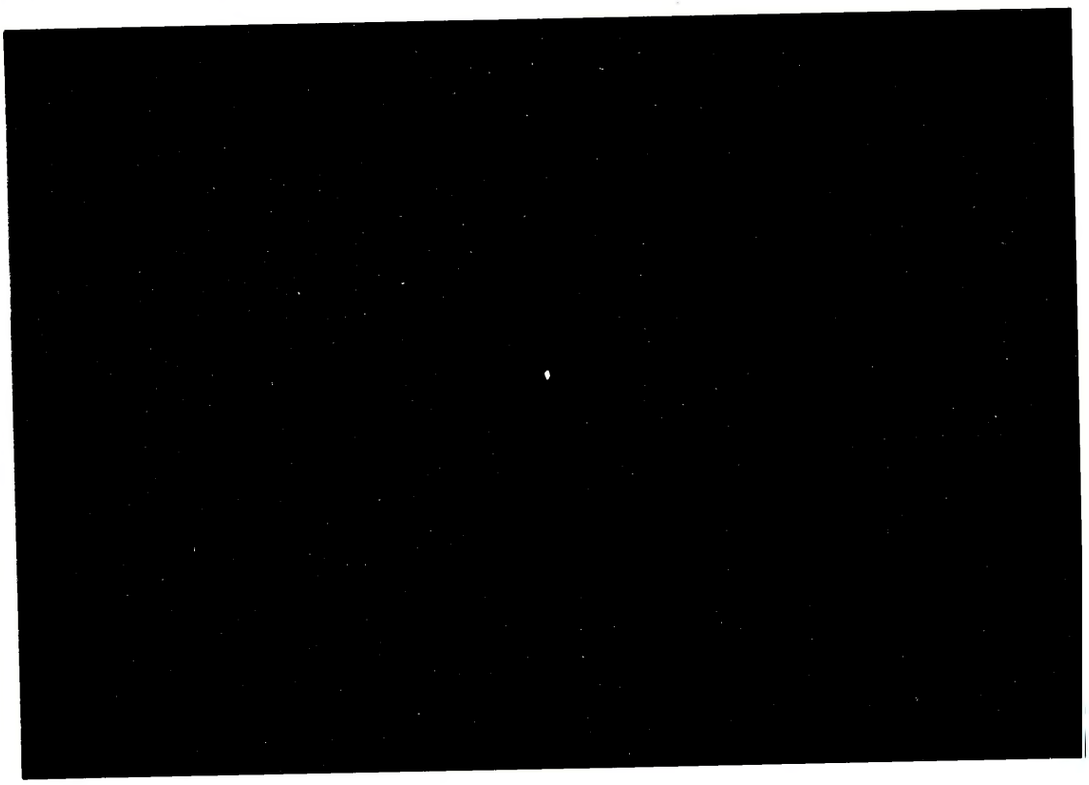

(b)

Fig.4.5 Photographs of the *m* lines for (a) an ion-exchanged glass waveguide; (b) a proton-exchanged $LiNbO_3$ waveguide.

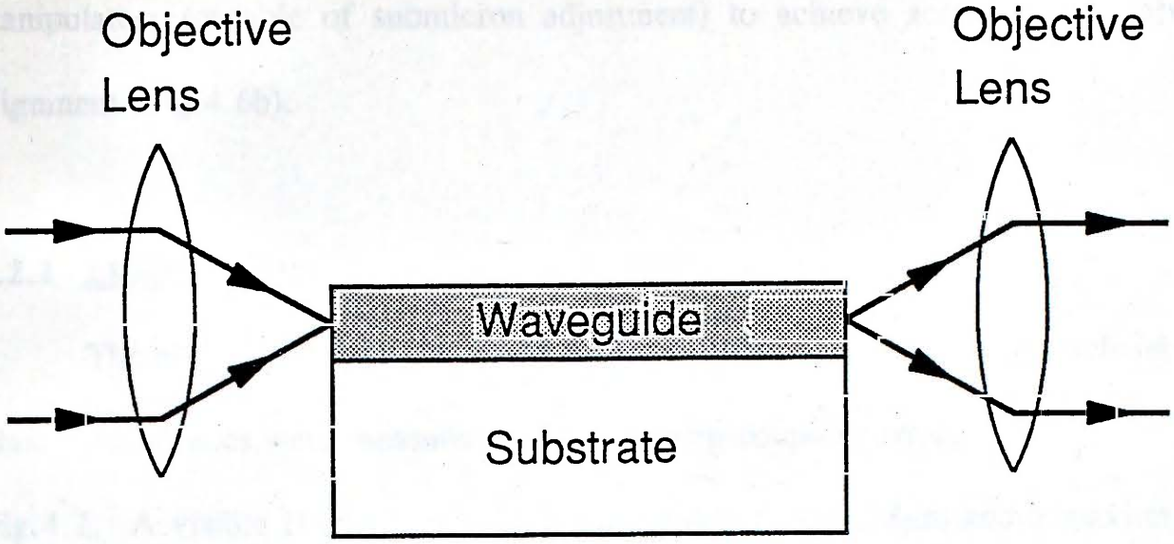

(a)

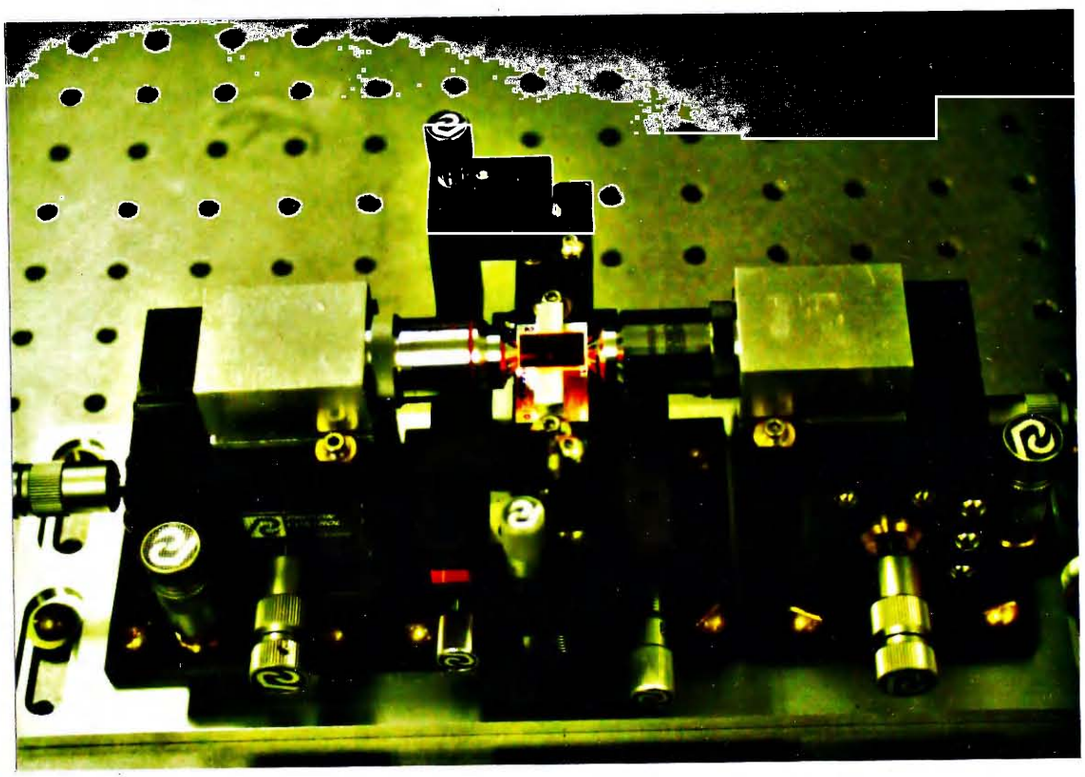

(b)

Fig.4.6 (a) Schematic showing the principles of the end-fire coupling technique; (b) Photograph of the experimental arrangement.

manipulators (capable of submicron adjustment) to achieve accurate and stable alignment (Fig.4.6b).

4.2.2 Effective Index

The effective indices and the number of guided modes of proton-exchanged planar waveguides were measured using the prism-coupling arrangement shown in Fig.4.7. A visible HeNe laser with a wavelength of 0.6328μm and a maximum power of 5mW was used as the light source. A pair of right-angle rutile (TiO_2) prisms with optical axis parallel to the polished base surface were used to couple the laser beam into and out of the waveguide. The prisms were pressed against the waveguide with adjustable pressure by U-shaped clamps. The prism-coupling assembly was mounted on a high-precision rotating stage so that the incident angle can be varied arbitrarily. The synchronous angles for different modes of propagation were measured with an accuracy of $\pm$6 second. The base angle α of the input-prism was 62.95°. The ordinary and extraordinary refractive index of the rutile prisms are $n_{p(o)} = 2.8650$ and $n_{p(e)} = 2.5835$ at 0.6328μm [4.6]. Since only transverse magnetic (TM) waves are supported in z-cut proton-exchanged waveguides, $n_{p(o)}$ should be used in Eq.4.2 for calculation of the effective index.

4.2.3 Refractive Index Profile

The refractive index profile of proton-exchanged waveguides can be inferred from the proton or lithium concentration profile measured by micro-analytical techniques such as Rutherford backscattering spectrometry (RBS) and secondary ion mass spectrometry (SIMS). The equipment, however, is expensive and is not

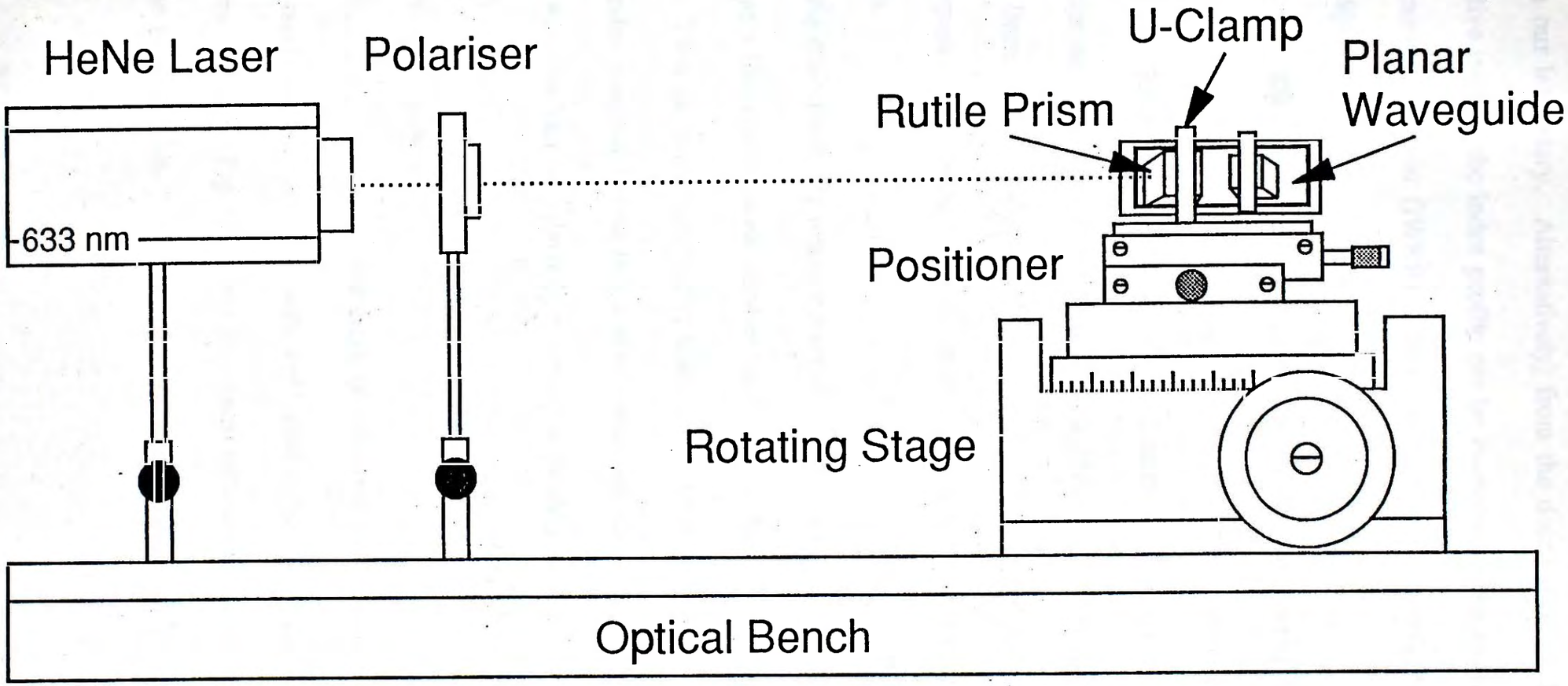

Fig.4.7 Experimental arrangement for effective index measurement employing the prism-coupling technique.

available in our laboratory. Alternatively, from the distribution of the measured mode effective indices, the index profile can be recovered using either the inverse Wentzel-Kramers-Brillouin (IWKB) method [4.7] or the effective-index function method [4.8].

In the IWKB method, the waveguide depth at each measured mode index is calculated by a recursive formula which is a solution of the approximated discrete WKB equation. The refractive index profile is then reconstructed by connecting the mode indices against the computed depth with piecewise linear segments. The number of linear segments used equals the number of measured waveguide modes. As a consequence, this method will give more accurate results for highly multimode waveguides.

In the effective-index function method, a *continuous* effective-index function is defined as a function of mode number using the measured mode indices (discrete in nature). Then the surface refractive index is interpolated from the newly formed effective-index function. With this surface index and the effective-index function, the WKB equation can be solved by a recursive formula and hence the refractive index profile is recovered. This method is superior to the IWKB method and gives a continuous and smooth reconstructed index profile. The effective-index function method, however, is less computationally efficient and sensitive to errors in measured mode indices. Both methods were used in our measurements and similar results were obtained. Fig.4.8 shows the typical refractive index profiles computed using these two methods.

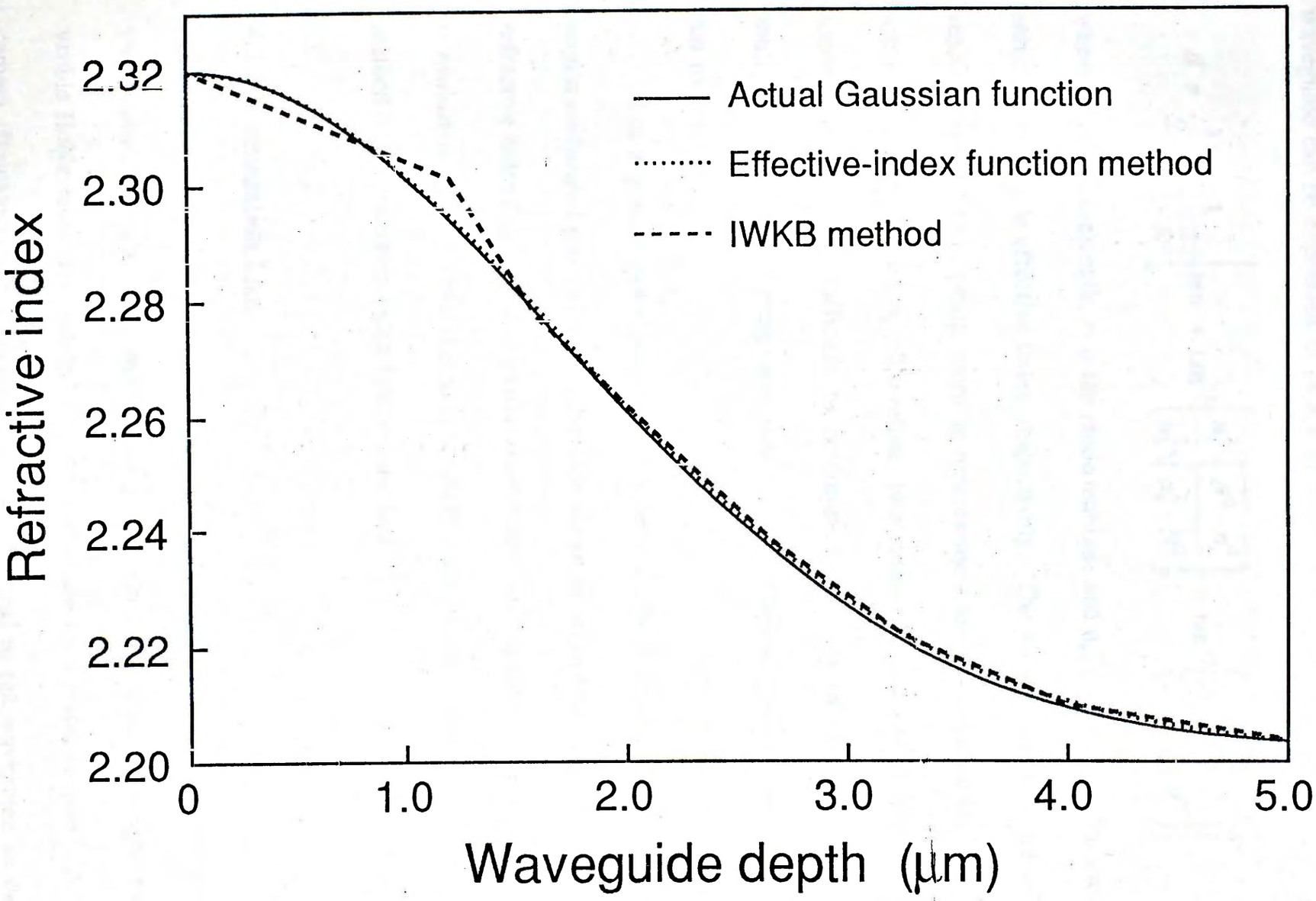

Fig.4.8 Typical refractive index profiles reconstructed by the effective-index function method and the IWKB method.

4.2.4 Waveguide Depth

For TM modes of propagation, the waveguide depth d of a step-index planar waveguide can be expressed as [4.4,4.5]

$$d = \frac{\lambda}{2\pi}\frac{1}{\sqrt{n_s^2 - N^2}}\left[m\pi + \tan^{-1}\left(\frac{n_s^2}{n_b^2}\sqrt{\frac{N^2 - n_b^2}{n_s^2 - N^2}}\right) + \tan^{-1}\left(n_s^2\sqrt{\frac{N^2 - 1}{n_s^2 - N^2}}\right)\right] \qquad (4.3)$$

where λ is the wavelength, m is the mode number, and n_s, n_b and N are the surface, substrate and mode effective index, respectively. The waveguide mode indices are readily available from prism-coupling measurement and other quantities in Eq.4.3 are known except d and n_s. Therefore, two measured values of N with different mode number m are sufficient to determine the values of both d and n_s. A multimode waveguide having more than two modes allows to check the accuracy of the results.

For a graded-index planar waveguide (e.g. those obtained by the annealed proton-exchanged process), the waveguide depth is defined as the depth where the refractive index falls to $1/e$ of its maximum value. In this case, the waveguide depth is evaluated directly from the reconstructed index profile using either the IWKB method or the effective-index function method.

4.2.5 Propagation Loss

The waveguide propagation losses were measured by a computer-assisted video camera system [4.9] shown in Fig.4.9. In this method, the light from a visible HeNe laser was coupled into the waveguide by a prism-coupler. A video camera (Hamamatsu IRRS-1000) was placed normal to the waveguide surface to

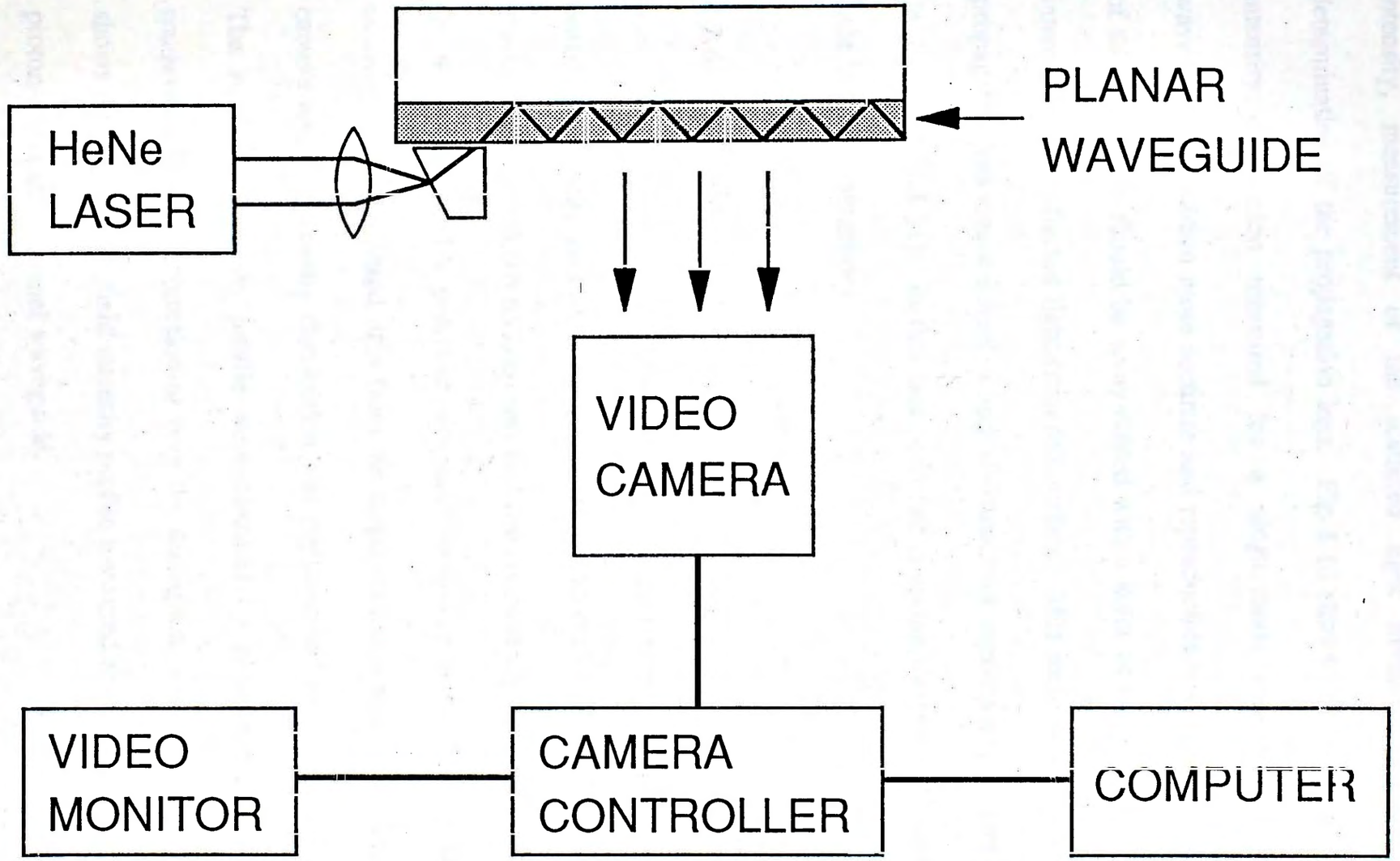

Fig.4.9 Experimental arrangement for propagation loss measurement using a computer assisted video camera system.

sample the scattered radiation along the propagation path. Assuming that the scattered light intensity along the propagation path is proportional to the guided-light intensity, measurement of the scattered light intensity distribution allows determination of the propagation loss. Fig.4.10 shows the typical scattered light intensity distribution measured for a single-mode proton-exchanged planar waveguide. To obtain more accurate and reproducible results, the bottom surface of the waveguide should be spray-coated with a layer of black paint to reduce the intensity of the reflected light from this surface. This method is also applicable to propagation loss measurement of optical channel waveguides and devices with width $\geq 10\mu m$ [4.10,4.11]. In this case, end-fire coupling method was used to launch light into the waveguides.

4.2.6 Near-field Intensity Profile

Figs.4.11 and 4.12 shows the schematic and experimental arrangement for near-field intensity profile measurement of proton-exchanged channel waveguides. The incident light ($\lambda=0.633\mu m$) was end-fire coupled into the polished end-face of the waveguide, and a polarizer was used to ensure that only TM modes were excited. The transmitted light from the output end-face was directed onto a video camera and the intensity distribution was digitized and processed by a computer. The near-field intensity profile were obtained by plotting the intensity of the transmitted light as a function of both the waveguide width and depth. Fig.4.13 shows the typical near-field intensity profile measured for a $2\mu m$ wide single-mode proton-exchanged channel waveguide.

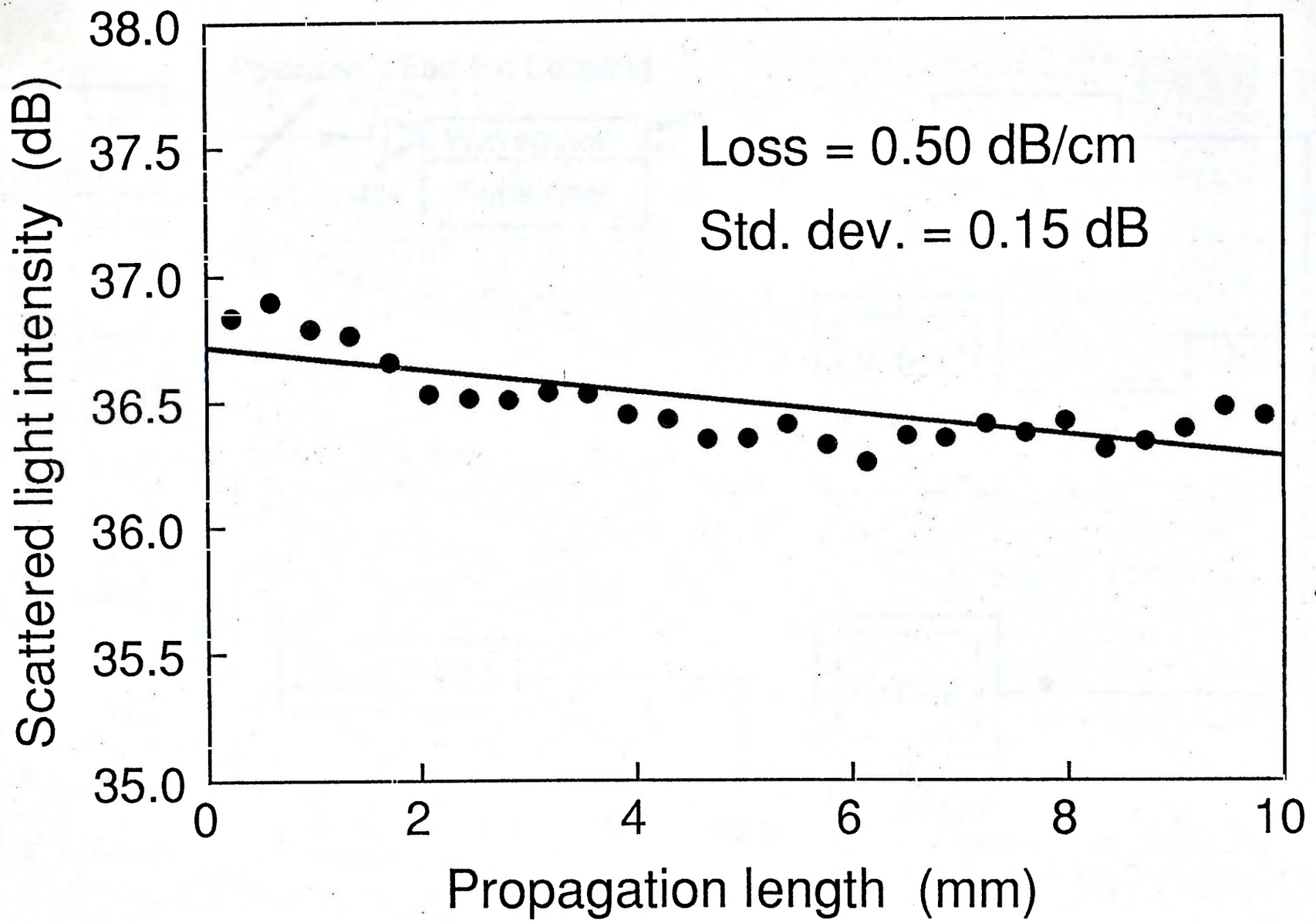

Fig.4.10 Propagation loss measurement for an annealed proton-exchanged planar waveguide.

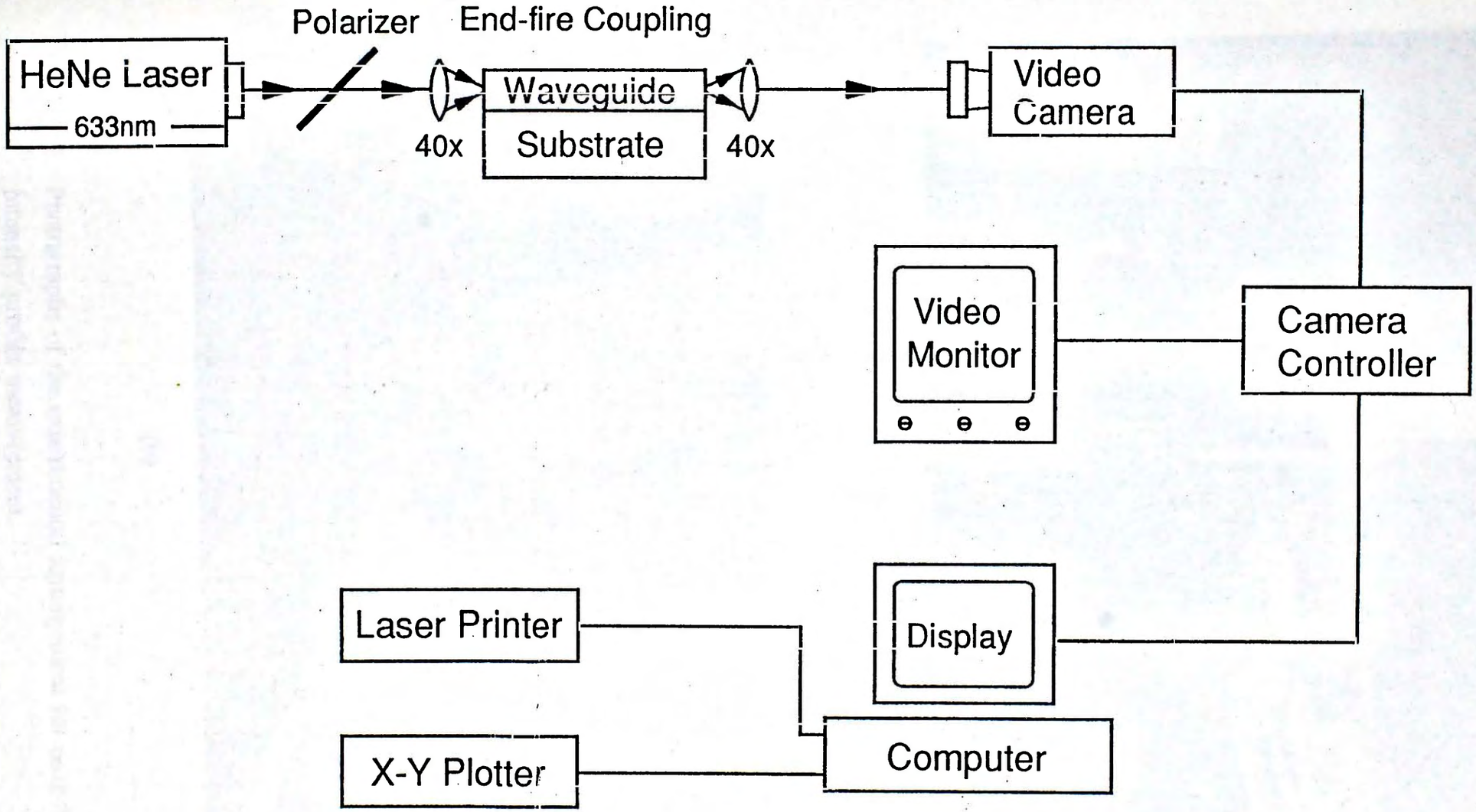

Fig.4.11 Schematic of the experimental arrangement for near-field intensity profile measurement.

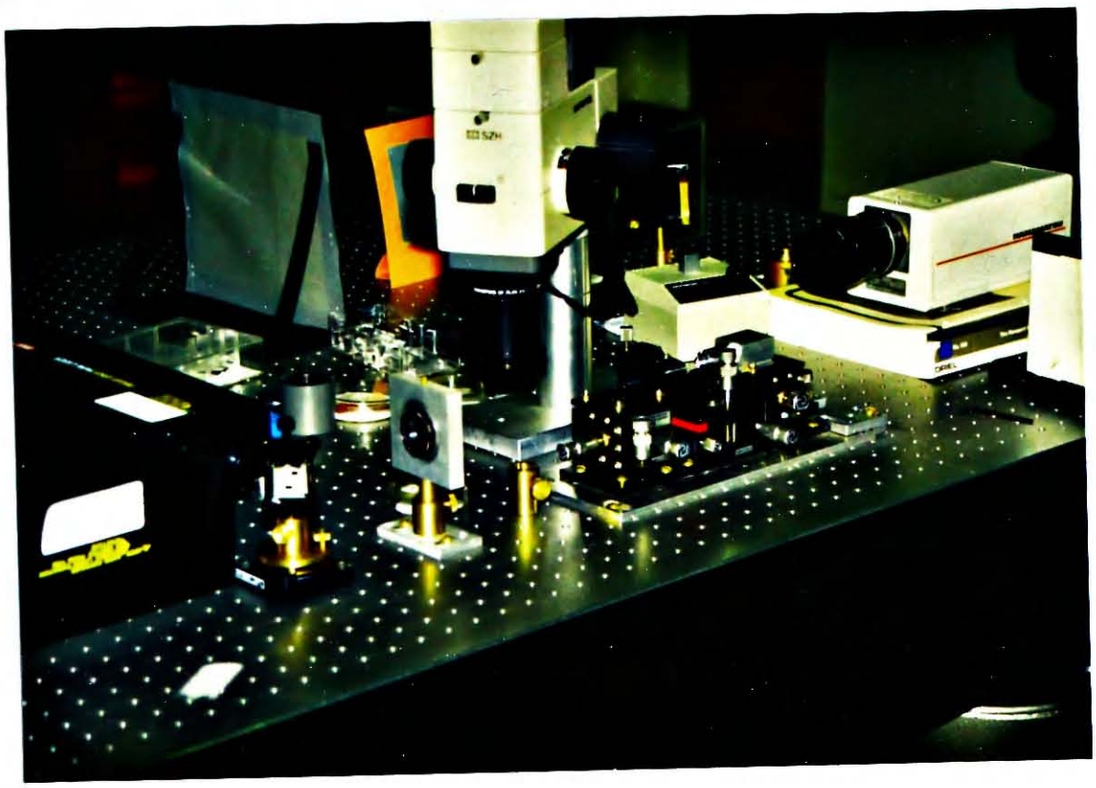

(a)

(b)

Fig.4.12 Photographs of the experimental arrangement for near-field intensity profile measurement.

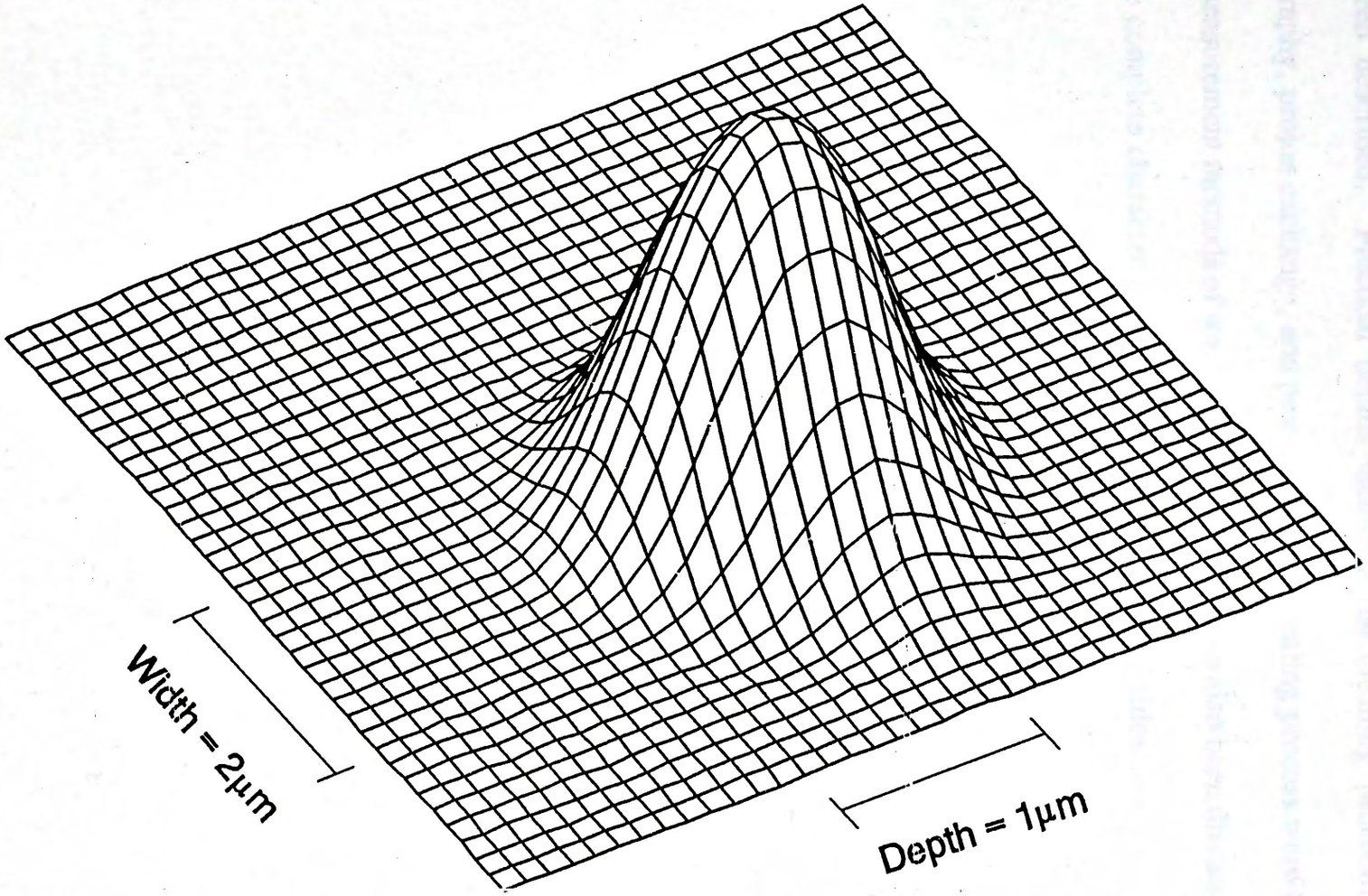

Fig.4.13 Measured near-field intensity profile for a 2μm wide proton-exchanged channel waveguide.

4.3 Summary

The process of fabricating proton-exchanged planar and channel waveguides has been described. Practical details including the cleaning procedure, photo-lithography, proton exchange, and post-exchange annealing process were discussed. The measurement methods of waveguide parameters have also been discussed, which enable complete characterization of the fabricated waveguides.

Chapter 5

Results and Discussions

Proton exchange in lithium niobate ($LiNbO_3$) is the replacement of lithium (Li^+) with hydrogen (H^+). It takes place when the substrate is immersed in an acidic medium at an elevated temperature ($\sim$150-300°C). The most commonly used proton source is benzoic acid (C_6H_5COOH). It is well established that proton-exchanged (PE) optical waveguides using benzoic acid have propagation losses of typically between 2-5 $dBcm^{-1}$, a surface index increase Δn_s of 0.12, and a step function index profile [5.1-5.3]. In our work, different proton sources have been used to fabricate PE waveguides in z-cut $LiNbO_3$, viz. phosphoric, toluic, stearic and cinnamic acids. The optical properties of these PE waveguides have been studied in detail and the results are discussed.

5.1 Proton-exchanged Waveguides Using Phosphoric Acid

Ortho-phosphoric acid (H_3PO_4) is a colourless, odourless liquid in a syrup form, and is conceptually the parent of all phosphoric acids. It is very soluble in water and acts as a triprotic acid. It has only one strong ionizing hydrogen atom and dissociates according to the following reaction [5.4]:

$$H_3PO_4 \overset{K_{\alpha(1)}}{\longleftrightarrow} H^+ + H_2PO_4^- \overset{K_{\alpha(2)}}{\longleftrightarrow} 2H^+ + HPO_4^{2-} \overset{K_{\alpha(3)}}{\longleftrightarrow} 3H^+ + PO_4^{3-} \qquad (5.1)$$

where the dissociation constant (or acidity) $K_{\alpha(1)}$, $K_{\alpha(2)}$ and $K_{\alpha(3)}$ is 7.1×10^{-3}, 8.0×10^{-8} and 4.8×10^{-13}, respectively.

The commercially available ortho-phosphoric acid has a concentration of

85wt.% and becomes anhydrous at 150°C. This acid has a tendency to polymerize, and loses half its water content to form pyro-phosphoric acid ($H_4P_2O_7$) when heated to 213°C. The reaction is rapid at 240°C and above. With further heating, poly-phosphoric acid ($H_{n+2}P_nO_{3n+1}$, n >2) and meta-phosphoric acid [$(HPO_3)_m$, m is an integer] are formed as a complex sticky mixture of polymeric acids of various chain length [5.4]. All these condensed oxyacids, regardless of pyro-, poly- or meta-phosphoric acid, are hygroscopic, and will hydrolyse to form ortho-phosphoric acid when kept for some time. Moreover, pyro-phosphoric acid will reorganize to form an equilibrium mixture of ortho-, pyro- and higher member of the series [5.5].

The proton-exchanged process is usually carried out in molten acid at exchange temperatures ranging from 160°C to 250°C. Therefore, even if ortho-phosphoric acid is used initially as the proton source, the exchange medium could be expected to be an equilibrium mixture of ortho, pyro- and higher member of the series. Since the exact composition of the acid melt is difficult to realise, the general term 'phosphoric' acid is used to represent this mixed acids proton source.

Fig.5.1.1 shows the propagation loss measurement of a single-mode PE waveguide exchanged at 205°C for 15 minutes (sample A1). The waveguide losses of our PE samples are typically < 1 $dBcm^{-1}$ for unannealed waveguides, and are lower than those obtained using the popular benzoic acid. It has been shown that the lower propagation loss for PE waveguides fabricated using phosphoric acid is due to improved uniformity of the waveguiding layer when compared to that of benzoic acid [5.6]. On the other hand, we found that the propagation loss varies from sample to sample, and the higher the mode effective index (i.e. H^+ concentration), the higher is the propagation loss. For instance, a propagation loss

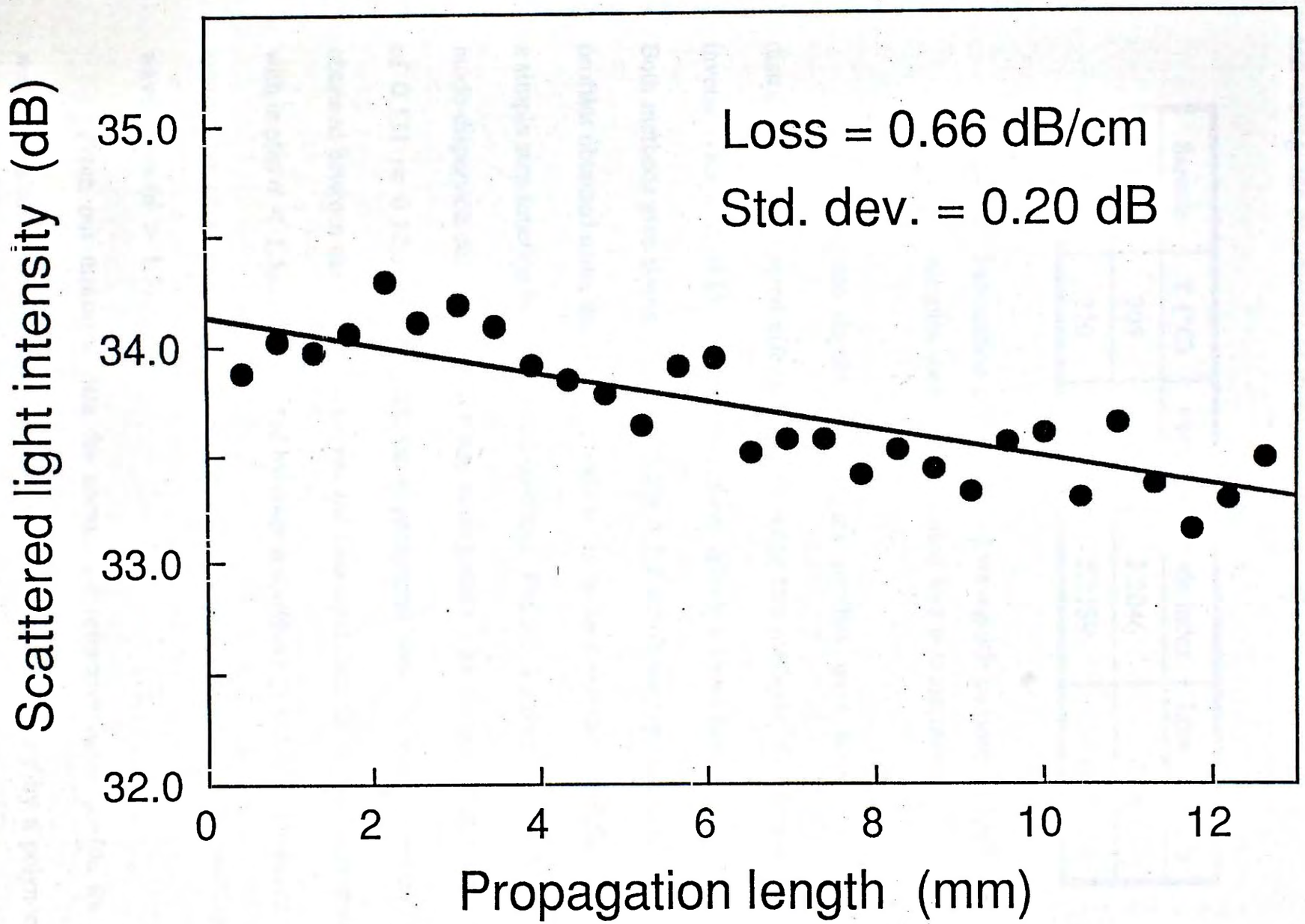

Fig.5.1.1 Propagation loss measurement of proton-exchanged waveguide using phosphoric acid (T = 205°C, t = 15min).

of 0.9 $dBcm^{-1}$ was measured for another single-mode PE waveguide exchanged at 220°C for 10 min (sample A2). Table 5.1 summarizes the fabrication conditions and waveguide parameters of these two PE samples.

Sample	T (°C)	t (min)	Mode index	Loss ($dBcm^{-1}$)
A1	205	15	2.2046	0.66
A2	220	10	2.2189	0.90

Table 5.1 Fabrication conditions and waveguide parameters for two samples used in propagation loss measurements.

The waveguide depths d and index profiles were computed from the distribution of measured effective indices using two methods: the piecewise-linear inverse WKB method [5.7] and the continuous effective-index function method [5.8]. Both methods give similar results, and Fig.5.1.2 shows the typical refractive index profiles obtained using the latter method. It can be seen that the index profile is not a simple step function but is a graded function. Fig.5.1.3 shows a set of theoretical mode-dispersion curves based on a step index profile with surface index change Δn_s of 0.131 or 0.124 together with the experimental data. Close agreement was obtained between the theoretical curves and measured data for shallow waveguides with depths $d < 1.5\mu m$, as reported by other researchers [5.9,5.10]. However, the assumption of a step index profile becomes inappropriate for highly multimode waveguides ($d > 1.5\mu m$).

From our measured data the *normalized* refractive index profile for PE waveguides using phosphoric acid could be modelled accurately by a polynomial expression of the form

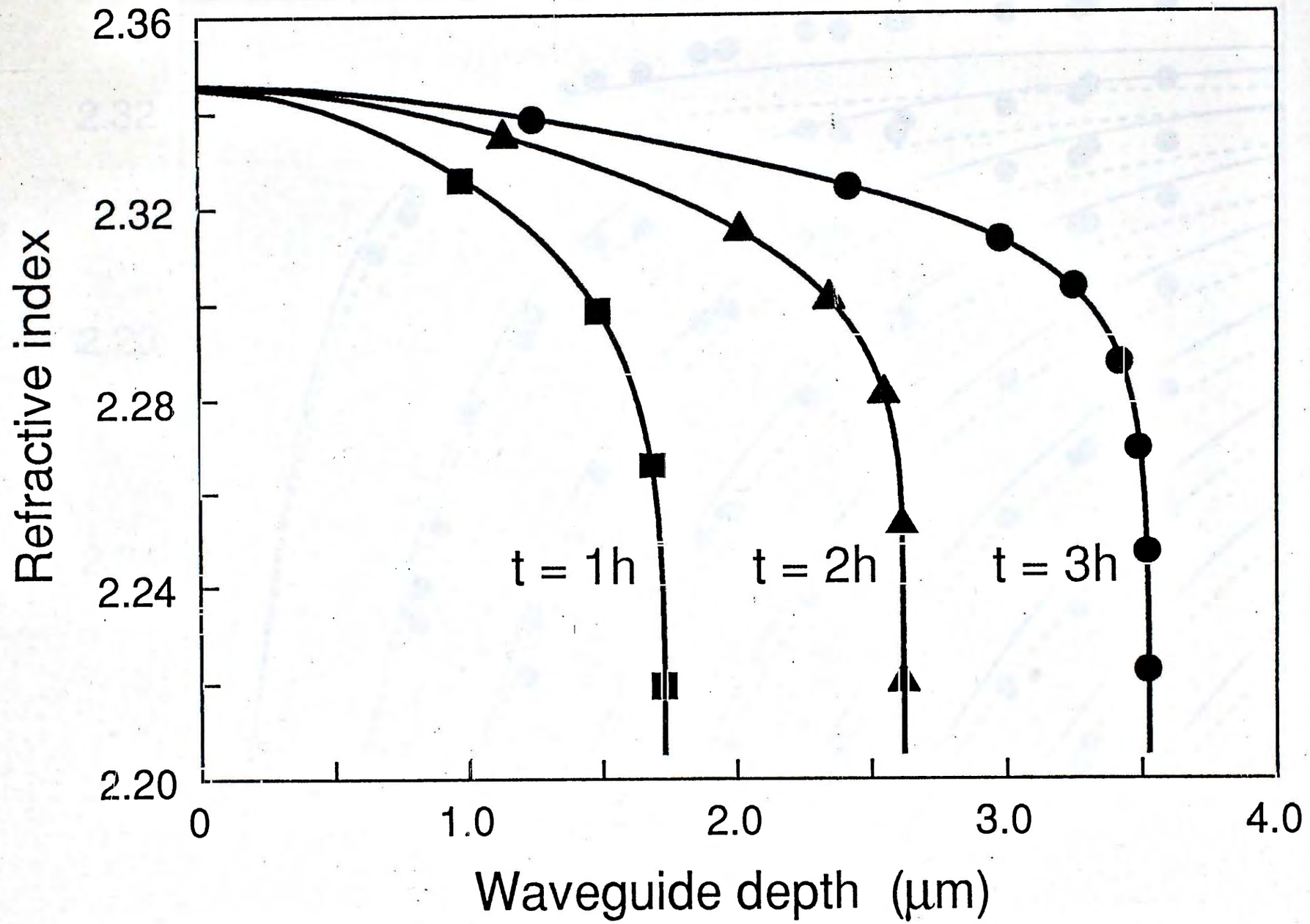

Fig.5.1.2 Refractive index profiles of PE waveguides using phosphoric acid as the proton source (T = 250°C).

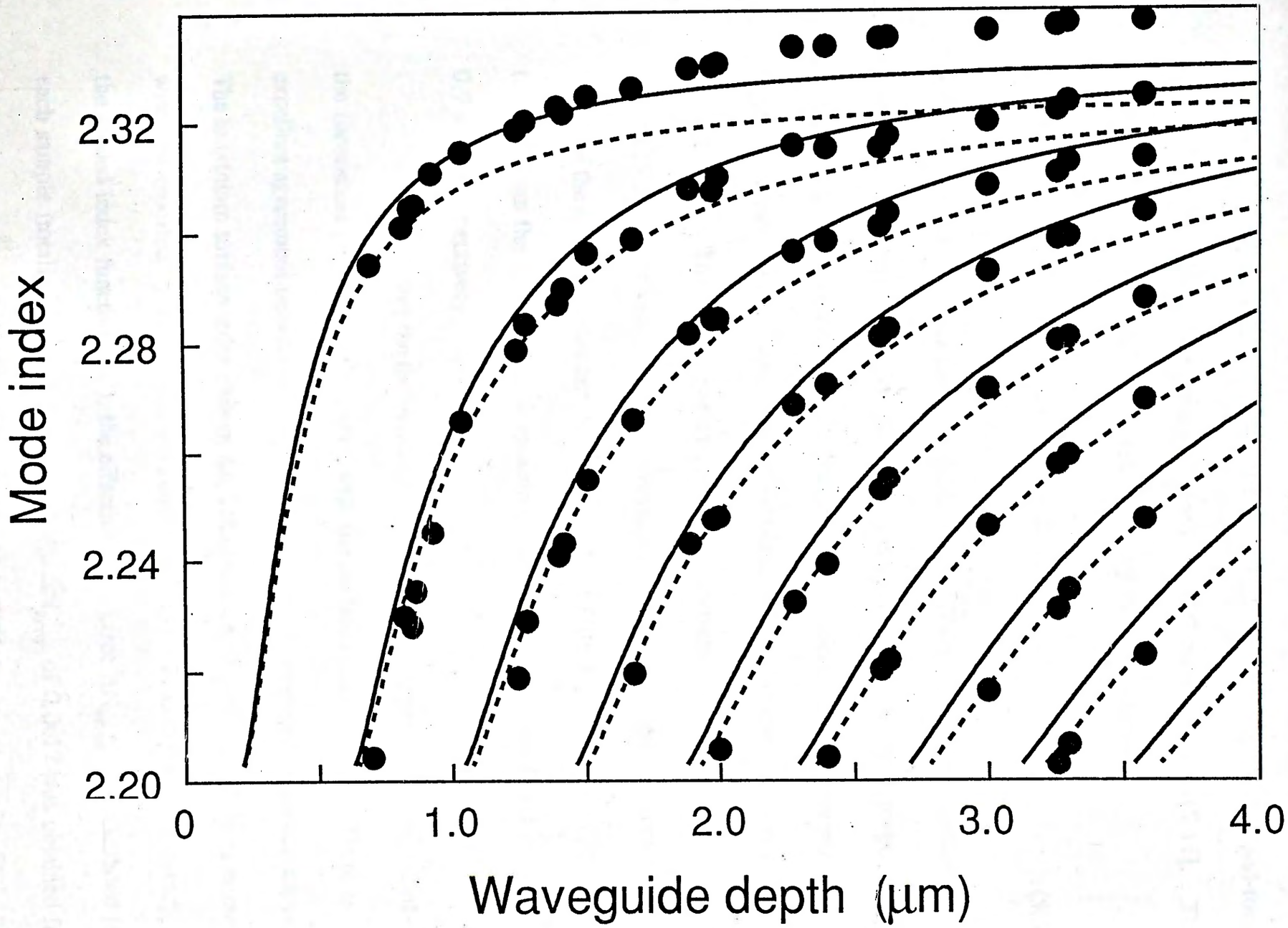

Fig.5.1.3 Theoretical mode-dispersion curves based on a step-index function together with experimental data. Solid and dotted curves refer to $\Delta n_s = 0.131$ and 0.124, respectively.

$$f(x) = (1 + ax^2 + bx^4)^{1/r} \qquad (5.2)$$

where x is the normalized waveguide depth, r is an integer ≥ 1, a and b are constants such that (a + b) = -1 (i.e. f(0) = 1, f(1) = 0), and f(x) is a closed-form solution of a nonlinear concentration-dependent diffusion equation [5.11]. The refractive index profile n(x') is related to f(x) by the expression

$$n(x') = n_{sub} + \Delta n_s f(x'/d) \qquad (5.3)$$

where n_{sub} is the substrate index (=2.202 at 0.6328μm), Δn_s is the surface index increase, and *d* is the waveguide depth defined by $n(d) = n_{sub}$. With proper values for the profile parameters a, b and r, f(x) can fit the experimentally obtained profile. Fig.5.1.4 shows the theoretical normalized index profile f(x) and the experimentally obtained ones. The profile parameters were determined using the least squares method [5.12]. The values of these parameters were varied until a minimum of the square of the effective index error ΔN_{error} (=abs. | N(theo.) - N(meas.) |) has been found. From the analysis of our measured data, a, b and r were found to be -1.7, 0.7 and 6, respectively.

Fig.5.1.5 shows the theoretically generated mode-dispersion curves based on the theoretical profile n(x') together with the measured data [5.13]. There is an excellent agreement between the experimental data and computed dispersion curves. The maximum surface index change Δn_s calculated was 0.145 which is in agreement with that reported by Taniuchi and Yamamoto [5.14]. To confirm the accuracy of the graded index function n(x'), the effective index error ΔN_{error} was calculated for each sample (totally 23 samples). An average ΔN_{error} of 0.0017 was obtained for n(x'), while ΔN_{error} has values of 0.0045 and 0.0052 for step index profiles with

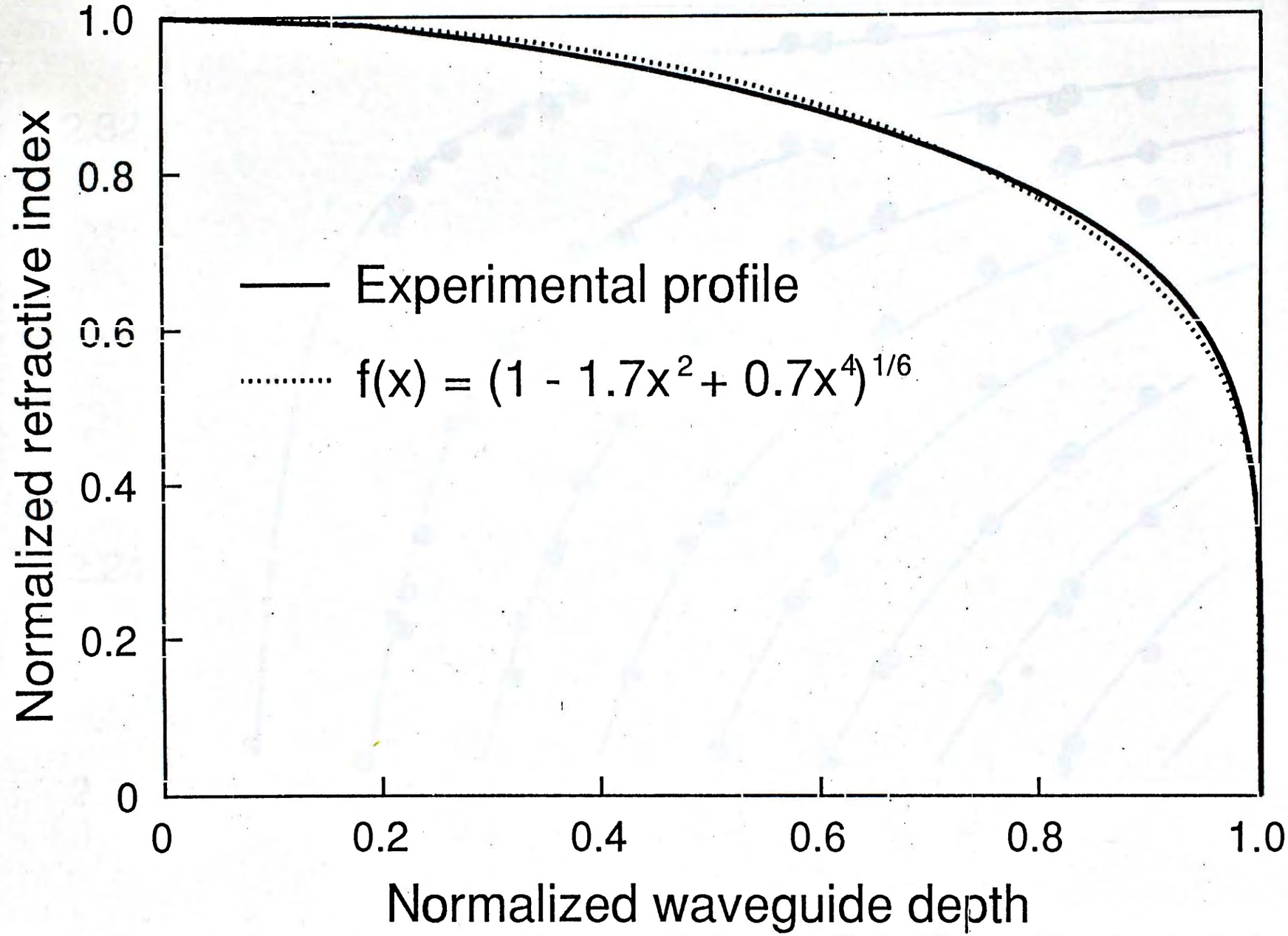

Fig.5.1.4 Comparison of experimental and postulated normalized index profile for PE waveguides using phosphoric acid.

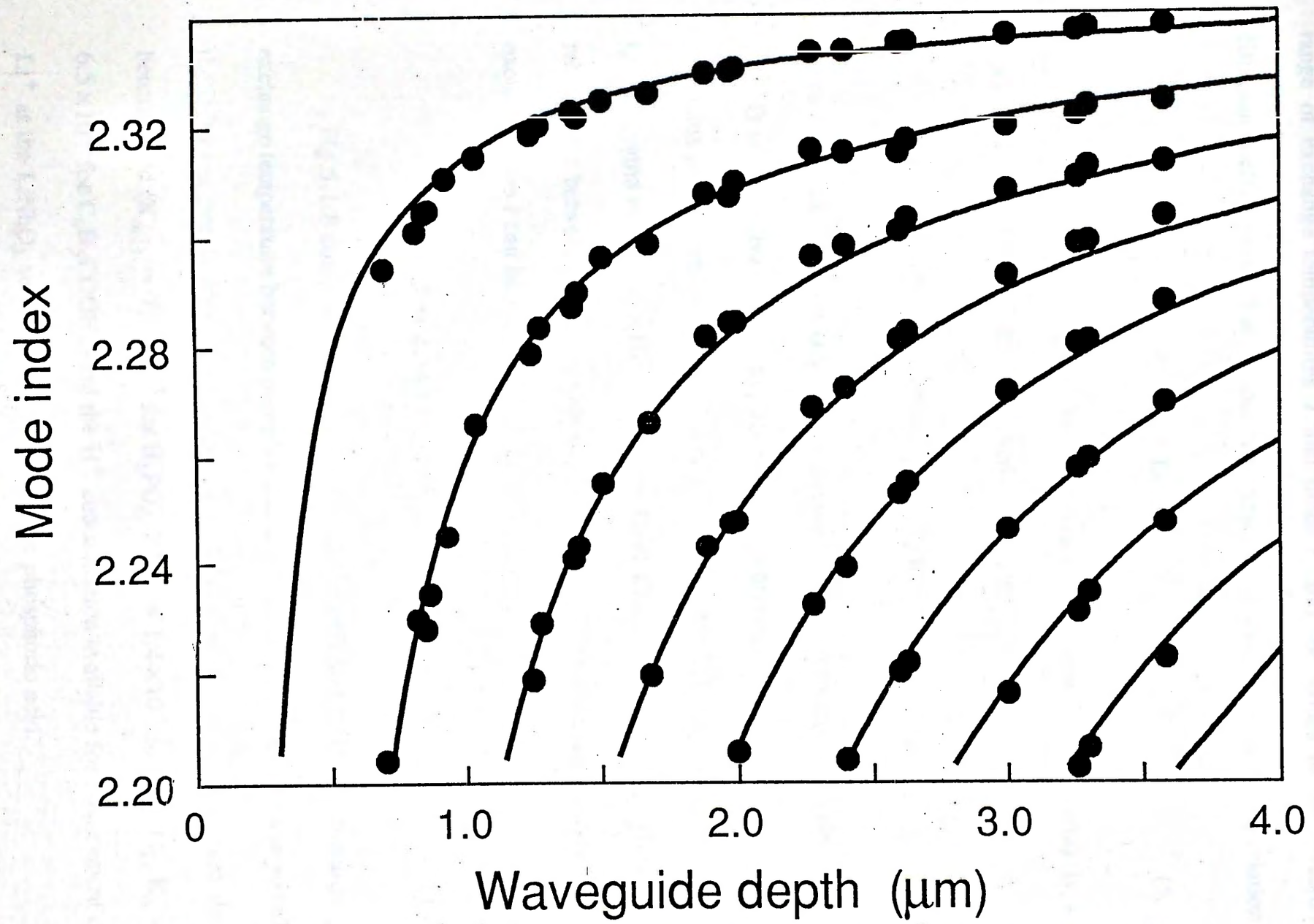

Fig.5.1.5 Theoretical mode-dispersion curves based on n(x) together with experimental data.

Δn_s = 0.131 and 0.124, respectively.

Fig.5.1.6 shows a plot of diffusion depths *d* of the PE waveguides over a range of exchange temperatures *T* and times *t*, and the values of the effective diffusion coefficient D(T) at various temperatures are calculated using the relation

$$d = [t \times D(T)]^{1/2} \tag{5.4}$$

The dependence of D(T) on exchange temperature *T* (in Kelvin) is an exponential relation and follows the Arrhenius Law

$$D(T) = D_o \exp(-Q/RT) \tag{5.5}$$

where D_o is the diffusion constant for proton-exchange process using phosphoric acid, Q is the activation energy, and R is the universal gas constant. From the Arrhenius plot shown in Fig.5.1.7, i.e. ln[D(T)] versus 1/T, the values of D_o and Q were found to be 6.43×10^8 μm^2h^{-1} and 82.91 $kJmol^{-1}$, respectively. Hence the relationship between the waveguide depth *d* and the fabrication temperature *T* and exchange time *t* can be expressed as

$$d = 2.54\times10^4 \sqrt{t} \exp(-4.99\times10^3/T) \ \mu m \tag{5.6}$$

Fig.5.1.8 compares the effective diffusion coefficient D(T) as a function of exchange temperature between phosphoric acid and benzoic acid [5.3]. As expected, the diffusion rate is faster for phosphoric acid because it is a stronger acid than benzoic acid ($K_{\alpha(1)} = 7.1\times10^{-3}$ for H_3PO_4, $K_{\alpha(1)} = 1.4\times10^{-1}$ for $H_4P_2O_7$, $K_\alpha = 6.5\times10^{-5}$ for C_6H_5COOH), and the H^+ concentration available for replacement of Li^+ at the $LiNbO_3$ surface should be higher in phosphoric acid.

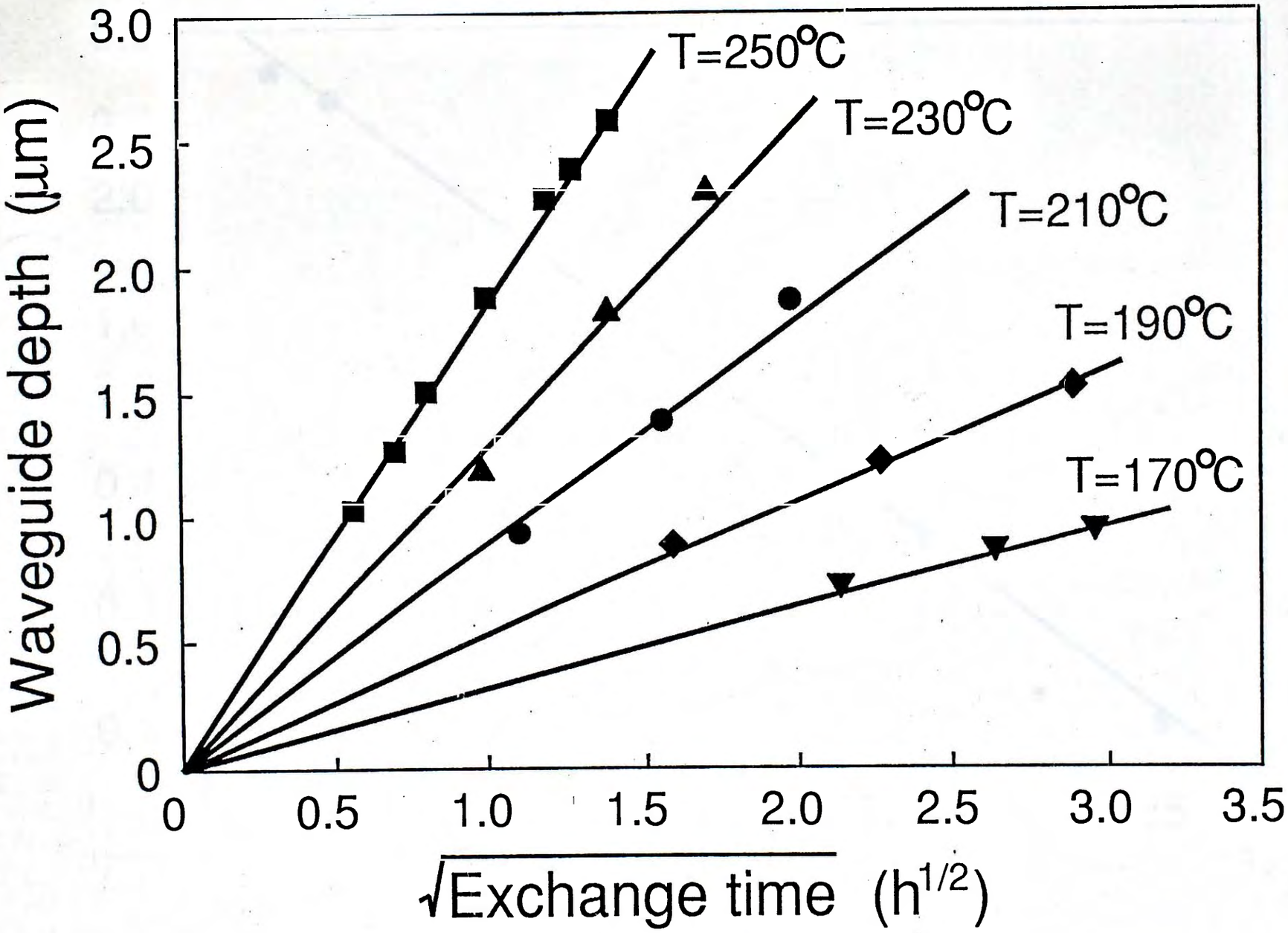

Fig.5.1.6 PE waveguide depth versus square root of exchange time.

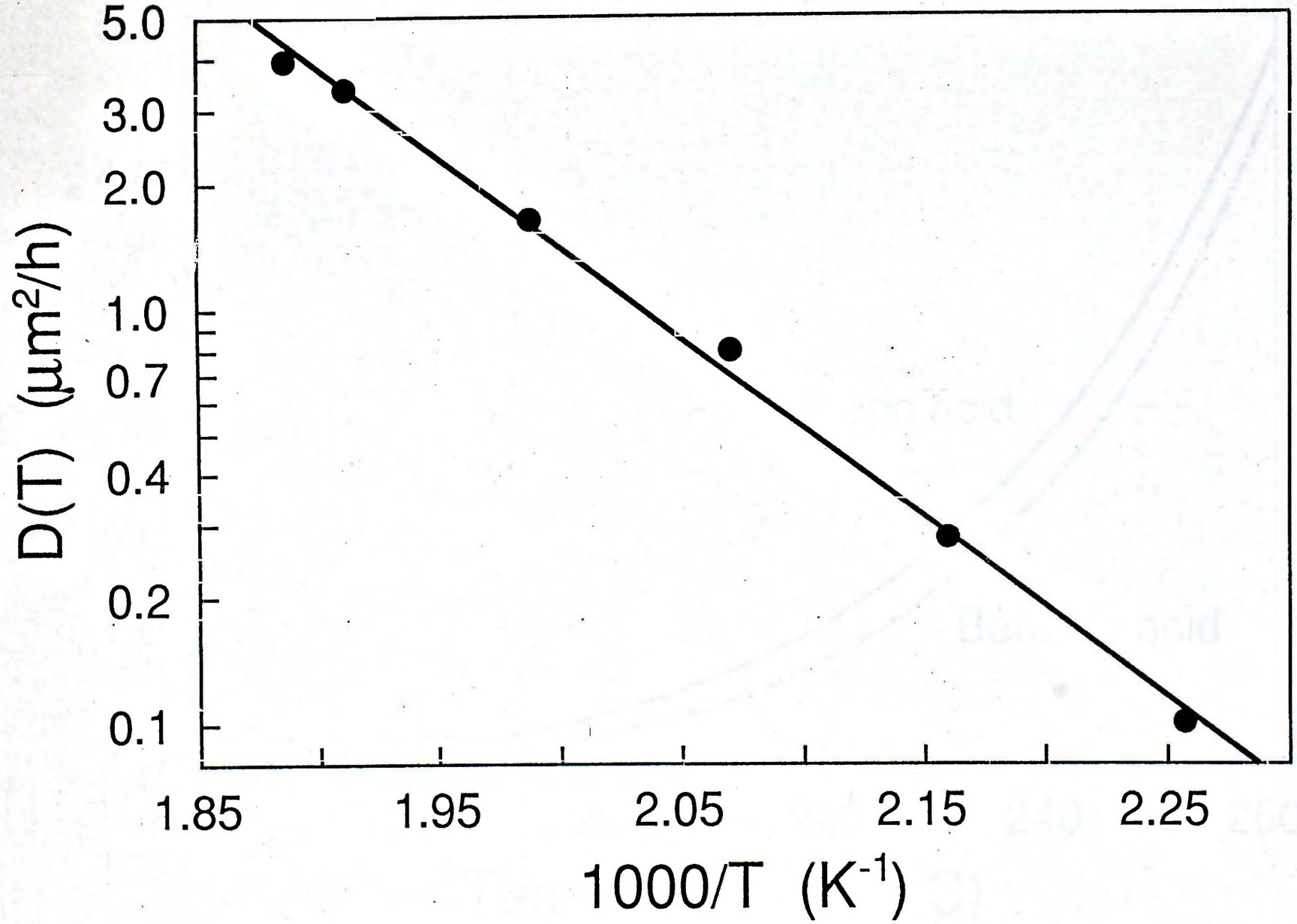

Fig.5.1.7 Plot of effective diffusion coefficient ln[D(T)] versus inverse of exchange temperature 1/T.

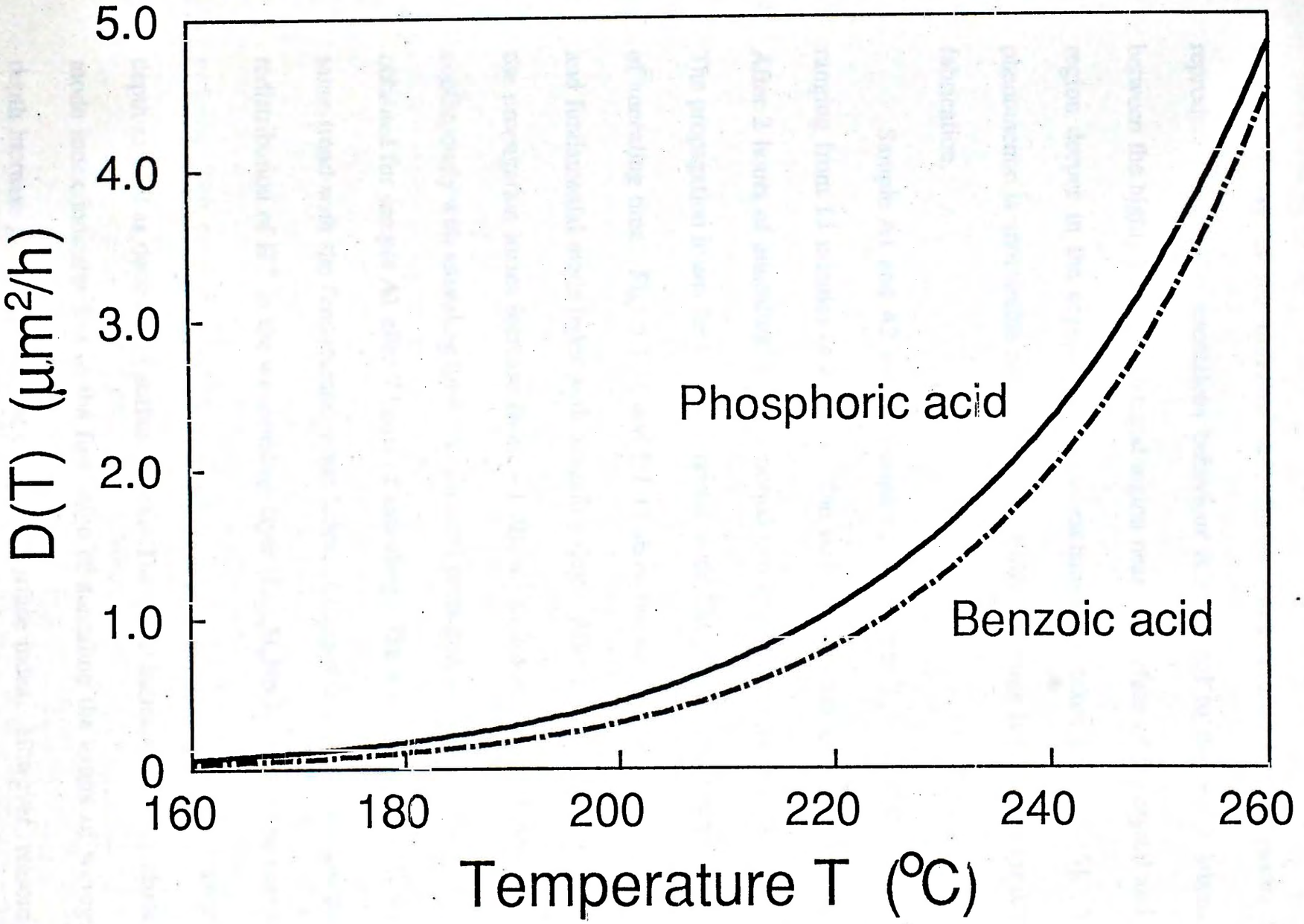

Fig.5.1.8 Comparison of effective diffusion coefficient D(T) between phosphoric acid and benzoic acid.

Side-shifted m-spots with faded m-lines were observed for multimode waveguides under certain fabrication conditions, viz. under high temperature (2.5 hours at 250°C) or long exchange time (25 hours at 200°C). Fig.5.1.9 shows a graphic display of the observed side-shifted mode spectra. The results are reproducible, and this anomalous behaviour is attributed to the lattice mismatch between the highly proton-exchanged region near the surface of the crystal and the region deeper in the crystal where less exchange has taken place [5.15]. This phenomenon is undesirable and hence a short diffusion time is preferred for device fabrication.

Sample A1 and A2 were annealed at temperature T_a = 300°C for times t_a ranging from 15 minutes to 7 hours. The waveguides were single-mode initially. After 2 hours of annealing, they supported two transverse magnetic (TM) modes. The propagation losses for the fundamental mode TM_0 were measured as a function of annealing time. Figs.5.1.10 and 5.1.11 show the variations of propagation loss and fundamental mode index with annealing time. After annealing for 15 minutes, the propagation losses increase from $\sim$1 dBcm^{-1} to 2-4 dBcm^{-1} and then decrease continuously with annealing time. A minimum propagation loss of 0.30 dBcm^{-1} was obtained for sample A1 after 7 hours of annealing. The waveguide loss follows the same trend with the fundamental mode index. Changes in mode index are due to redistribution of H^+ in the waveguiding layer ($Li_{1-x}H_xNbO_3$) during the annealing process. This drive-in diffusion of H^+ leads to continuous increase of waveguide depth as well as decrease of surface index. The initial increase in the fundamental mode index indicates that at the first stage of annealing the extent of waveguide depth increase is higher than that of drop in surface index. However, reasons for

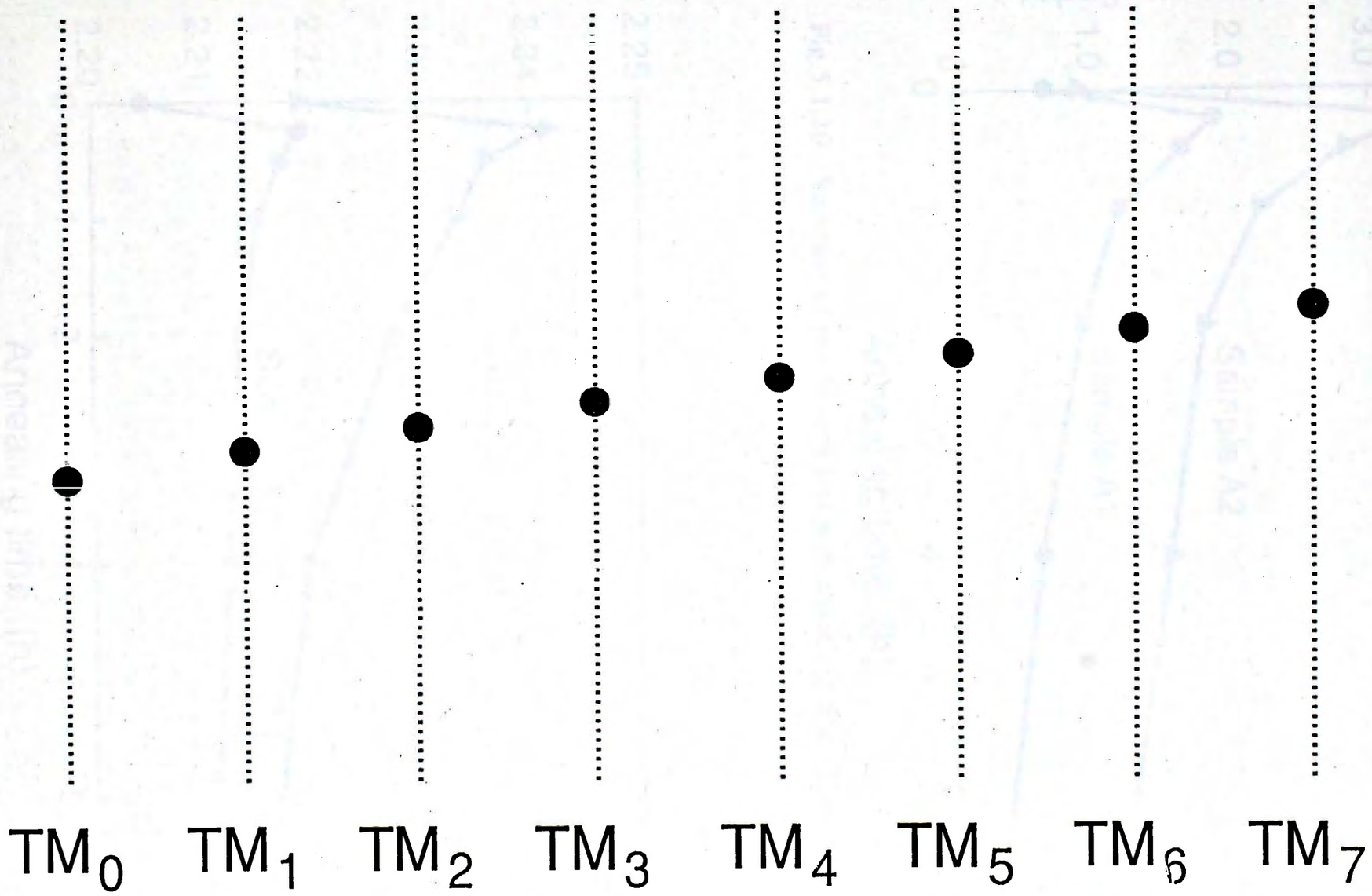

Fig.5.1.9 Schematic diagram of side-shifted mode pattern (m-spots) of PE waveguide (T = 250°C, t = 2.5h).

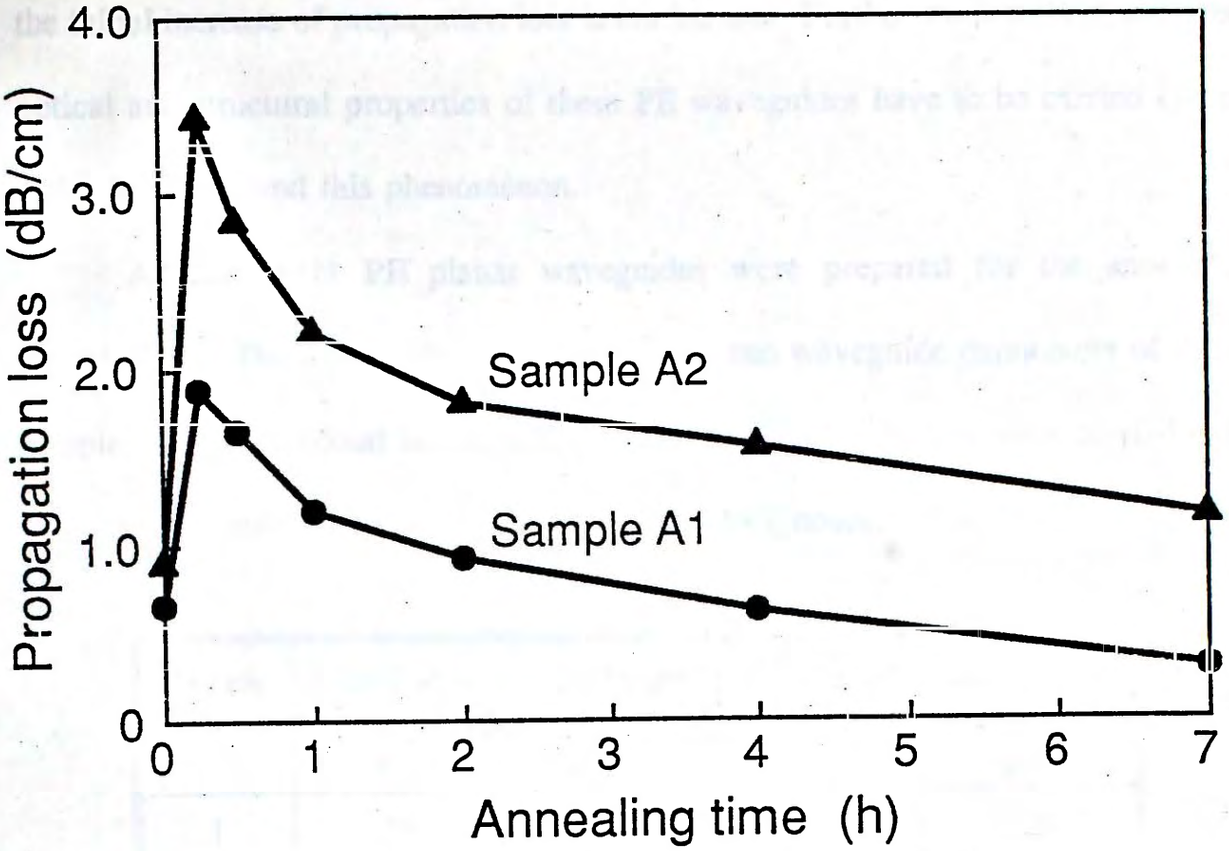

Fig.5.1.10 Variation of propagation loss with annealing time (T_a=300°C).

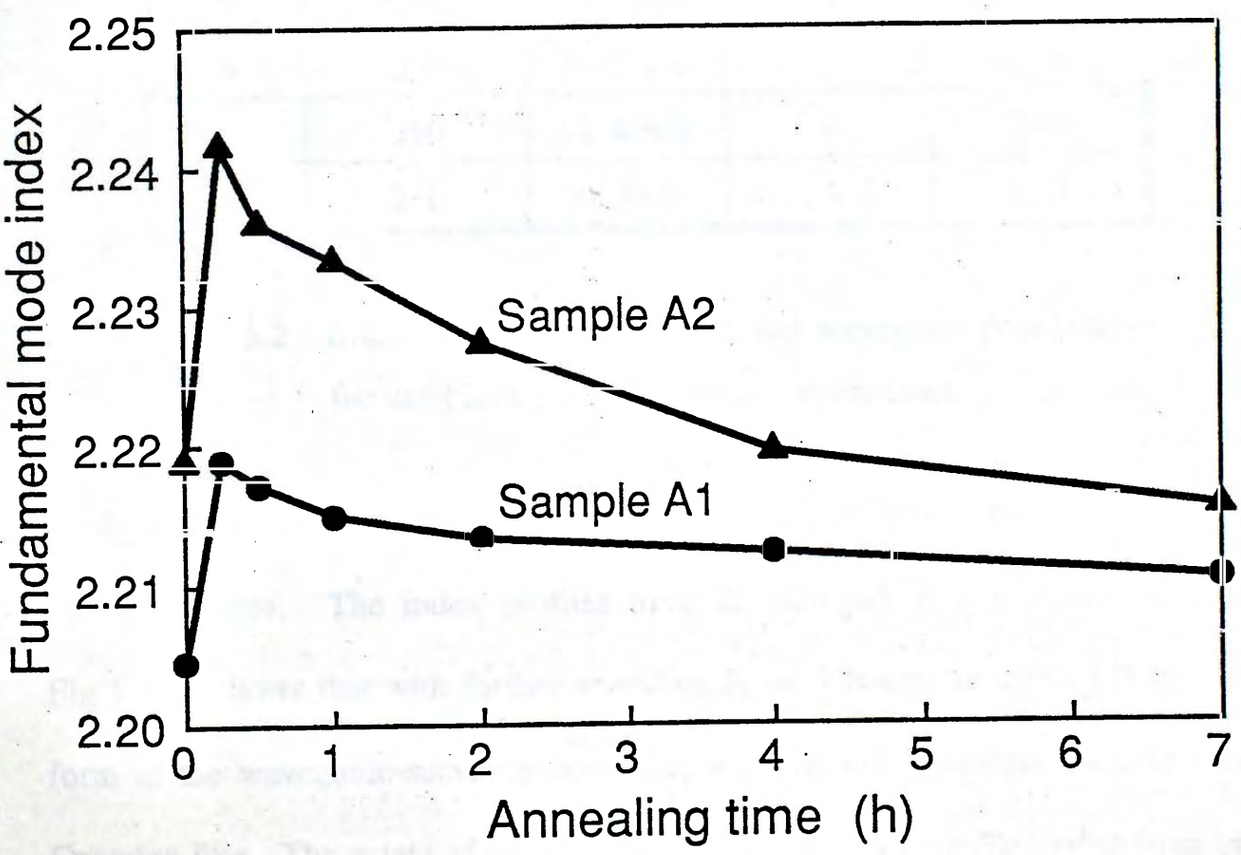

Fig.5.1.11 Variation of fundamental mode index with annealing time.

the initial increase of propagation loss is not known. Further studies correlating the optical and structural properties of these PE waveguides have to be carried out in order to understand this phenomenon.

Another eight PE planar waveguides were prepared for the annealing experiments. The initial fabrication conditions and waveguide parameters of these samples are summarized in Table 5.2. Five stages of annealing were carried out, with duration time t_a ranging from 30 minutes to 7 hours.

Sample	Exchange temperature (°C)	Exchange time	Number of modes	Waveguide depth d_o (μm)
1	250	20 min	2	1.04
2	250	30 min	3	1.28
3	250	40 min	3	1.51
4	250	1 h	4	1.89
5	250	1h 15min	5	2.00
6	250	1h 28min	5	2.28
7	250	1h 40min	6	2.40
8	250	2h 5min	6	2.63

Table 5.2 Initial fabrication conditions and waveguide parameters for samples used in annealing experiments.

Fig.5.1.12 shows the index profiles of the eight PE samples after annealing for 30 minutes. The index profiles have all changed to a step-like function. Fig.5.1.13 shows that with further annealing (t_a = 7 hours) an index tail starts to form at the waveguide-substrate boundary, and the index profiles become more Gaussian-like. The extent of the modification on the index profile varied from one

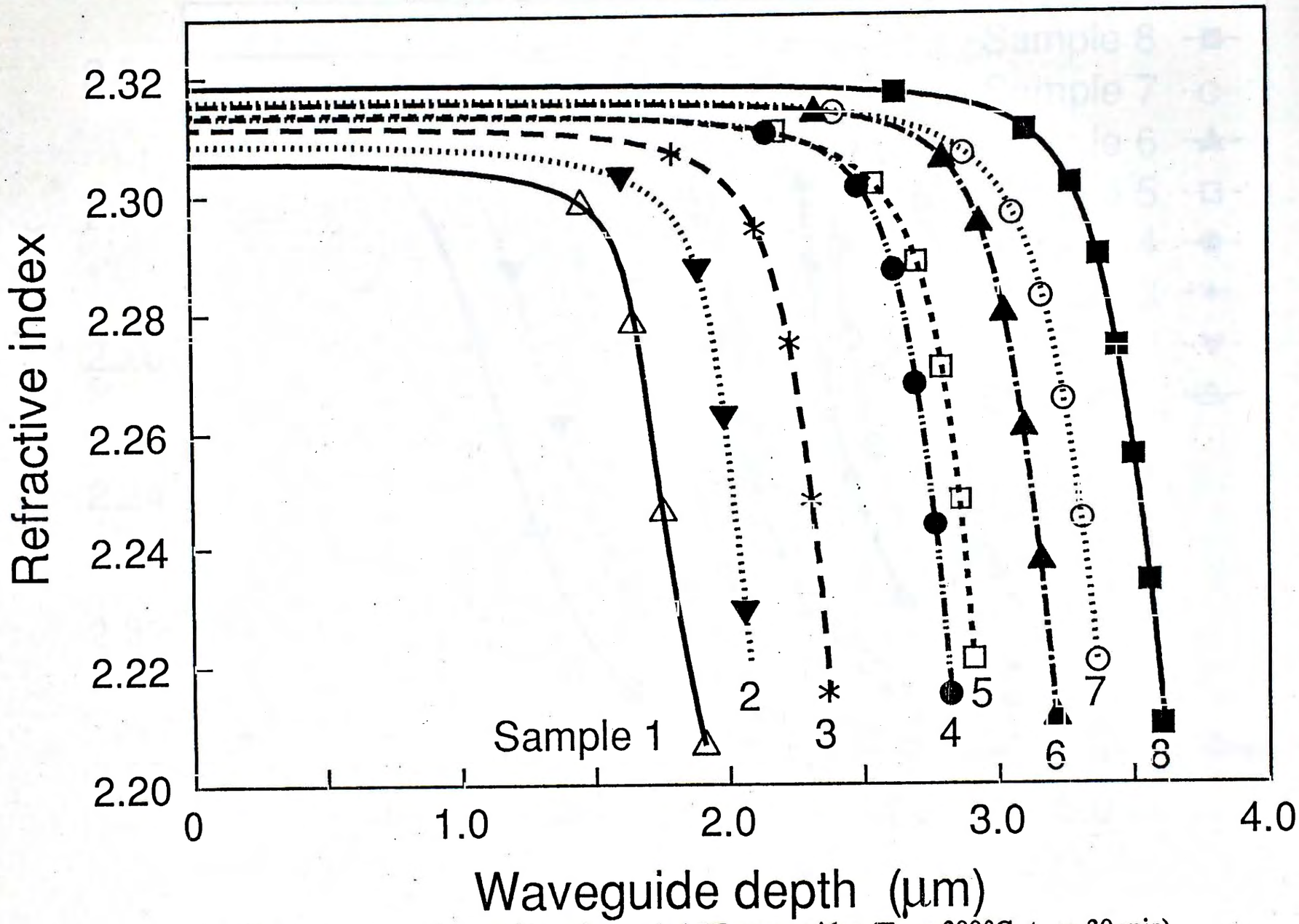

Fig.5.1.12 Refractive index profiles of annealed PE waveguides (T_a = 300°C, t_a = 30 min).

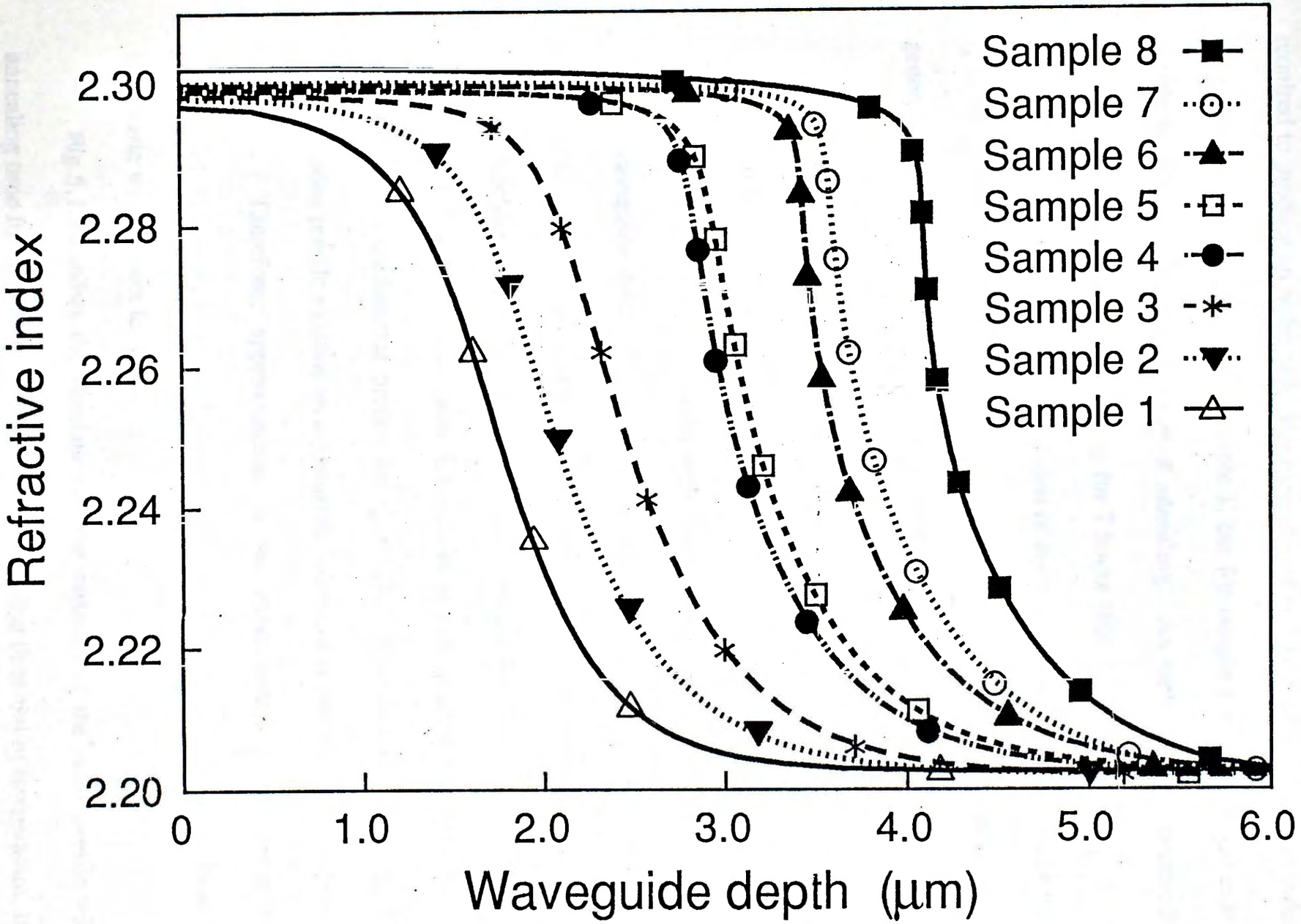

Fig.5.1.13 Refractive index profiles of annealed PE waveguides (T_a = 300°C, t_a = 7 h).

sample to another, and depends on the initial exchange time. The longer the initial exchange time (ie. more H^+ within the substrate), the longer the annealing time is required to produce an index tail. For example, after 1 hour of annealing an index tail could already be observed for sample 1, but for sample 8 a step-function index profile preserved even after 4 hours of annealing. An index tail was eventually observed in this sample after annealing for 7 hours (Fig.5.1.13).

Fig.5.1.14 shows a typical variation of the index profile with annealing time t_a as the parameter (sample 4). The annealed index profiles can be modelled by a generalized Gaussian function defined as [5.16]

$$n(x) = n_{sub} + \Delta n_s \exp\left[-\left(\frac{x}{d_a}\right)^c\right] \qquad (5.7)$$

where c is the parameter associated with the shape of the profile, and d_a is the *effective* waveguide depth defined by $n(d_a)=n_{sub}+\Delta n_s/e$. Figs.5.1.15 to 5.1.19 show the experimentally obtained annealed index profile and the best-fit generalized Gaussian function for different annealing times (sample 4). The computed profile parameters are summarized in Table 5.3. There is a close agreement between the theoretical and experimental profile for $t_a < 2h$. With further annealing, the annealed index profile exhibits an asymmetric index tail at the waveguide-substrate boundary. Therefore, approximation of the experimental profile using the generalized Gaussian function becomes less accurate because this function is symmetric with respect to d_a.

Fig.5.1.20 shows the simulation of the variation of the index profile with annealing time for sample 4. By varying the annealing time and/or temperature, the

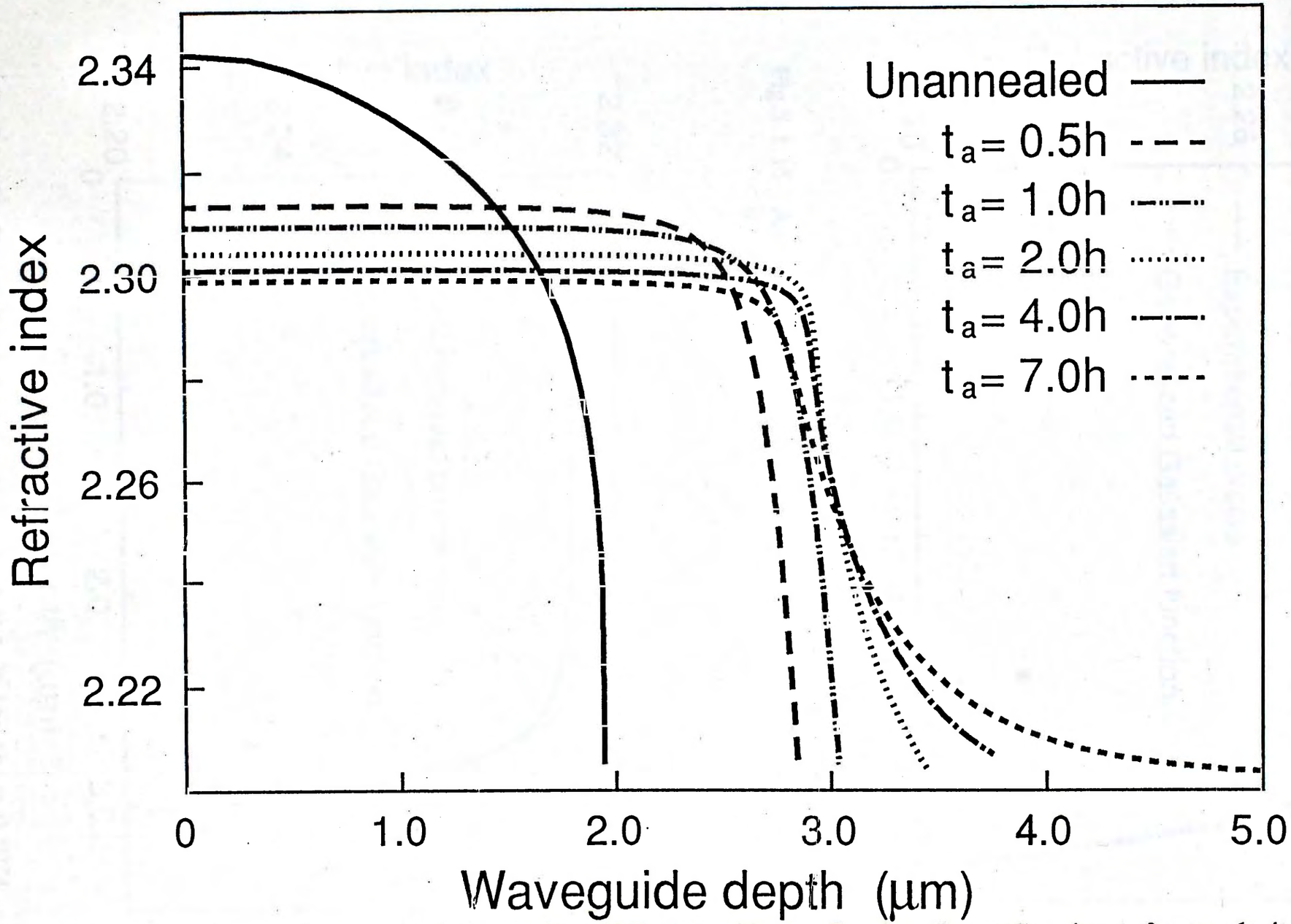

Fig.5.1.14 Changes in refractive index profile of PE waveguide as a function of annealing time t_a for sample 4.

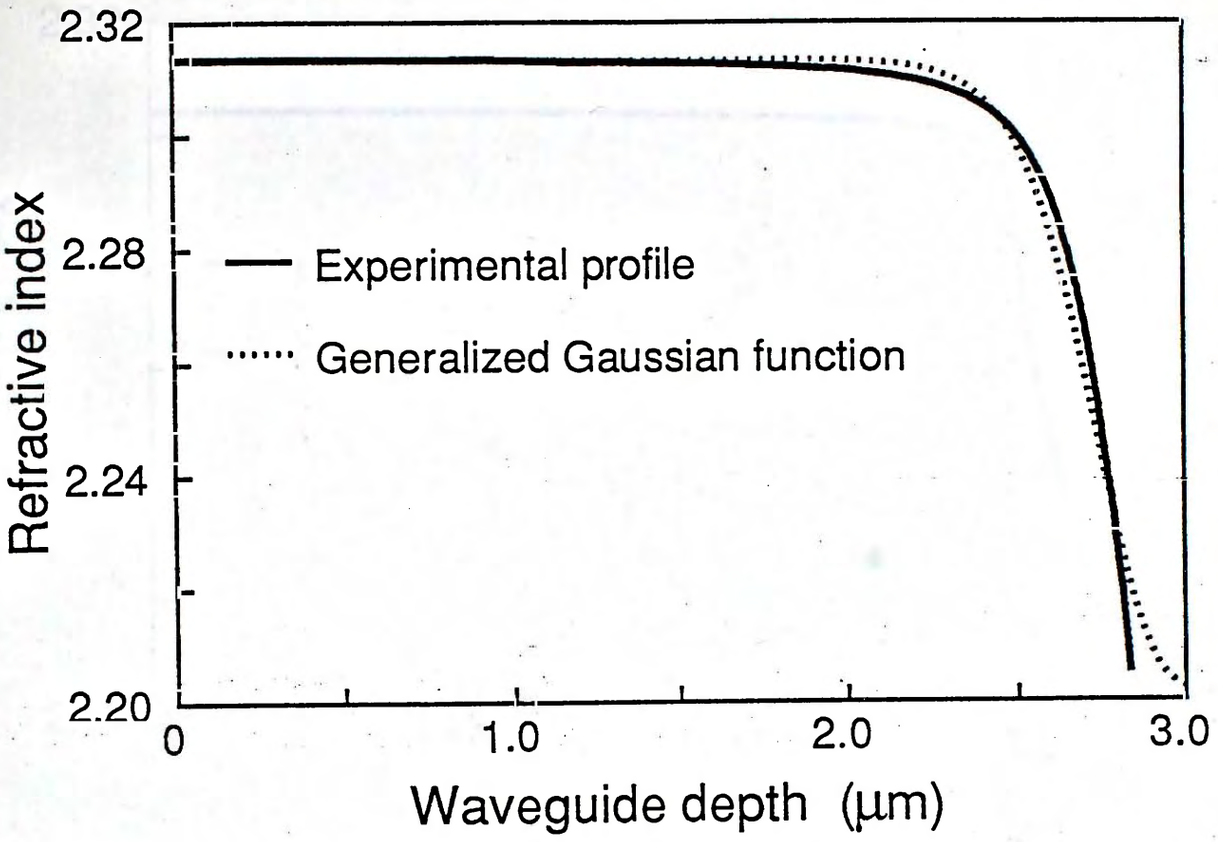

Fig.5.1.15 Annealed index profile of sample 4 at t_a = 0.5h (Δn_s = 0.1114, d_a = 2.757μm, c = 20).

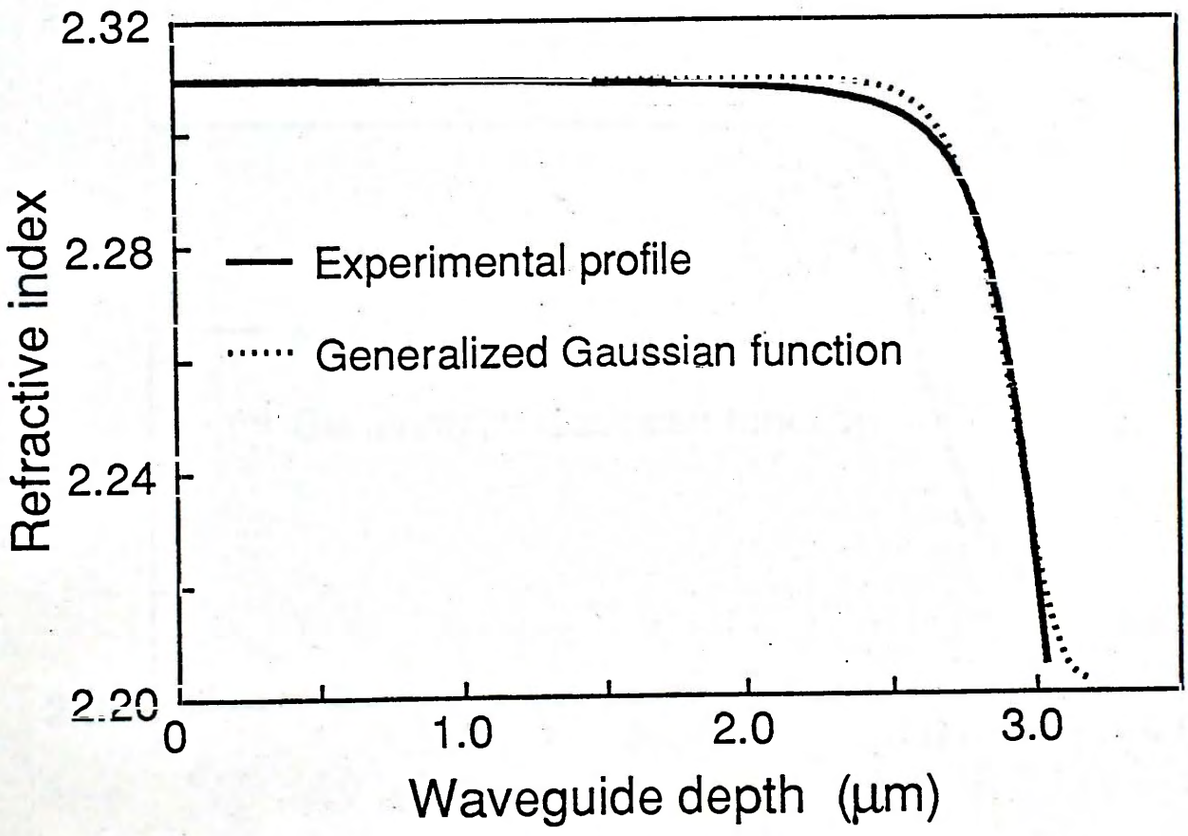

Fig.5.1.16 Annealed index profile of sample 4 at t_a = 1h (Δn_s = 0.1074, d_a = 2.949μm, c = 24).

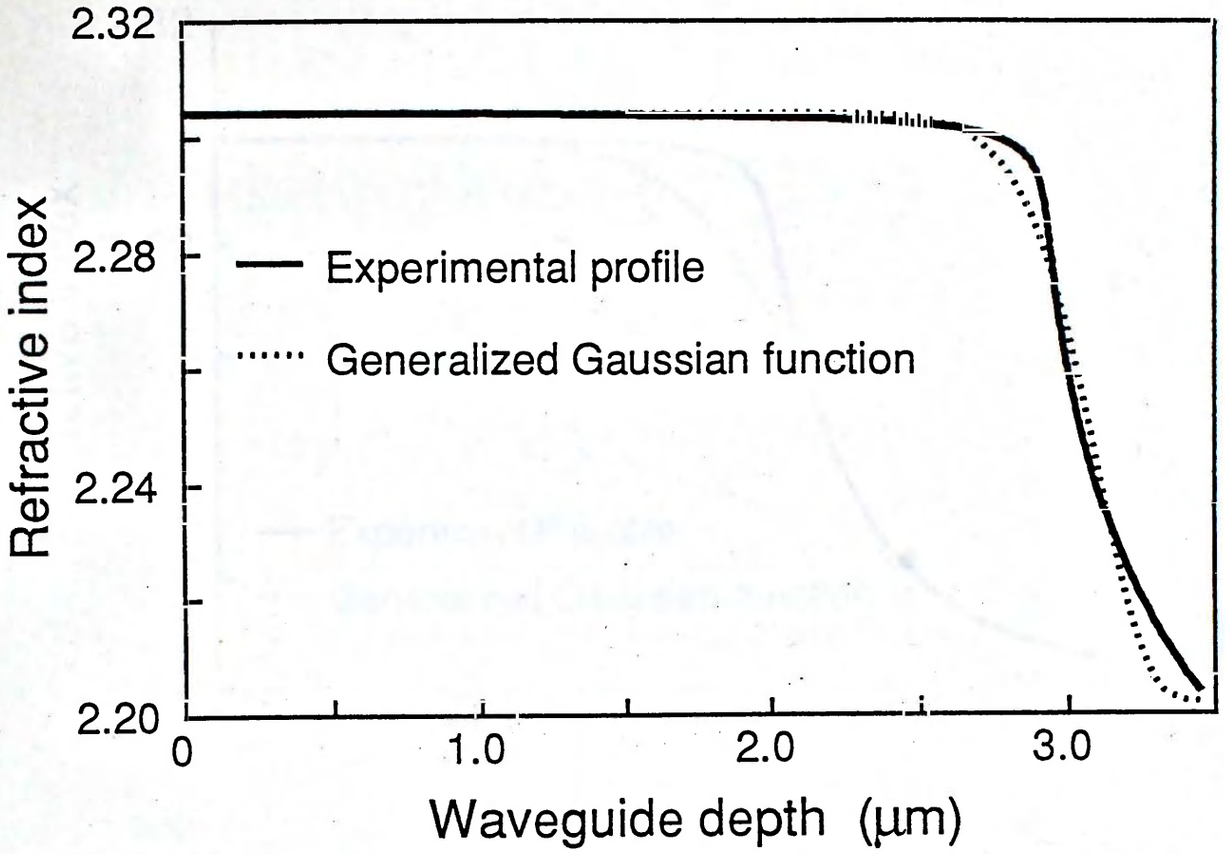

Fig.5.1.17 Annealed index profile of sample 4 at t_a = 2h (Δn_s = 0.1022, d_a = 3.115μm, c = 21).

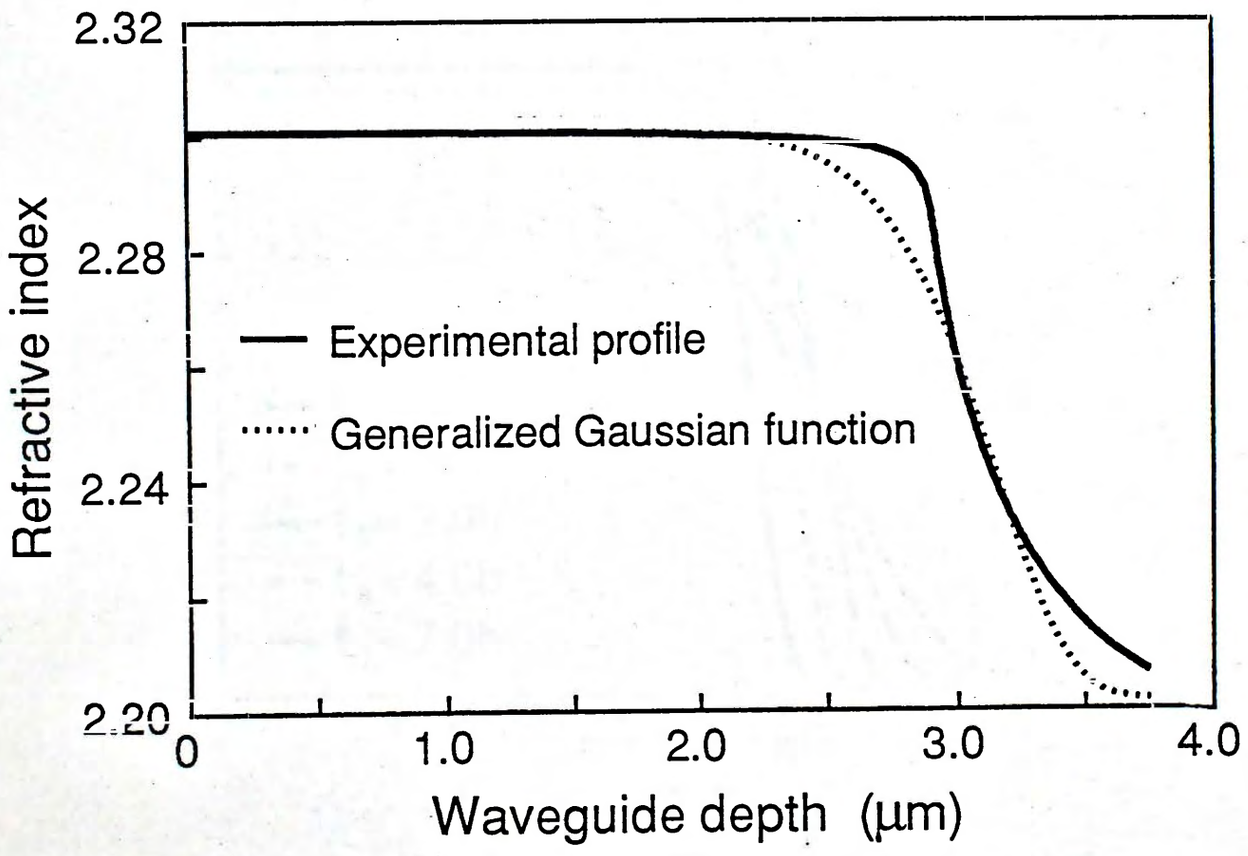

Fig.5.1.18 Annealed index profile of sample 4 at t_a = 4h (Δn_s = 0.0989, d_a = 3.17μm, c = 12).

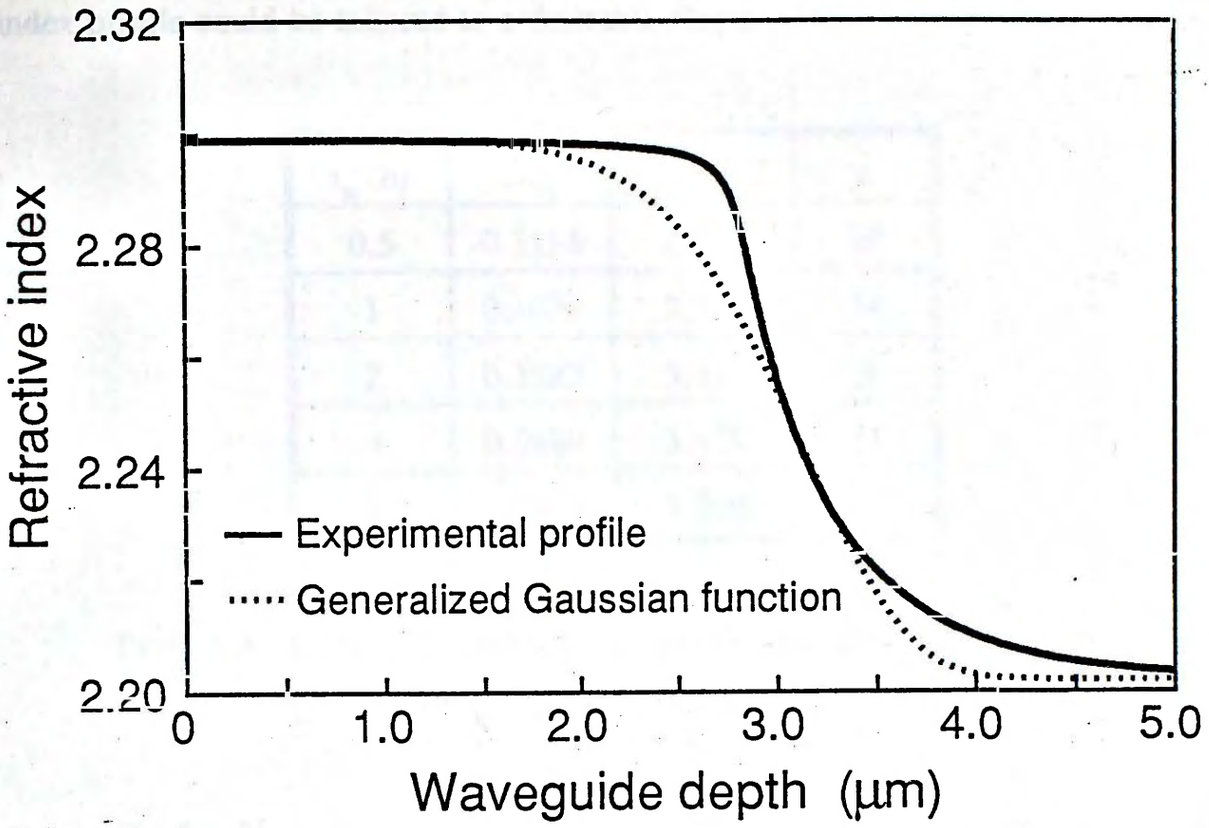

Fig.5.1.19 Annealed index profile of sample 4 at t_a = 7h (Δn_s = 0.0968, d_a = 3.208μm, c = 7).

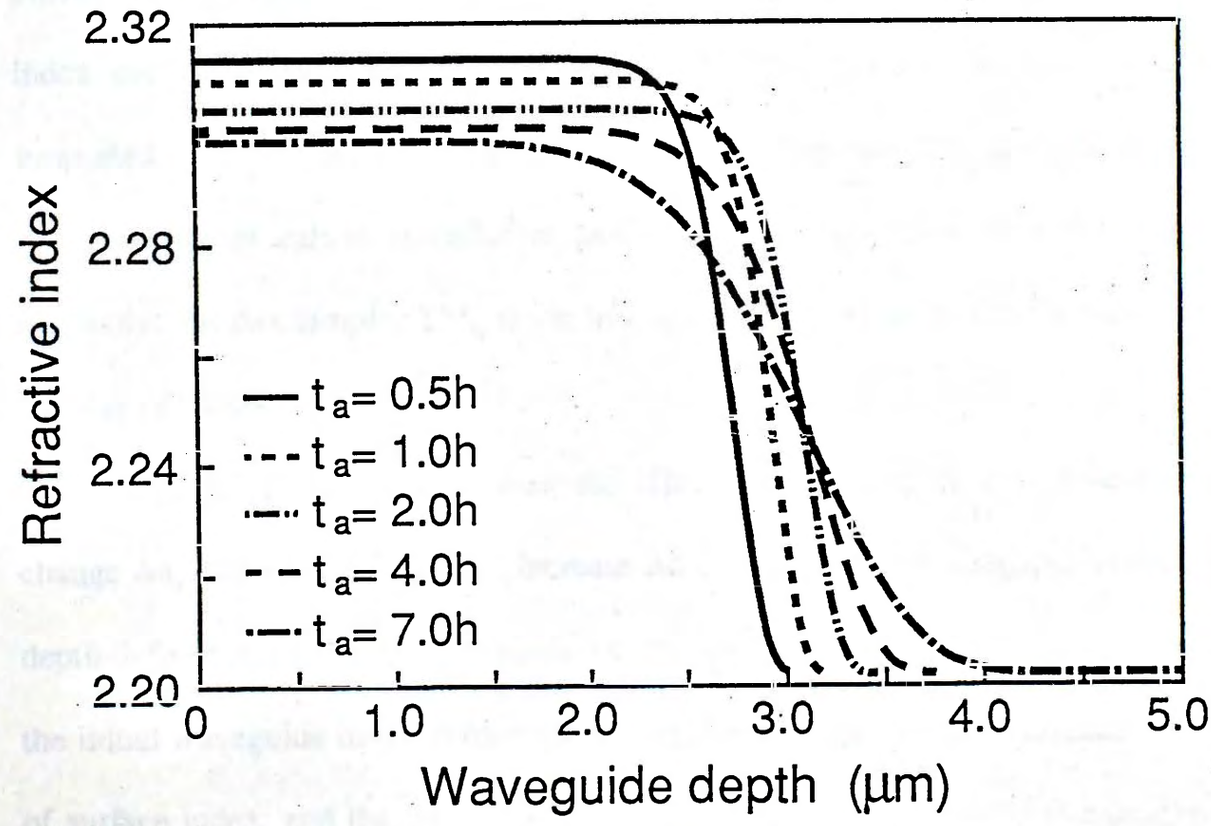

Fig.5.1.20 Theoretical annealed index profiles of sample 4 at various annealing time t_a

index profile could be tailored to a desirable shape.

t_a (h)	Δn_s	d_a (μm)	c
0.5	0.1114	2.757	20
1	0.1074	2.949	24
2	0.1022	3.115	21
4	0.0989	3.170	12
7	0.0968	3.208	7

Table 5.3 Computed annealed waveguide parameters for a generalized Gaussian index profile.

Fig.5.1.21 shows the effect of annealing on the mode effective indices of a multimode PE waveguide (sample 4). The solid and dotted curves refer to the measured data and theoretical values calculated using the generalized Gaussian profile with parameters shown in Table 5.3. In general, the fundamental mode index decreases monotonically with annealing time, and the number of modes supported by the waveguide increases. The effective indices of higher order modes reach maximum values at different annealing times and then start to decrease gradually. In this sample, TM_6 mode has not yet reached its maximum value after 7 hours of annealing.

Figs.5.1.22 and 5.1.23 show the effect of annealing on the surface index change Δn_s and waveguide depth increase Δd ($=d-d_o$, d is the annealed waveguide depth defined at $1/e$ of the maximum Δn_s for a graded index waveguide, and d_o is the initial waveguide depth before annealing). Annealing causes a continuous drop of surface index, and the rate of decrease is not uniform but is more abrupt during

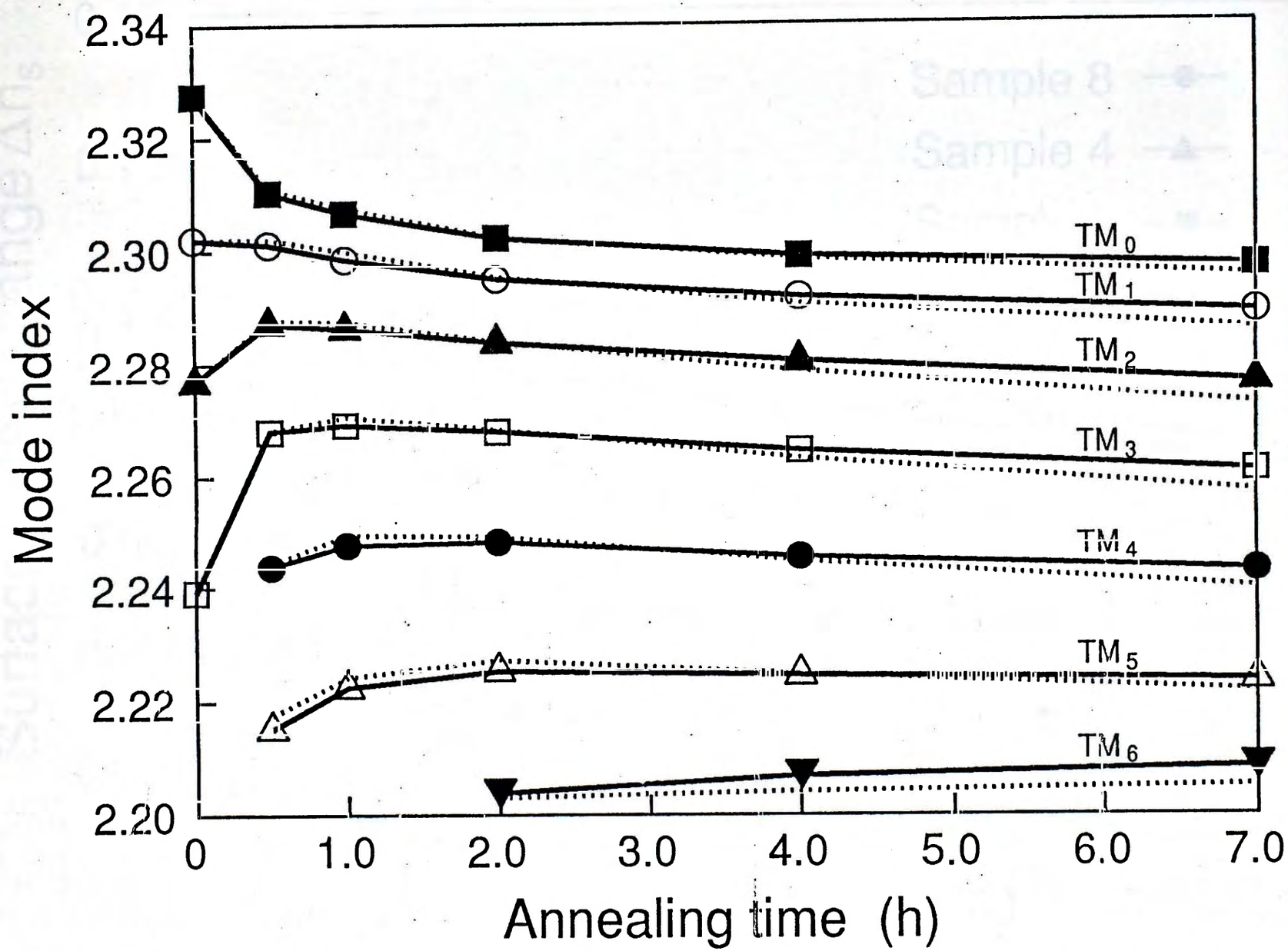

Fig.5.1.21 Changes in mode effective indices versus annealing time for sample 4. Solid and dotted curves refer to the experimental data and theoretical values calculated using the generalized Gaussian function.

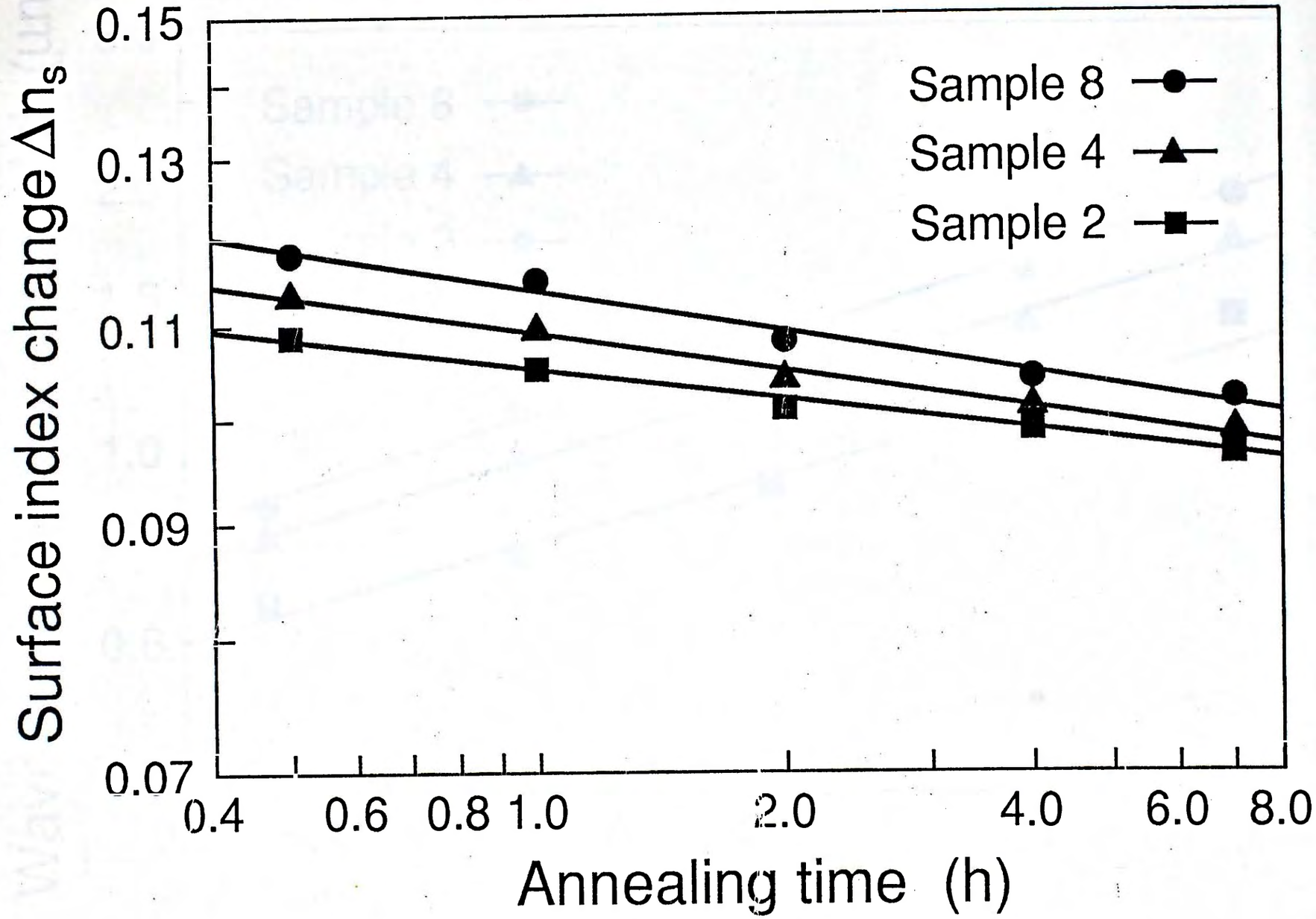

Fig.5.1.22 Surface index change Δn_s as a function of annealing time for sample 2, 4, 8.

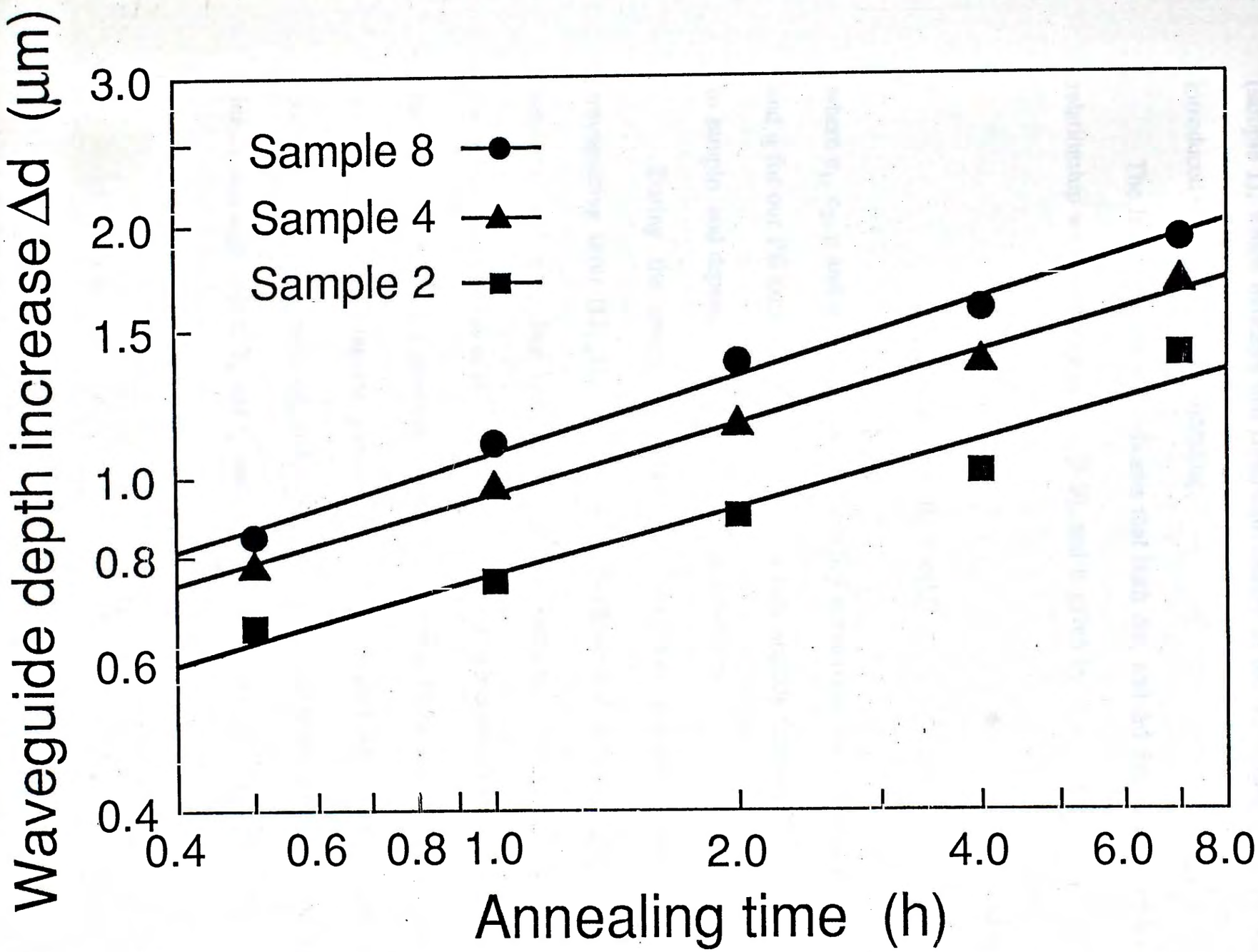

Fig.5.1.23 Waveguide depth increase Δd as a function of annealing time for sample 2, 4, 8.

the first hour of annealing. On contrary to the surface index, there is a continuous increase of the waveguide depth. The maximum depth increase measured was 119% (sample 1), which indicates that significant change in the waveguide depth can be introduced by post-exchange annealing.

The linear dependence indicates that both Δn_s and Δd follow a power-law relationship with annealing time t_a [5.9], and is given by

$$\Delta n_s = c_1 t_a^{\,p} \tag{5.8}$$

$$\Delta d = d - d_o = c_2 t_a^{\,q} \tag{5.9}$$

where c_1, c_2, p and q are constants. Table 5.4 summarizes the values of c_1, c_2, p and q for our PE samples. These parameters vary slightly from individual sample to sample, and depend on the initial exchange condition.

During the annealing process, H^+ that was present initially in the waveguiding layer ($Li_{1-x}H_xNbO_3$) would redistribute and diffuse deeper into the substrate, and its surface concentration would decrease. This drive-in diffusion depends on the amounts of H^+, T_a and t_a, and could be modelled by diffusion of the redistributed H^+ into a semi-infinite substrate from a finite source [5.17]. As a consequence, the waveguide parameters of the annealed PE samples, such as reduction in surface index Δn_s and increase in waveguide depth Δd, depend on the initial exchange time t, T_a and t_a used in our experiments.

Sample	c_1	p	c_2	q
1	0.114	-0.060	0.695	0.204
2	0.112	-0.058	0.756	0.262
3	0.111	-0.057	0.842	0.265
4	0.109	-0.055	0.939	0.269
5	0.109	-0.054	0.950	0.279
6	0.107	-0.048	0.973	0.282
7	0.105	-0.040	1.008	0.298
8	0.103	-0.032	1.056	0.314

Table 5.4 Values of annealed waveguide parameters c_1, c_2, p and q for PE waveguides using phosphoric acid.

PE planar waveguides have also been fabricated in z-cut MgO doped (4.5 mole%) $LiNbO_3$ using phosphoric acid as the proton source. Fig.5.1.24 shows the propagation loss measurement of a single-mode PE MgO:$LiNbO_3$ waveguide exchanged at 210°C for 1 hour ($N_{eff.}$ = 2.2873). The waveguide losses are typically about 1 $dBcm^{-1}$, and are similar to those obtained in undoped substrates.

Fig.5.1.25 shows the normalized refractive index profile reconstructed from the distribution of measured effective indices together with the index profile for undoped $LiNbO_3$. Both index profiles are graded functions, and the profile for MgO:$LiNbO_3$ exhibits more abrupt change near the waveguide-substrate boundary. This graded index profile can be approximated by the polynomial expression

$$g(x) = (1 - 1.88x^2 + 0.88x^4)^{1/8} \qquad (5.10)$$

where g(x) is again a closed-form solution of a nonlinear diffusion equation.

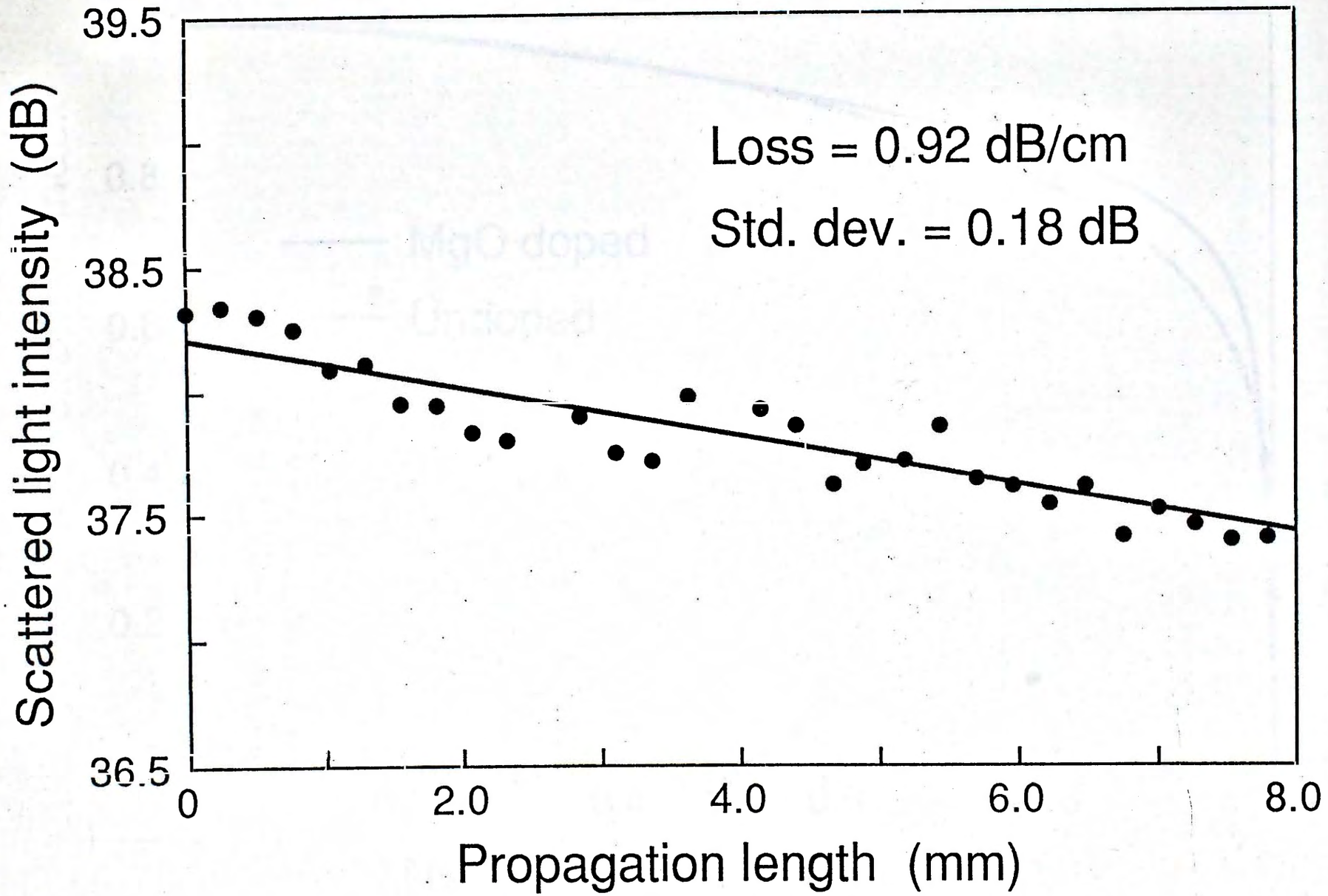

Fig.5.1.24 Propagation loss measurement of PE MgO:$LiNbO_3$ waveguide using phosphoric acid (T = 210°C, t = 1h).

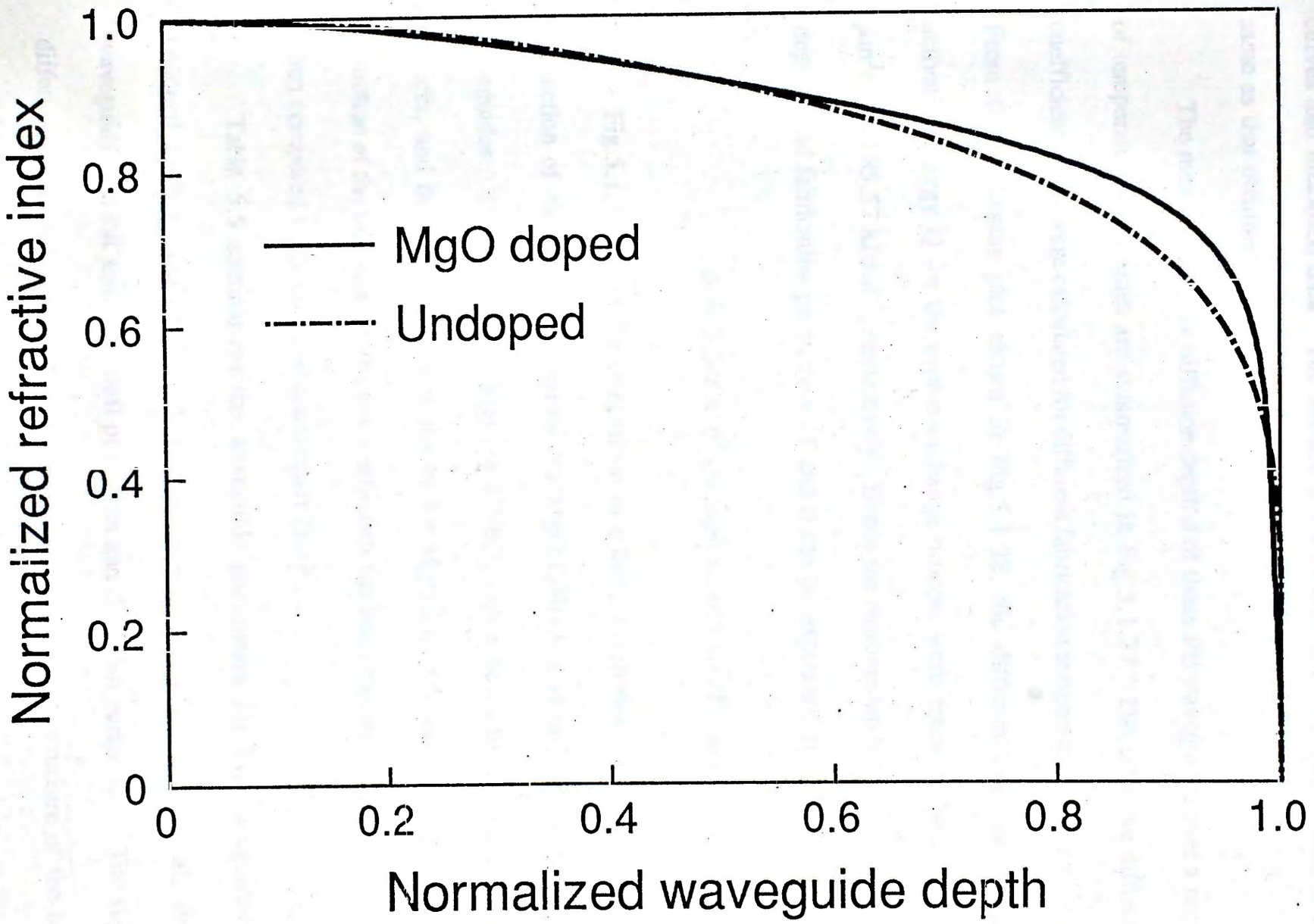

Fig.5.1.25 Comparison of index profiles for PE waveguides in undoped $LiNbO_3$ and MgO:$LiNbO_3$ using phosphoric acid.

Fig.5.1.26 shows the theoretical mode-dispersion curves based on Eq.5.10 together with the experimental data. There is excellent agreement between the theoretical curves and measured data. The surface index change Δn_s is 0.145, which is the same as that obtained in undoped $LiNbO_3$.

The measurements of diffusion depth *d* of these PE waveguides over a range of temperatures and times are summarized in Fig.5.1.27. The effective diffusion coefficients D(T) were calculated for different fabrication temperatures using Eq.5.4. From the Arrhenius plot shown in Fig.5.1.28, the diffusion constant D_o and activation energy Q for the proton-exchange process were found to be 1.06×10^9 μm^2h^{-1} and 85.57 $kJmol^{-1}$, respectively. Hence the relationship between waveguide depth *d* and fabrication parameters (T and t) can be expressed as

$$d = 3.248\times10^4 \sqrt{t}\, \exp(-5.146\times10^3/T) \quad \mu m \qquad (5.11)$$

Fig.5.1.29 shows the comparison of effective diffusion coefficient D(T) as a function of exchange temperature for MgO:$LiNbO_3$ and undoped $LiNbO_3$ PE waveguides. The presence of MgO in $LiNbO_3$ slows down the proton-exchange process, and the diffusion rate is slower for MgO:$LiNbO_3$ substrates. A similar reduction of the titanium indiffusion coefficients has been reported for MgO:$LiNbO_3$ when compared to its undoped counterpart [5.18].

Table 5.5 summarizes the waveguide parameters for PE waveguides in undoped $LiNbO_3$ and MgO:$LiNbO_3$ using phosphoric acid. In general, these waveguides exhibit similar optical properties and diffusion parameters. The slight differences are probably related to differences in crystalline structure of the bulk substrates.

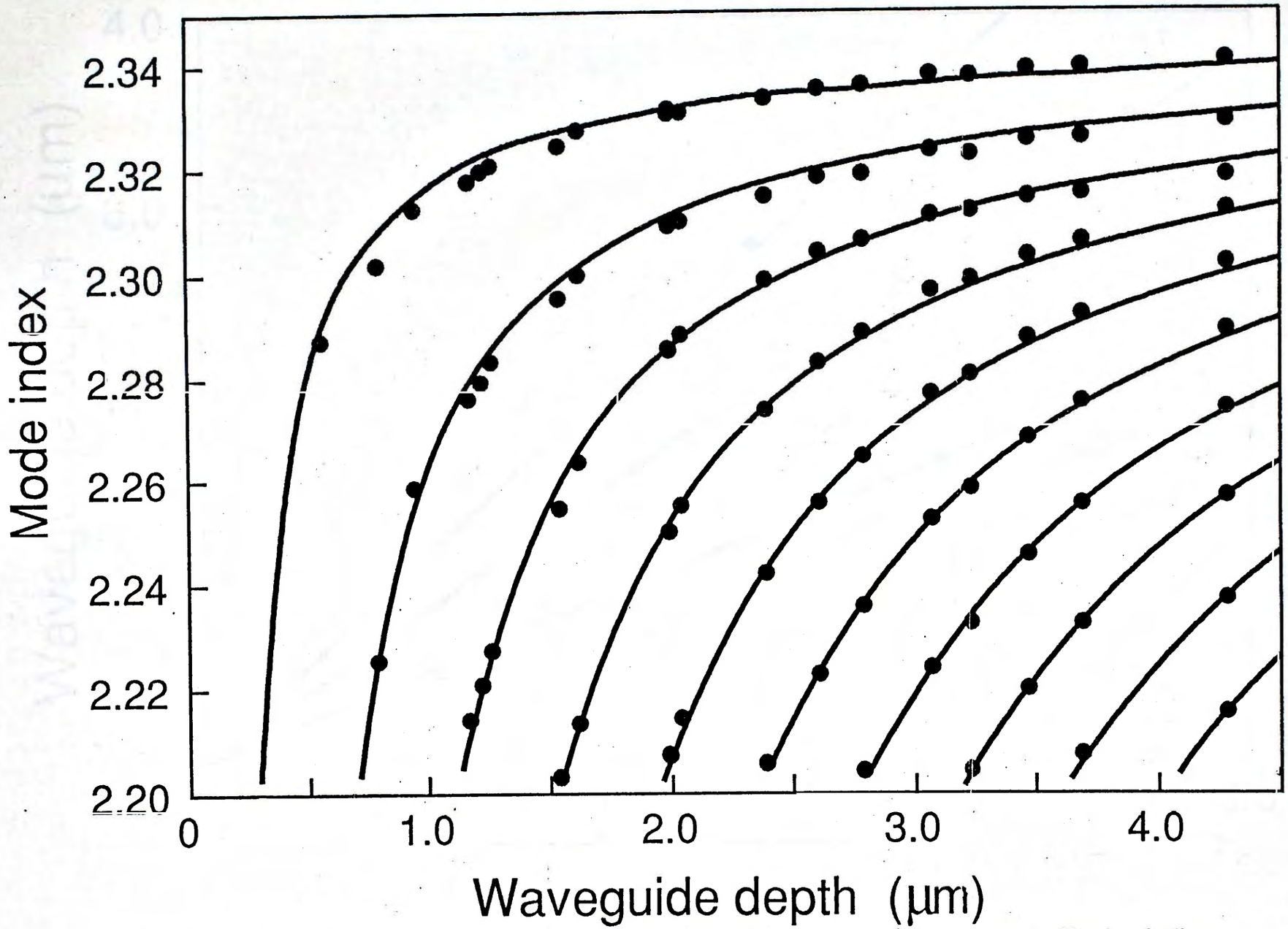

Fig.5.1.26 Theoretical mode-dispersion curves based on g(x) together with measured effective indices.

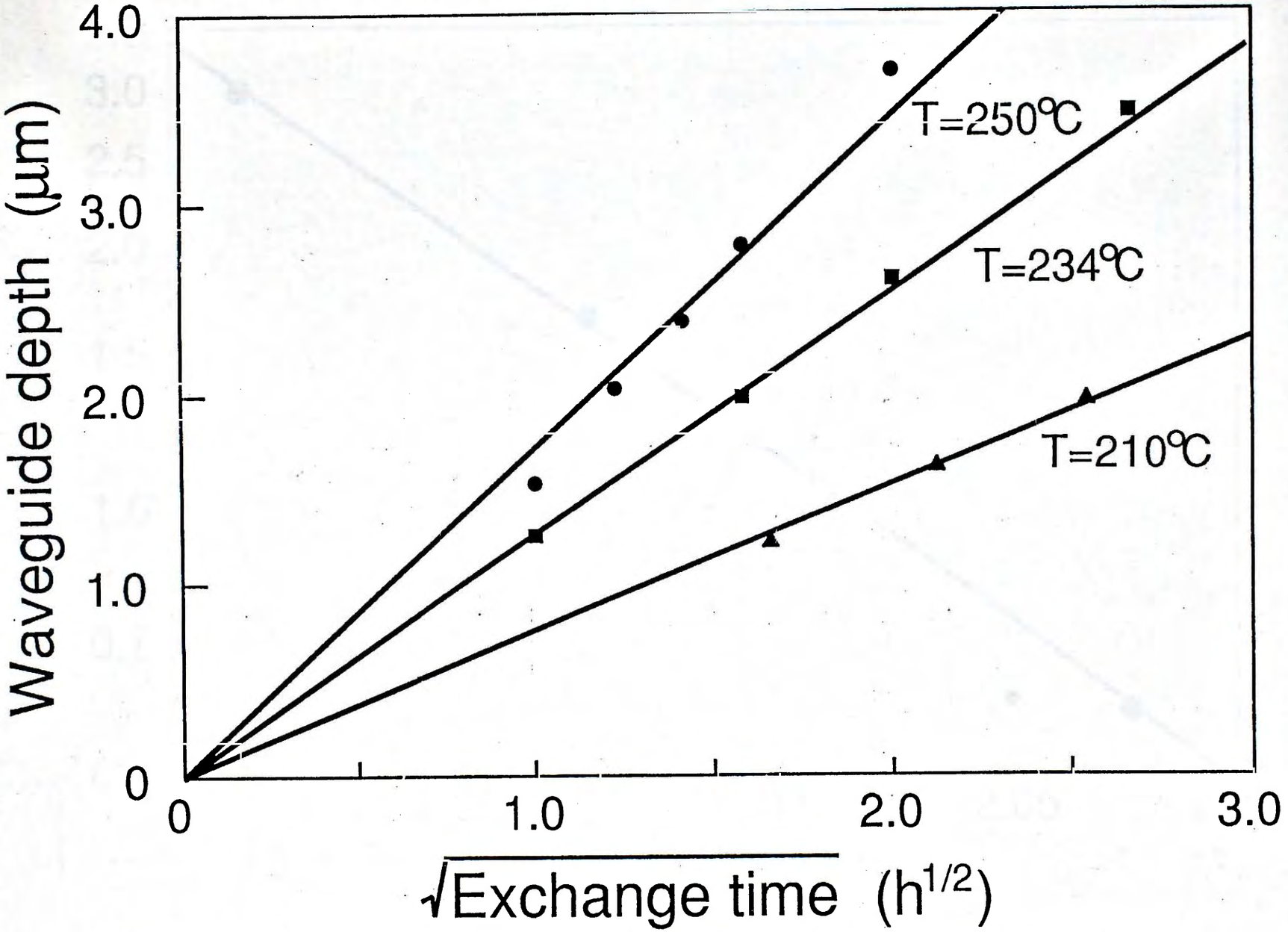

Fig.5.1.27 PE waveguide depth as a function of square root of diffusion time for MgO:$LiNbO_3$.

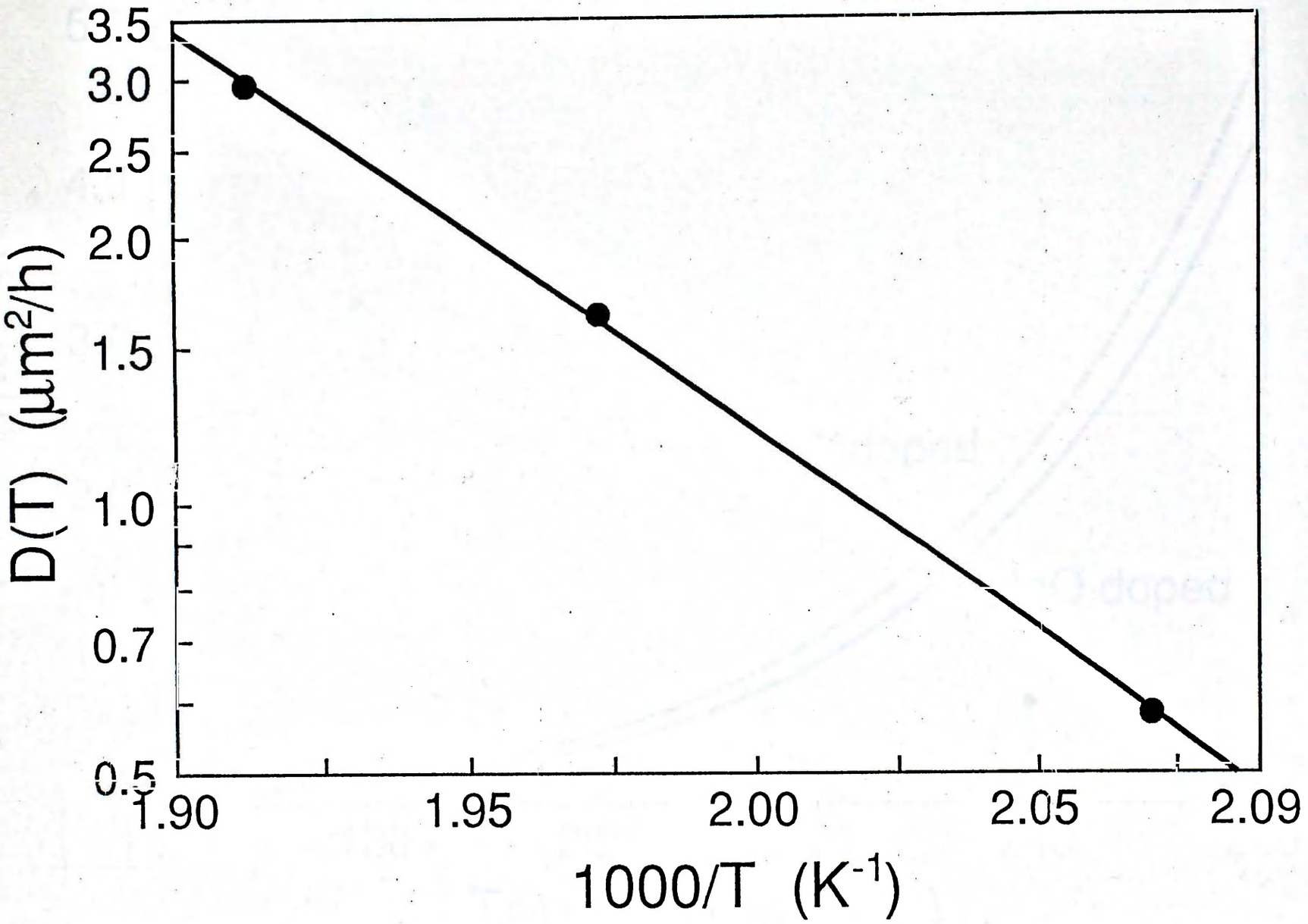

Fig.5.1.28 Plot of effective diffusion coefficient ln[D(T)] versus inverse of exchange temperature 1/T.

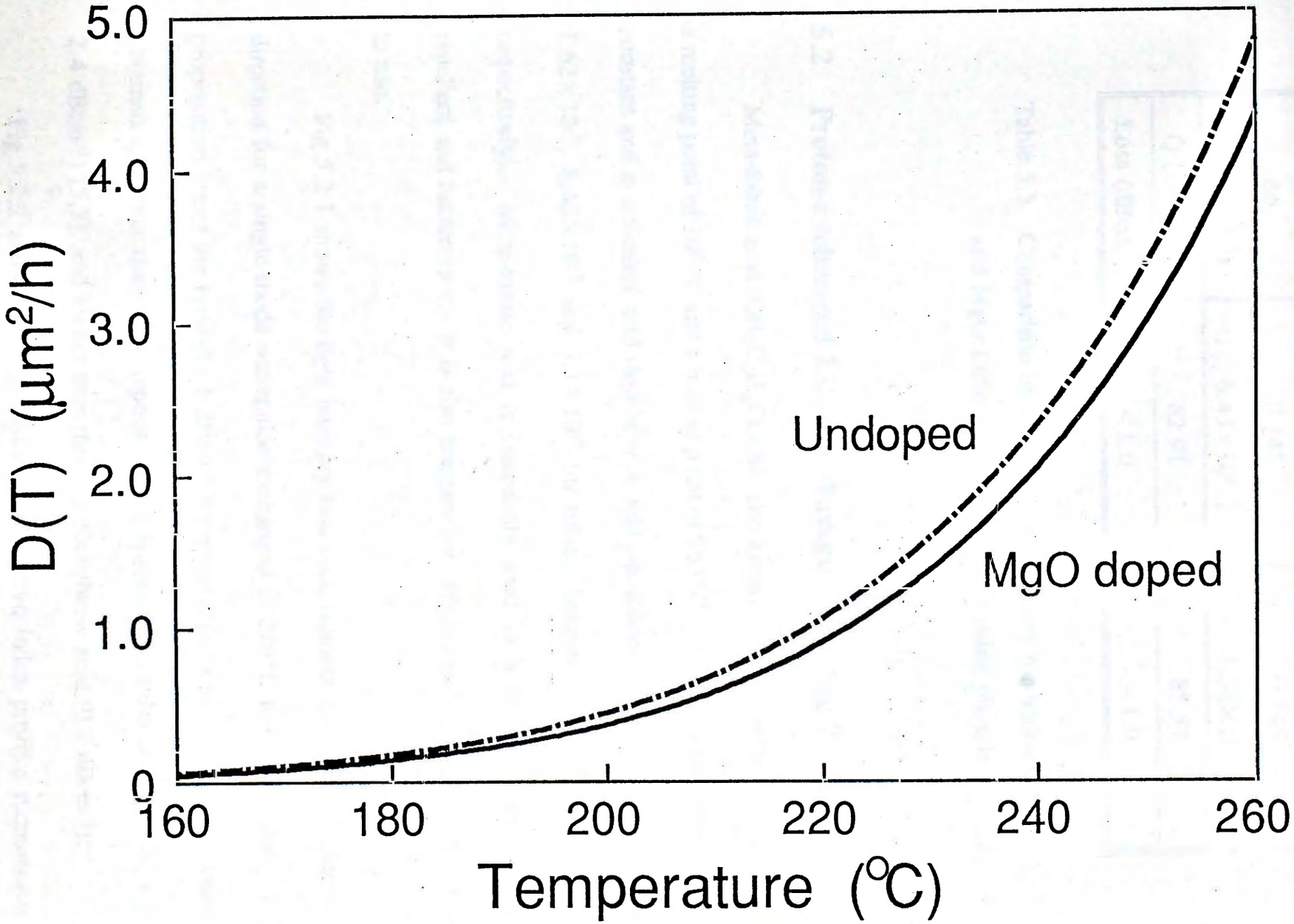

Fig.5.1.29 Comparison of effective diffusion coefficient D(T) for undoped $LiNbO_3$ and MgO:$LiNbO_3$ using phosphoric acid.

	Undoped	MgO doped
Index profile	Graded function: $(1-1.7x^2+0.7x^4)^{1/6}$	Graded function: $(1-1.88x^2+0.88x^4)^{1/8}$
Δn_s	0.145	0.145
D_o (μm^2h^{-1})	6.43×10^8	1.06×10^9
Q ($kJmol^{-1}$)	82.91	85.57
Loss ($dBcm^{-1}$)	<1.0	~1.0

Table 5.5 Comparison of waveguide parameters for undoped $LiNbO_3$ and MgO:$LiNbO_3$ PE waveguides using phosphoric acid.

5.2 Proton-exchanged $LiNbO_3$ Waveguides Using Toluic Acid

Meta-toluic acid ($CH_3C_6H_4COOH$, also known as 3-methylbenzoic acid) has a melting point of 109°C and a boiling point of 263°C. It has a smaller dissociation constant and is a weaker acid than benzoic and phosphoric acids (i.e. $K_\alpha(25°C) = 5.62\times10^{-5}$, 6.46×10^{-5} and 7.1×10^{-3} for toluic, benzoic, and phosphoric acid, respectively). Meta-toluic acid is commonly used as a broad-spectrum insect repellent and bacteriostat. It is also inexpensive, noncorrosive, nontoxic and safe to use.

Fig.5.2.1 shows the light intensity loss measurement along the propagation direction for a single-mode waveguide exchanged at 220°C for 15 minutes. The propagation losses are typically 1 $dBcm^{-1}$ for unannealed waveguides. The values obtained are lower than those reported using benzoic acid (also a carboxylic acid, 2.4 $dBcm^{-1}$) [5.3], and higher than those of phosphoric acid (0.7 $dBcm^{-1}$).

Fig.5.2.2 shows the representative refractive index profiles reconstructed

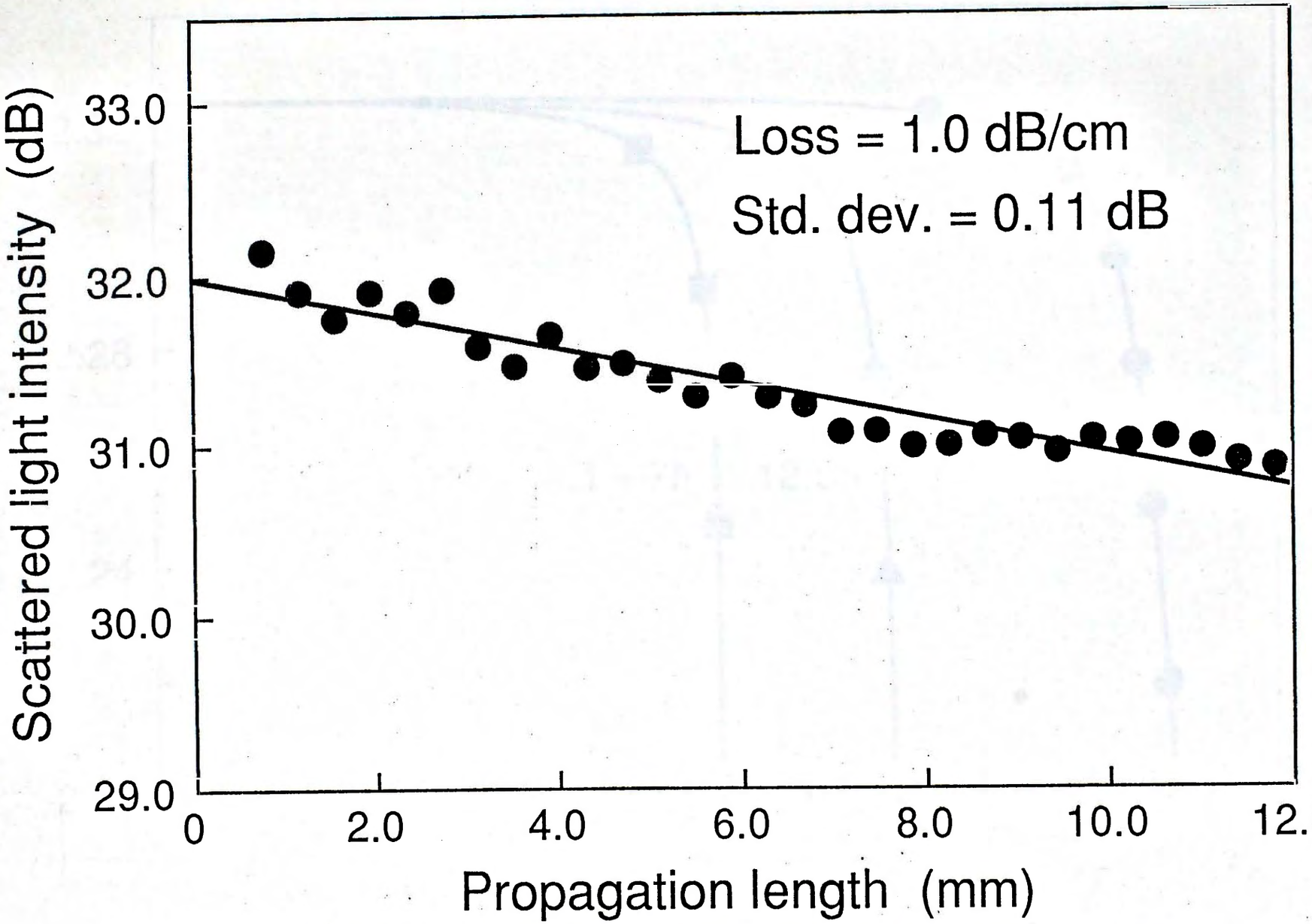

Fig.5.2.1 Propagation loss measurement of a single-mode PE planar waveguide using toluic acid (T = 220°C, t = 15min).

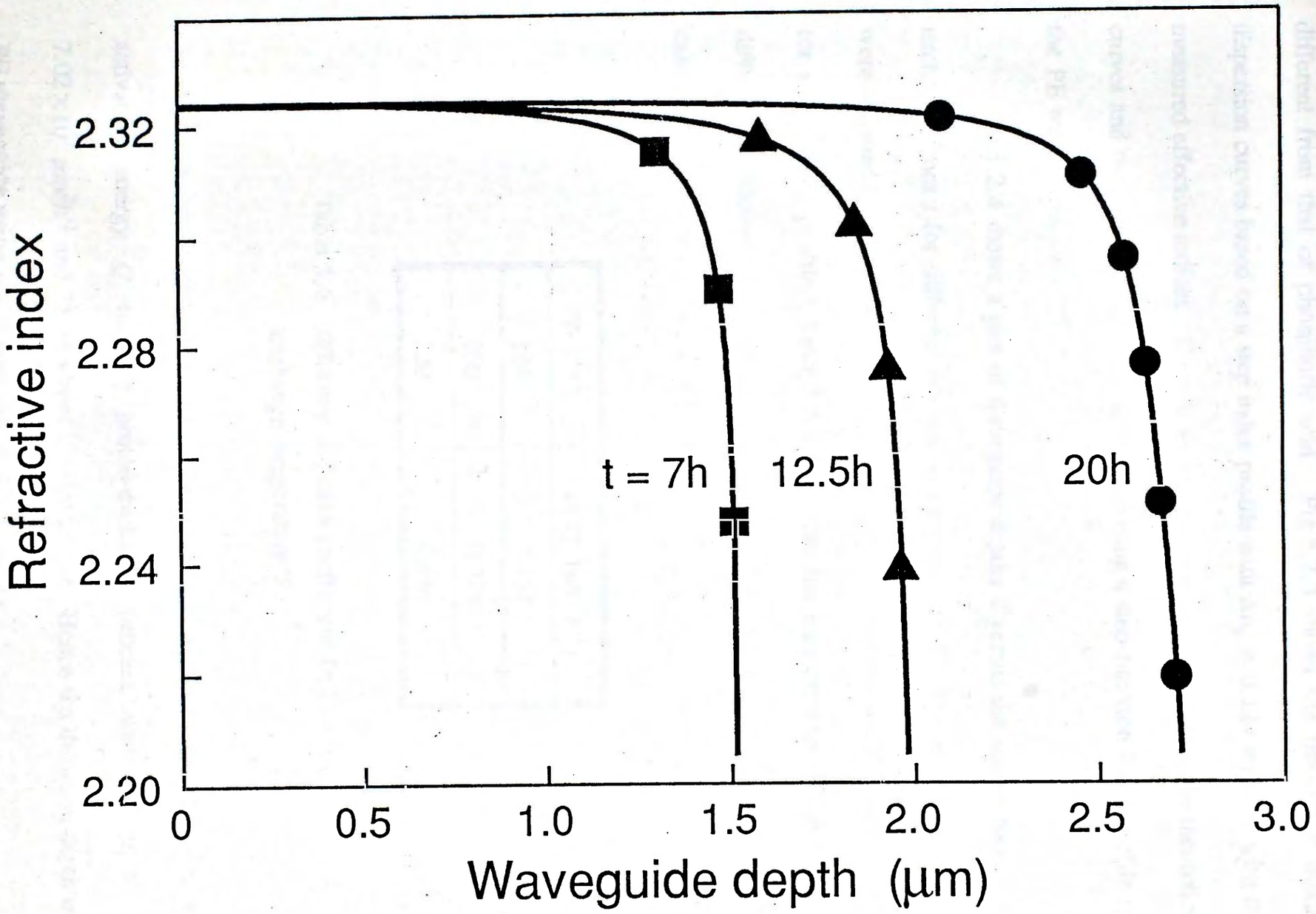

Fig.5.2.2 Refractive index profiles of PE waveguides using toluic acid (T = 200°C).

using the continuous effective-index function method [5.8]. The PE waveguides using toluic acid exhibit a step index profile similar to that of benzoic acid, but are different from that of phosphoric acid. Fig.5.2.3 shows the theoretical mode-dispersion curves based on a step index profile with $\Delta n_s = 0.124$ together with the measured effective indices. There is an excellent agreement between the theoretical curves and the experimental data, thus confirming a step-function index profile for the PE waveguide.

Fig.5.2.4 shows a plot of waveguide depths d versus the square root of the exchange times t for different fabrication temperatures T. The waveguide depths were obtained by solving the transcendental equation derived from the WKB integral for a step index profile. Table 5.6 summarizes the measurement of the effective diffusion coefficient $D(T)$ at three different exchange temperatures, and $D(T)$ was calculated using the relation $d = [t \times D(T)]^{1/2}$.

T (°C)	D(T) ($\mu m^2 h^{-1}$)
184	0.162
200	0.314
220	0.689

Table 5.6 Effective diffusion coefficient D(T) at various exchange temperature T.

From our experimental data, the values of diffusion constant D_o and activation energy Q for the proton-exchange process were found to be 7.02×10^7 $\mu m^2 h^{-1}$ and 75.58 $kJmol^{-1}$, respectively. Hence the diffusion depth of a PE waveguide using toluic acid can be expressed as

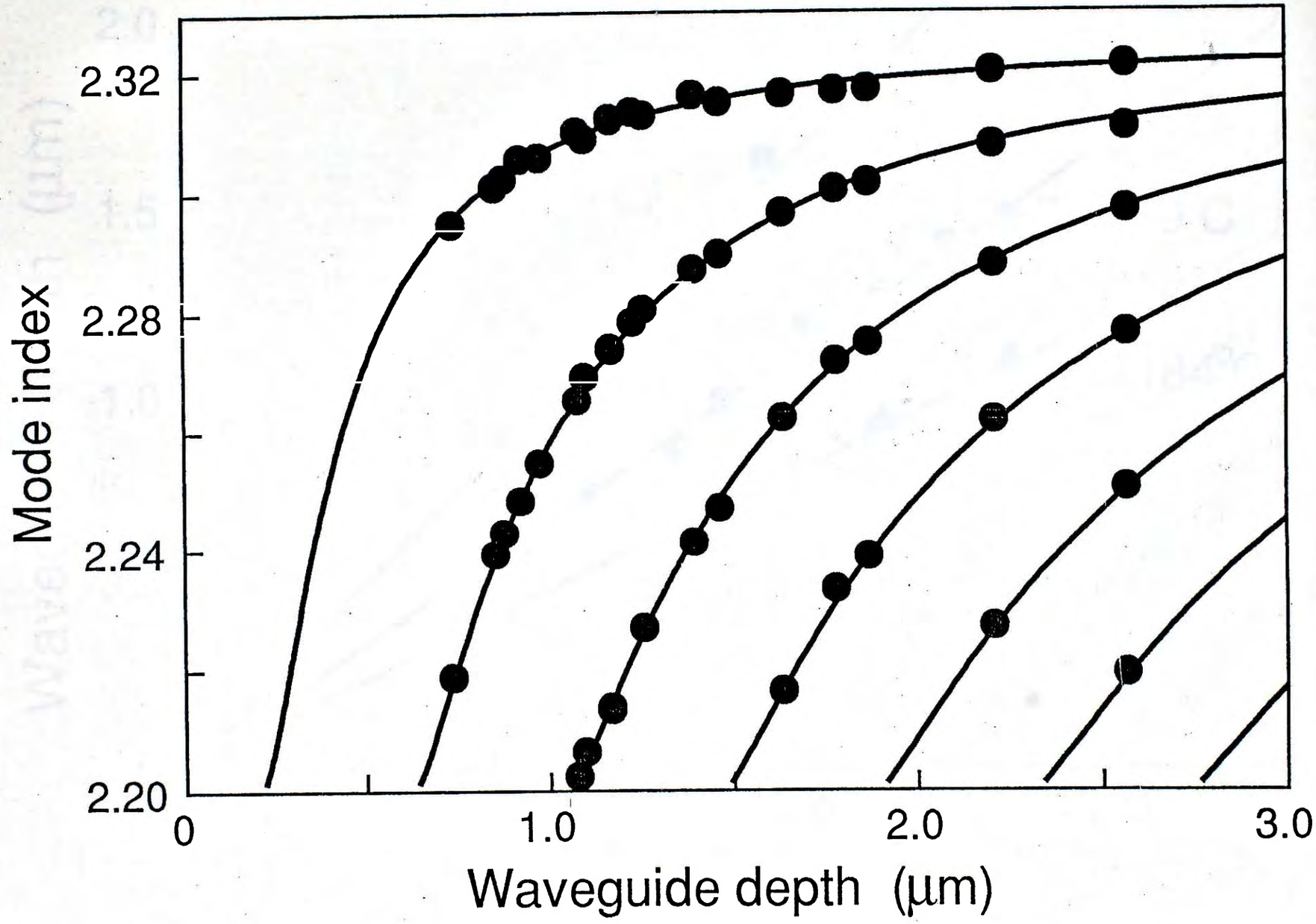

Fig.5.2.3 Theoretical mode-dispersion curves using a step index profile ($\Delta n_s = 0.124$) together with measured effective indices.

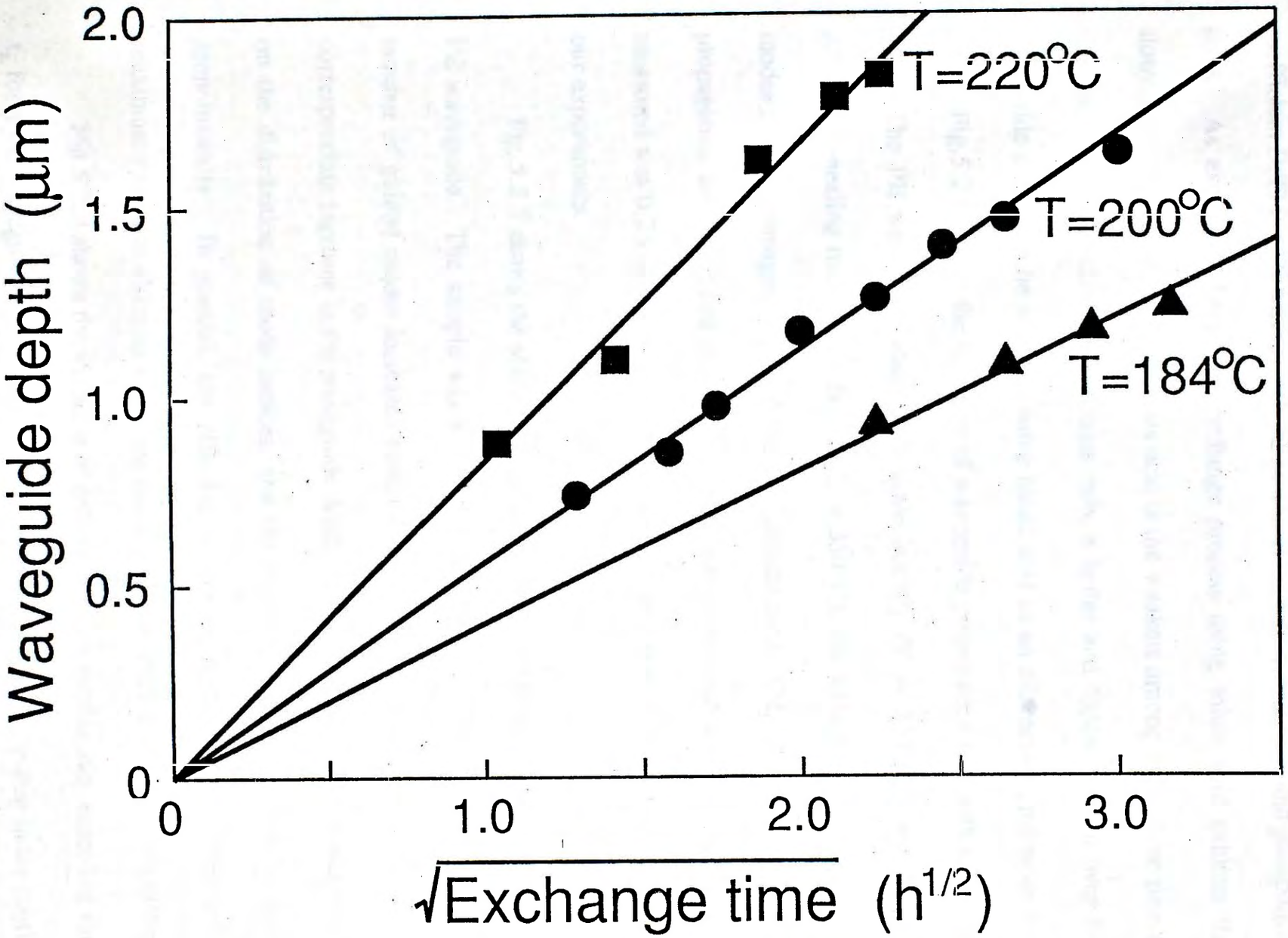

Fig.5.2.4 PE waveguide depth as a function of square root of exchange time.

$$d = 8.38\times10^3 \sqrt{t}\ \exp(-4.55\times10^3/T)\ \ \mu m \qquad (5.12)$$

Fig.5.2.5 shows the temperature dependence of the effective diffusion coefficient *D(T)* for PE waveguides fabricated using toluic, benzoic, and phosphoric acids. As expected, the proton-exchange process using toluic acid exhibits the slowest rate of diffusion because this acid is the weakest among these three proton sources. Owing to the slow diffusion rate, a better and tighter control over the waveguide depth can be achieved using toluic acid as an alternative proton source.

Fig.5.2.6 shows the variation of waveguide propagation loss with annealing time. The PE waveguide was single-mode initially (T = 220°C, t = 15 min). After an annealing time t_a of 2 hours (T_a = 350°C), the waveguide supported two modes and the propagation loss of the fundamental mode TM_0 was measured. The propagation loss decreases continuously with annealing time and the lowest value measured was 0.23 $dBcm^{-1}$, i.e. a maximum loss reduction of 77% was obtained in our experiments.

Fig.5.2.7 shows the effect of annealing on TM mode indices of a multimode PE waveguide. The sample was initially exchanged at 200°C for 3 hours. The number of guided modes increases continuously with annealing time, indicating a corresponding increase in the waveguide depth. There is a substantial modification on the distribution of mode indices, and the fundamental mode index decreases monotonically. In general, the effective indices of higher order modes reach maximum values at different annealing times and then start to decrease gradually.

Fig.5.2.8 shows the variation of refractive index profile with annealing time t_a for a PE waveguide exchanged at 200°C for 12.5 hours. The step index profile preserves its shape after 15 minutes of annealing. With further annealing, an index

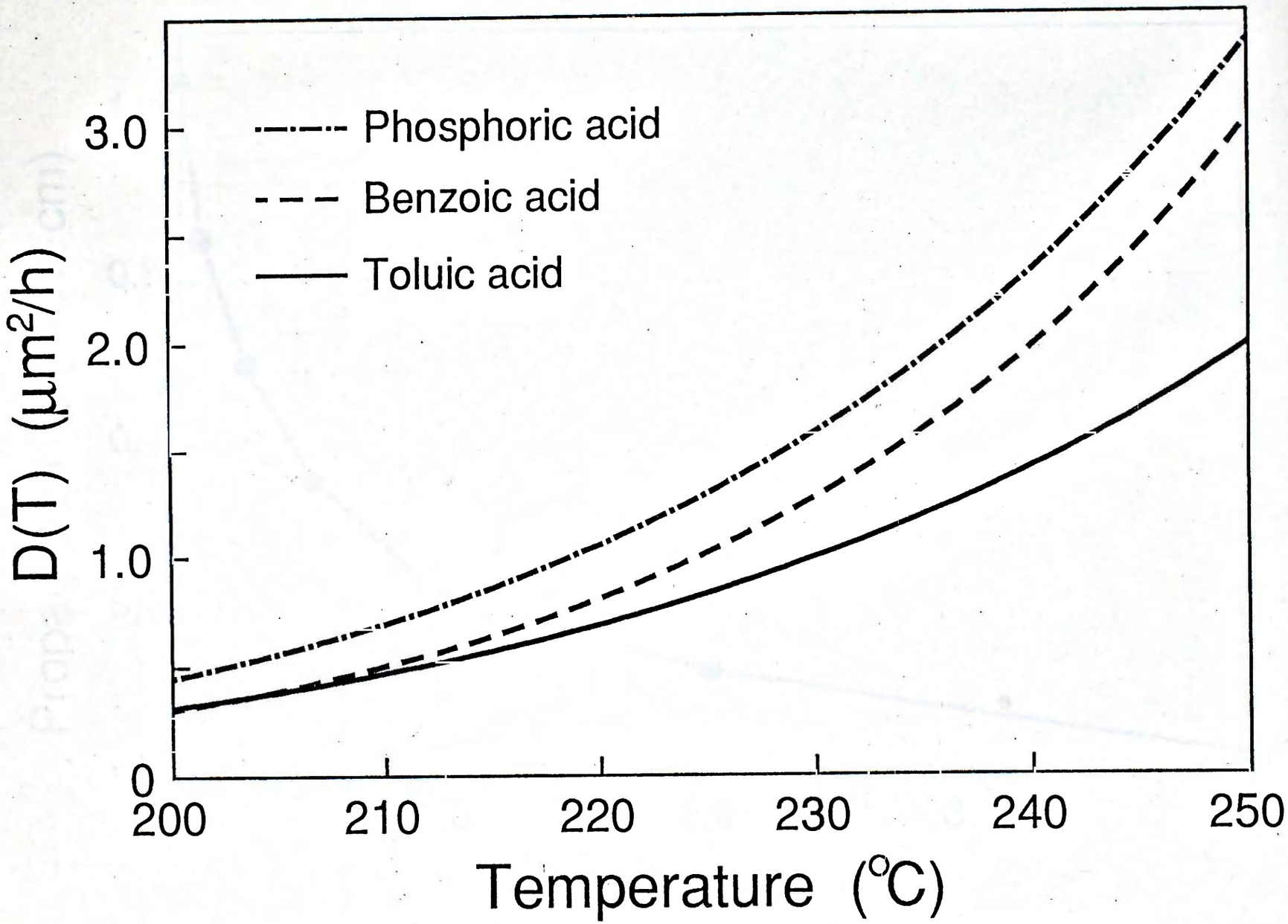

Fig.5.2.5 Comparison of effective diffusion coefficient D(T) as a function of temperature.

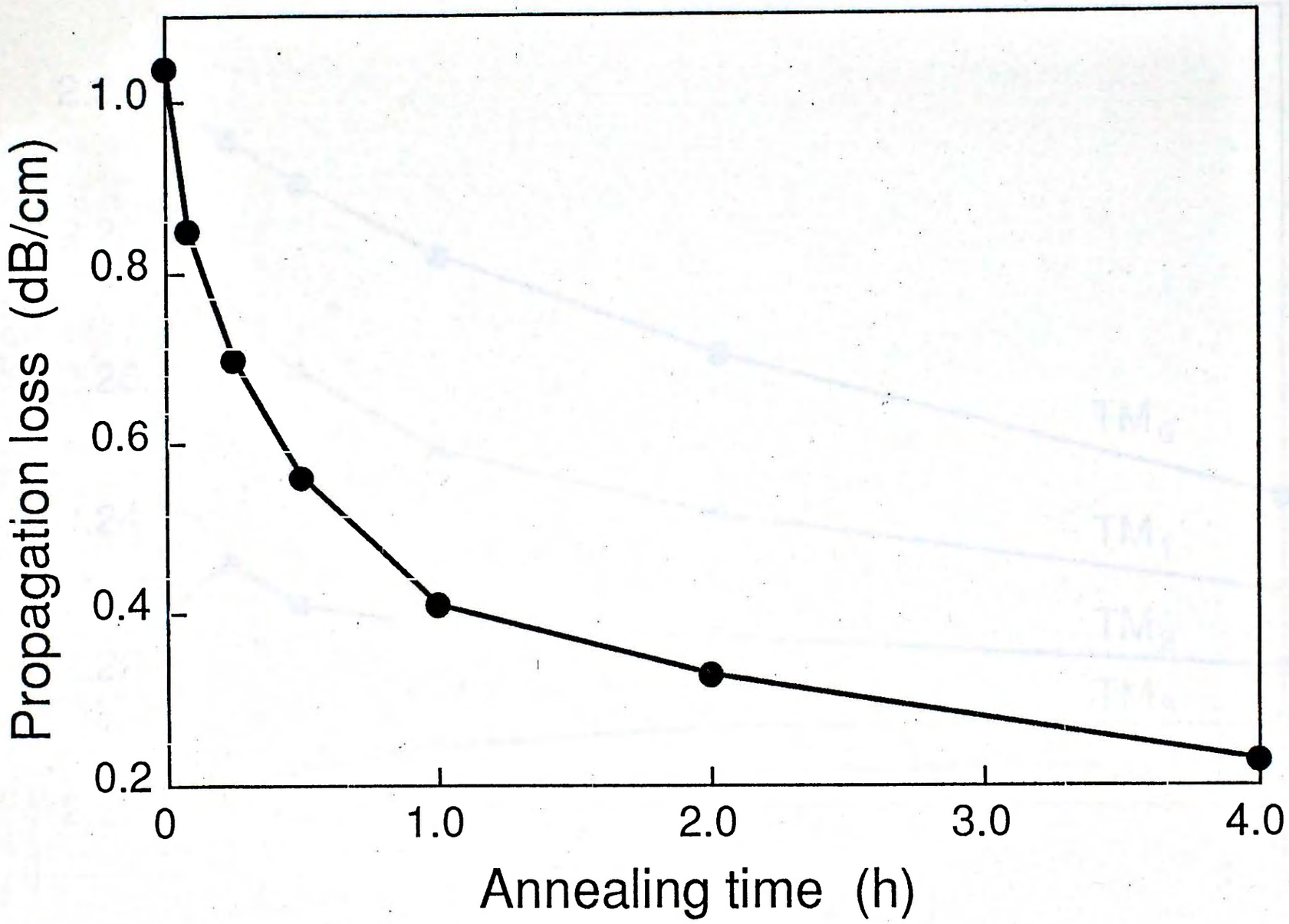

Fig.5.2.6 Propagation loss of PE waveguide as a function of annealing time (T = 220°C, t = 15 min, T_a = 350°C).

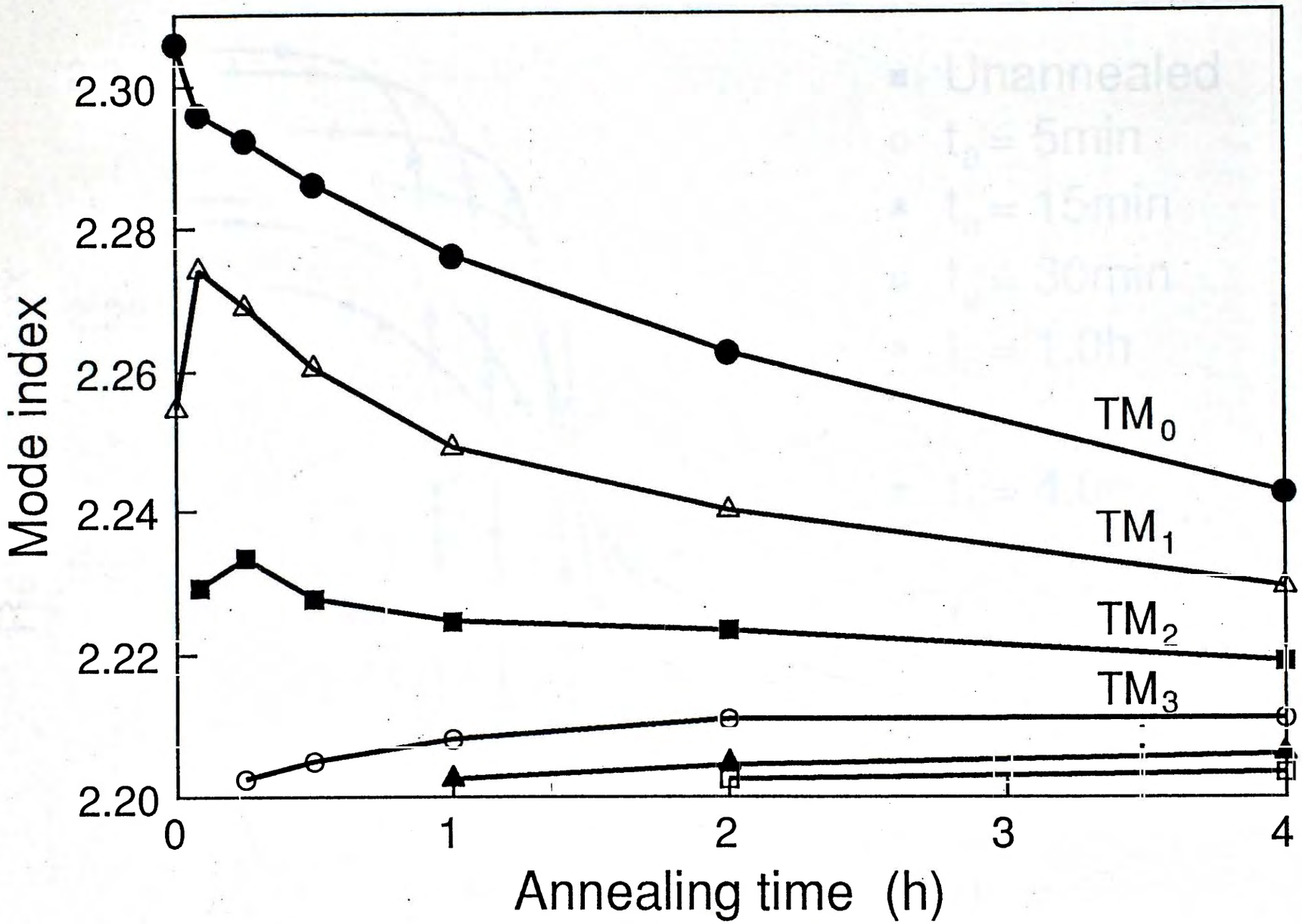

Fig.5.2.7 TM mode effective indices as a function of annealing time (T = 200°C, t = 3 h).

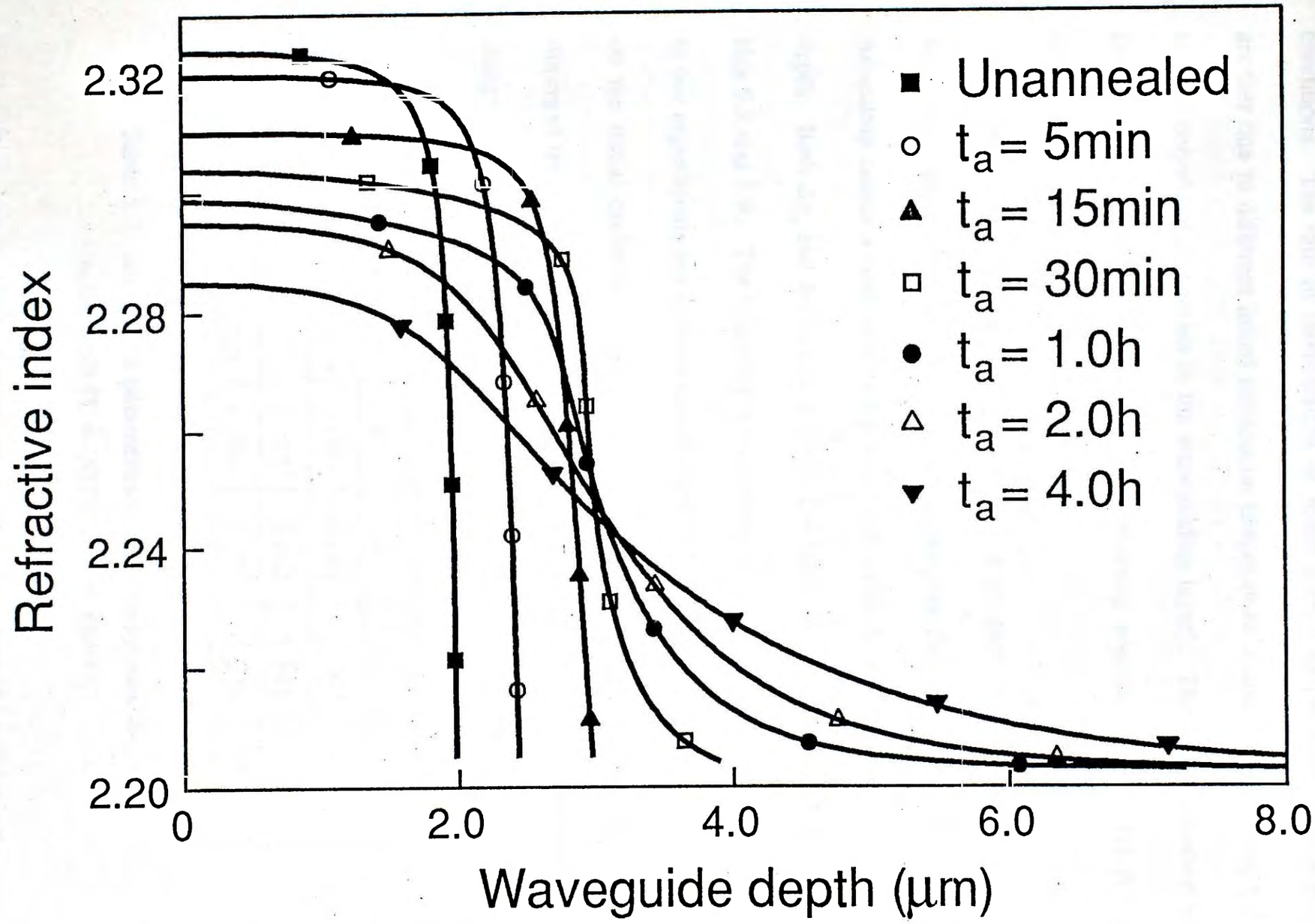

Fig.5.2.8 Changes in the refractive index profiles as a function of annealing time (T = 200°C, t = 12.5 h, T_a = 350°C).

tail forms at the waveguide-substrate boundary, and the profile becomes a graded index function. Similar results were obtained for samples prepared under different conditions. The rate of modification on index profile varied from one sample to another due to different initial fabrication temperature T and exchange time t (i.e. the H^+ concentration present in the waveguiding layer). This is in agreement with those obtained for PE waveguides fabricated using benzoic acid [5.19,5.20] and phosphoric acid [5.9].

Fig.5.2.9 shows the effects of annealing on surface index change Δn_s and waveguide depth increase Δd for three PE samples fabricated with T = 200°C. Annealing causes a continuous drop in surface index and an increase in waveguide depth. Both Δn_s and Δd follow a power-law relationship with annealing time (i.e. Eqs.5.8 and 5.9). The values of the annealing parameters c_1, c_2, p and q measured in our experiments are summarized in Table 5.7. As expected, these values depend on the initial exchange condition. From the annealing parameters obtained fine tuning of the waveguide depth and surface index is possible, adding flexibility in the design of PE $LiNbO_3$ devices.

Sample	t (h)	c_1	p	c_2	q
1	3	0.090	-0.085	1.797	0.515
2	7	0.095	-0.082	1.965	0.509
3	12.5	0.099	-0.077	2.224	0.505

Table 5.7 Annealing parameters of PE waveguides fabricated using toluic acid (T = 200°C, T_a = 350°C).

Proton-exchanged channel waveguides have also been fabricated in z-cut

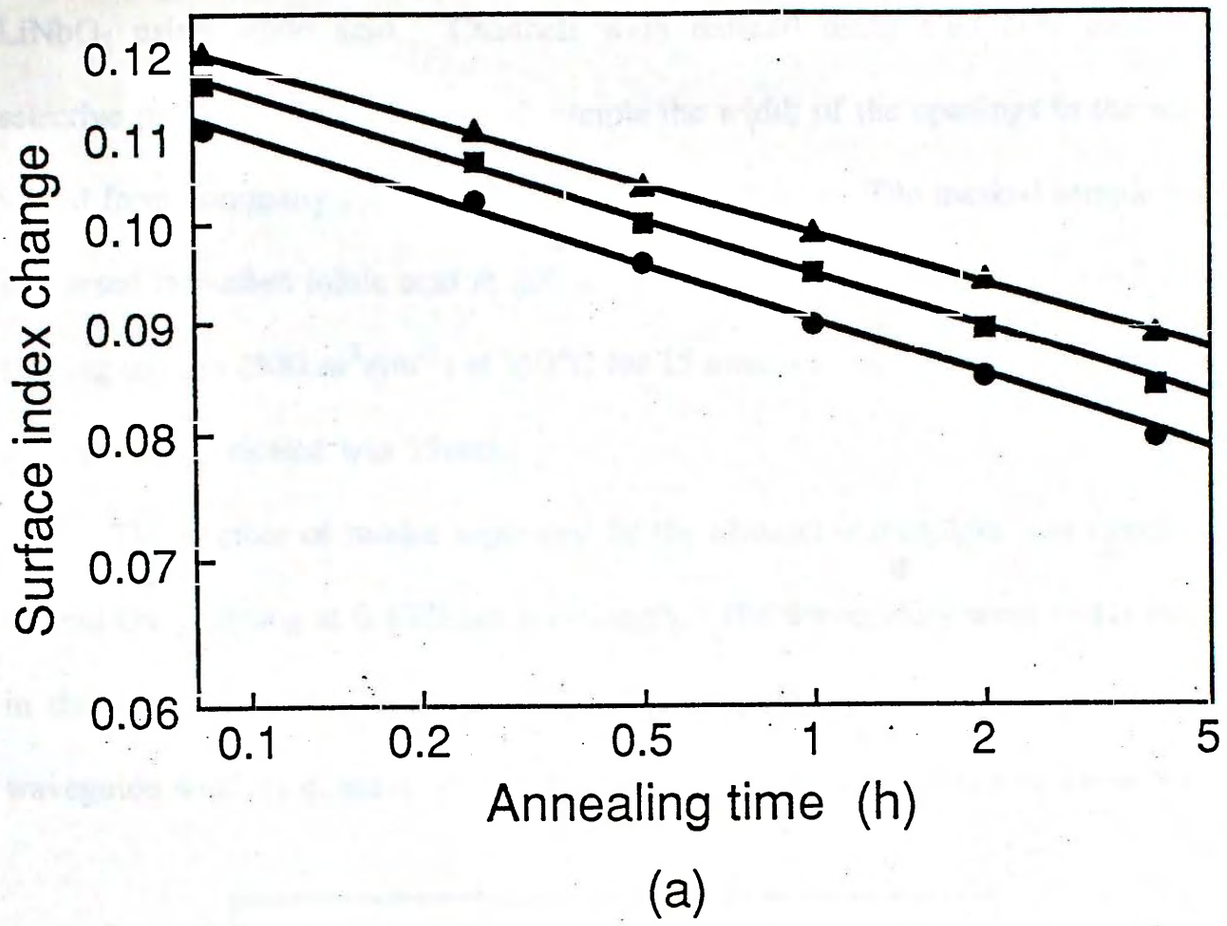

(a)

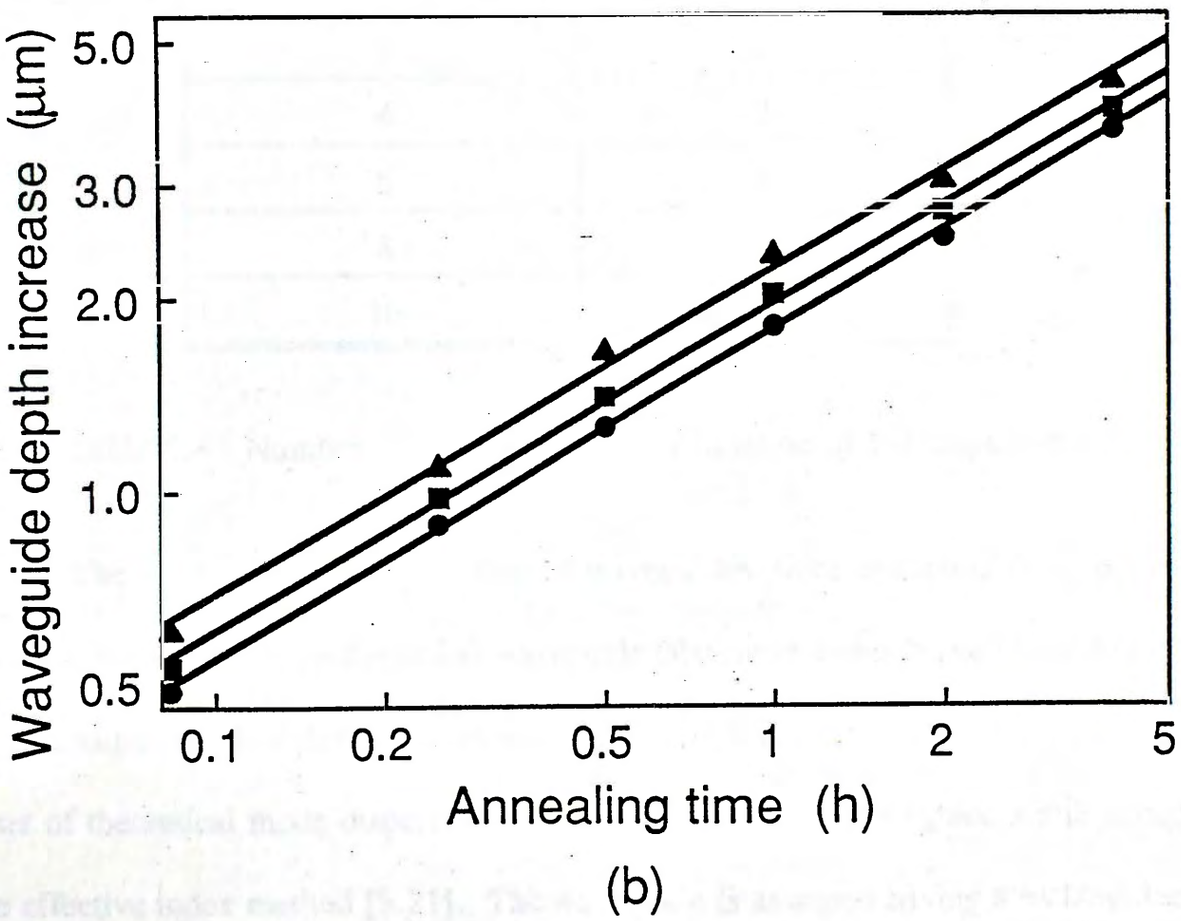

(b)

Fig.5.2.9 Variations in (a) surface index change and (b) waveguide depth increase as a function of annealing time (T = 200°C, ● t = 3 h, ■ t = 7 h, ▲ t = 12.5 h).

$LiNbO_3$ using toluic acid. Channels were defined using aluminum mask for selective proton exchange. On each sample the width of the openings in the mask varied from nominally 2μm to 10μm in 2μm increments. The masked sample was immersed in molten toluic acid at 200°C for 30 minutes, followed by annealing in flowing oxygen ($500cm^3min^{-1}$) at 350°C for 15 minutes. The length of the channel waveguides fabricated was 15mm.

The number of modes supported by the channel waveguides was measured by end-fire coupling at 0.6328μm wavelength. The waveguides were single mode in the depth direction. The number of lateral modes supported depends on the waveguide width (i.e. mask width), and the results are summarized in Table 5.8.

Waveguide width (μm)	No. of lateral modes
2	1
4	2
6	3
8	4
10	5

Table 5.8 Number of lateral modes as a function of PE stripe width.

The mode indices of the channel waveguides were evaluated from prism coupling measurement on the planar waveguide fabricated under the same condition. The measured mode index of this planar waveguide was 2.2187. Fig.5.2.10 shows a set of theoretical mode-dispersion curves as a function of waveguide width using the effective index method [5.21]. The waveguide is assumed having a rectangular cross-section with a core index of 2.2187 and a depth of 1μm. The number of

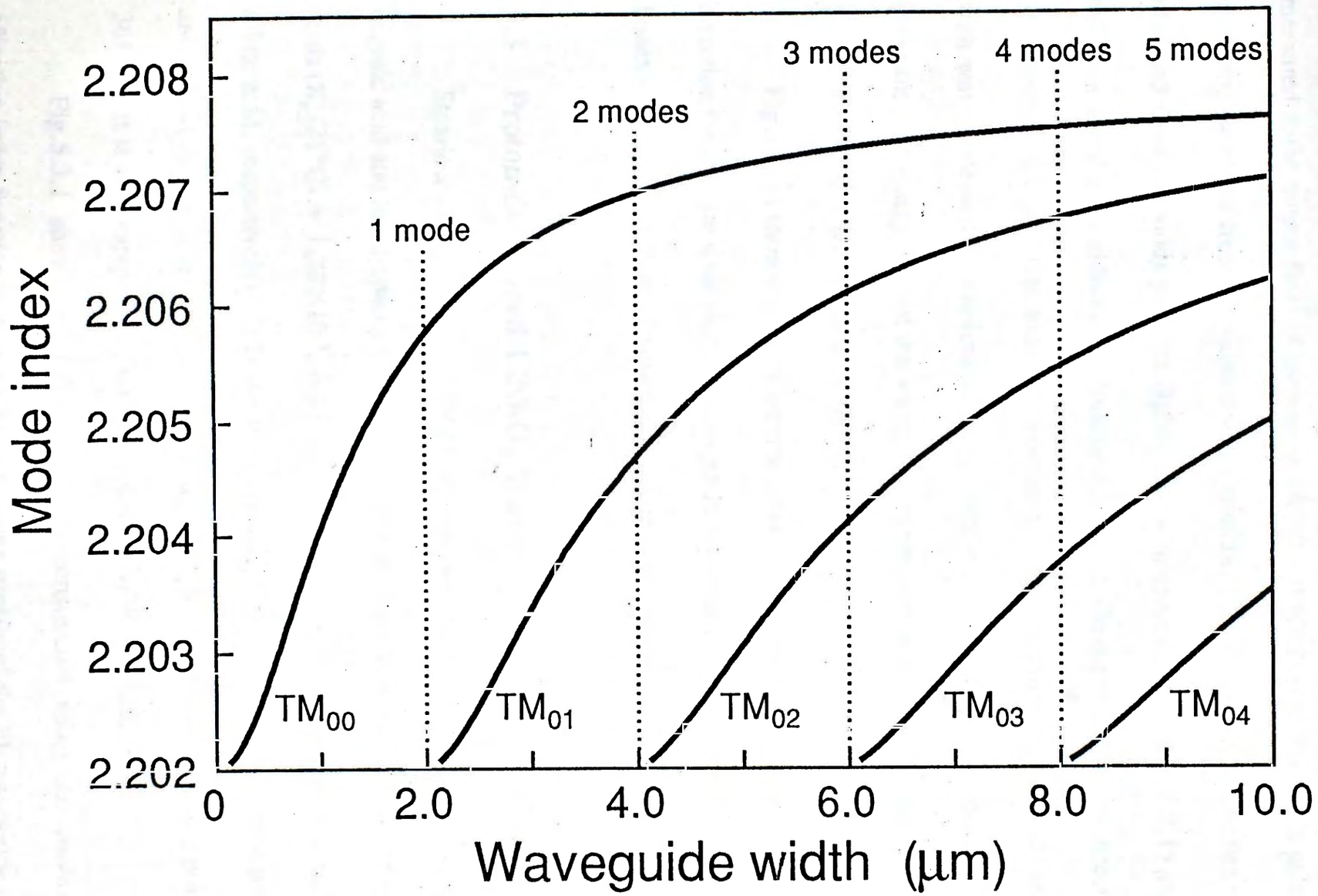

Fig.5.2.10 Mode effective index as a function of waveguide width for a step-index channel waveguide using effective index method (n_{core} = 2.2187, n_{sub} = 2.202, d = 1 μm, λ = 0.6328 μm).

modes calculated for channel waveguides with 2μm, 4μm, 6μm, 8μm and 10μm width agrees with our measured results.

Figs.5.2.11 to 5.2.14 show the mode patterns and near-field intensity profiles measured at the output facet of the waveguides (λ=0.6328μm). The mode patterns were photographed from the video camera monitor, and the near-field profiles were obtained from the mode patterns digitized by a microcomputer. Fig.5.2.15 shows the variation of 1/*e* widths of the mode profiles along the depth and lateral directions as a function of waveguide width. The lateral mode size w_l increases almost linearly with waveguide width, whereas the mode size w_d in the depth direction remains invariant. This suggests that the waveguide modes are well confined and the extent of side-diffusion is independent of the mask width.

Fig.5.2.16 shows the light intensity loss measurement along the propagation direction for a 10μm wide channel waveguide. As expected, the channel waveguide losses are similar to those obtained for their planar counterparts.

5.3 Proton-exchanged $LiNbO_3$ Waveguides Using Stearic Acid

Stearic acid ($CH_3(CH_2)_{16}COOH$, also known as octadecanoic acid) is a weak organic acid and has a dissociation constant smaller than those of benzoic and toluic acids ($K_\alpha(25°C) = 1.28\times10^{-5}$, 6.46×10^{-5} and 5.62×10^{-5}, for stearic, benzoic and toluic acid, respectively). It is the most common fatty acid that occurs in natural animal and vegetable fats, and has a melting point of 69.6°C and a boiling point of 361°C. It is also inexpensive, nontoxic, noncorrosive and safe to use.

Fig.5.3.1 shows the index profiles reconstructed using the continuous effective-index function method [5.8]. The index profile of the PE waveguide using

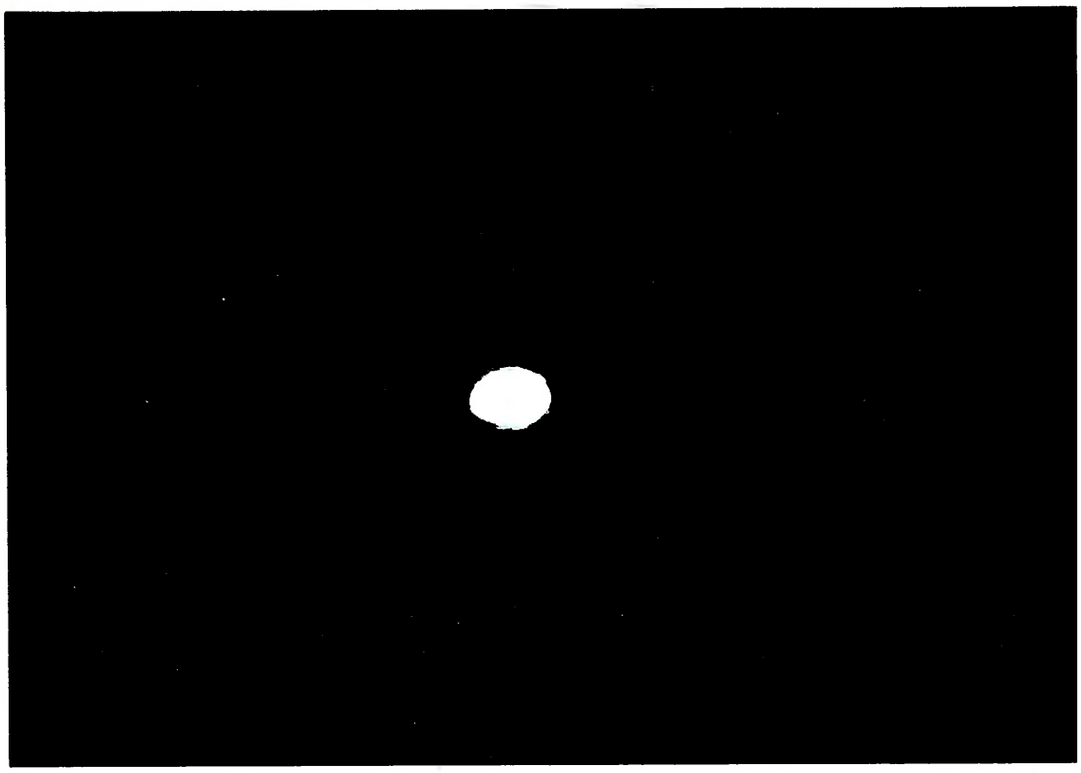

(a)

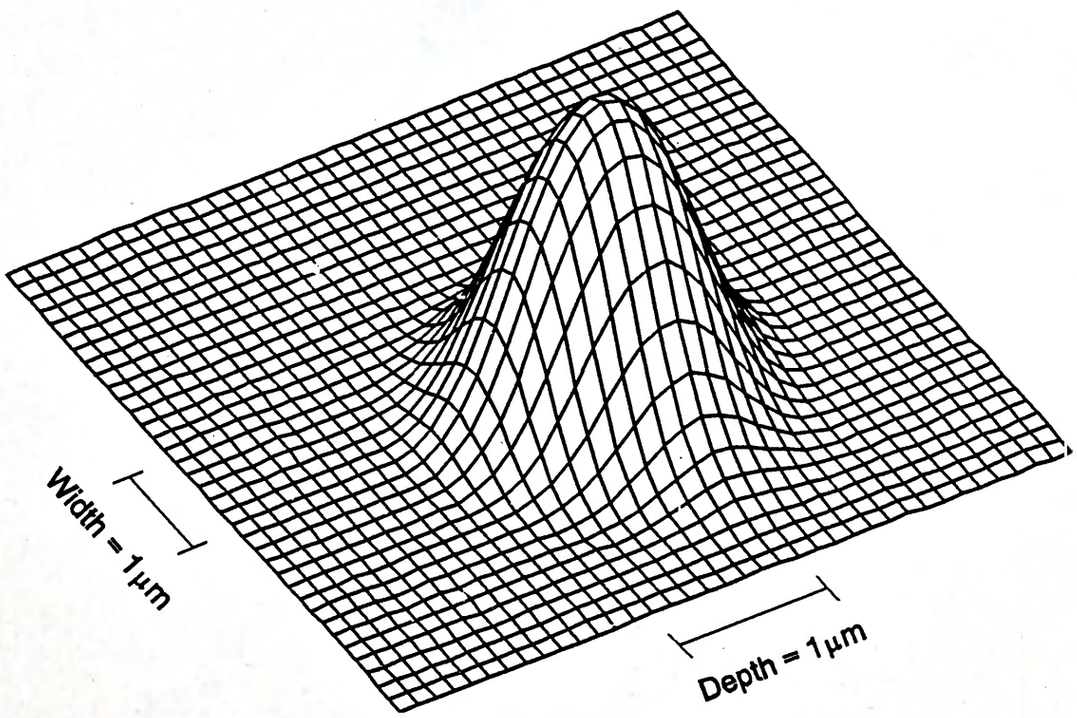

(b)

Fig.5.2.11 Near-field mode pattern and intensity profile of a 2μm wide PE channel waveguide using toluic acid (λ = 0.6328μm).

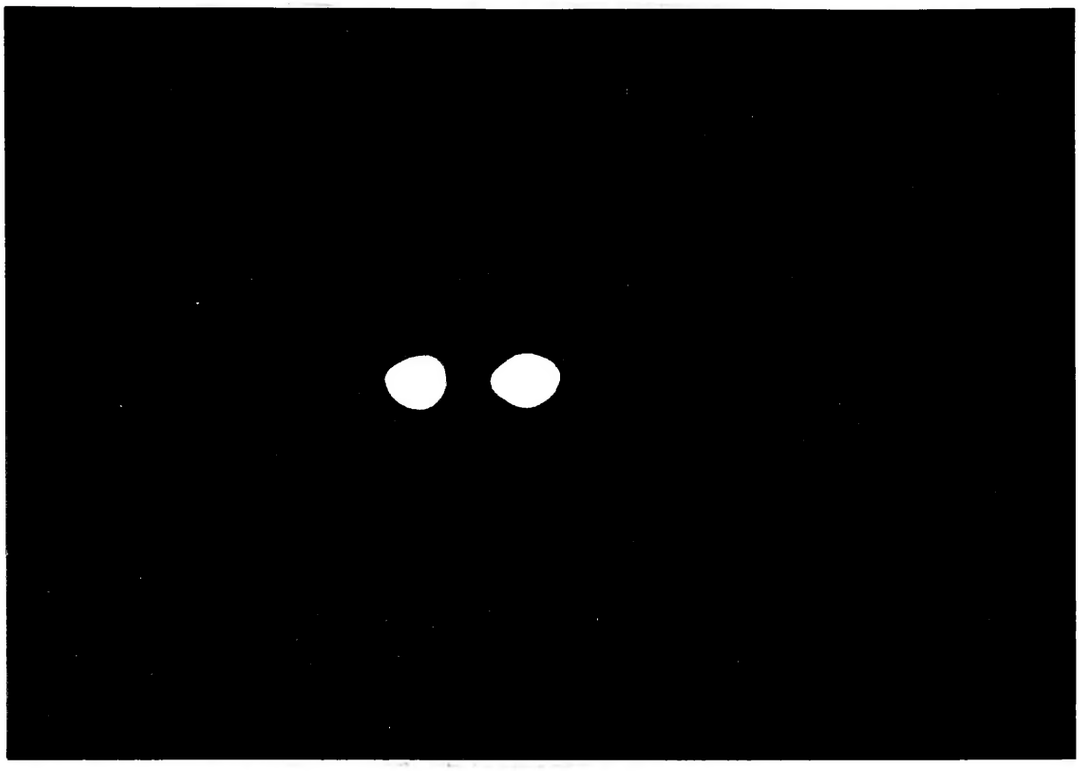

(a)

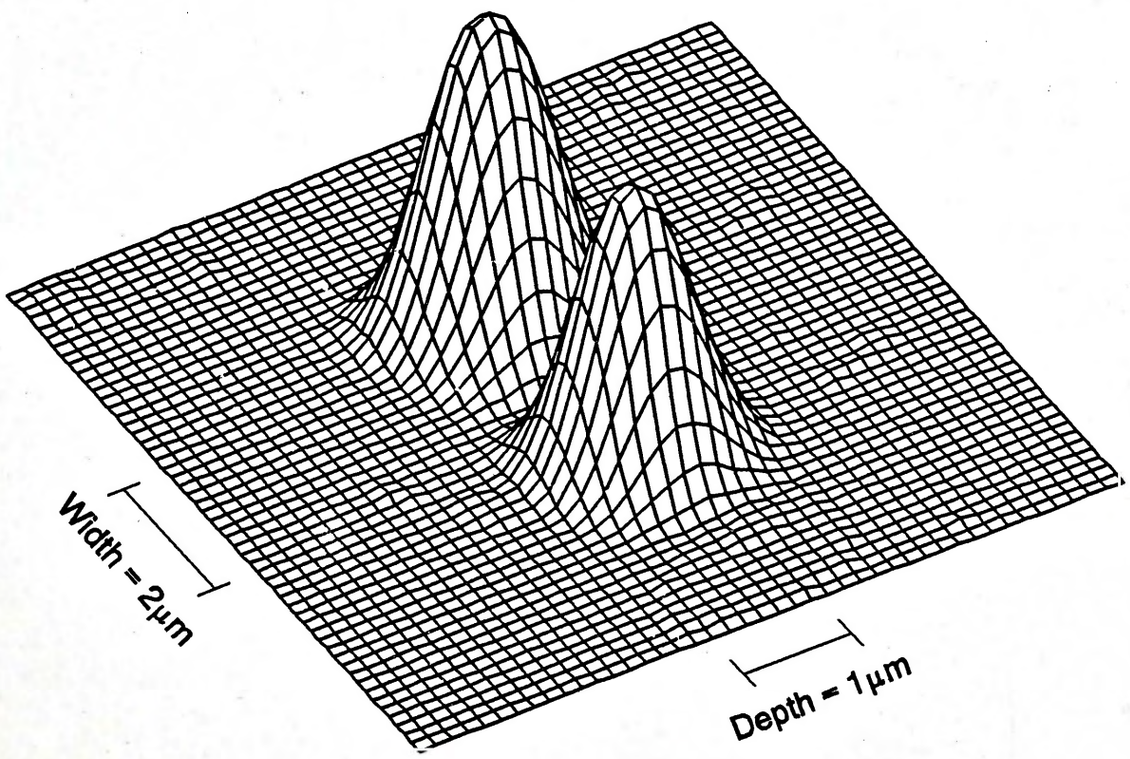

(b)

Fig.5.2.12 Near-field mode pattern and intensity profile of a 4μm wide PE channel waveguide using toluic acid.

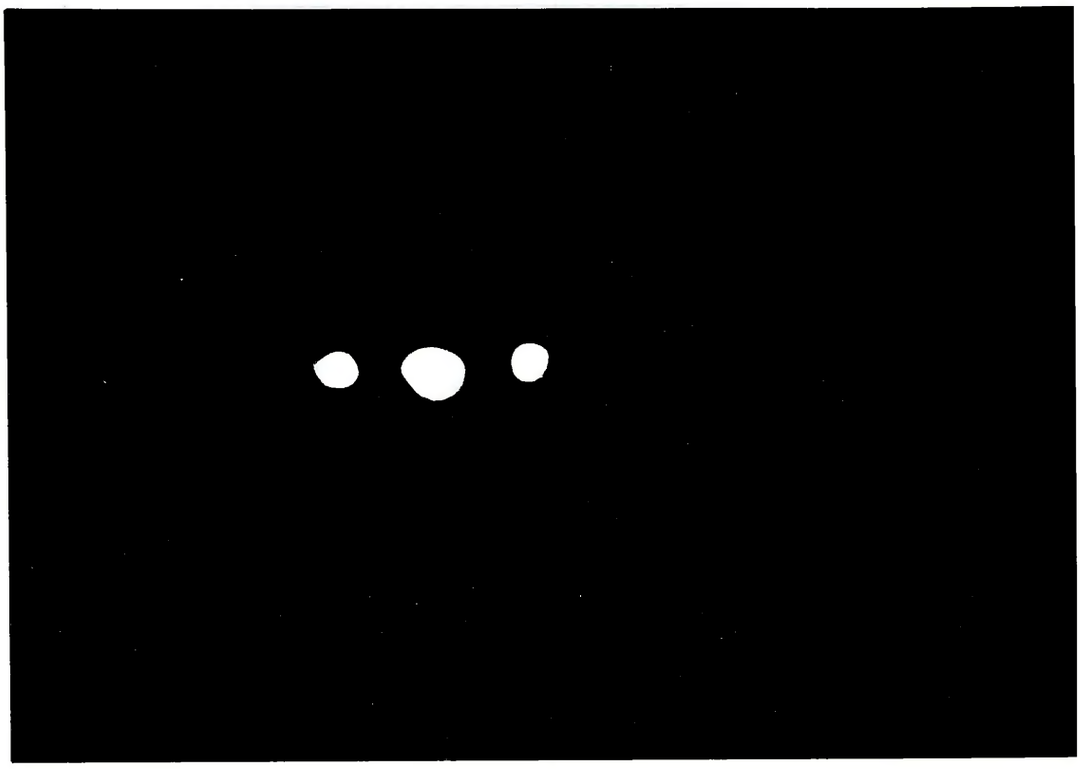

(a)

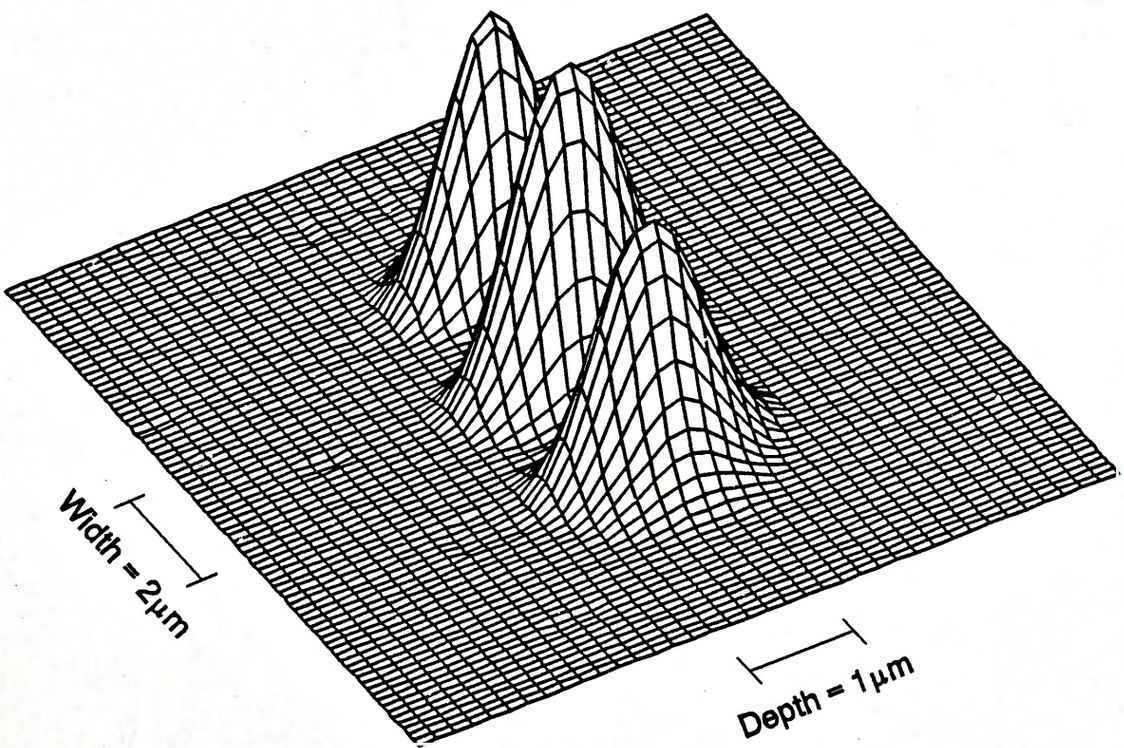

(b)

Fig.5.2.13 Near-field mode pattern and intensity profile of a 6μm wide PE channel waveguide using toluic acid.

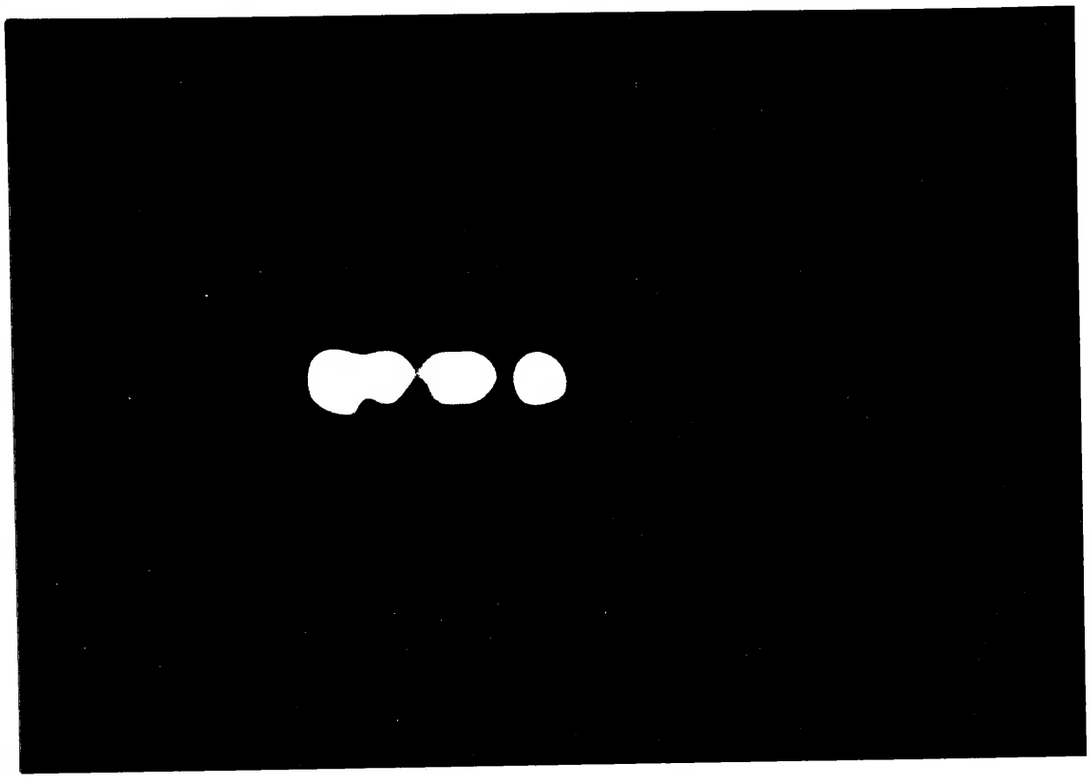

(a)

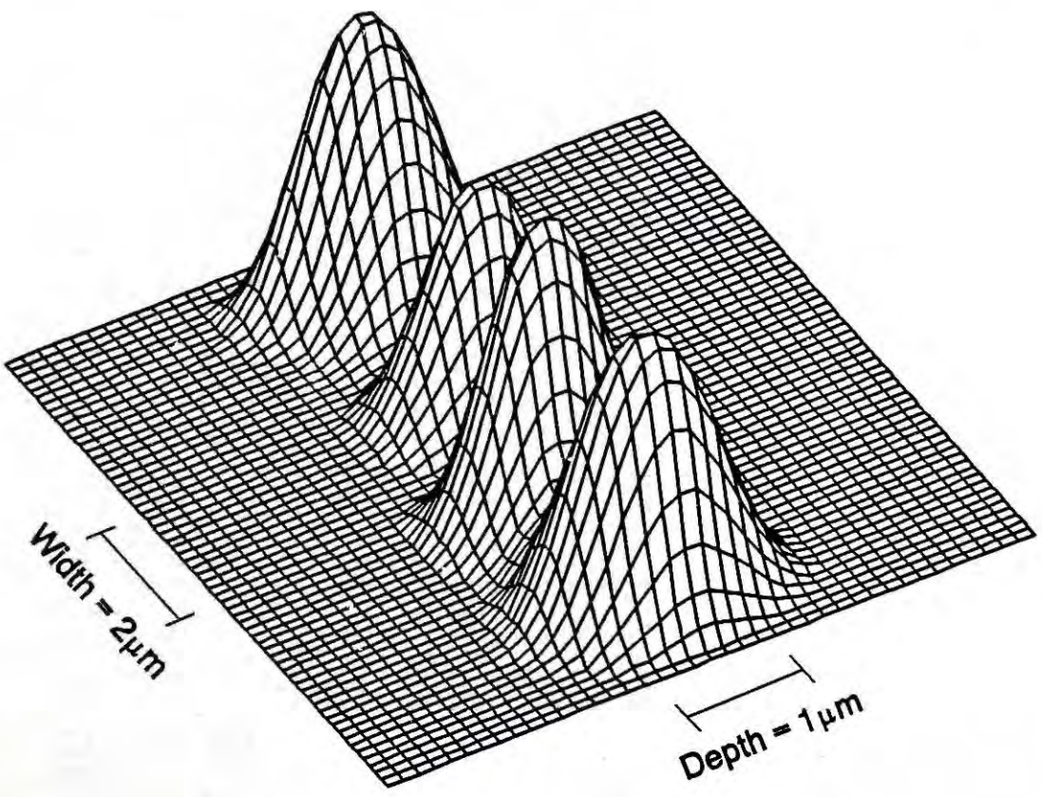

(b)

Fig.5.2.14 Near-field mode pattern and intensity profile of a 8μm wide PE channel waveguide using toluic acid.

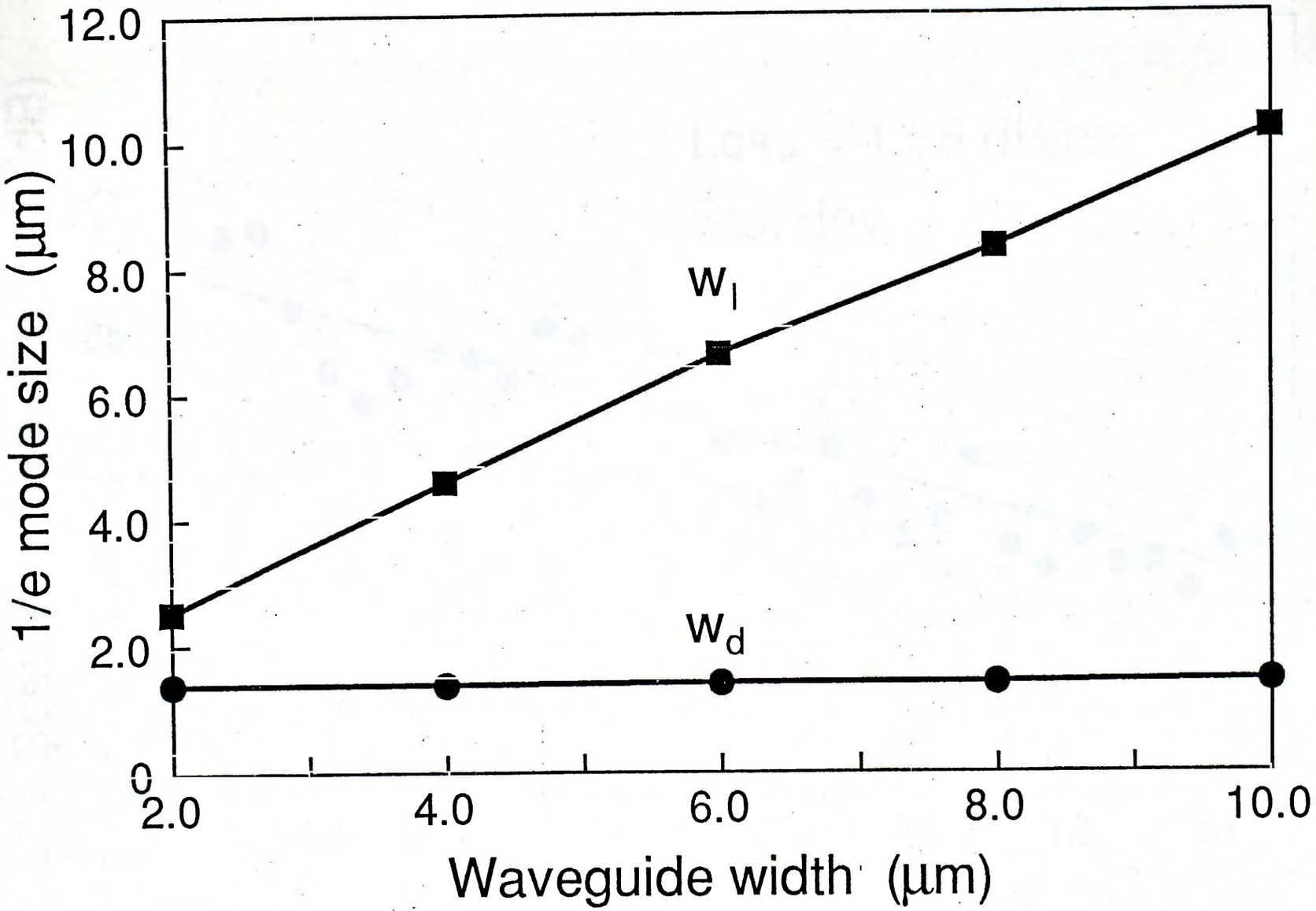

Fig.5.2.15 1/*e* width w_l and depth w_d of the near-field intensity profile as a function of waveguide width.

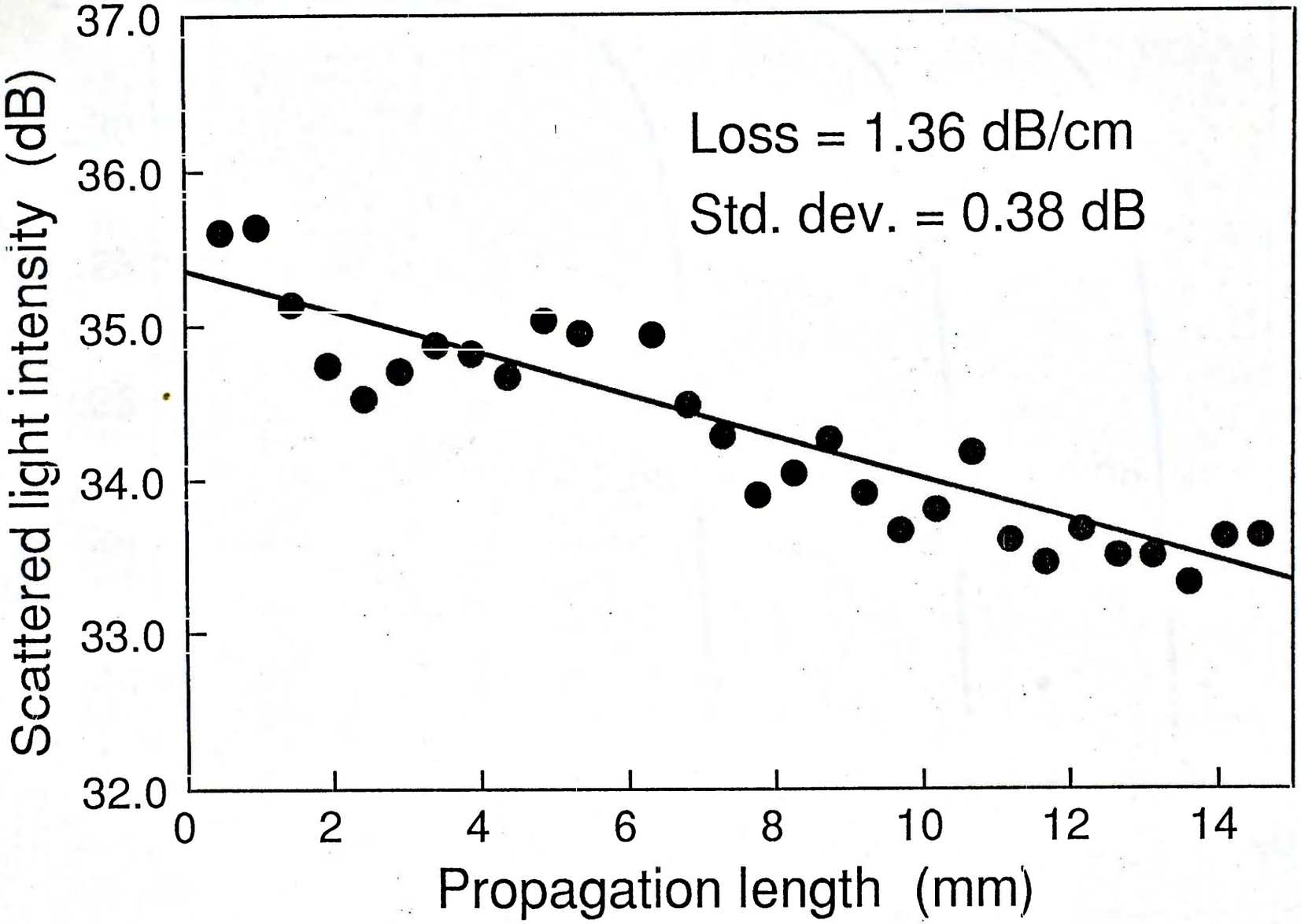

Fig.5.2.16 Propagation loss measurement of a 10μm wide PE channel waveguide using toluic acid.

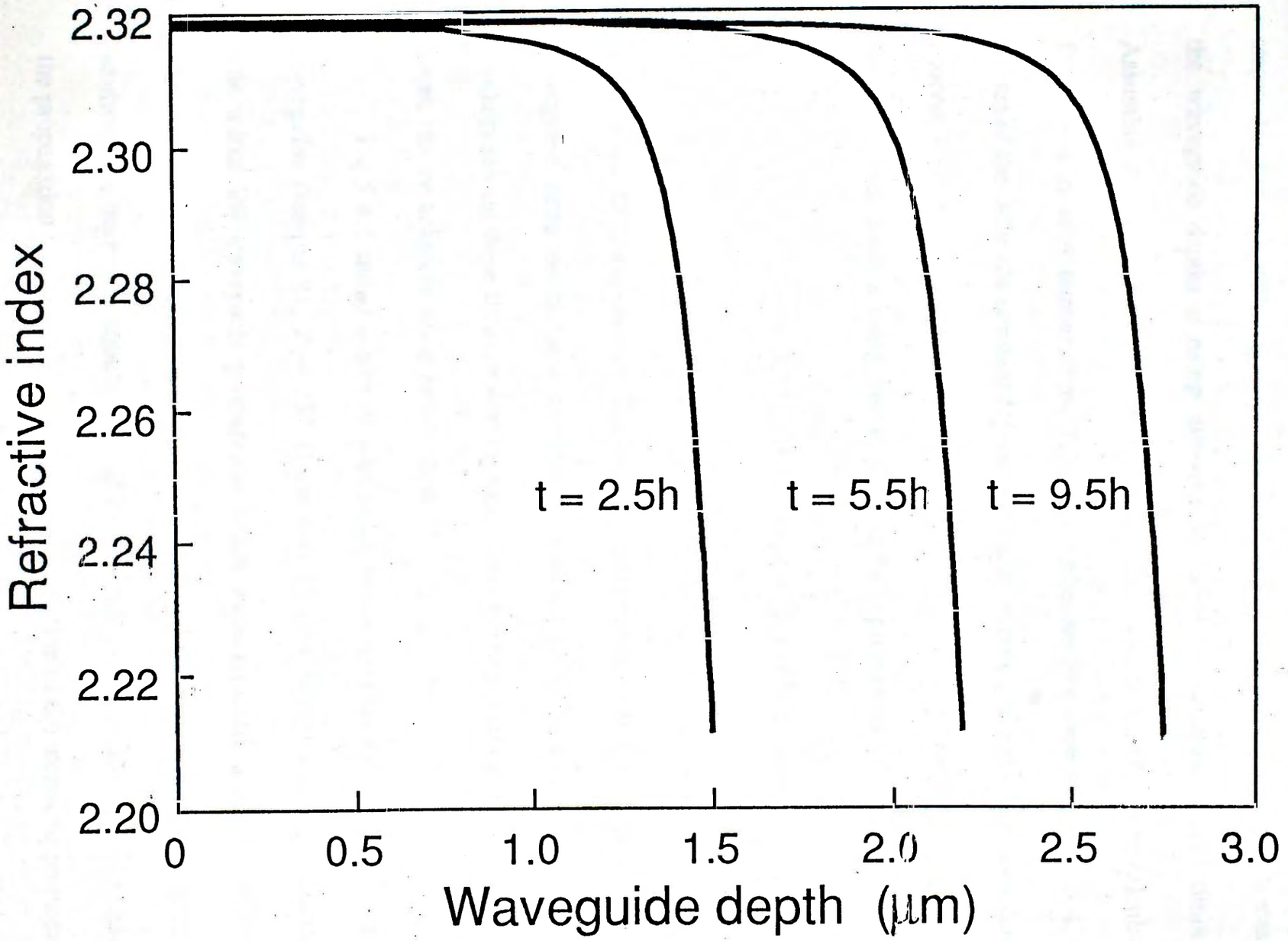

Fig.5.3.1 Refractive index profiles of PE waveguides using stearic acid (T = 250°C).

stearic acid is also a step-index function similar to those obtained using benzoic and toluic acids. Fig.5.3.2 shows that there is an excellent agreement between the measured effective indices and the theoretical mode-dispersion curves based on a step-index function with $\Delta n_s = 0.118$. Fig.5.3.3 summarizes the measurements of the waveguide depths d using different exchange temperatures T and times t. Assuming $d = [t \times D(T)]^{1/2}$, the effective diffusion coefficient $D(T)$ can be calculated for each fabrication temperature. From the Arrhenius plot shown in Fig.5.3.4, the values of the diffusion constant D_o and activation energy Q for the proton-exchange process were found to be 5×10^6 $\mu m^2 h^{-1}$ and 69 $kJmol^{-1}$, respectively. Hence the PE waveguide depth d using stearic acid can be expressed as

$$d = 2.236 \times 10^3 \sqrt{t} \exp(-4.15 \times 10^3 / T) \quad \mu m \qquad (5.13)$$

Fig.5.3.5 shows the temperature dependence of the effective diffusion coefficients $D(T)$ for stearic, benzoic and toluic acids. It can be seen that PE waveguide using stearic acid exhibits the smallest D(T) because this acid is the weakest among these three proton sources. Thus better control over the waveguide depth can be achieved using stearic acid.

Fig.5.3.6 shows a plot of attenuation measurements for a single-mode PE waveguide (sample S1, $T = 250°C$ and $t = 15$ min) before and after annealing. The initial PE waveguide propagation losses were typically around 1 $dBcm^{-1}$. These values were similar to those obtained using toluic acid. With better controlled environment the propagation loss could be lowered. The annealing process reduces the propagation loss, and Fig.5.3.7 shows the variation of the measured propagation loss versus annealing time t_a (sample S1). After 4 hours of annealing at a

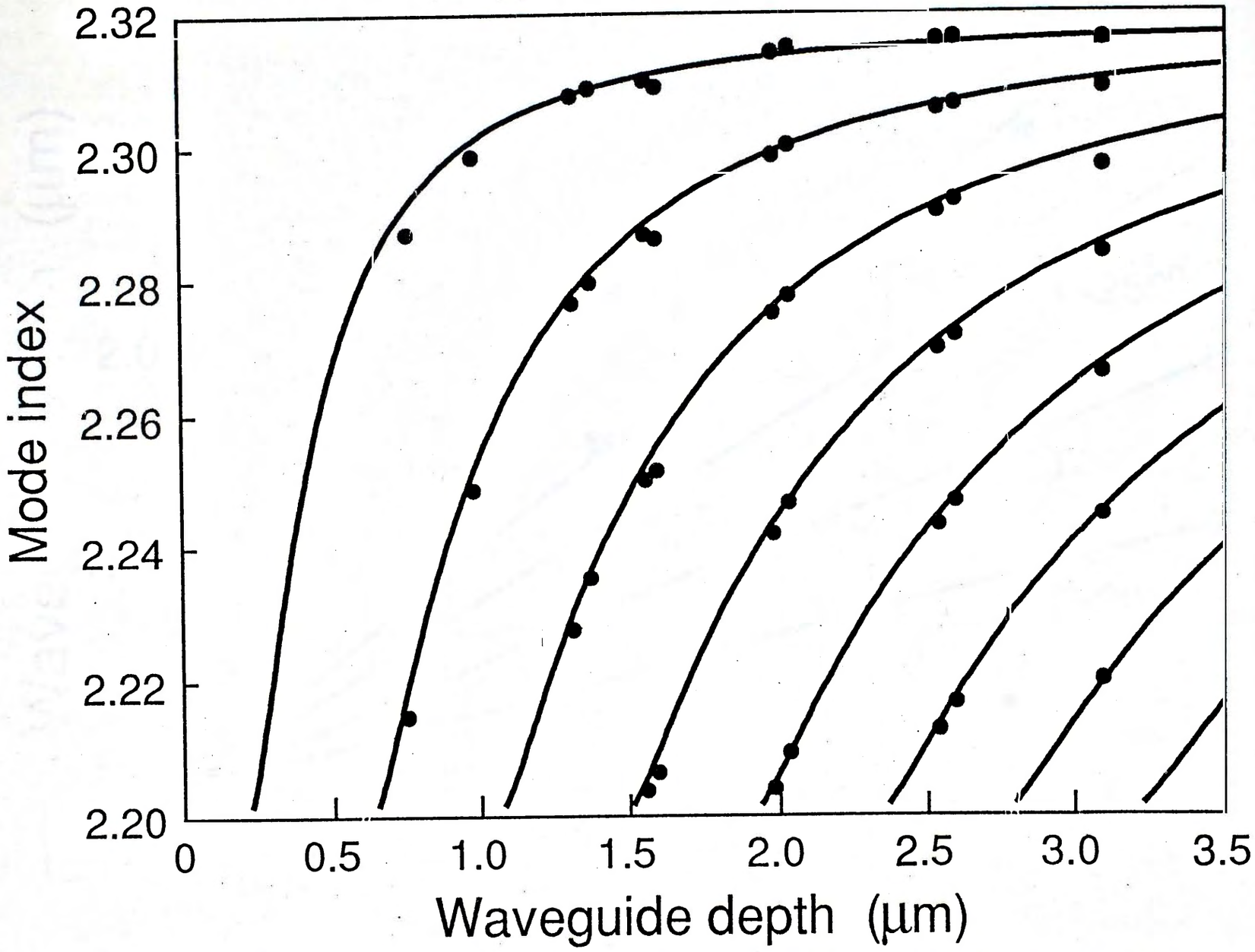

Fig.5.3.2 Theoretical mode-dispersion curves using a step index profile ($\Delta n_s = 0.118$) and experimental data.

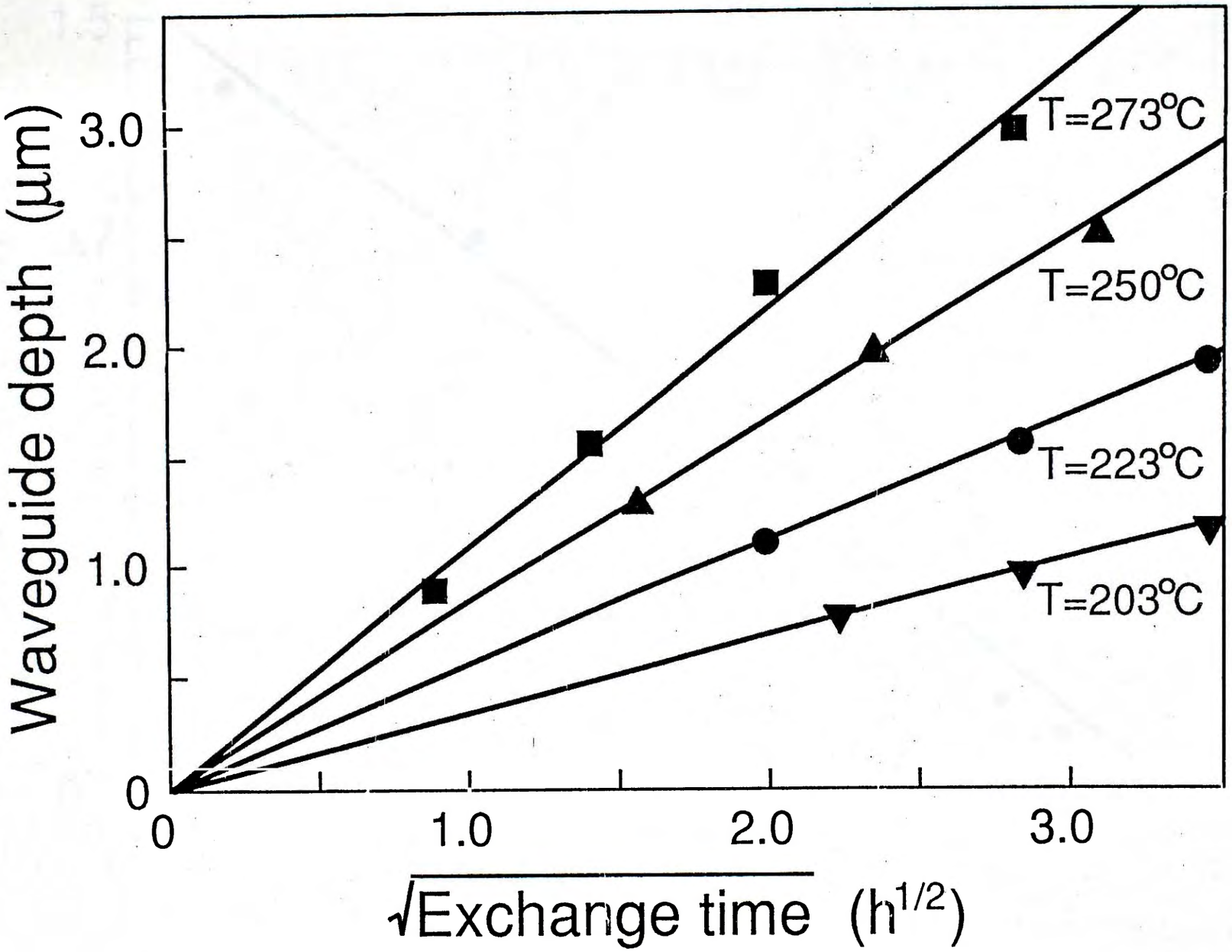

Fig.5.3.3 PE waveguide depth as a function of square root of exchange time.

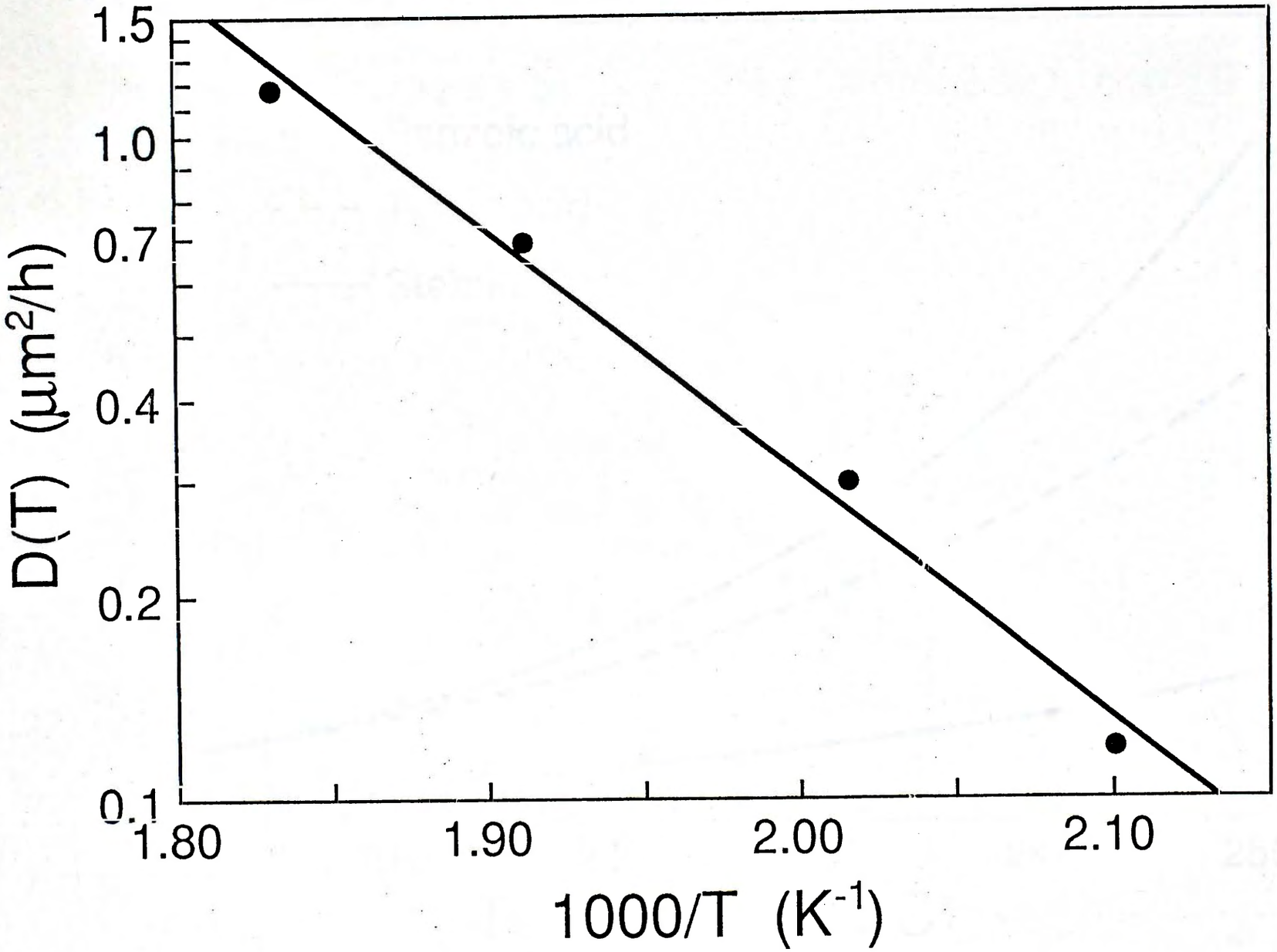

Fig.5.3.4 Plot of effective diffusion coefficient ln[D(T)] versus inverse of exchange temperature 1/T.

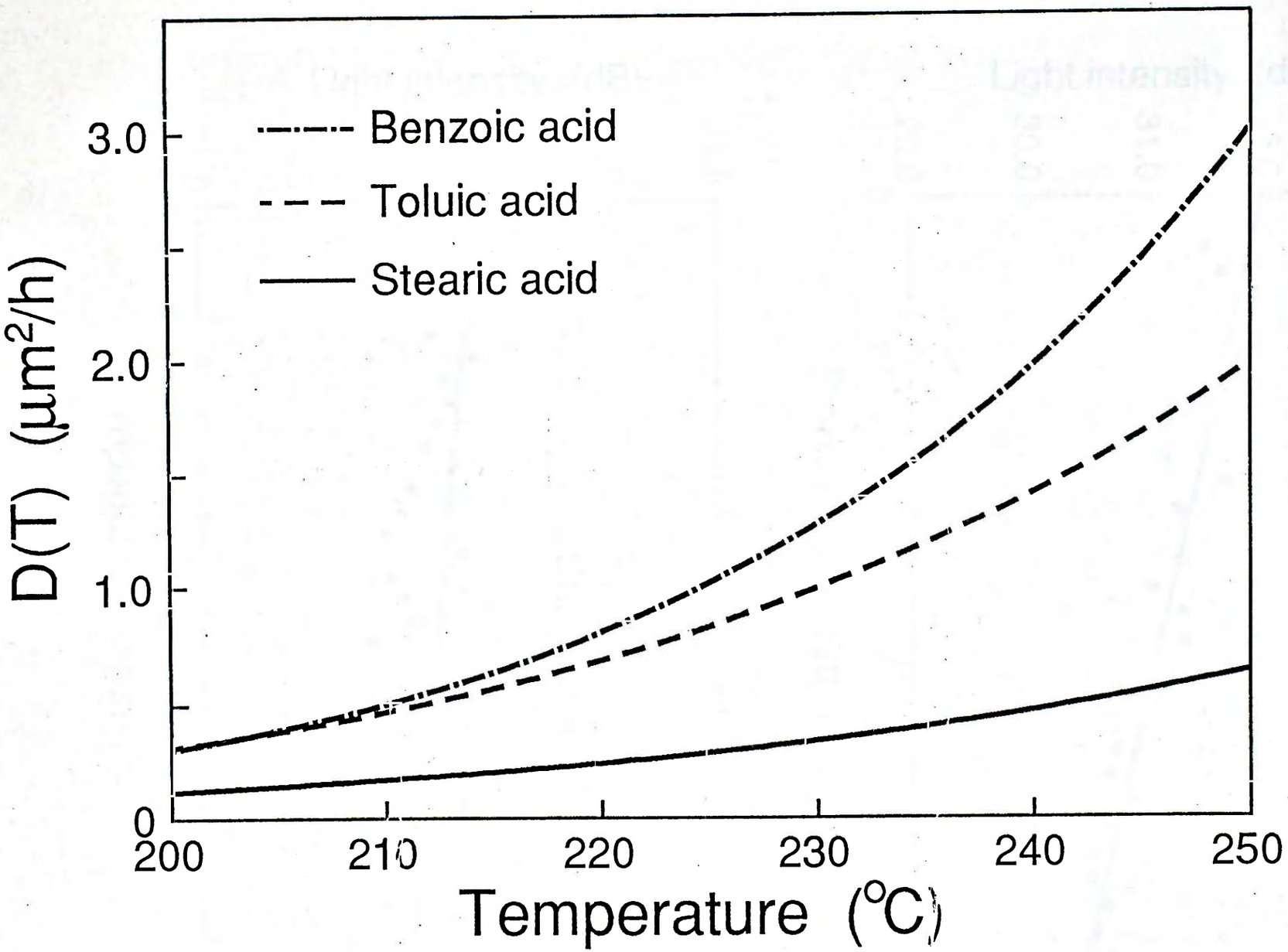

Fig.5.3.5 Comparison of effective diffusion coefficient D(T) as a function of temperature for stearic, benzoic, and toluic acid.

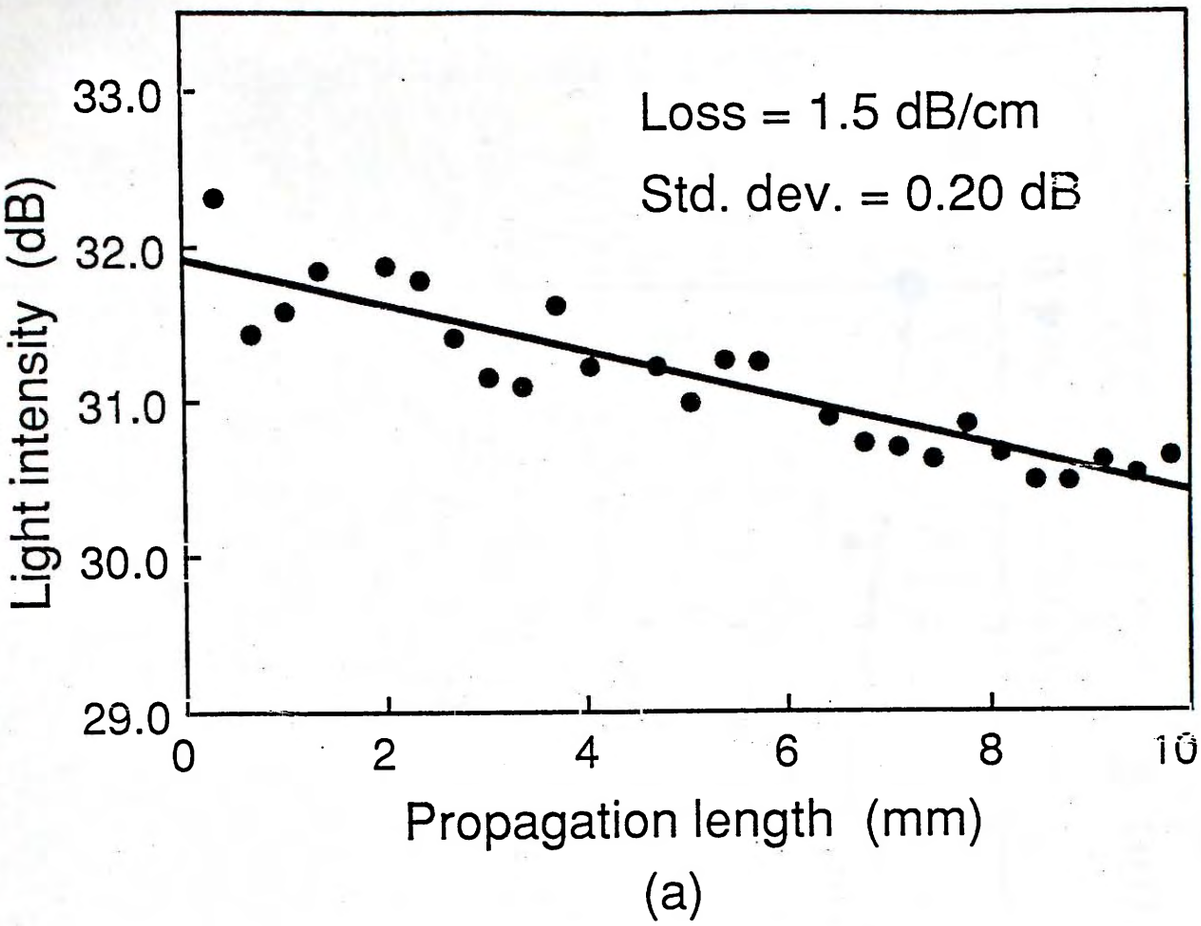

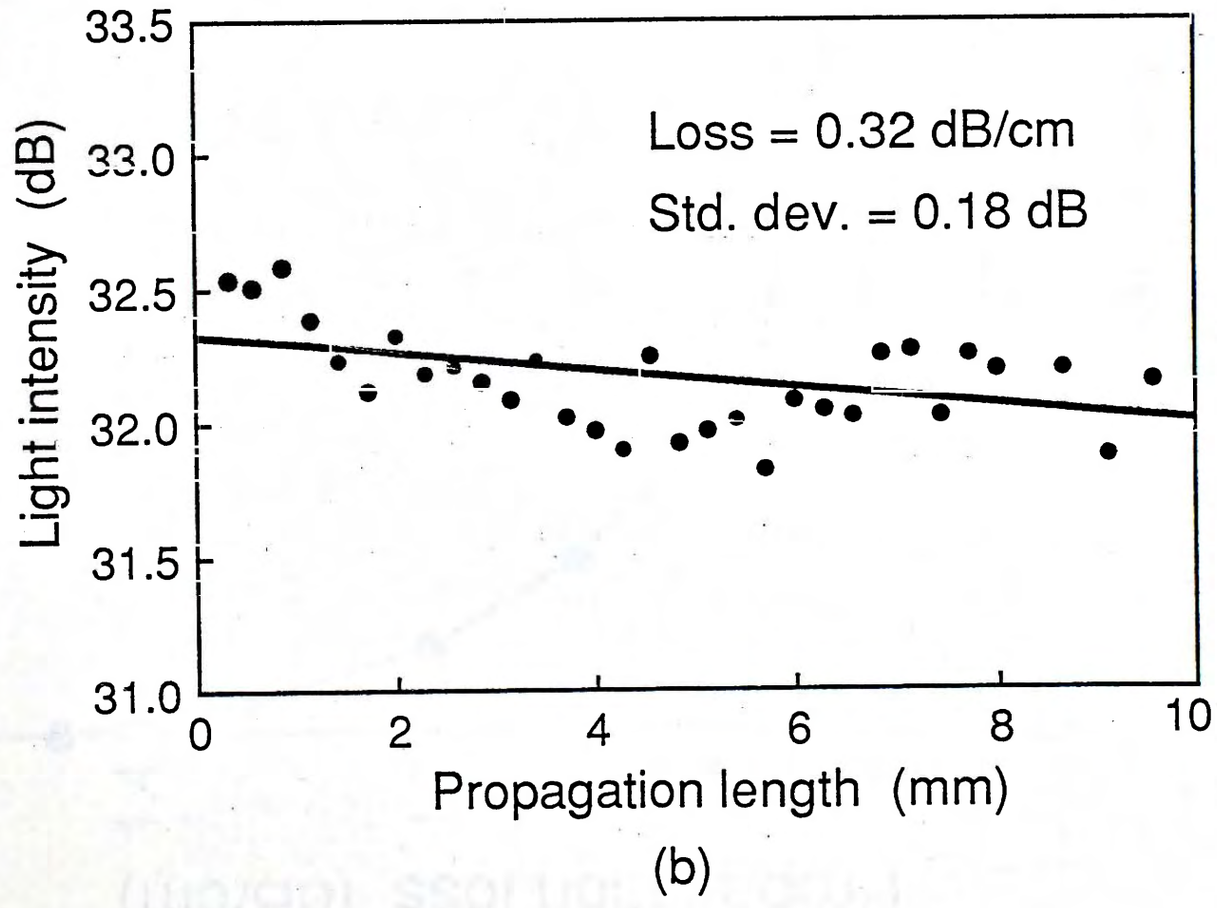

Fig.5.3.6 Propagation loss measurement of PE planar waveguide using stearic acid. (a) Before annealing, (b) after annealing (T_a=350°C, t_a=4h).

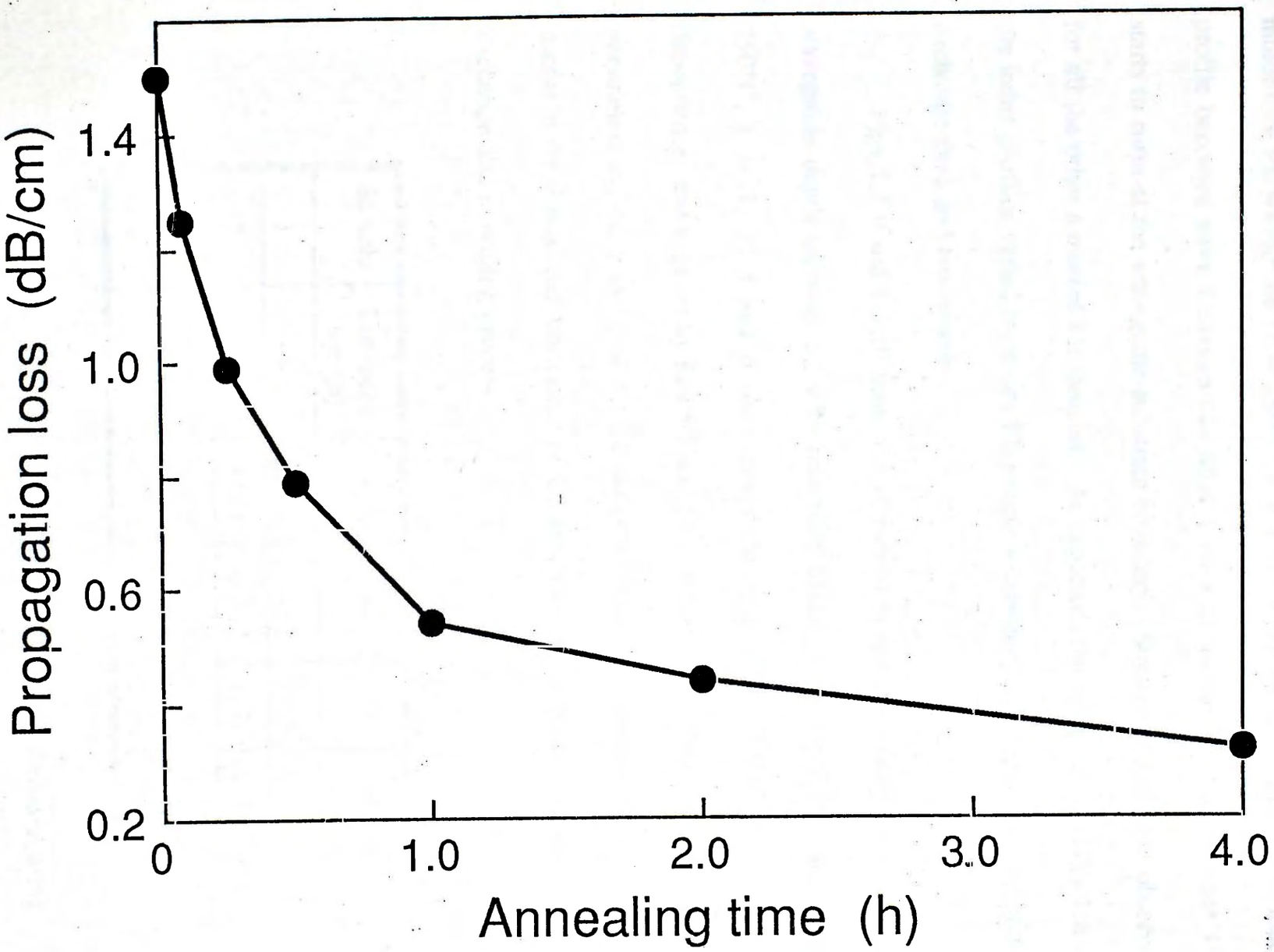

Fig.5.3.7 Plot of propagation loss versus annealing time (T = 250°C, t = 15 min, T_a = 350°C).

temperature T_a of 350°C, the propagation loss was reduced by 80% from 1.5 dBcm^{-1} to 0.3 dBcm^{-1}.

Fig.5.3.8 shows the effect of annealing on refractive index profile of a multimode PE waveguide (T = 250°C, t = 4 h). It can be seen that the step index profile becomes more Gaussian-like after 1 hour of annealing, and an index tail starts to form at the waveguide-substrate boundary. Similar results were observed for all the other annealed PE samples. As expected, the extent of modification on the index profiles varied from one PE sample to another, and depends on the initial exchange time and temperature.

Figs.5.3.9 and 5.3.10 show the variations in surface index change Δn_s and waveguide depth increase Δd with annealing time t_a for four PE samples (T = 250°C, t = 1, 2, 4 and 6 h). Again the relationship follows a power-law dependence, and is given by Eqs.5.8 and 5.9. Table 5.9 summarizes the annealing parameters c_1, c_2, p and q of our PE samples. The parameters obtained would be useful in the design and fabrication of $LiNbO_3$ waveguide devices using the proton exchange and annealing process.

Sample	Exchange time (h)	c_1	p	c_2	q
1	1	0.082	-0.101	1.45	0.59
2	2	0.091	-0.082	1.64	0.58
3	4	0.096	-0.075	1.83	0.58
4	6	0.098	-0.072	2.00	0.58

Table 5.9 Annealing parameters of PE waveguides fabricated using stearic acid (T = 250°C, T_a = 350°C).

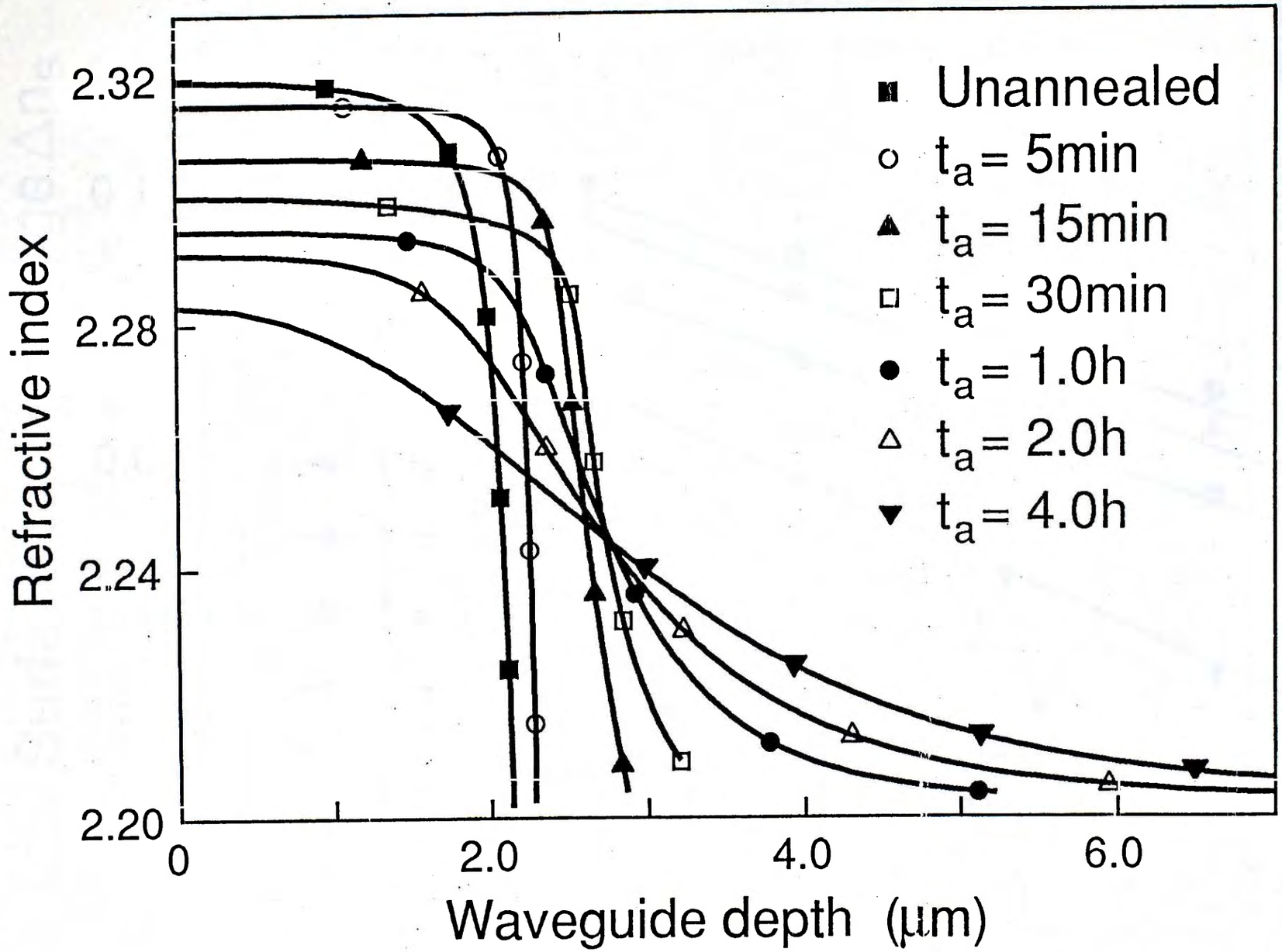

Fig.5.3.8 Variation of PE waveguide index profile with annealing time t_a (T = 250°C, t = 4 h, T_a = 350°C).

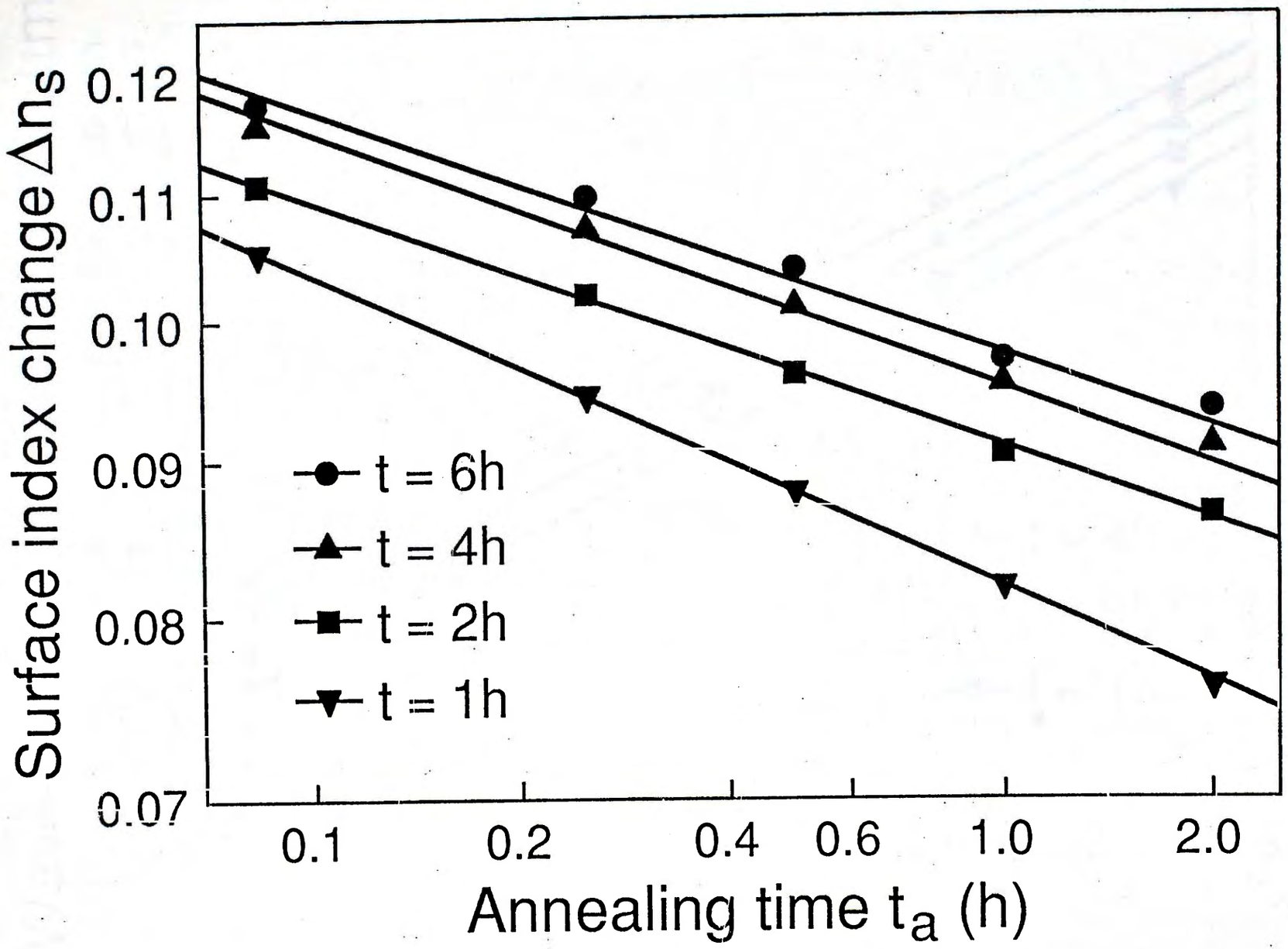

Fig.5.3.9 Variation of surface index change Δn_s with annealing time t_a (T = 250°C, T_a = 350°C).

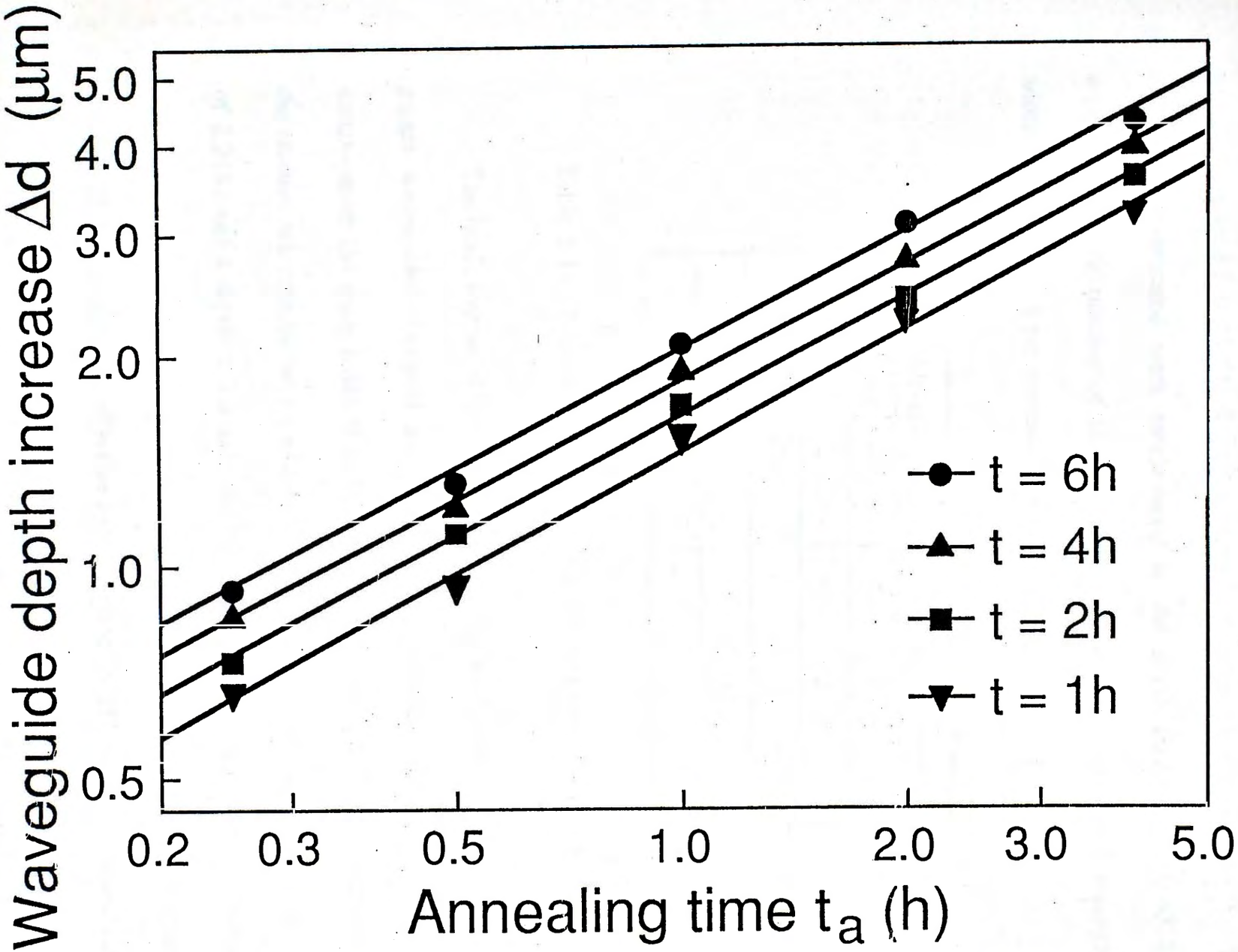

Fig.5.3.10 Variation of waveguide depth increase Δd with annealing time t_a (T = 250°C, T_a = 350°C).

Proton-exchanged channel waveguides with 2μm to 10μm width and 10mm length have also been fabricated in z-cut $LiNbO_3$ using stearic acid. Proton exchange was carried out at 200°C for 1 hour in molten stearic acid. The sample was then annealed at 350°C for 30 minutes in flowing O_2 ($500cm^3min^{-1}$). The waveguides fabricated were single-mode in the depth direction at 0.6328μm wavelength. The number of lateral modes supported increases with waveguide width, and the results are summarized in Table 5.10.

Waveguide width (μm)	No. of lateral modes
2	1
4	2
6	3
8	4
10	5

Table 5.10 Number of lateral modes as a function of PE stripe width.

The mode indices of the channel waveguides were evaluated from that of the planar waveguide fabricated under the same condition. From prism-coupling measurement the mode index of this planar waveguide was 2.2152. Assuming that the channel waveguides have a rectangular cross-section with a uniform core index of 2.2152 and a depth of 1.2 μm, the theoretical mode indices can be calculated. Fig.5.3.11 shows a set of theoretical mode-dispersion curves as a function of waveguide width using the effective index method [5.21]. It can be seen that the number of modes calculated for channel waveguides with 2μm, 4μm, 6μm, 8μm and 10μm width agrees with our measured results.

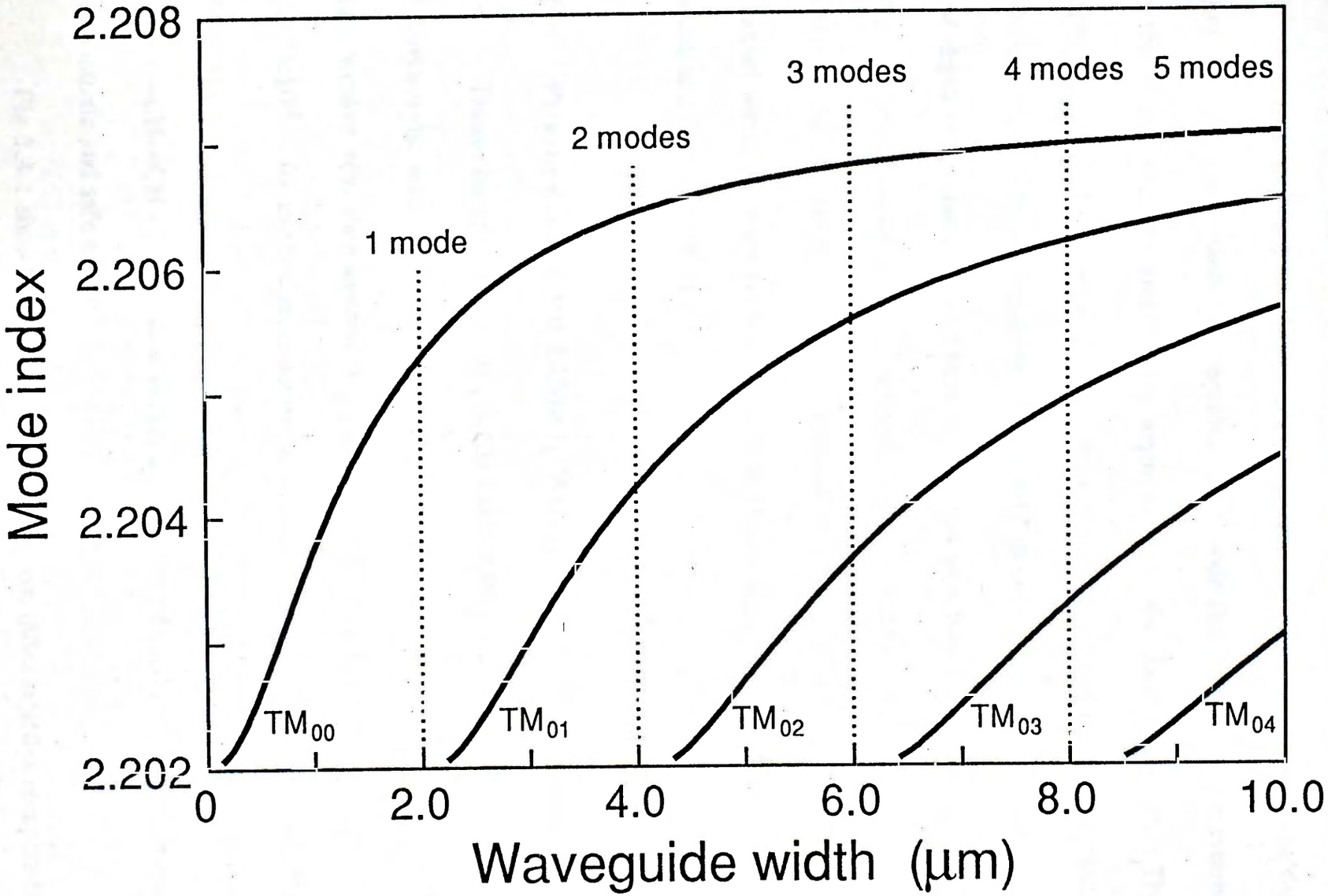

Fig.5.3.11 Mode effective index as a function of waveguide width for a step-index channel waveguide using effective index method (n_{core} = 2.2152, n_{sub} = 2.202, d = 1.2 μm, λ = 0.6328 μm).

Fig.5.3.12 shows the propagation loss measurement for a 10μm wide channel waveguide (λ=0.6328μm). The channel waveguide losses are typically around 1 dBcm^{-1}, and are similar to those obtained using toluic acid.

Figs.5.3.13 to 5.3.16 show the measured near-field intensity profiles for the 2μm and 4μm wide channel waveguides. The mode-field distribution is symmetric in the width direction and slightly asymmetric in the depth direction. This is expected because the index difference between waveguide and air is larger than that between waveguide and substrate. Fig.5.3.17 shows the variation of $1/e$ width w_l and depth w_d of the near-field intensity profiles as a function of waveguide width. The horizontal mode size w_l increases almost linearly with waveguide width, whereas the vertical mode size w_d remains invariant. This suggests that the PE channel waveguides are far from cutoff and exhibit tight optical confinement in both width and depth directions.

5.4 Proton-exchanged $LiNbO_3$ Waveguides Using Cinnamic Acid

Trans-cinnamic acid (C_6H_5CH:CHCOOH, also known as trans-3-Phenylacrylic acid) has a melting point of 133°C and a boiling point of 300°C. It is a weaker acid than benzoic acid and has a dissociation constant K_α(25°C) of 3.47×10^{-5}. Its molecular structure is similar to that of benzoic acid, but the carboxyl base (—COOH) is displaced from the benzene ring due to the vinylene base (—CH=CH—). The acid occurs naturally in tobacco and some balsams, and is nontoxic and safe to use.

Fig.5.4.1 shows the representative refractive index profiles computed using the continuous effective-index function method [5.8]. The index profile of the PE

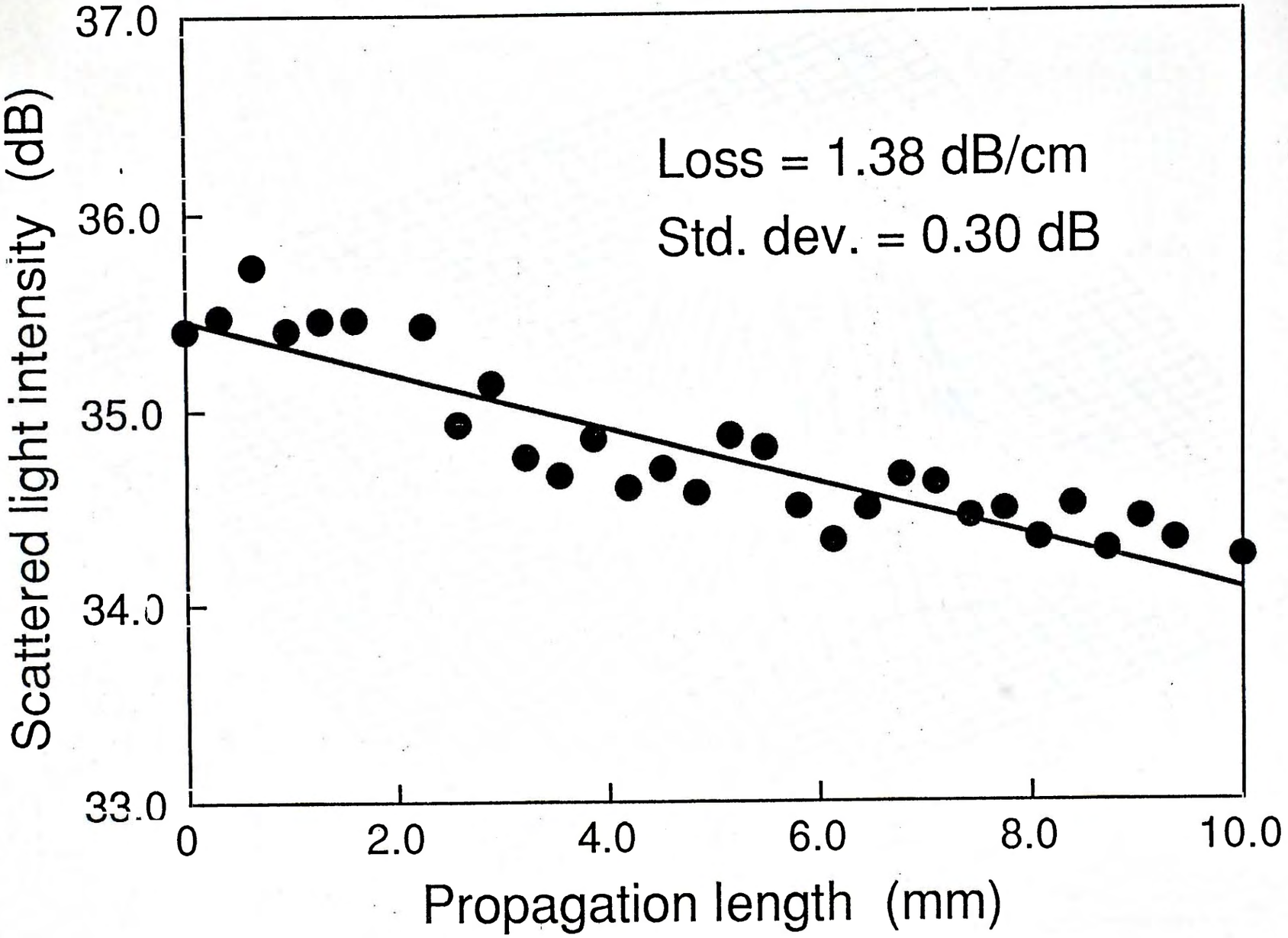

Fig.5.3.12 Propagation loss measurement of a 10μm wide PE channel waveguide using stearic acid (λ = 0.6328μm).

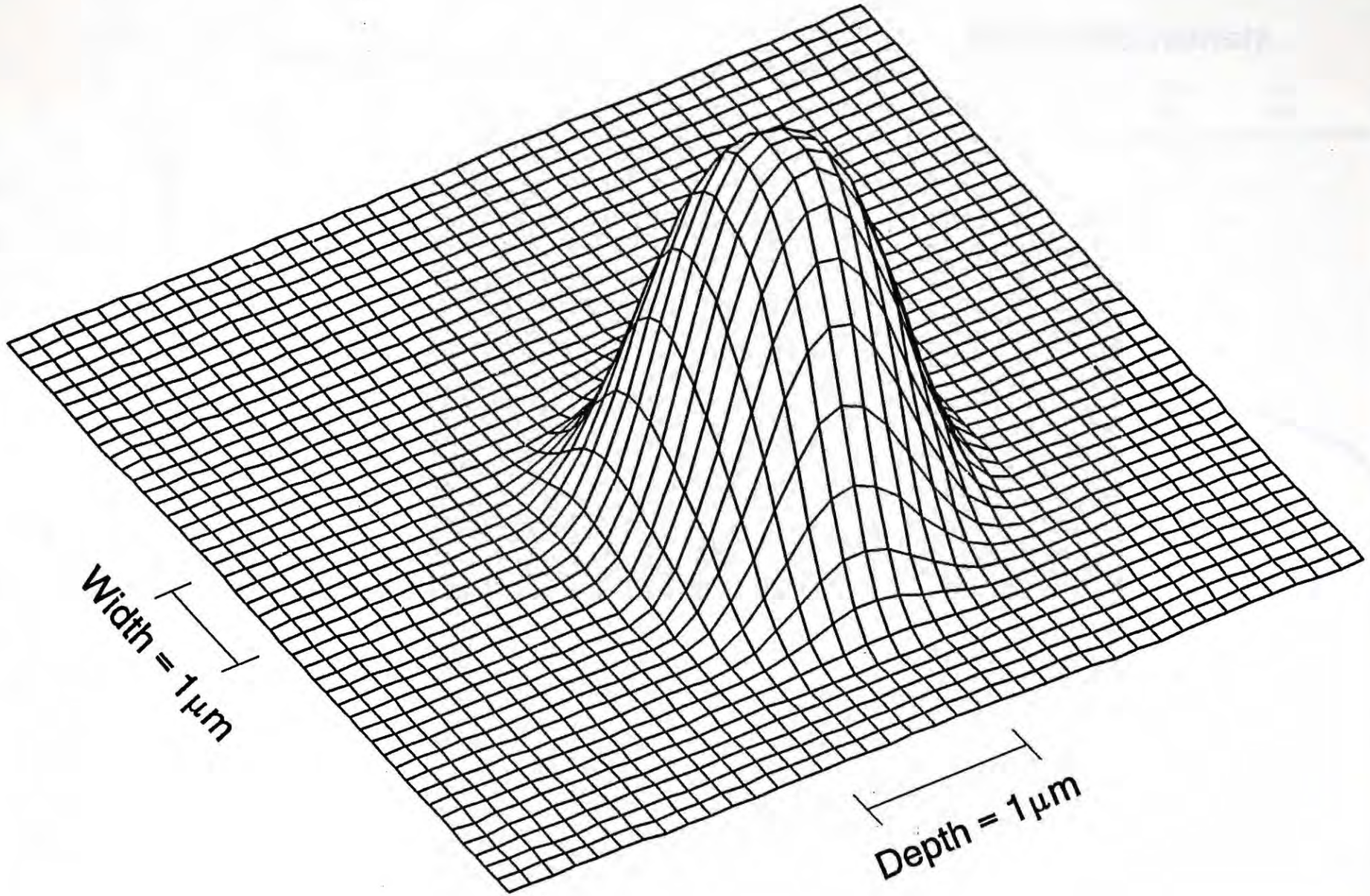

Fig.5.3.13 Near-field intensity profile of a single-mode PE channel waveguide of 2μm width at 0.6328μm wavelength.

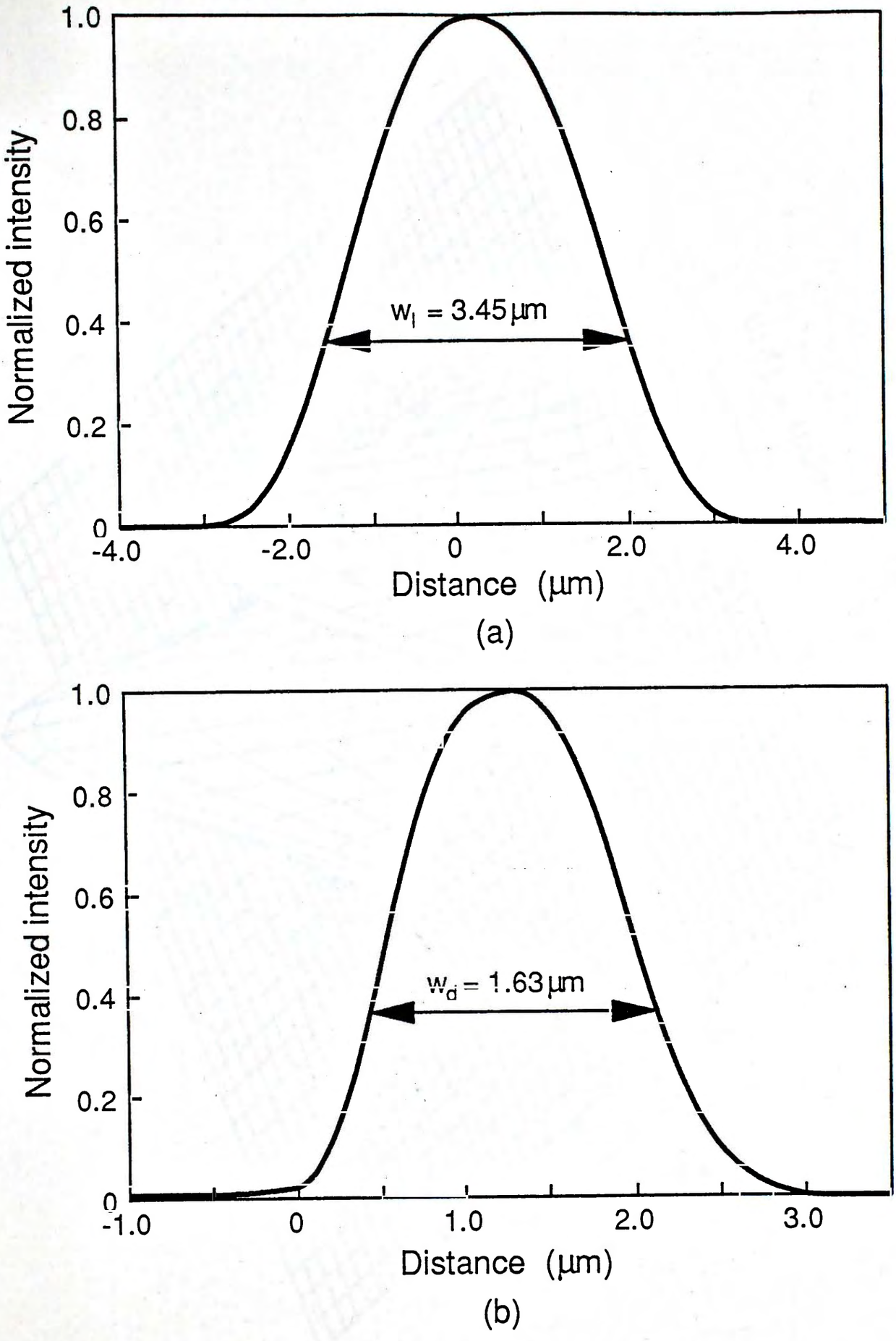

Fig.5.3.14 Near-field intensity profile along (a) width and (b) depth direction for a 2μm wide channel waveguide using stearic acid.

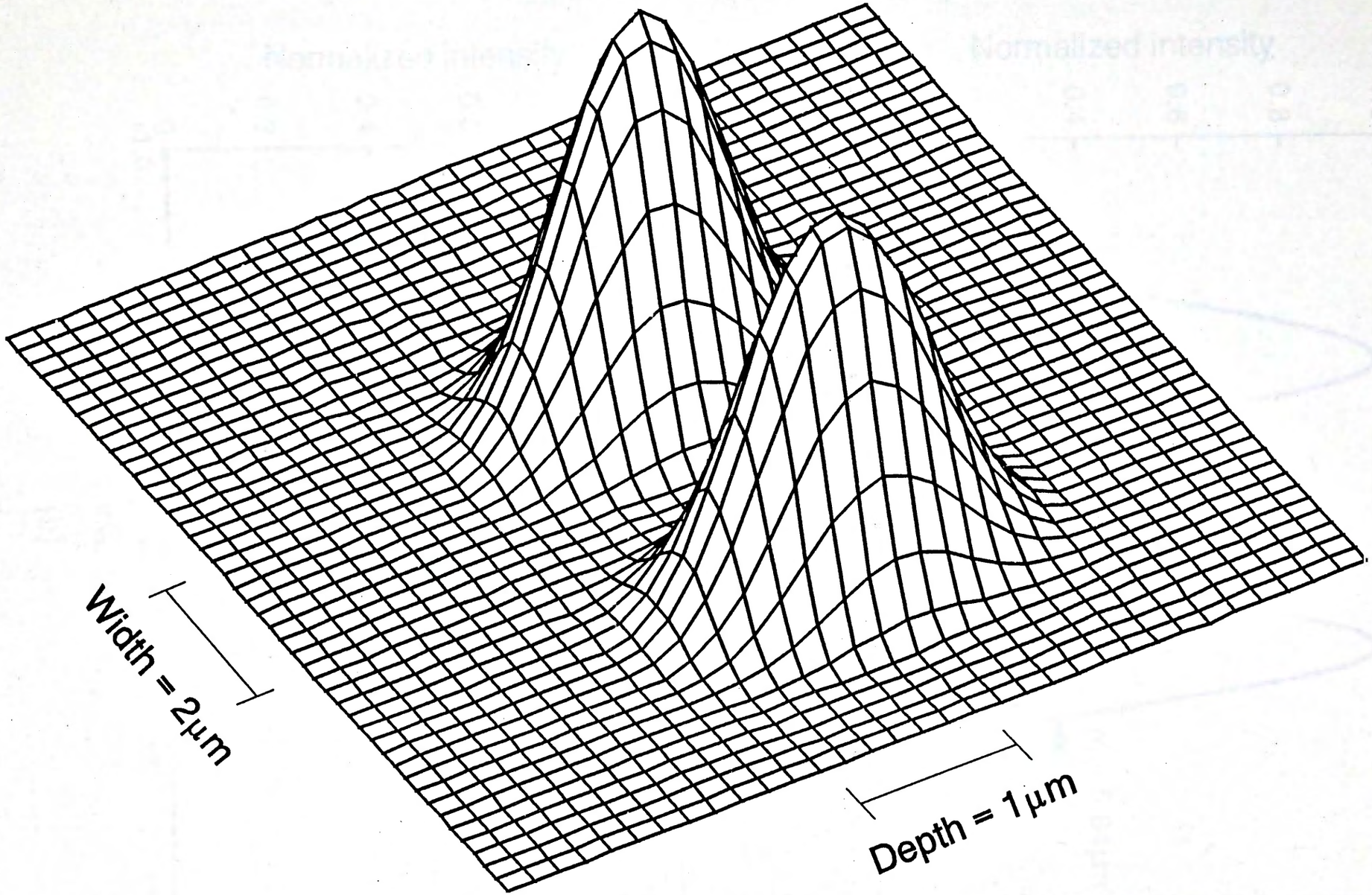

Fig.5.3.15 Near-field intensity profile of a 4μm wide PE channel waveguide using stearic acid (λ = 0.6328μm).

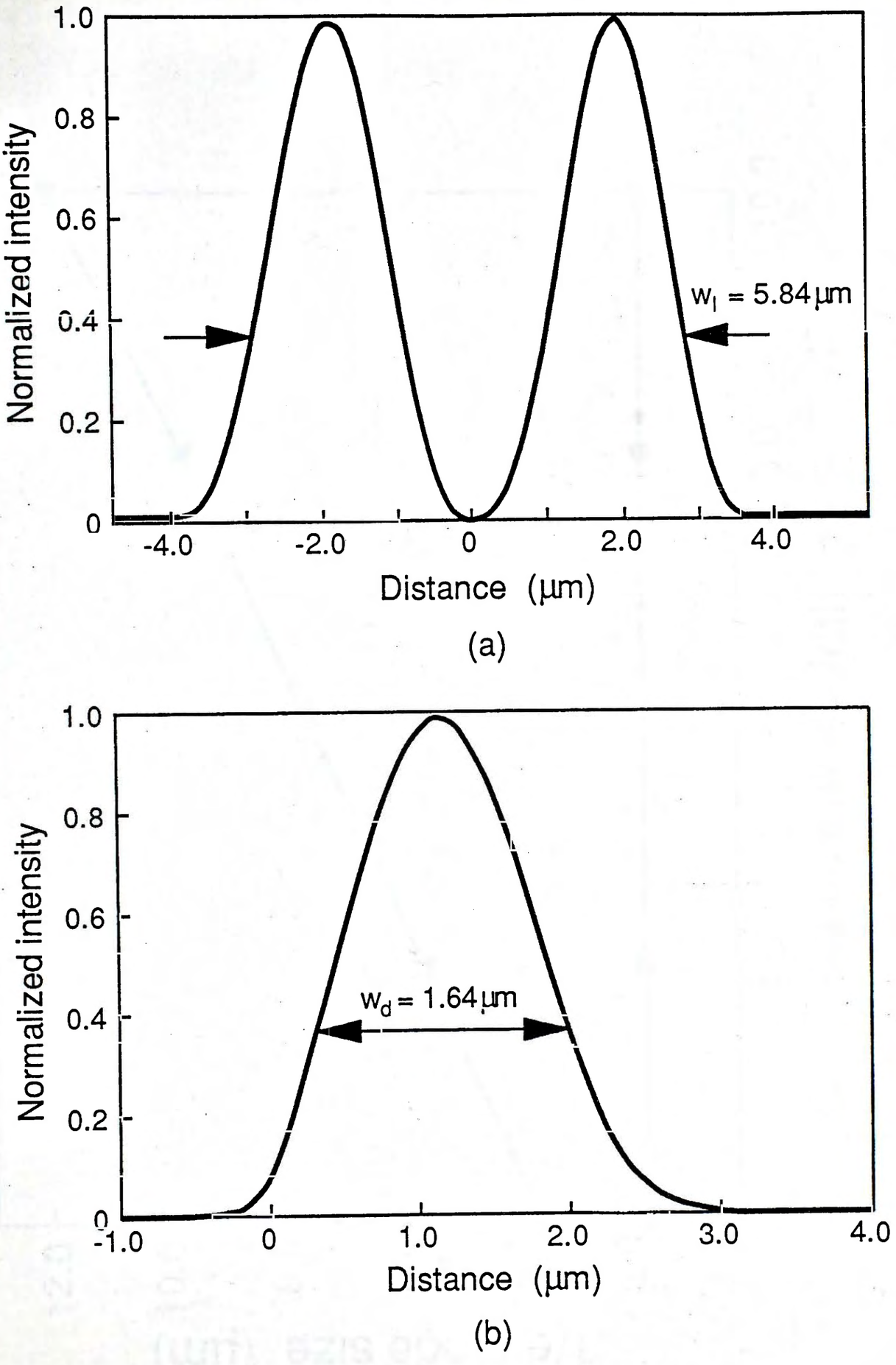

Fig.5.3.16 Near-field intensity profile along (a) width and (b) depth direction for a 4μm wide channel waveguide using stearic acid.

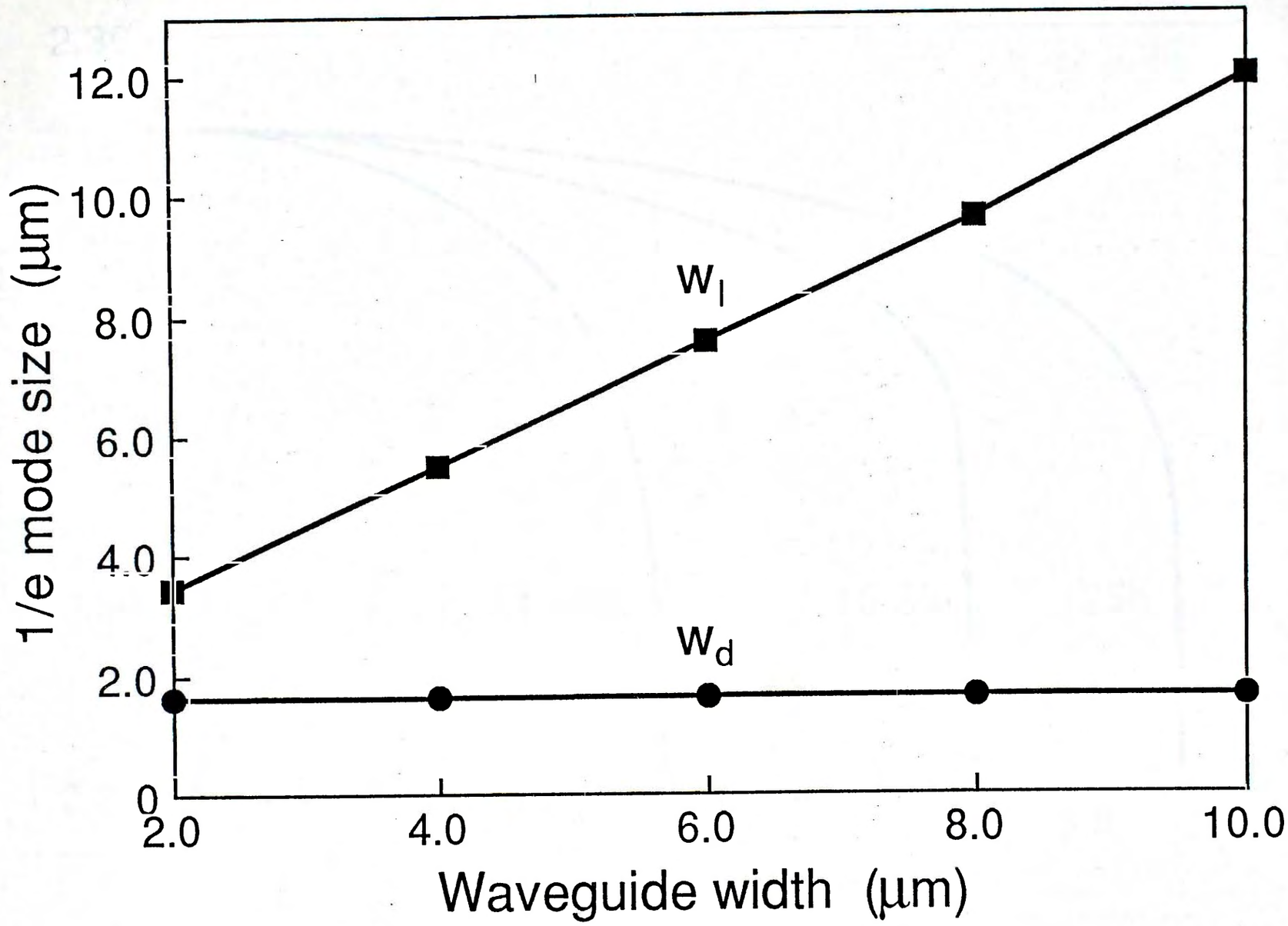

Fig.5.3.17 1/*e* width w_l and depth w_d of the near-field intensity profile as a function of waveguide width.

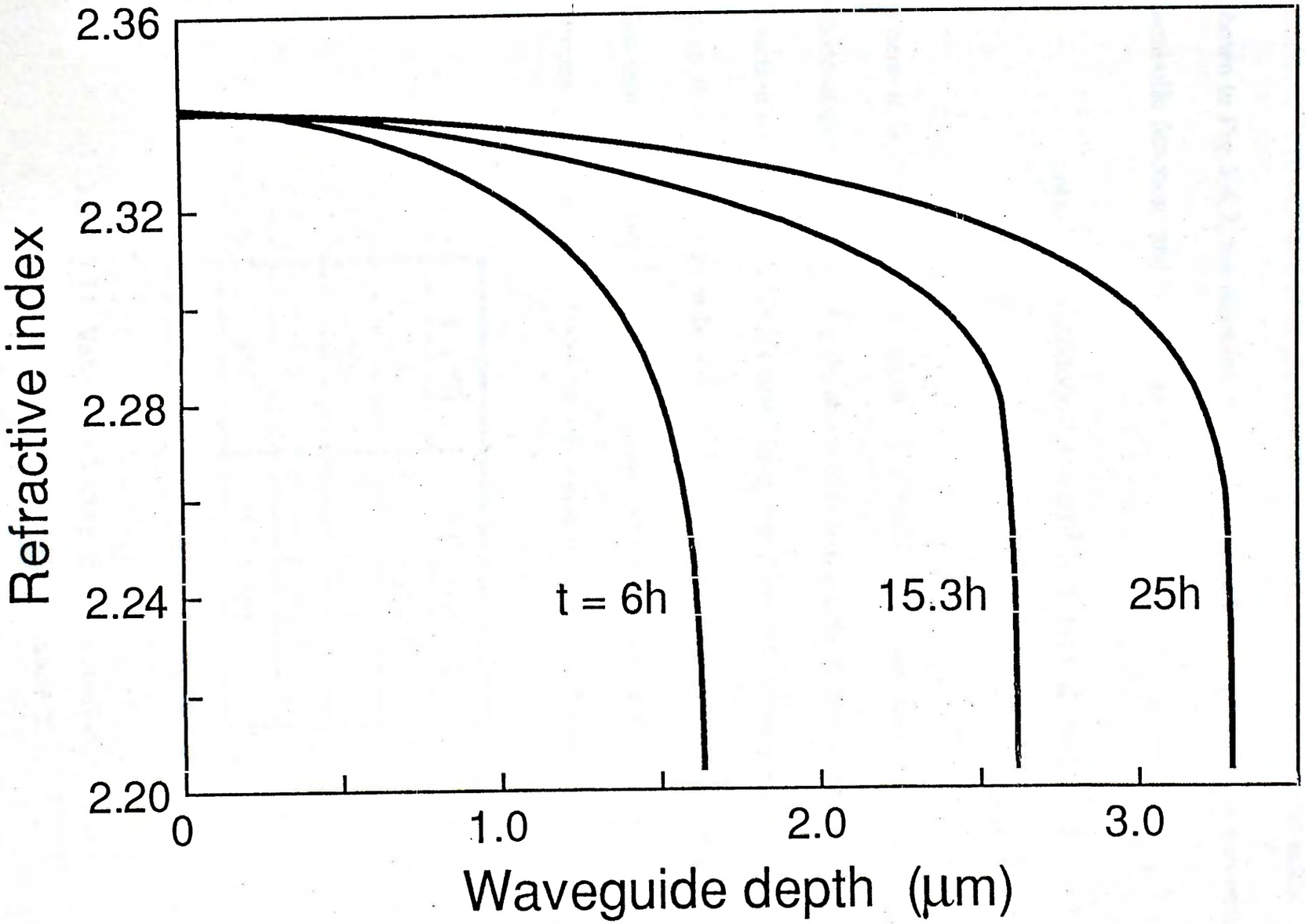

Fig.5.4.1 Refractive index profiles of PE waveguides using cinnamic acid (T = 200°C).

waveguide using cinnamic acid is a graded index function similar to that obtained using phosphoric acid, and is different from that of PE waveguide using other organic acids which has a step index profile. The maximum surface index change measured is 0.141, and is larger than values reported for other organic acids. As shown in Fig.5.4.2, the reconstructed index profile can be modelled by a truncated-parabolic function, and is given as

$$\begin{aligned} n(x) &= -0.0336(x/d + 0.05)^2 + 2.3411 \qquad \text{for } x < d \\ &= 2.202 \qquad\qquad\qquad\qquad\qquad\quad \text{for } x \geq d \end{aligned} \tag{5.14}$$

where d is the waveguide depth. Fig.5.4.3 shows the theoretically generated mode-dispersion curves using the above truncated-parabolic function and a step index function with $\Delta n_s = 0.129$ for best fitting, together with the measured data. There is an excellent agreement between theoretical curves using the truncated-parabolic function and experimental data, indicating that the truncated-parabolic index function proposed is an accurate model for PE waveguides using cinnamic acid.

T (°C)	D(T) ($\mu m^2 h^{-1}$)
180	0.329
200	0.579
235	1.145
258	1.555
265	1.695

Table 5.11 Values of effective diffusion coefficient D(T) at various exchange temperature T.

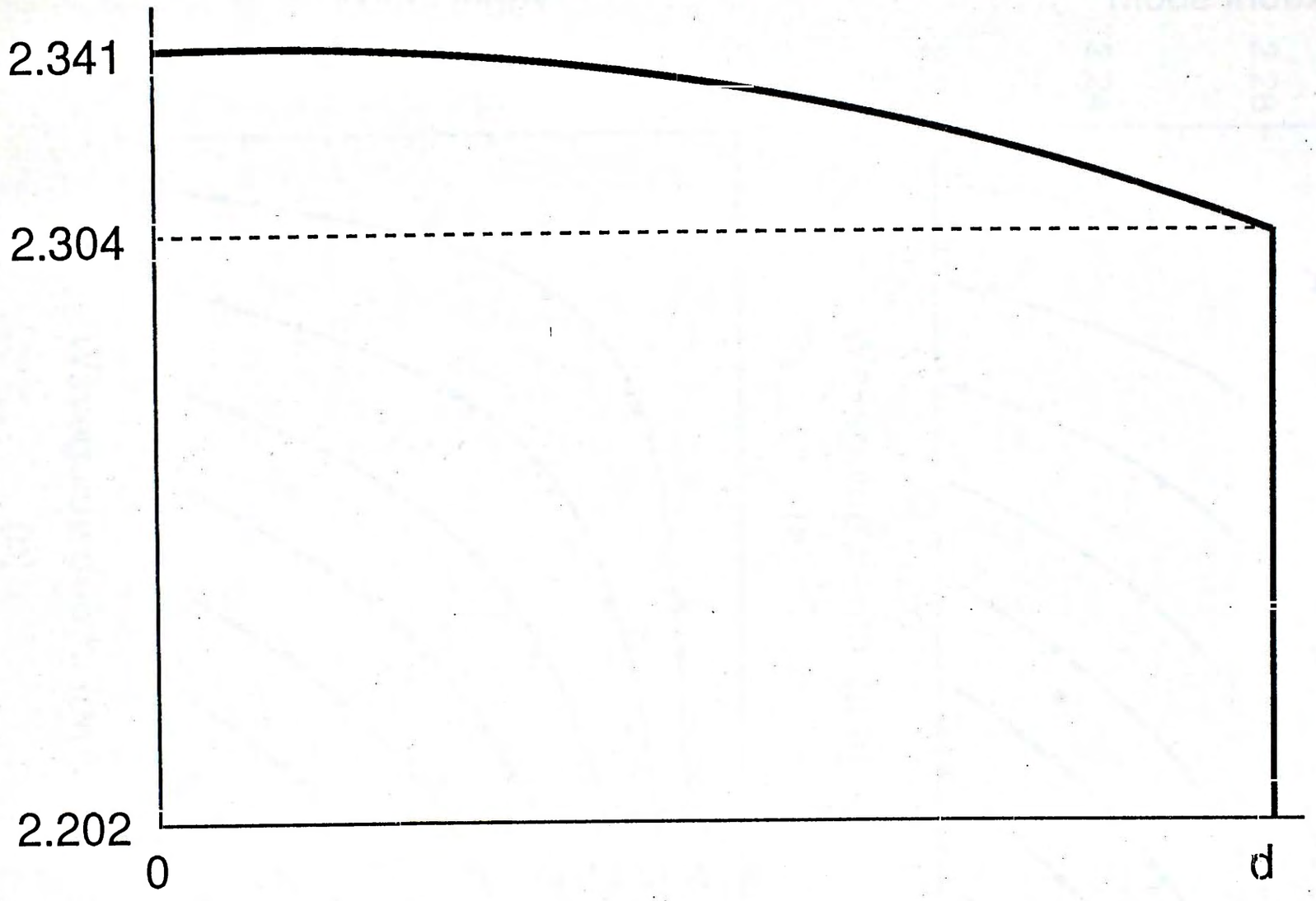

Fig.5.4.2 Truncated-parabolic index profile of PE waveguides using cinnamic acid.

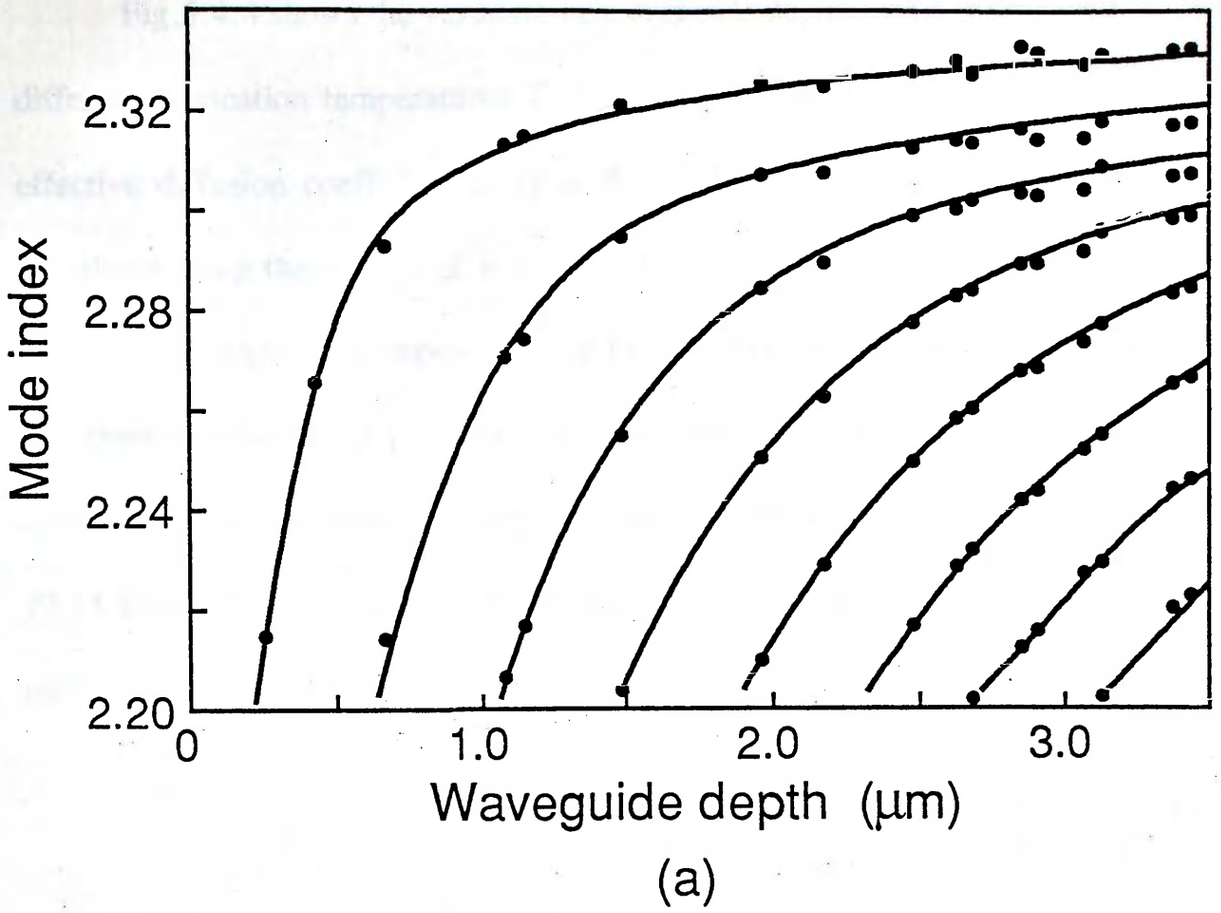

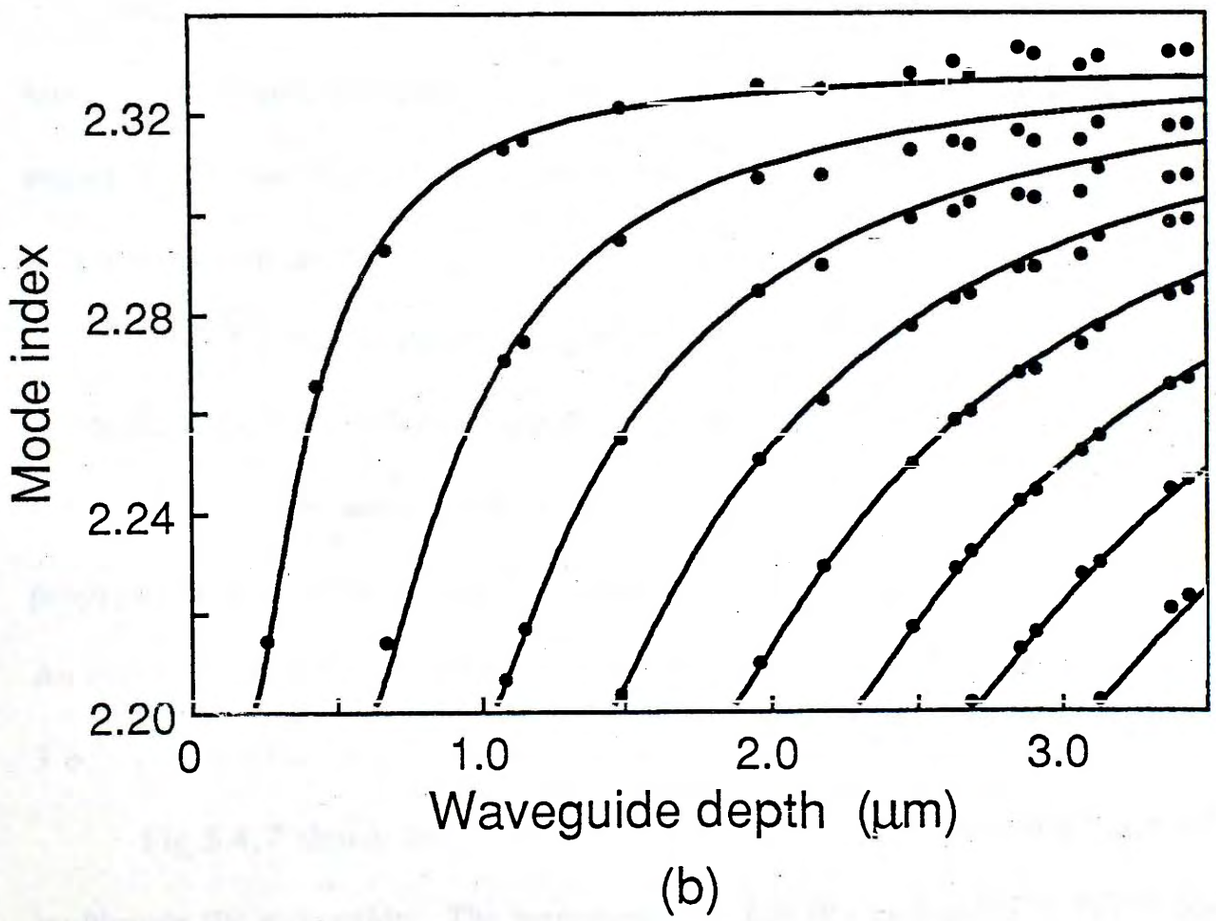

Fig.5.4.3 Theoretical mode-dispersion curves using (a) a truncated-parabolic index profile and (b) a step index profile together with measured data.

Fig.5.4.4 shows the variation of waveguide depth d with exchange time t for different fabrication temperatures T. Table 5.11 summarizes the measurement of effective diffusion coefficient $D(T)$ at five different temperatures, and $D(T)$ was calculated using the relation $d = [t \times D(T)]^{1/2}$.

The temperature dependence of D(T) follows the Arrhenius Law (Eq.5.5), and from the Arrhenius plot, i.e. $\ln[D(T)]$ versus $1/T$, the values of the diffusion constant D_o and activation energy Q were found to be 9.78×10^7 $\mu m^2 h^{-1}$ and 77.15 $kJmol^{-1}$, respectively. Hence the diffusion depth of a PE waveguide using cinnamic acid can be expressed as

$$d = 9.89 \times 10^3 \sqrt{t} \exp(-4.64 \times 10^3 / T) \quad \mu m \qquad (5.15)$$

Fig.5.4.5 shows the comparison of effective diffusion coefficient $D(T)$ as a function of exchange temperature T between cinnamic acid and benzoic acid. As expected, the rate of diffusion is slower for cinnamic acid because it is a weaker acid than benzoic acid.

Fig.5.4.6 shows the light intensity loss measurement for a single-mode waveguide before and after annealing. The propagation losses were typically less than 1 $dBcm^{-1}$ for unannealed samples. The annealing process reduces the propagation loss and the lowest value obtained in our experiment was 0.33 $dBcm^{-1}$. An initial exchange time of 15 minutes at 258°C was used. The annealing time was 3 hours at 350°C.

Fig.5.4.7 shows the variation of index profile with annealing time for a multimode PE waveguide. The waveguide was initially exchanged at 235°C for 2 hours (sample C1). The annealing temperature T_a was 350°C and the times t_a

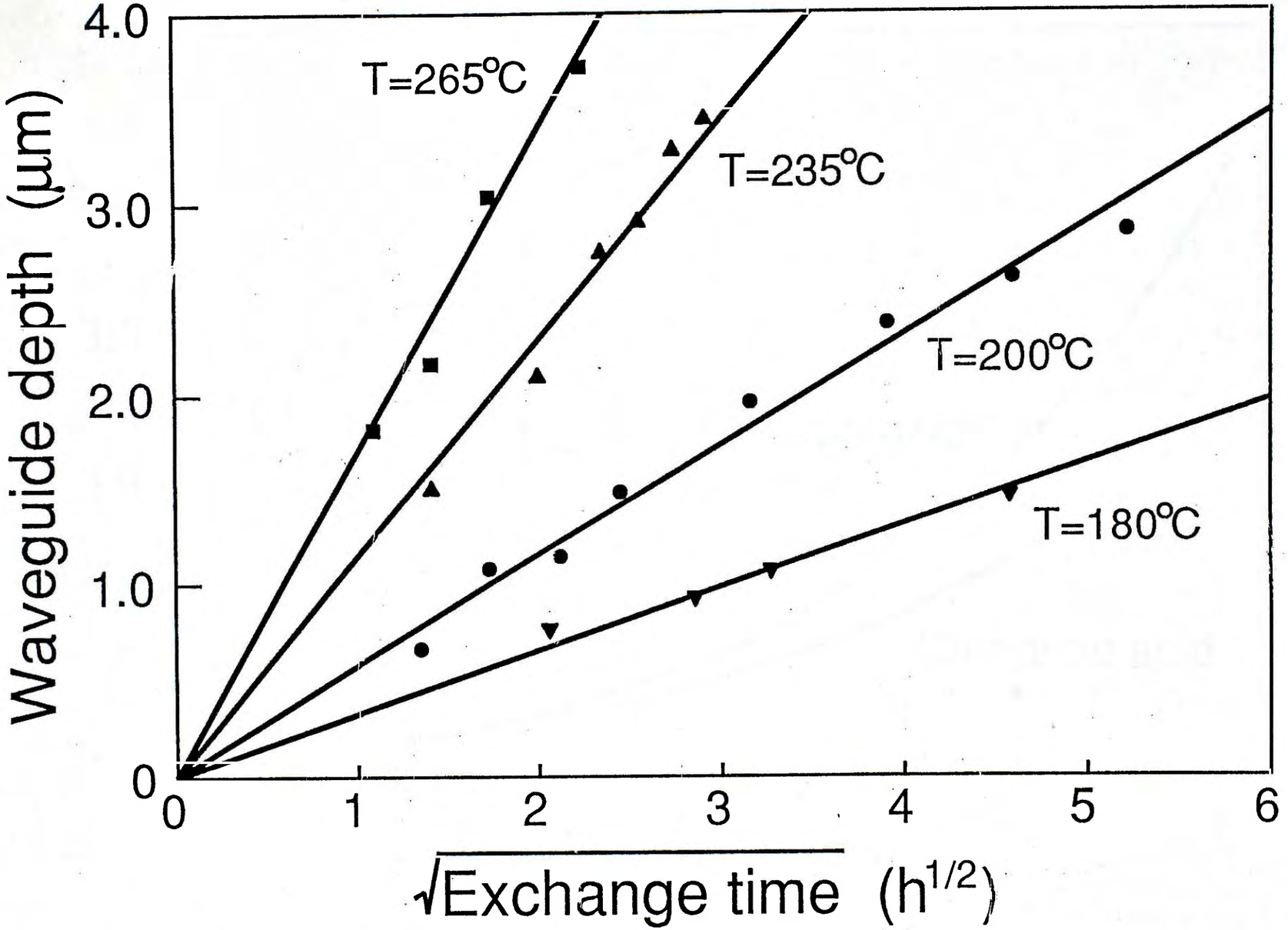

Fig.5.4.4 PE waveguide depth as a function of square root of exchange time.

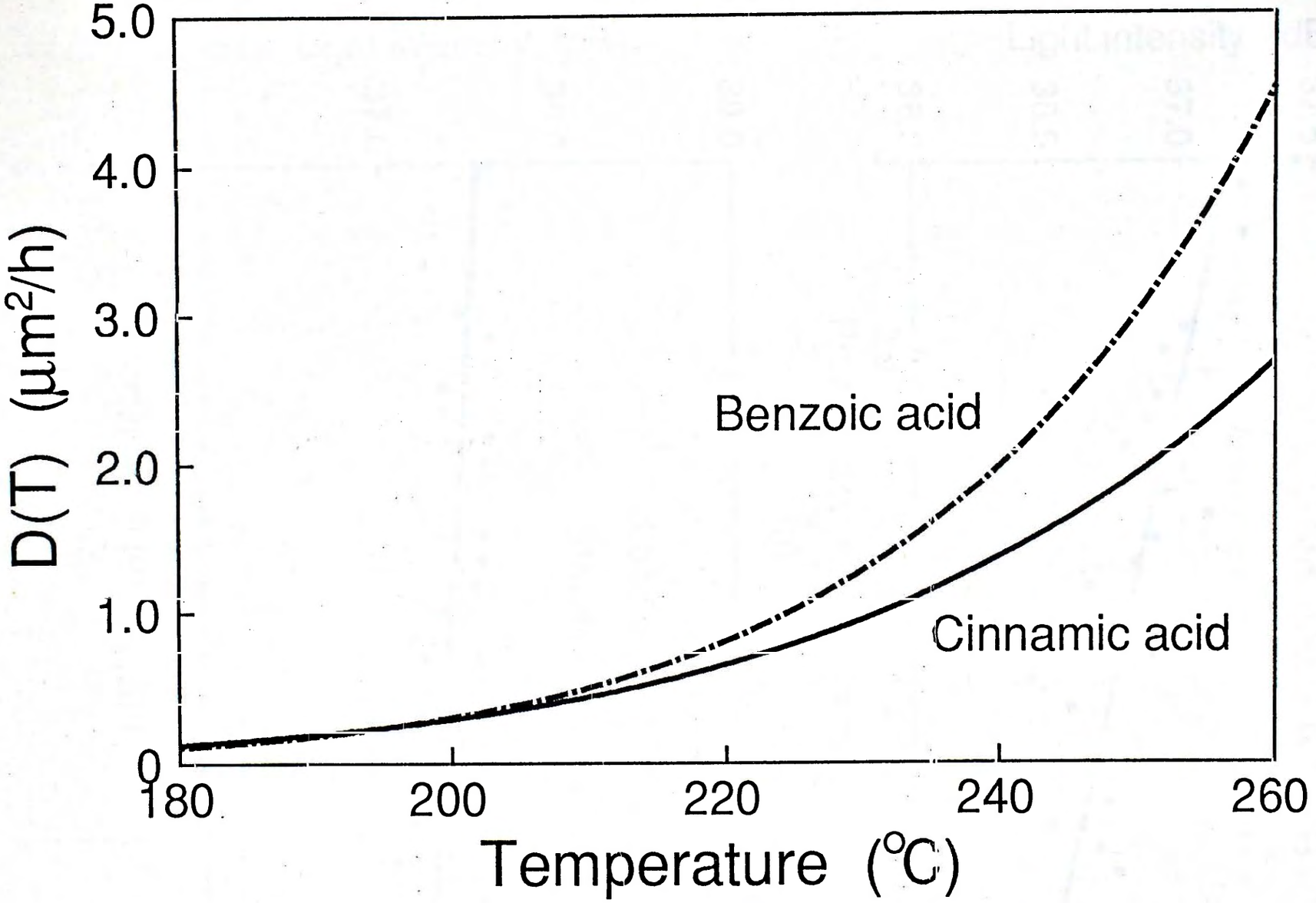

Fig.5.4.5 Temperature dependence of effective diffusion coefficient D(T) for cinnamic acid and benzoic acid.

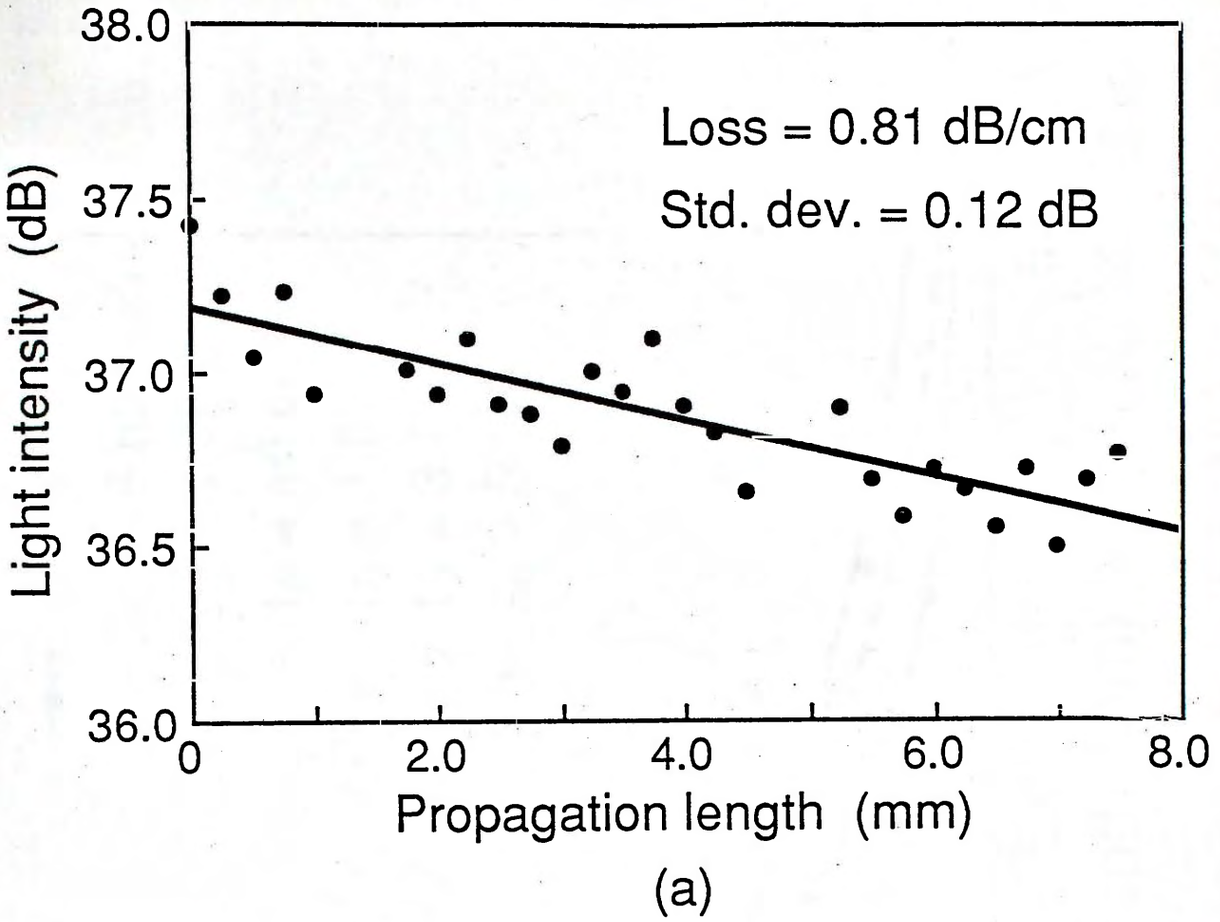

(a)

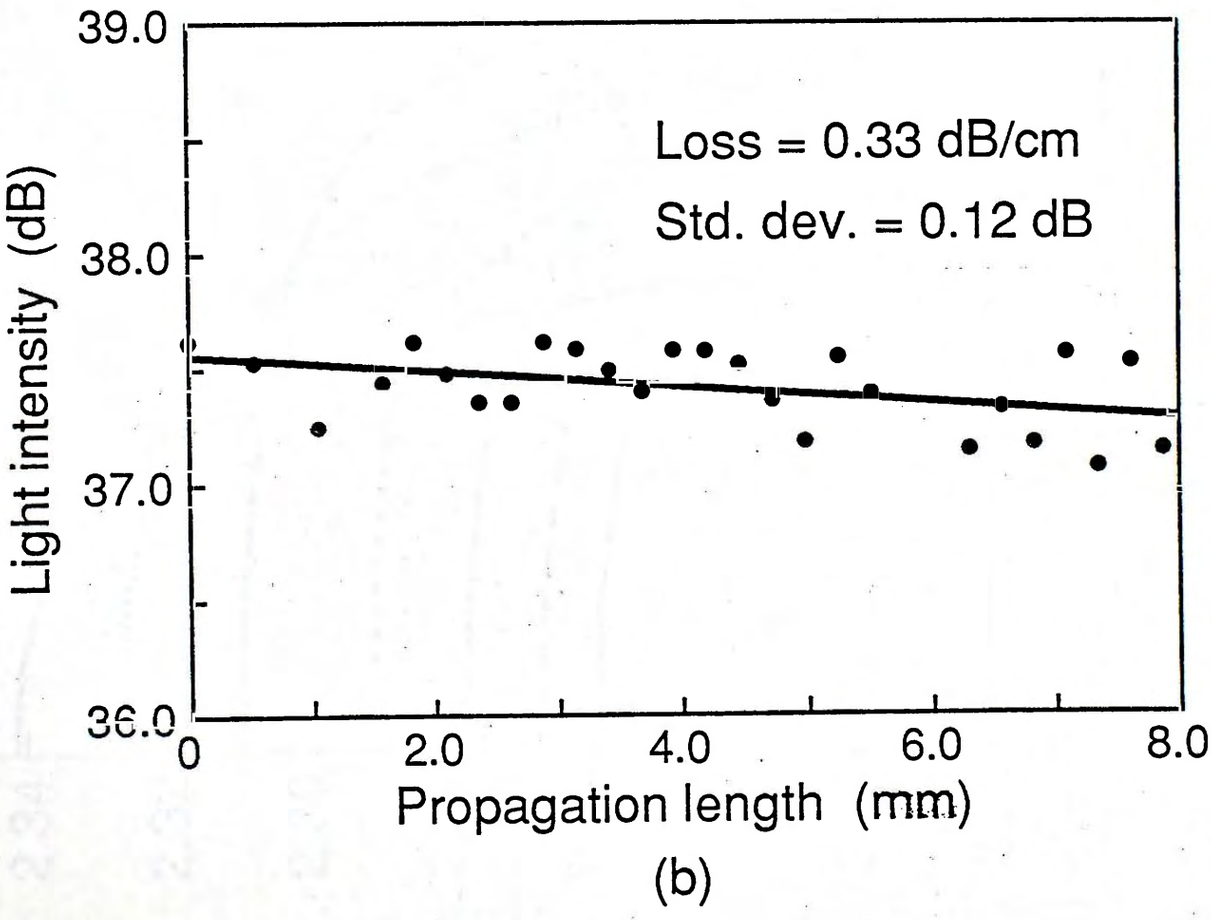

(b)

Fig.5.4.6 Propagation loss measurement of PE planar waveguide using cinnamic acid (T=258°C, t=15min). (a) Before annealing, (b) after annealing (T_a=350°C, t_a=3h).

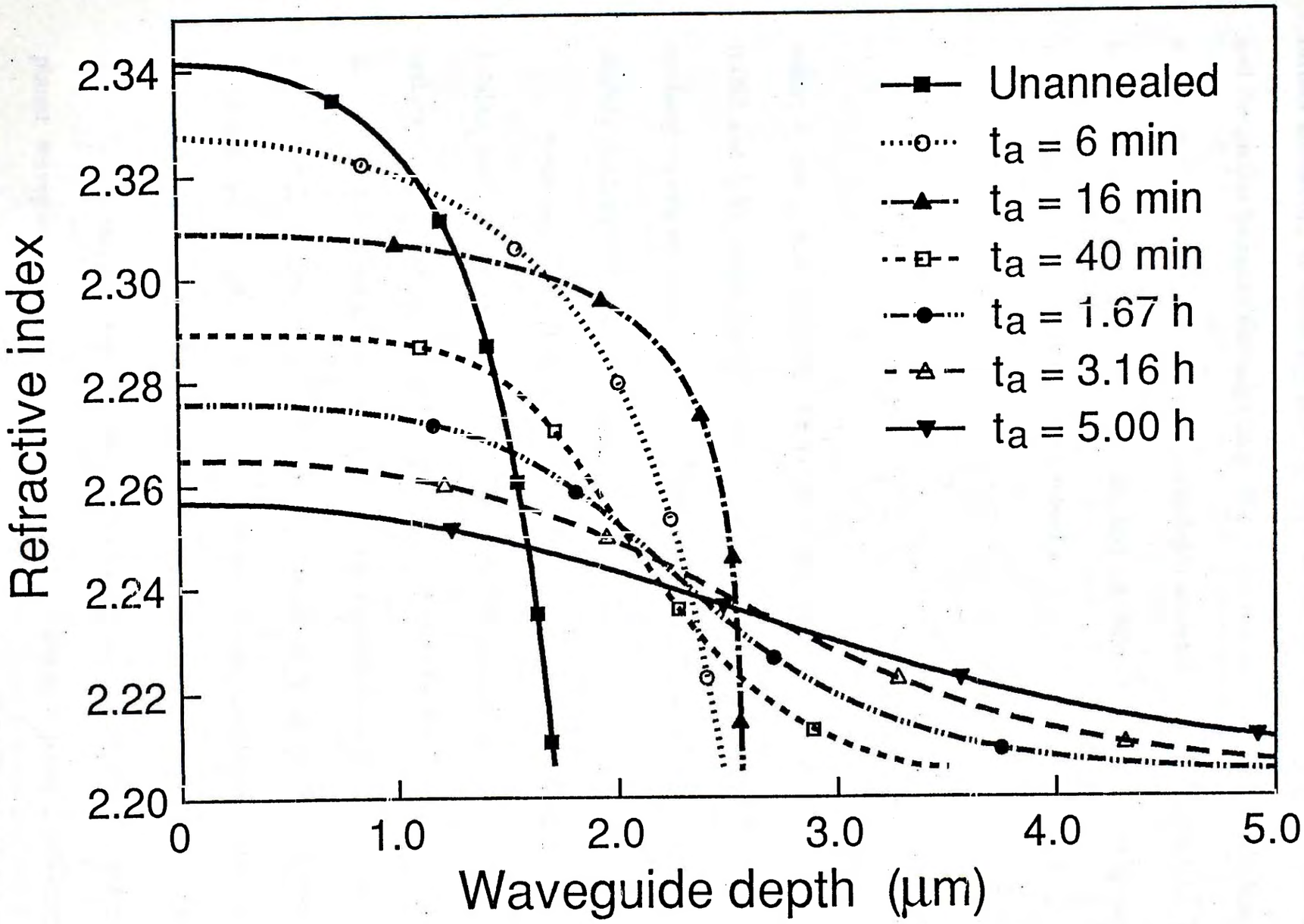

Fig.5.4.7 Index profile of PE waveguide as a function of annealing time t_a (T = 235°C, t = 2 h, T_a = 350°C).

varied from 6 minutes to 5 hours. The index profile changes from a truncated-parabolic function to a step function after an annealing time of 16 minutes. With further annealing, an index tail starts to form at the waveguide-substrate boundary and the profile becomes Gaussian-like. Fig.5.4.8 shows the effect of annealing on surface index change Δn_s and waveguide depth increase Δd for sample C1. The linear dependence indicates that both Δn_s and Δd follow a power-law relationship with annealing time t_a, and can be expressed as

$$\Delta n_s = c_1 t_a^{-0.2} \tag{5.16}$$

$$\Delta d = c_2 t_a^{0.41} \tag{5.17}$$

where c_1 and c_2 are constants. From our measured data, c_1 and c_2 have values of 0.082 and 1.81, respectively. Other waveguides prepared using different initial exchange times and temperatures exhibit similar curves after annealing, but with slightly different values of c_1 and c_2.

Proton-exchanged channel waveguides have also been fabricated in z-cut $LiNbO_3$ using cinnamic acid. The sample was exchanged at 200°C for 30 minutes, and annealed in flowing O_2 ($500cm^3min^{-1}$) at 350°C for 15 minutes. The waveguides fabricated were 10mm long, and the waveguide width varied from 2μm to 10μm in 2μm steps. The waveguides were single-mode in the depth direction at 0.6328μm wavelength. The number of lateral modes supported depend on the waveguide width, and the results are summarized in Table 5.12.

The mode indices of the channel waveguides were evaluated from that of the planar waveguide fabricated under the same condition. From prism-coupling measurement the mode index of this planar waveguide was 2.2178. Fig.5.4.9 shows

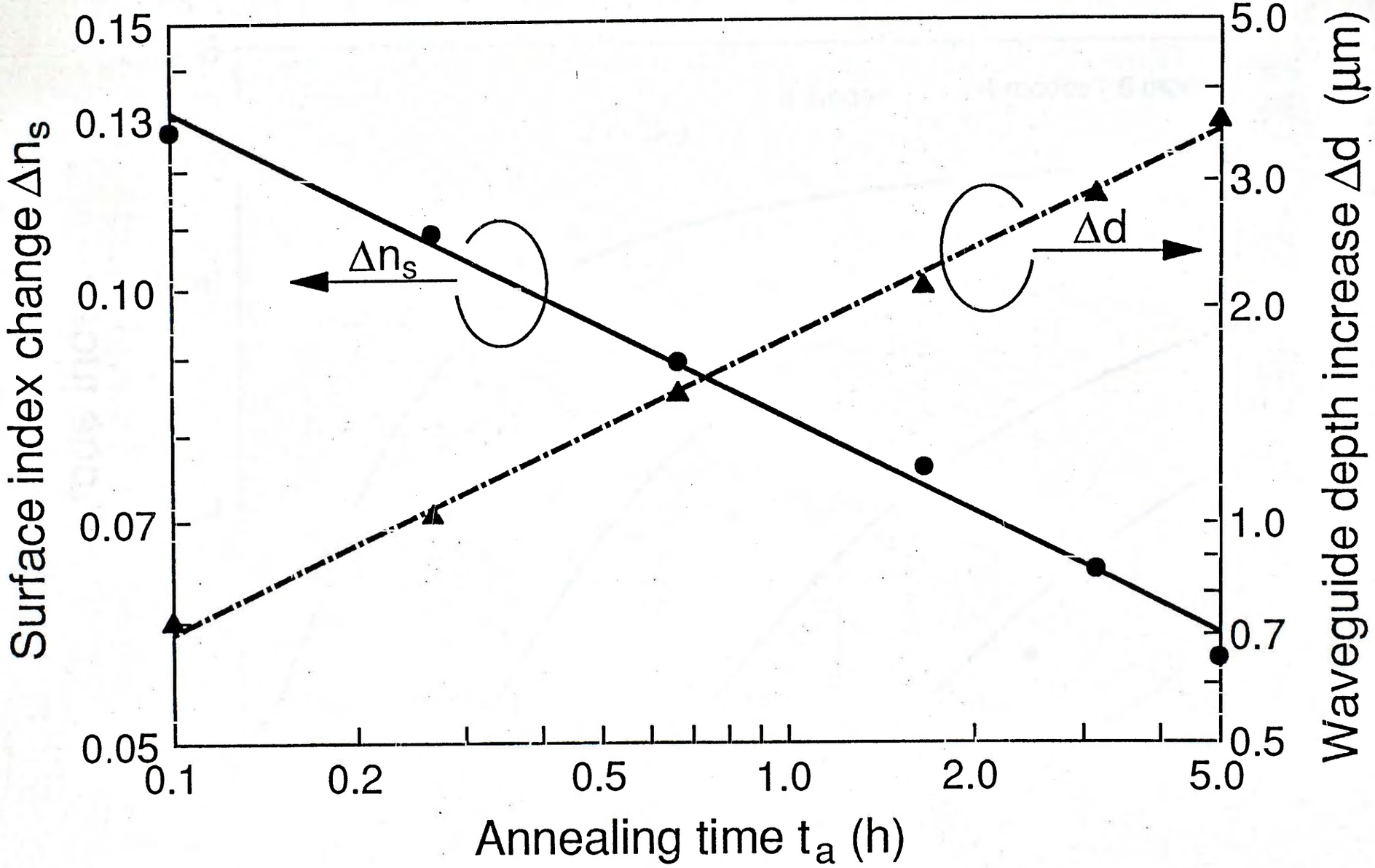

Fig.5.4.8 Surface index change Δn_s and waveguide depth increase Δd as a function of annealing time t_a.

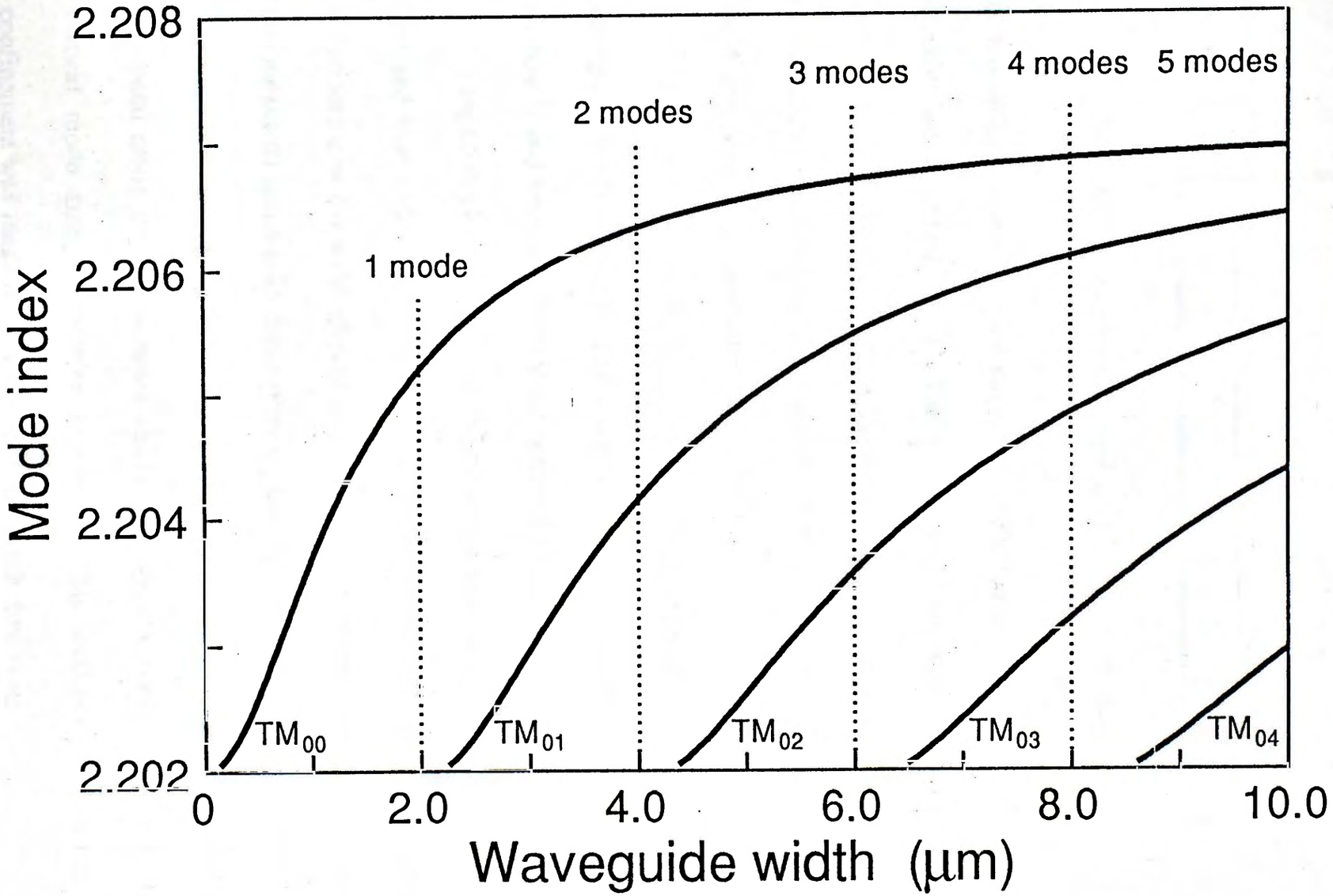

Fig.5.4.9 Mode effective index as a function of waveguide width for a step-index channel waveguide using effective index method (n_{core} = 2.2178, n_{sub} = 2.202, d = 1 μm, λ = 0.6328 μm).

Waveguide width (μm)	No. of lateral modes
2	1
4	2
6	3
8	4
10	5

Table 5.12 Number of lateral modes versus PE stripe width.

the theoretical mode-dispersion curves as a function of waveguide width using the effective index method [5.21]. The waveguide is assumed to have a rectangular cross-section with a core index of 2.2178 and a depth of 1 μm. The number of modes calculated for channel waveguides with 2μm, 4μm, 6μm, 8μm and 10μm width agrees with our measured data.

Fig.5.4.10 shows the propagation loss measurement of a 10μm wide channel waveguide (λ=0.6328μm). The channel waveguide losses were typically around 1 dBcm^{-1}, and were similar to those obtained using toluic and stearic acids.

Figs.5.4.11 to 5.4.14 show the measured near-field intensity profiles for the 2μm and 4μm wide channel waveguides. As expected, the mode-field distribution is symmetric in the width direction and slightly asymmetric in the depth direction. The measured mode-field dimensions w_d and w_l, where intensity falls to $1/e$ of its maximum value, were plotted in Fig.5.4.15 as a function of waveguide width. The horizontal mode size w_l increases almost linearly with waveguide width, and the vertical mode size w_d remains invariant. This indicates that strong modal confinement was realized in both width and depth directions.

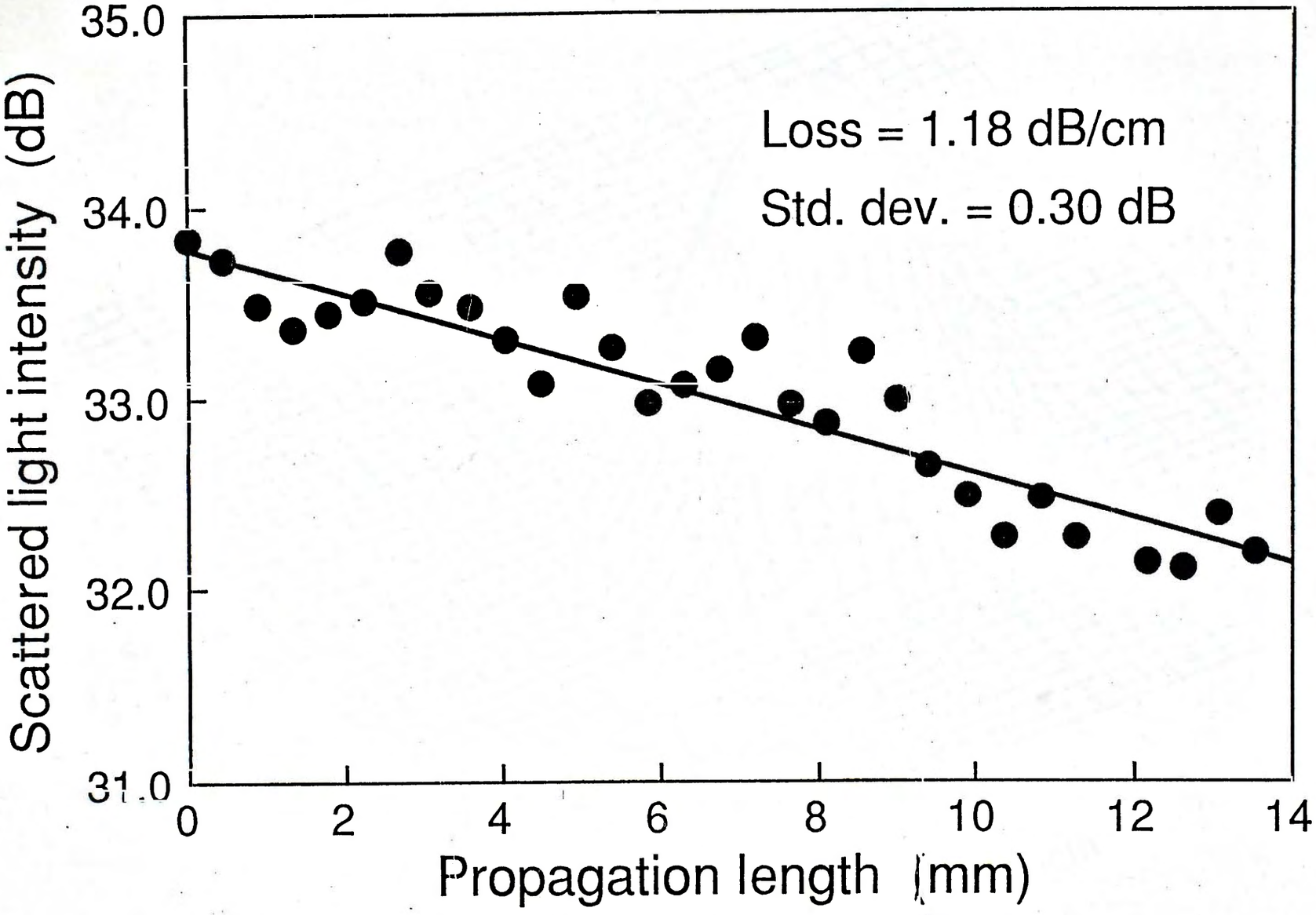

Fig.5.4.10 Propagation loss measurement of a 10μm wide PE channel waveguide using cinnamic acid (λ = 0.6328μm).

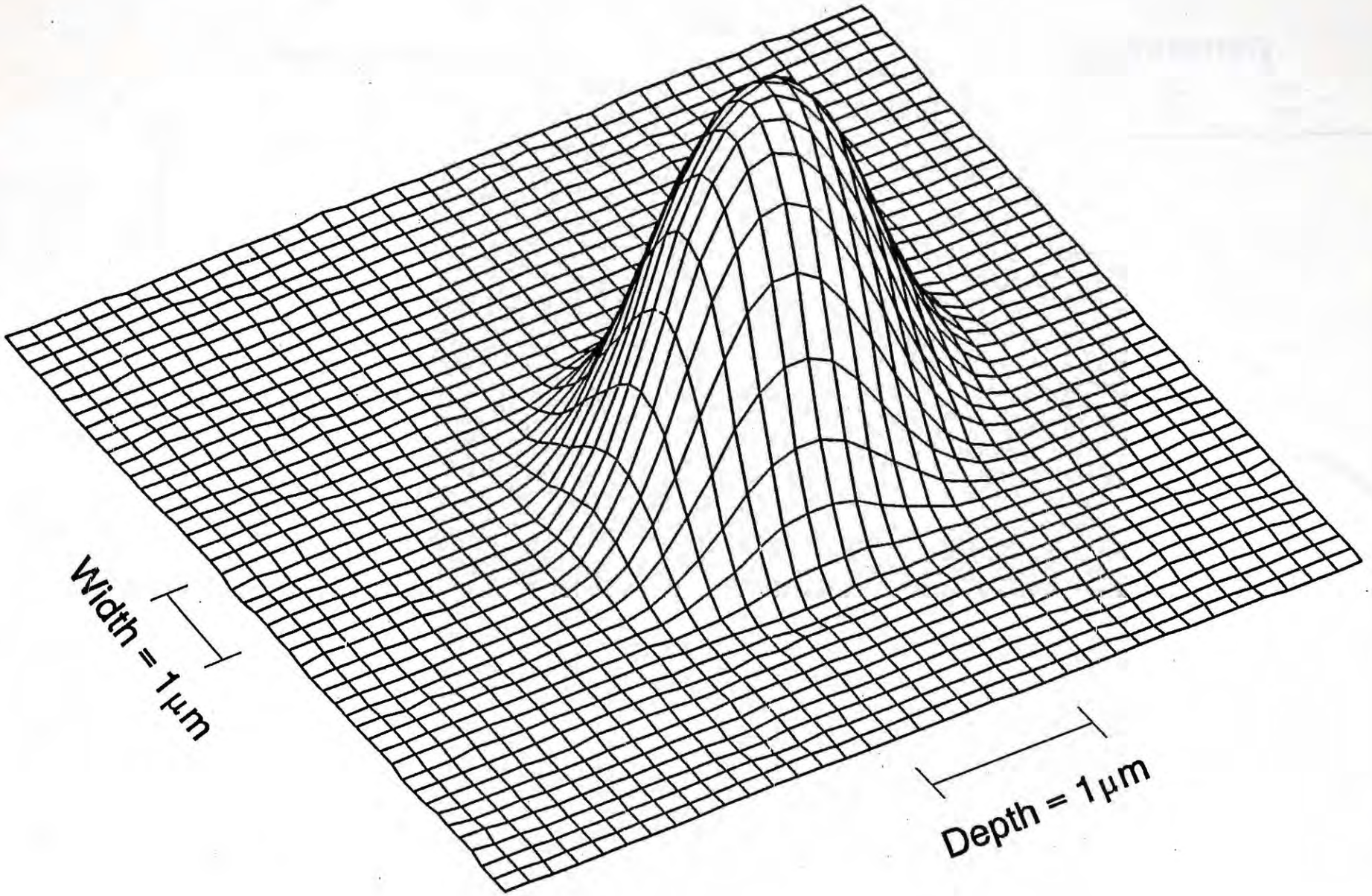

Fig.5.4.11 Near-field intensity profile of a single-mode PE channel waveguide of 2μm width at 0.6328μm wavelength.

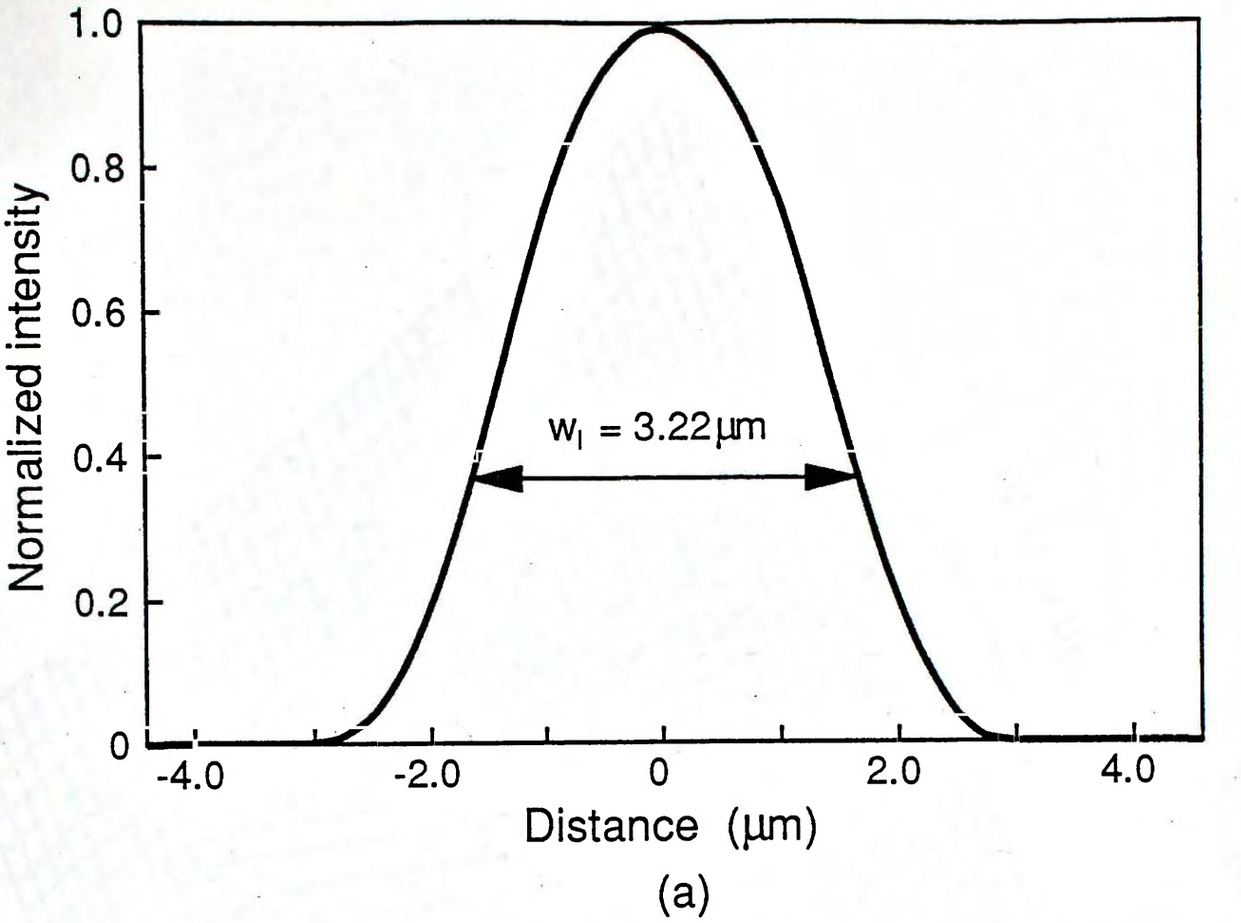

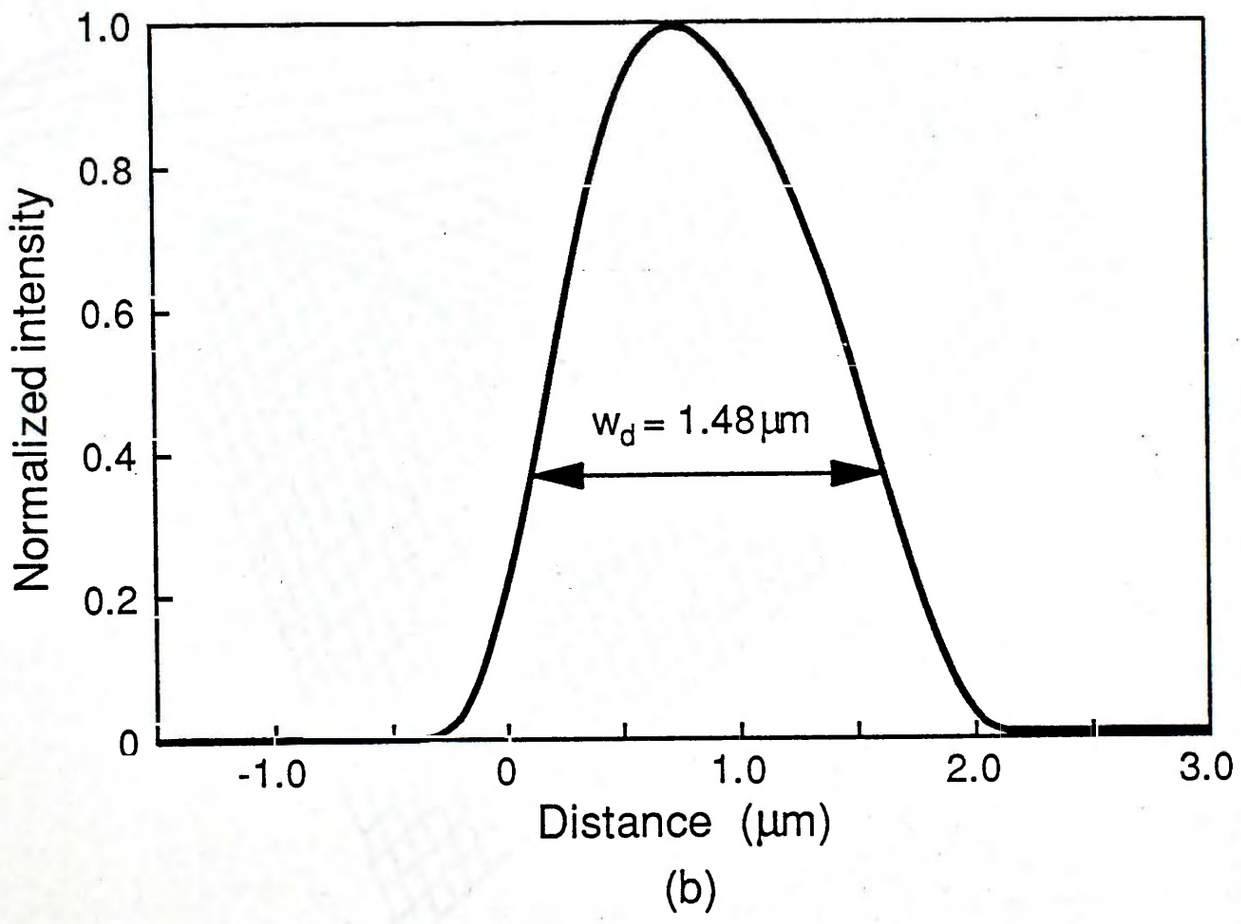

Fig.5.4.12 Near-field intensity profile along (a) width and (b) depth direction for a 2μm wide channel waveguide using cinnamic acid.

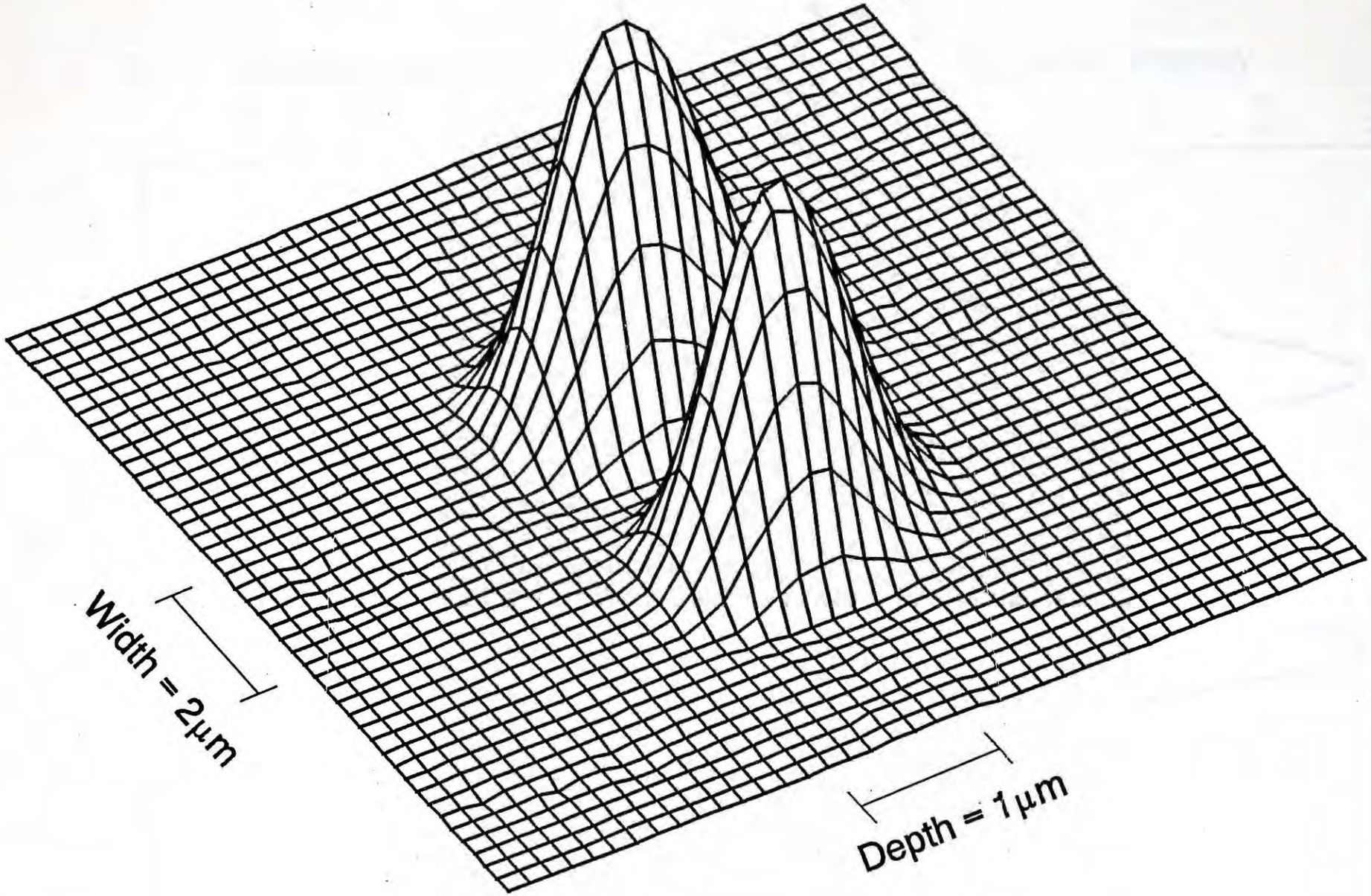

Fig.5.4.13 Near-field intensity profile of a 4μm wide PE channel waveguide using cinnamic acid (λ = 0.6328μm).

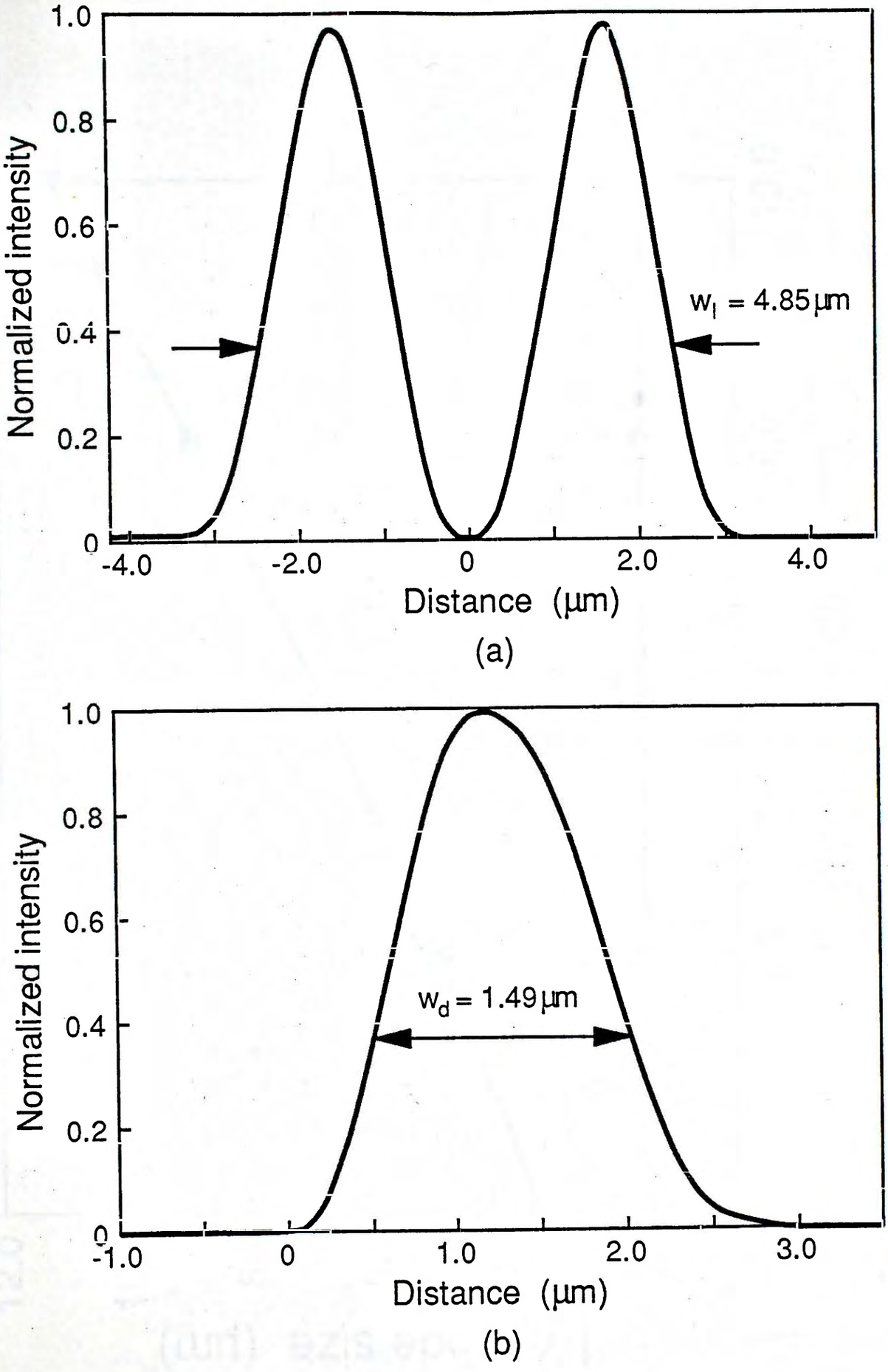

Fig.5.4.14 Near-field intensity profile along (a) width and (b) depth direction for a 4μm wide channel waveguide using cinnamic acid.

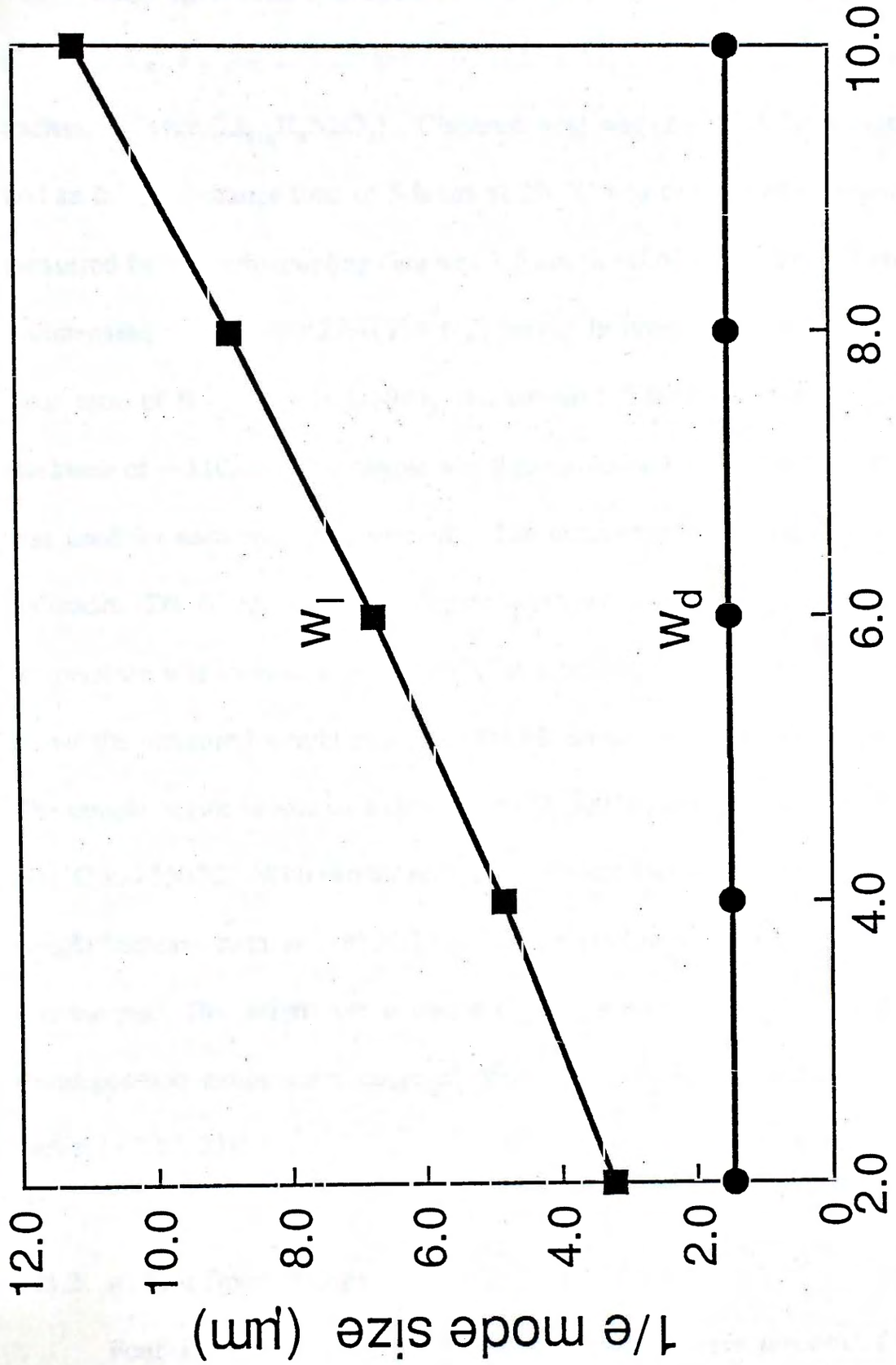

Fig.5.4.15 1/*e* width w_l and depth w_d of the near-field intensity profile as a function of waveguide width.

5.5 Structural Characteristics of Proton-exchanged Waveguides

5.5.1 Thermogravimetric Analysis

Thermogravimetric analysis (TGA) was performed on a highly multimode (TM_0 - TM_8) PE planar waveguide to confirm the presence of H^+ in the proton-exchanged layer ($Li_{1-x}H_xNbO_3$). Cinnamic acid was chosen as the proton source, and an initial exchange time of 5 hours at 250°C was used. The waveguide depth measured from prism-coupling data was 3.6 μm (λ=0.633μm). The PE sample has a dimension of 16.9(X)×27.4(Y)×1(Z) mm^3. In order to increase the molecular mass ratio of H^+ to virgin $LiNbO_3$, the sample (-Z face) was polished down to a thickness of ~110μm. The sample was then pulverized and a weight of 15 to 45mg was used for each run of experiment. The measurement was carried out using a Shimadzu DT-40 thermal gravimetric analyzer under nitrogen purge. The temperature was increased up to 800°C at a heating rate of 5°Cmin^{-1}. Fig.5.5.1 shows the measured weight change of the PE sample as a function of temperature. The sample begins to lose its weight at around 500°C, and the loss is rapid between 500°C and 550°C. With further heating the weight loss slows down and the sample weight becomes static at ~650°C. A total weight loss of 1.38% was measured for this sample. The weight loss is due to dehydration of $Li_{1-x}H_xNbO_3$ and a similar decomposition temperature range of 350-550°C has been reported by Rice and Jackel [5.22,5.23].

5.5.2 Raman Spectroscopy

Four PE planar waveguides in z-cut $LiNbO_3$ were prepared for Raman spectroscopy measurement. The fabrication conditions and waveguide parameters

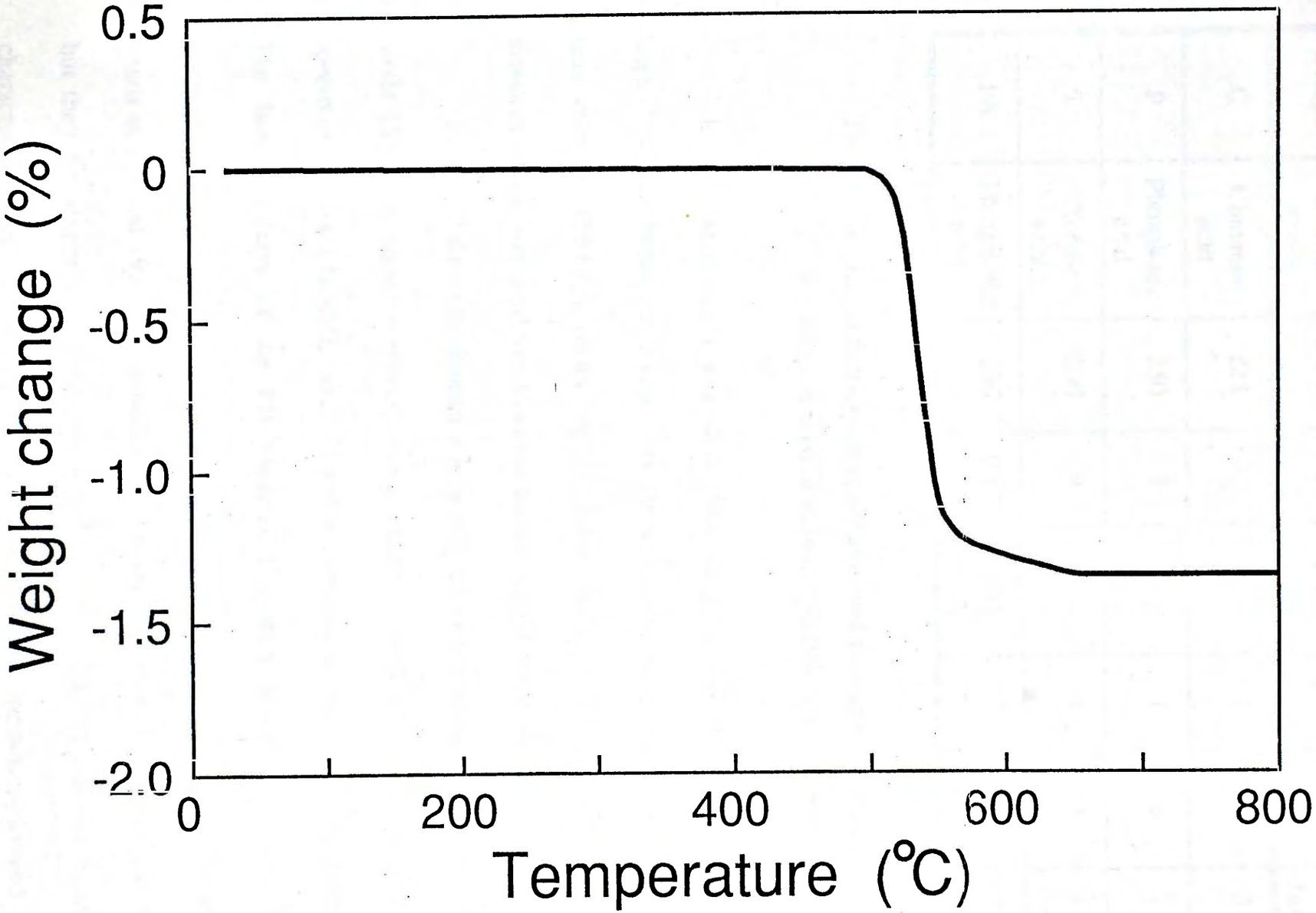

Fig.5.5.1 Thermogravimetric analysis measurement of a PE waveguide using cinnamic acid (T = 250°C, t = 5 h).

of these PE samples are summarized in Table 5.13.

Sample	Proton source	T (°C)	t (h)	T_a (°C)	t_a (h)	No. of modes	d (μm)
C	Cinnamic acid	235	7.5	200	1	9	3.4
P	Phosphoric acid	250	2	200	1	6	2.6
T	Toluic acid	200	9	200	1	4	1.6
PA	Phosphoric acid	250	0.67	300	7	7	3.0

Table 5.13 Initial fabrication conditions and waveguide parameters for samples used in Raman spectroscopy measurement.

Raman spectroscopy was carried out using the 647.1nm line of a krypton laser. The laser beam was coupled into the waveguide along the crystallographic x-axis using a $PbMoO_3$ prism (n_o = 3.386 at λ = 647.1nm). A double monochromator was used to collect the Raman signal along z-axis.

Fig.5.5.2 shows the Raman spectra of the PE waveguides for the fundamental mode (TM_0) in x(zx)z scattering configuration. Fig.5.5.3 shows the reference spectrum for virgin $LiNbO_3$ obtained with a conventional 90° scattering geometry. The Raman spectra of the PE waveguides contain several additional bands superimposed on the sharp bands in the spectrum of the virgin crystal. The narrow bands at 127 and 192cm^{-1} are well defined in the spectrum of sample C, P and T, but they are absent in the strongly annealed sample PA. These two bands are characteristics of the equilibrium state of β-phase proton-exchanged layer ($Li_{1-x}H_xNbO_3$) [5.24]. Moreover, a new strong band at 69cm^{-1} emerges in the

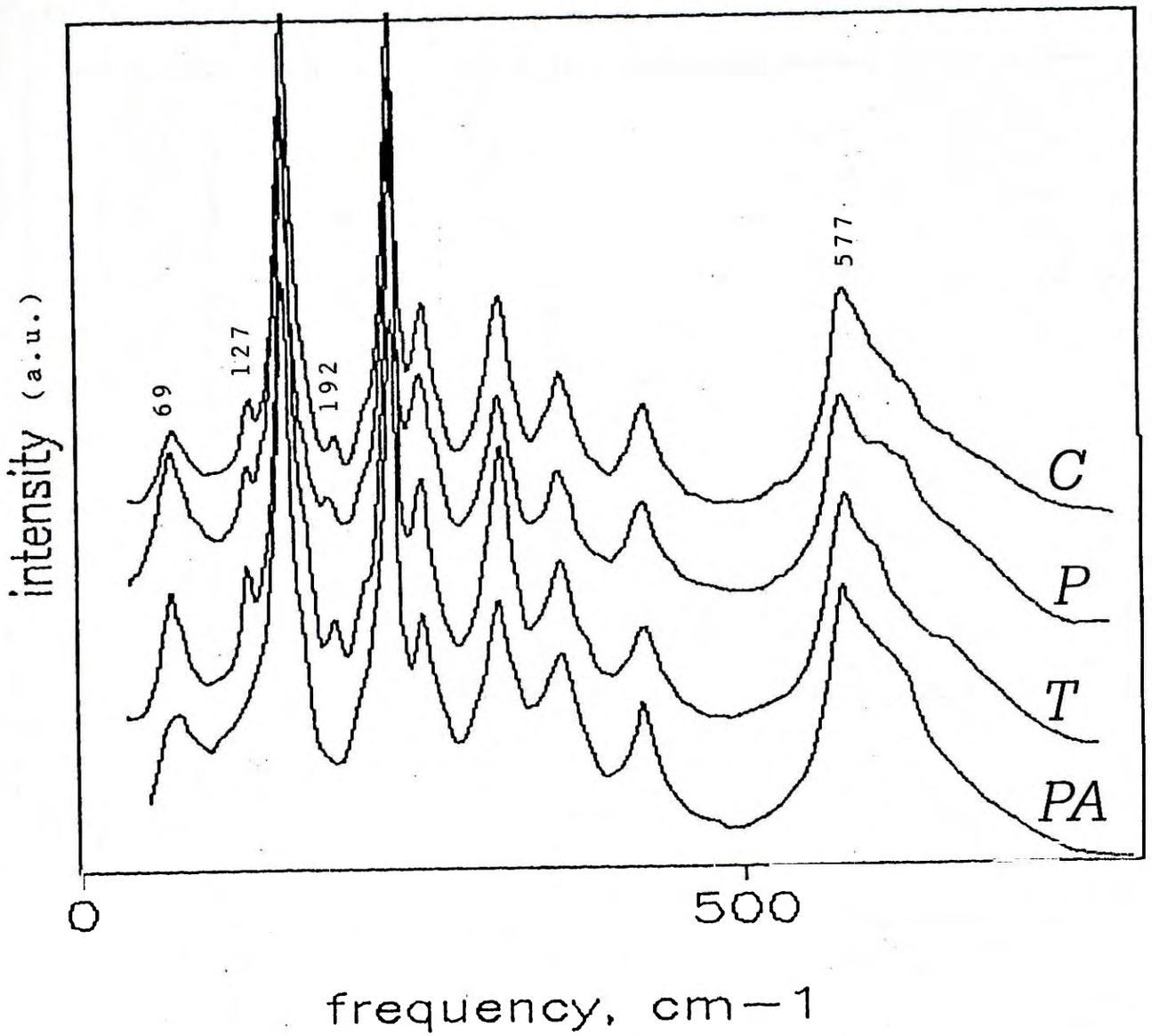

Fig.5.5.2 Raman spectra of proton-exchanged planar waveguides for the fundamental mode (λ = 647.1nm).

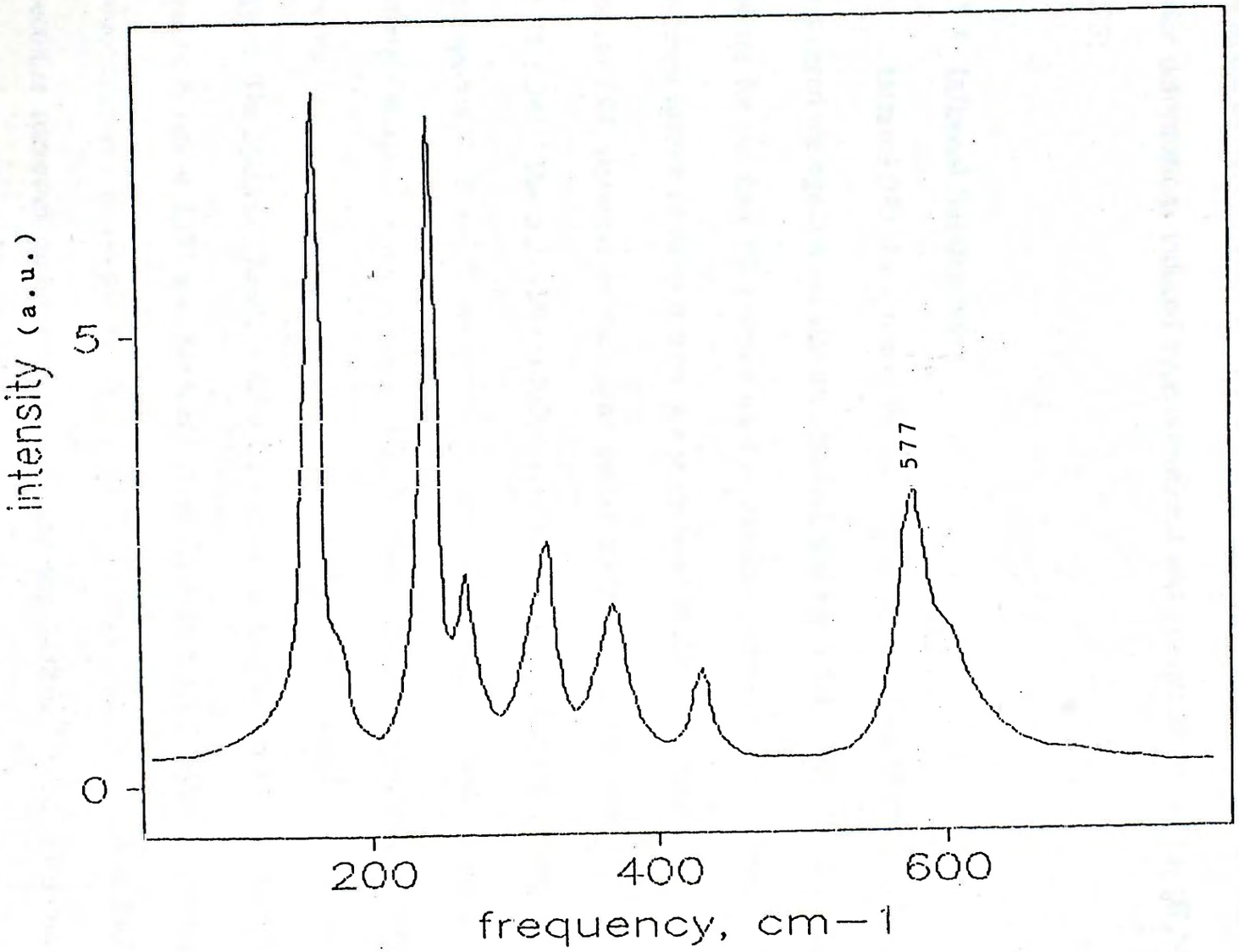

Fig.5.5.3 Raman spectrum of virgin z-cut $LiNbO_3$ obtained with the 90°-scattering geometry.

Raman spectra of all these four PE waveguides. This characteristic band corresponds to the normal lattice vibration of $Li_{1-x}H_xNbO_3$, and its intensity depends on the extent of H^+/Li^+ exchange (i.e. H^+ concentration x) [5.25]. Furthermore, the spectra of the PE waveguides exhibit a broader band at $577cm^{-1}$ compared to that in the reference spectrum. These changes in the Raman spectrum are due to the lattice deformations induced by substitutional and interstitial H^+ in $Li_{1-x}H_xNbO_3$ [5.25].

5.5.3 Infrared Spectrometry

Infrared (IR) absorption of the hydroxyl (OH) stretching vibrations in proton-exchanged waveguides has also been studied, and Fig.5.5.4 shows the IR absorption spectra for the four PE samples used in Raman spectroscopy measurement. The common feature of these spectra is a sharp band at about $3500cm^{-1}$. This band is due to OH vibration in the plane perpendicular to the crystallographic z-axis [5.23,5.26]. The full-width at half-maximum (FWHM) of the absorption band in the spectra C, P and T are nearly the same and relatively small ($30cm^{-1}$). The strongly annealed sample PA has a larger FWHM ($50cm^{-1}$), indicating a change of the state of OH bond (i.e. displacement of H^+) in the annealed proton-exchanged layer. The $3500cm^{-1}$ bands of these IR spectra can be decomposed into two closely spaced bands at 3507 and $3488cm^{-1}$ (Figs.5.5.5 to 5.5.8). With increasing H^+ concentration x in sample PA, T, P and C, the high frequency band at $3507cm^{-1}$ becomes narrower and gains intensity, and the $3488cm^{-1}$ band splits into two components (3494 and $3478cm^{-1}$) in spectrum T, P and C. These three bands (3507, 3494 and $3478cm^{-1}$) correspond to the OH vibrations in β-phase

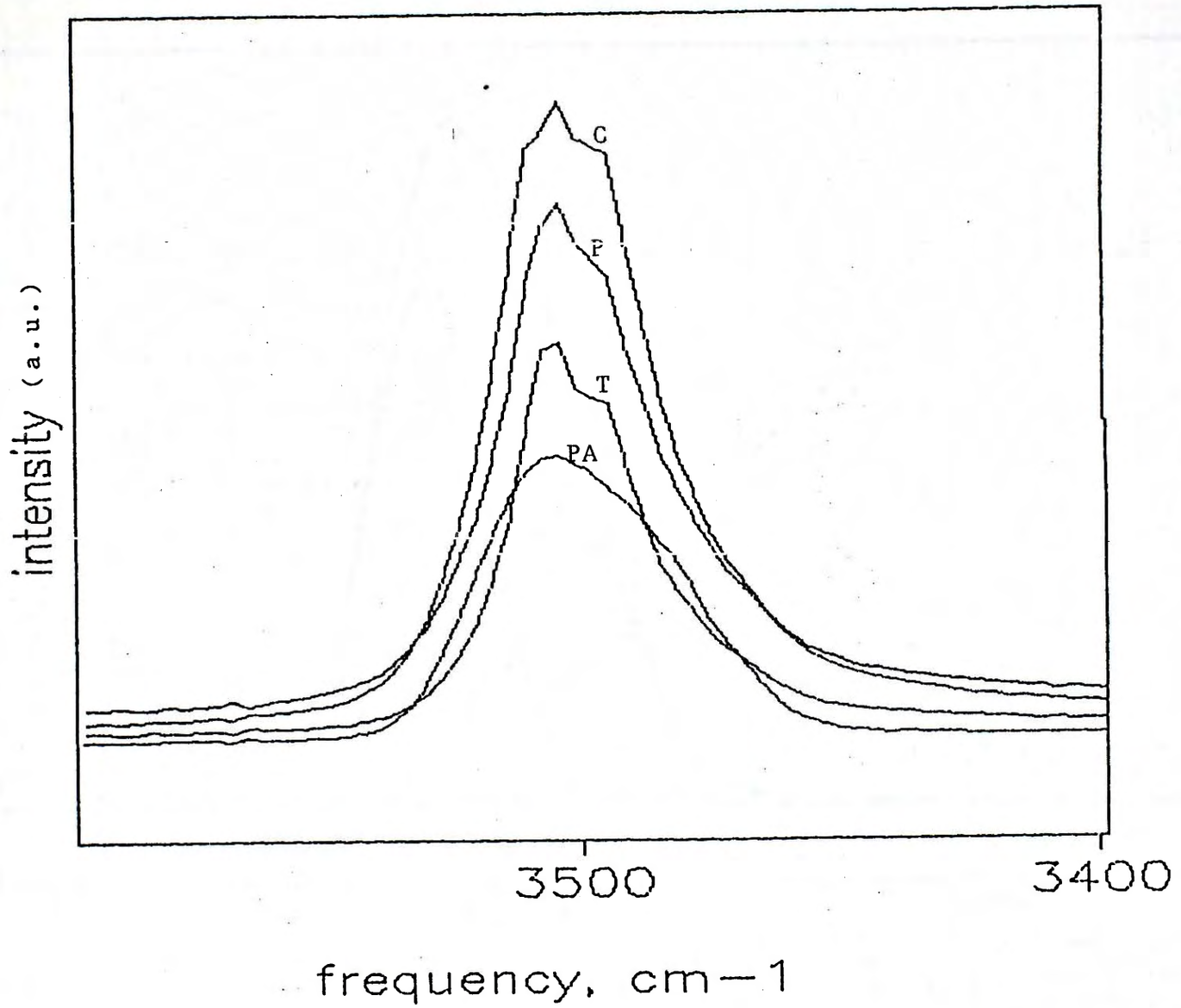

Fig.5.5.4 Infrared absorption spectra of proton-exchanged planar waveguides using different proton sources.

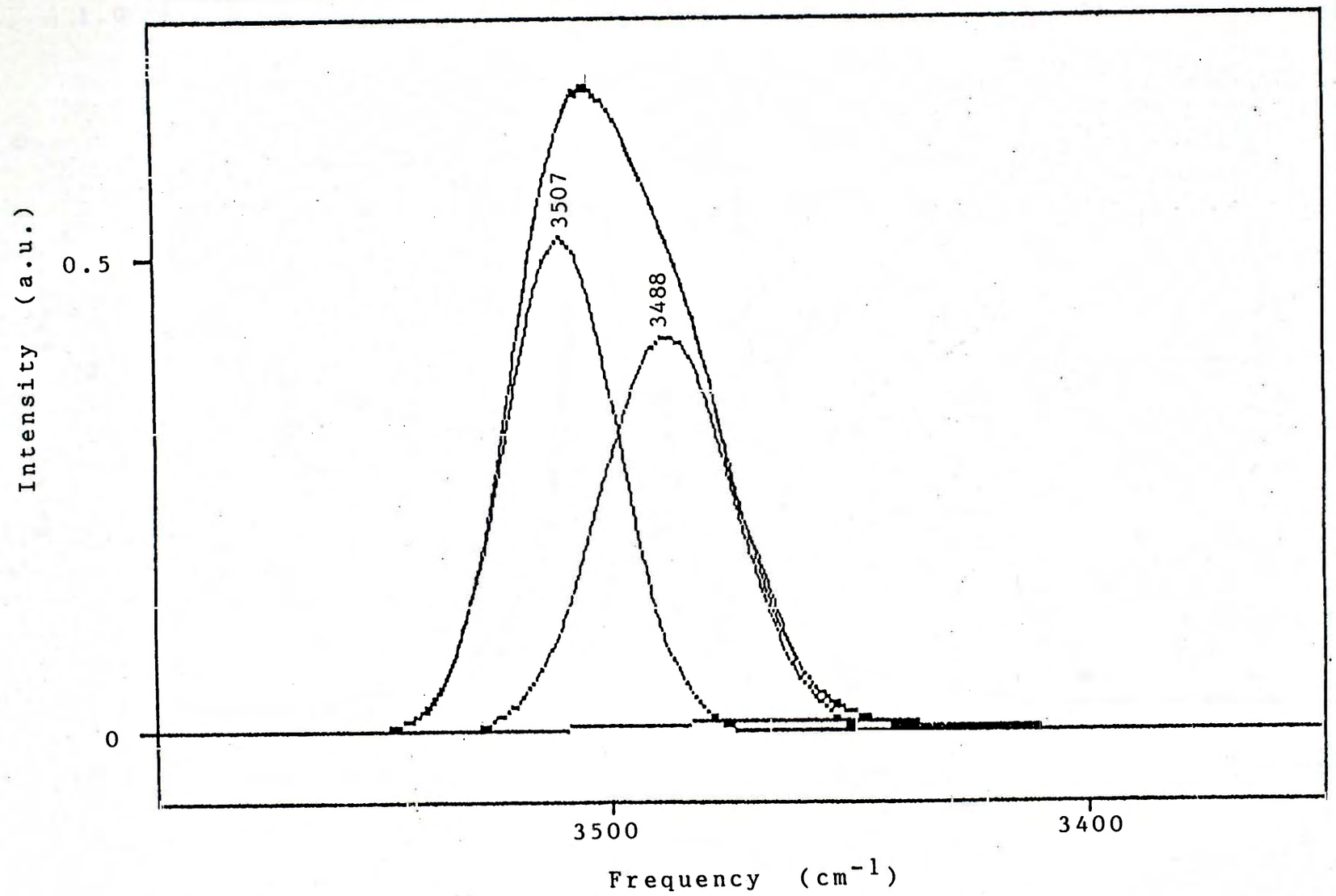

Fig.5.5.5 Infrared absorption spectrum of an annealed proton-exchanged planar waveguide using phosphoric acid (sample PA).

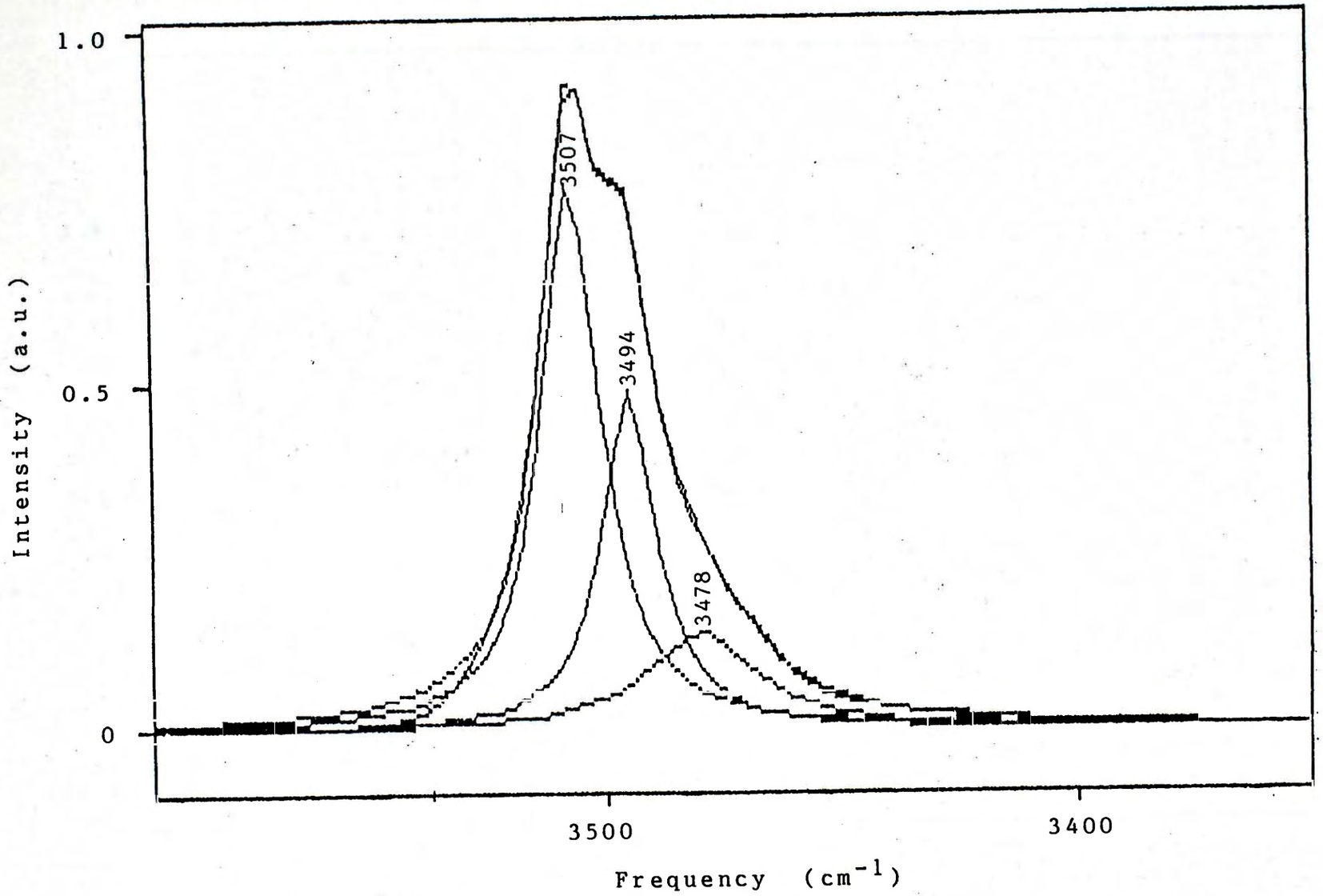

Fig.5.5.6 Infrared absorption spectrum of a proton-exchanged planar waveguide using toluic acid (sample T).

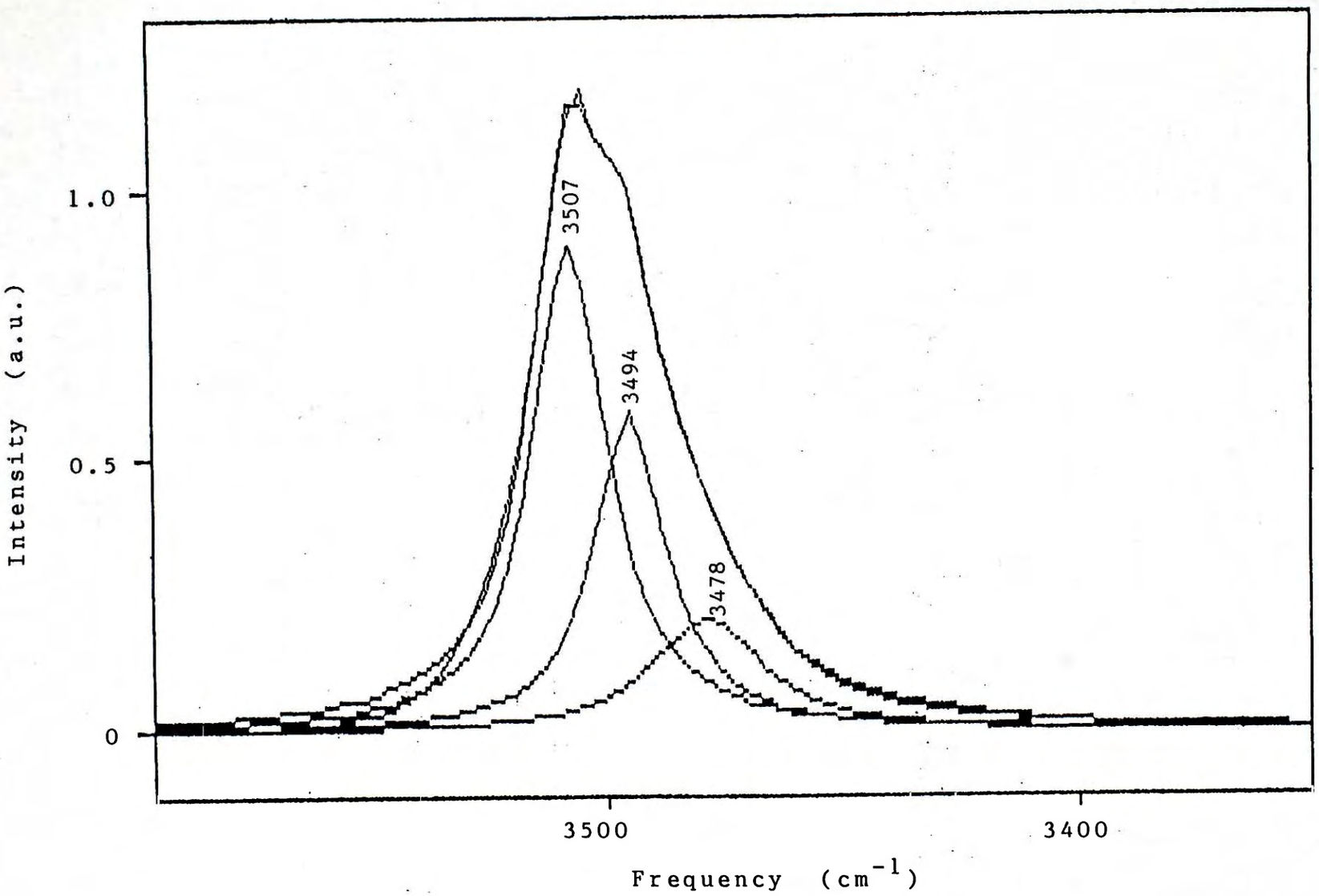

Fig.5.5.7 Infrared absorption spectrum of a proton-exchanged planar waveguide using phosphoric acid (sample P).

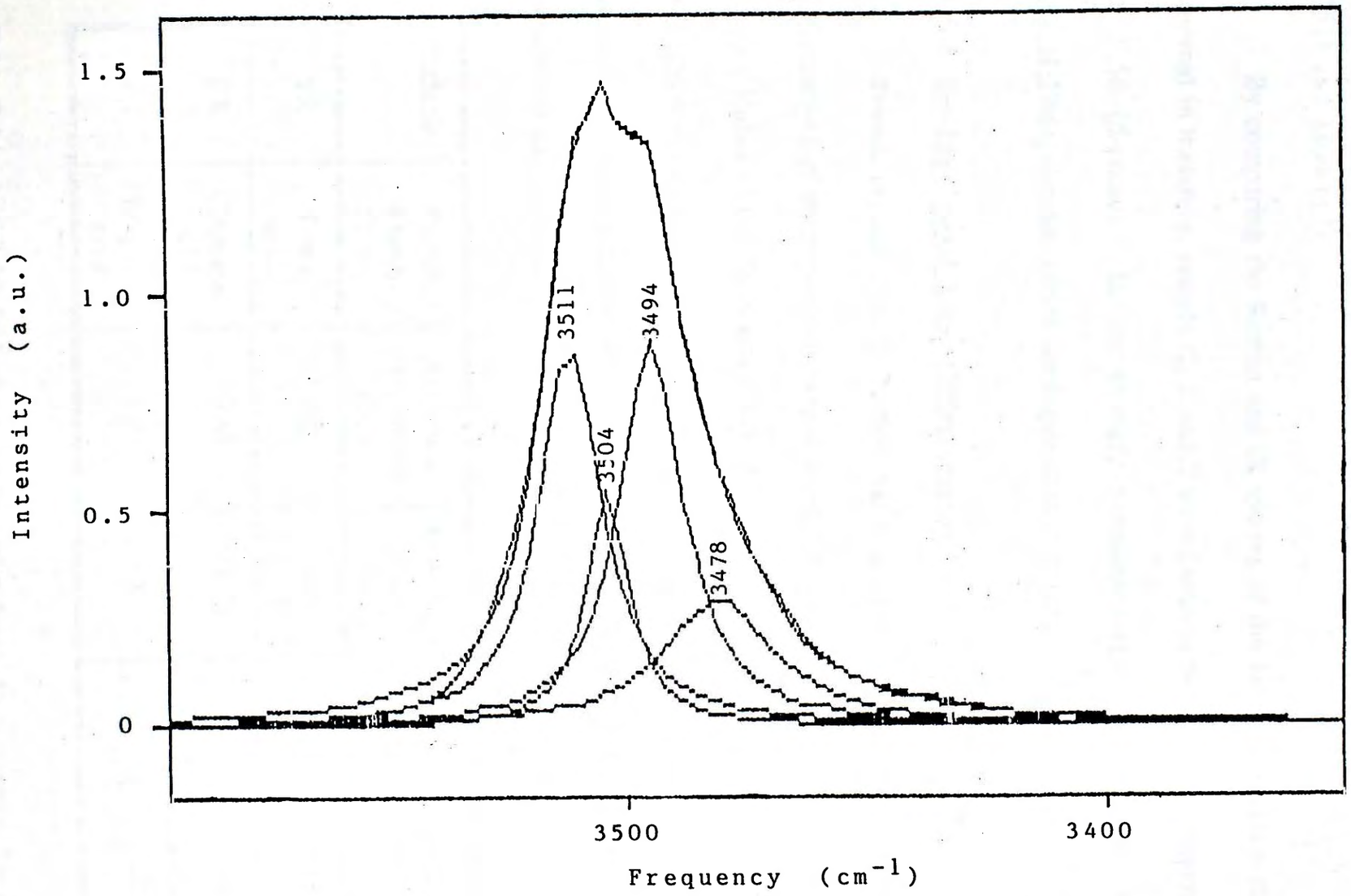

Fig.5.5.8 Infrared absorption spectrum of a proton-exchanged planar waveguide using cinnamic acid (sample C).

$Li_{1-x}H_xNbO_3$ [5.26,5.27], and the main absorptions are attributed to the two higher frequency bands. The intensity of the 3494cm^{-1} band increases gradually with x. In the spectrum of sample C, the 3507cm^{-1} band further splits into two components (3511 and 3504cm^{-1}).

By comparing the Raman and IR spectra of the PE waveguides with those reported in literature, sample C, P and T were found to have a H^+ concentration $x \geq 0.56$ (β-phase). In the strongly annealed sample PA, α- and β-phase $Li_{1-x}H_xNbO_3$ coexist, which corresponds to $x < 0.56$.

5.5.4 Double Crystal X-ray Diffractometry

Double crystal x-ray diffraction was employed to determine the strains and deformations of the proton-exchanged layer. X-ray rocking curves were obtained using a Huber 424 diffractometer with a CuKα radiation source (λ = 1.54056 and 1.54439Å for CuKα_1 and CuKα_2 radiation, respectively). Another three planar waveguides were prepared using different proton sources, and their fabrication conditions and waveguide parameters are summarized in Table 5.14.

Sample	Proton source	Exchange temperature (°C)	Exchange time (h)	No. of modes	Waveguide depth (μm)
TX	Toluic acid	200	28.5	6	2.53
CX	Cinnamic acid	200	27.25	7	2.86
PX	Phosphoric acid	250	3	8	3.58

Table 5.14 Initial fabrication conditions and waveguide parameters for samples used in double crystal x-ray diffraction measurement.

Figs.5.5.9 to 5.5.11 show the x-ray rocking curves for the (1 0 10) reflection. The two satellite peaks correspond to the proton-exchanged layer at different wavelengths. The substrate peak (removed from Figs.5.5.9 to 5.5.11) centers at the Bragg angle 2θ of 71.2° for CuKα_1 radiation. With increasing H^+ concentration x in samples TX, CX, and PX, the rocking curve broadens (FWHM = 285, 402, and 443 arcseconds for sample TX, CX, and PX, respectively). This is expected because the width of the rocking curve is a measure of the layer perfection, and the narrower the curve, the more perfect is the layer. The degree of lattice deformation induced in proton-exchanged layer increases with x, and hence the width of the rocking curve broadens.

The lattice constant c along the crystallographic z-axis *expands* in the exchanged layer, as evidenced by a negative Bragg angle shift of the satellite peak with respect to the substrate peak (Figs.5.5.9 to 5.5.11). The strain S_c ($=\Delta c/c$) can be calculated using the following expression [5.28]:

$$S_c = -\left[\frac{4c^2}{3a^2}\left(\frac{h^2+k^2+l^2}{l^2}\right) + 1\right]\cot\theta\,\Delta\theta \qquad (5.18)$$

where a and c are the lattice constants of virgin crystal, h, k, and l are Miller indices of the reflection plane, θ is the substrate Bragg angle for (h k l) reflection, and $\Delta\theta$ is the angular separation between the substrate and satellite peak in the rocking curve.

By measuring $\Delta\theta$ from the rocking curves illustrated in Figs.5.5.9 to 5.5.11, the *positive* strain S_c were found to be 3.98×10^{-3}, 3.64×10^{-3}, and 3.48×10^{-3} for sample TX, CX, and PX respectively. These values are similar to those obtained using benzoic acid (4.6×10^{-3}) [5.29].

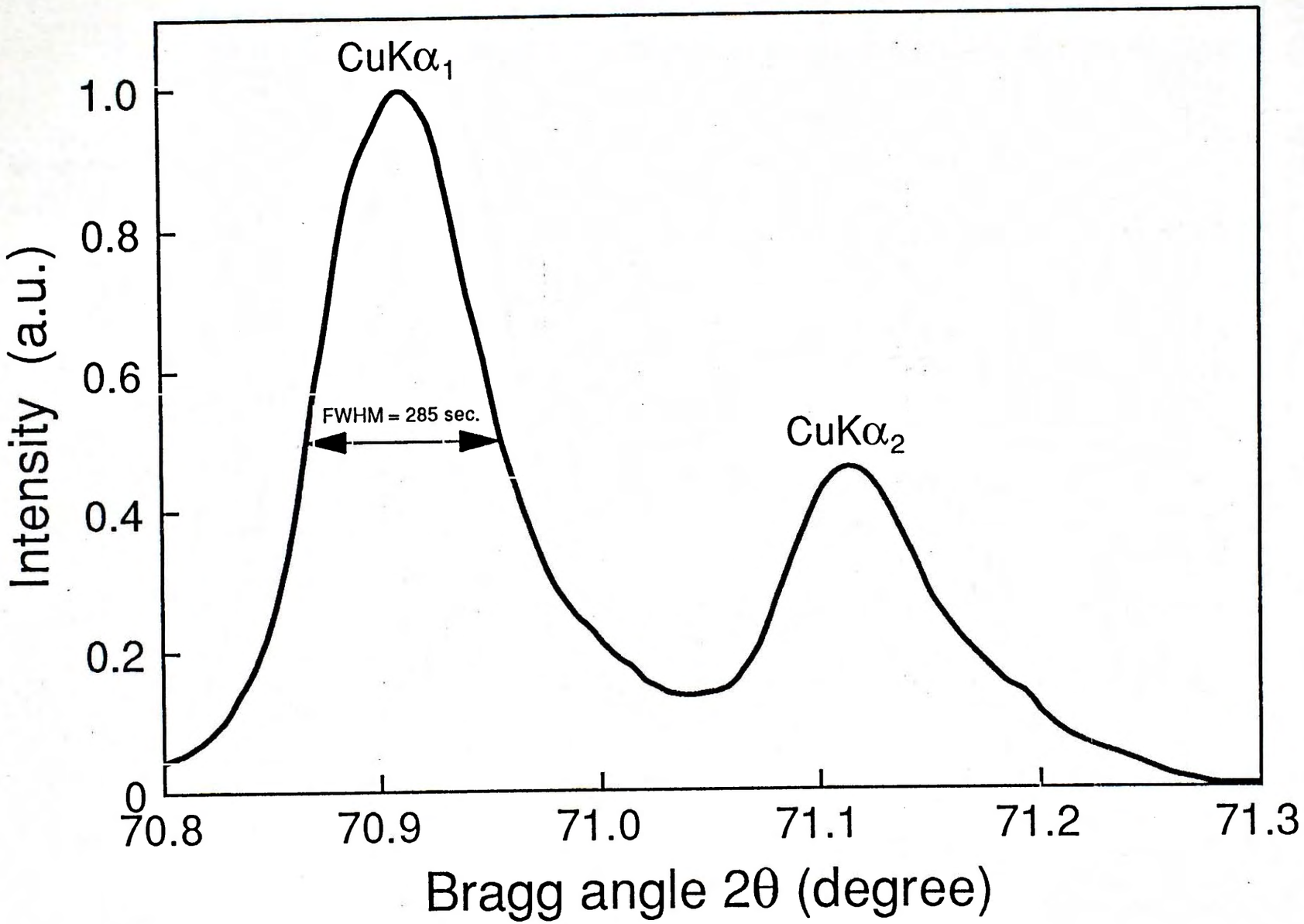

Fig.5.5.9 Double-crystal x-ray (1 0 10) rocking curve of a PE planar waveguide using toluic acid (sample TX).

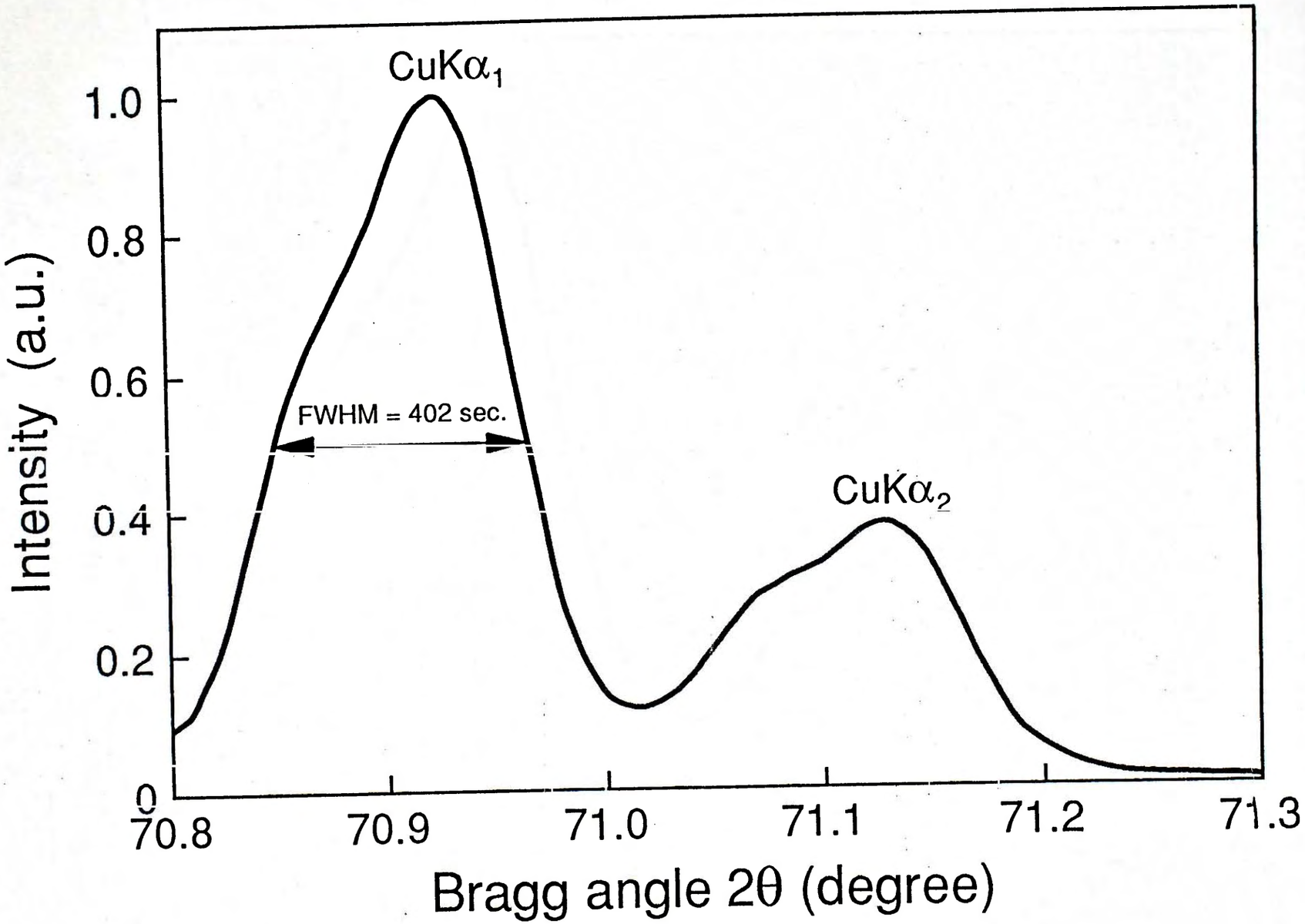

Fig.5.5.10 Double-crystal x-ray (1 0 10) rocking curve of a PE planar waveguide using cinnamic acid (sample CX).

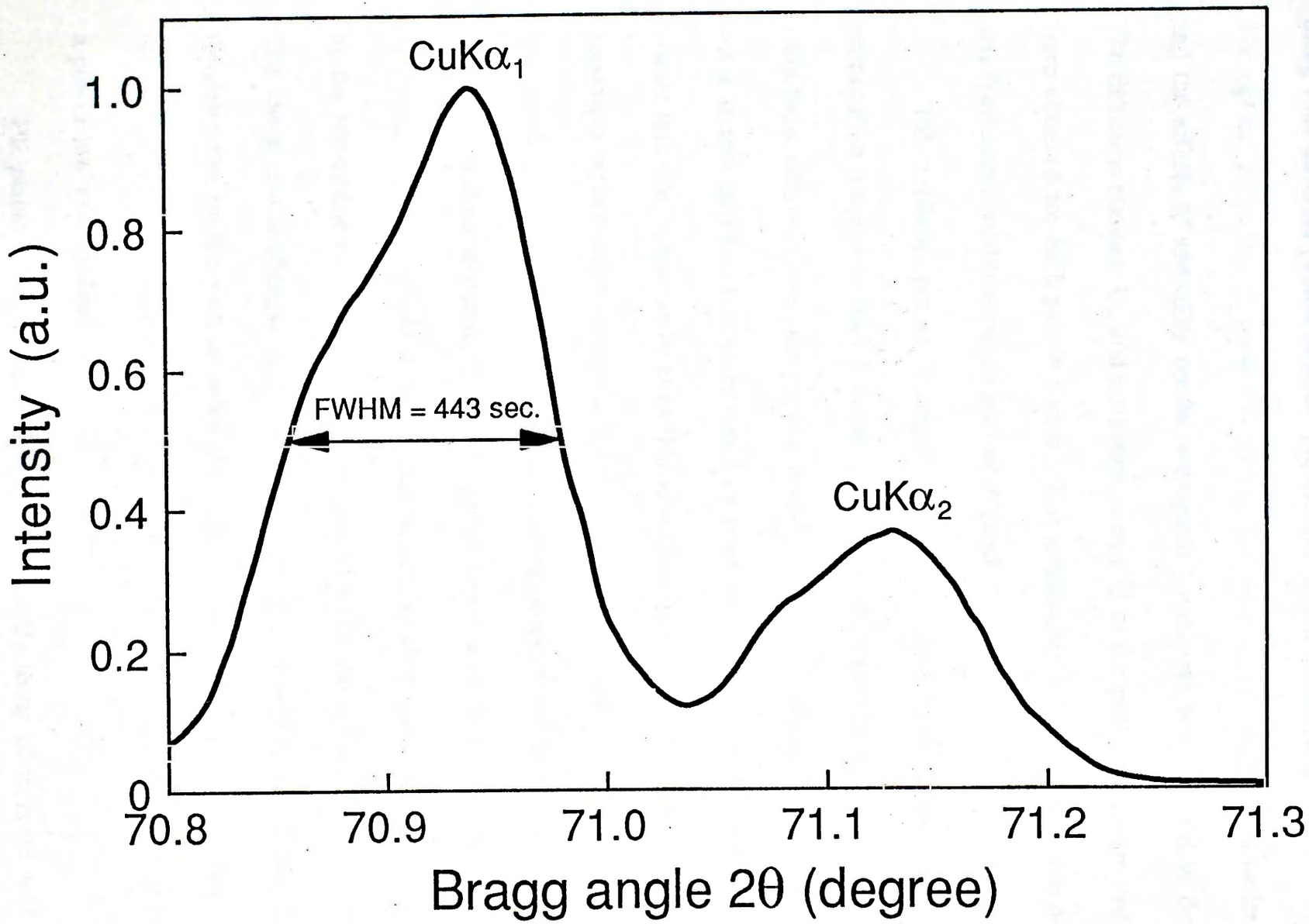

Fig.5.5.11 Double-crystal x-ray (1 0 10) rocking curve of a PE planar waveguide using phosphoric acid (sample PX).

5.6 Summary

Proton-exchanged optical waveguides have been fabricated in z-cut $LiNbO_3$ using four different proton sources: phosphoric, toluic, stearic and cinnamic acids. The optical properties of these PE waveguides were characterized systematically, and the effects of annealing on the waveguide parameters were studied in detail. The diffusion constant D_o and activation energy Q of the proton-exchange process were obtained for each proton source. The relationship between waveguide depth and fabrication conditions were also established.

PE $LiNbO_3$ planar waveguides formed using phosphoric acid have propagation losses less than 1 $dBcm^{-1}$, and exhibit properties which are different from those obtained using the popular benzoic acid. The refractive index profile is not a simple step function as reported by other researchers, and is found to be a graded function which can be modelled accurately by a polynomial expression. The maximum surface index change is 0.145 which is the largest value reported for PE waveguides measured at 0.633μm. The annealing properties of these PE waveguides have been studied in detail. The propagation losses drop below 0.5 $dBcm^{-1}$ after annealing. The waveguide depth and the number of propagation modes supported by the waveguide increases with annealing time while the surface index decreases. The index profile changes from a graded function to a step function, and then a Gaussian-like profile with an index tail at the waveguide-substrate boundary. The effect of annealing on surface index change and waveguide depth is found to follow a power-law relationship.

PE planar waveguides in z-cut MgO:$LiNbO_3$ using phosphoric acid also exhibit a graded index profile with a surface index change of 0.145. The graded

index profile can be approximated by a polynomial expression which is a closed-form solution of a nonlinear concentration-dependent diffusion equation. The diffusion rate in MgO:$LiNbO_3$ is found to be slower than that of undoped $LiNbO_3$.

PE waveguides in z-cut undoped $LiNbO_3$ using toluic acid exhibit a step index profile similar to that of benzoic acid, and is different from that of phosphoric acid. The surface index change is 0.124 measured at 0.633μm wavelength. The propagation loss is typically around 1 $dBcm^{-1}$ for unannealed waveguides, and is reduced to < 0.5 $dBcm^{-1}$ after annealing. Annealing changes the index profile from a step function to a graded function. Again the reduction in surface index and the increase in waveguide depth exhibit a power-law dependence on annealing time.

PE $LiNbO_3$ waveguides using stearic acid also exhibit a step-index profile similar to those of benzoic and toluic acids. The surface index change measured is 0.118, and the propagation loss is around 1 $dBcm^{-1}$. The diffusion rate using stearic acid is found to be the slowest reported among all the other acids. The annealing properties of these waveguides have also been studied in detail, and the results are similar to those of toluic acid.

The refractive index profile of PE $LiNbO_3$ waveguides using cinnamic acid is found to be different from those obtained using other organic acids. The profile is a graded function, and can be modelled accurately by a truncated-parabolic function with a surface index increase of 0.141. This is the largest value obtained for PE waveguides using organic acids. The waveguide propagation loss is around 1 $dBcm^{-1}$, and can be reduced further to 0.3 $dBcm^{-1}$ after annealing. Annealing changes the index profile from a truncated-parabolic function to a step function and then a Gaussian-like profile. Annealing is also shown to be an effective means of controlling and modifying the optical properties of these waveguides.

Chapter 6

CONCLUSIONS

Proton exchange is one of the two main methods used today for fabricating optical waveguides and devices in lithium niobate ($LiNbO_3$) [6.1-6.3]. The proton-exchange process is simple compared to the standard titanium indiffusion process, and does not require high temperatures and long diffusion times. Proton-exchanged (PE) waveguides exhibit tight optical confinement and reduced photorefractive response [6.4] which are desirable properties for waveguide devices. Many integrated optical devices have been demonstrated exploiting the unique properties of PE waveguides, e.g. high efficiency Bragg deflection gratings [6.5], optical frequency translators [6.6], Fresnel lenses [6.7], modulators [6.8], picosecond pulse generators [6.9], waveguide lasers [6.10] and amplifiers [6.11].

Since its first demonstration by Jackel *et al.* [6.1], benzoic acid has been the most popular and well established proton source [6.2-6.3]. There is an increased interest in using phosphoric acid, i.e. orthophosphoric acid and/or pyrophosphoric acid as an alternative proton source [6.12-6.17]. Taniuchi and Yamamoto [6.12,6.16] reported that PE optical waveguides fabricated using pyrophosphoric acid also exhibit a step index profile, but with a higher surface index change ($\Delta n_s = 0.145$) and much lower propagation losses (0.7 $dBcm^{-1}$) than those obtained using benzoic acid. However, an index increase of only 0.13 and a propagation loss around 2 $dBcm^{-1}$ have been reported by other researchers [6.14,6.15].

We have carried out a systematic study on PE z-cut $LiNbO_3$ waveguides using phosphoric acid. The optical properties of these PE waveguides have been

characterized, and the diffusion parameters of the proton-exchange process are obtained. We confirm that the surface index change is 0.145 and the propagation loss is less than 1 $dBcm^{-1}$. However, the refractive index profile is not a simple step function as reported by other researchers, and is found to be a graded function which can be modelled accurately by a polynomial expression. Yip and Nikolopoulos [6.17] also confirmed recently that the profile is not a simple step function, and could be modelled by a Fermi function. Since phosphoric acid is more stable and has a wider temperature range for exchange compared to benzoic acid, it is an attractive alternative proton source.

Unfortunately both benzoic and phosphoric acids are dangerous to use because they are either moderately toxic or corrosive. In our work, we have proposed and demonstrated the use of toluic, stearic and cinnamic acids for the fabrication of PE waveguides in z-cut $LiNbO_3$. These organic acids are nontoxic, noncorrosive and safe to use. PE waveguides fabricated using these *new* organic proton sources have been characterized in detail. The effects of annealing on waveguide parameters have also been studied systematically. Annealing is shown to be an effective means of controlling and modifying the optical properties of these PE waveguides. The annealing parameters obtained would be useful in the design and fine tuning of $LiNbO_3$ optical integrated circuits using the proton-exchange and annealing process.

Table 6.1 summarizes the PE waveguide parameters using benzoic, phosphoric, toluic, stearic, and cinnamic acids, and Fig.6.1 shows the comparison of the effective diffusion coefficient D(T) as a function of exchange temperature for these acids. It can be seen that D(T) increases with acidity K_α of the proton source,

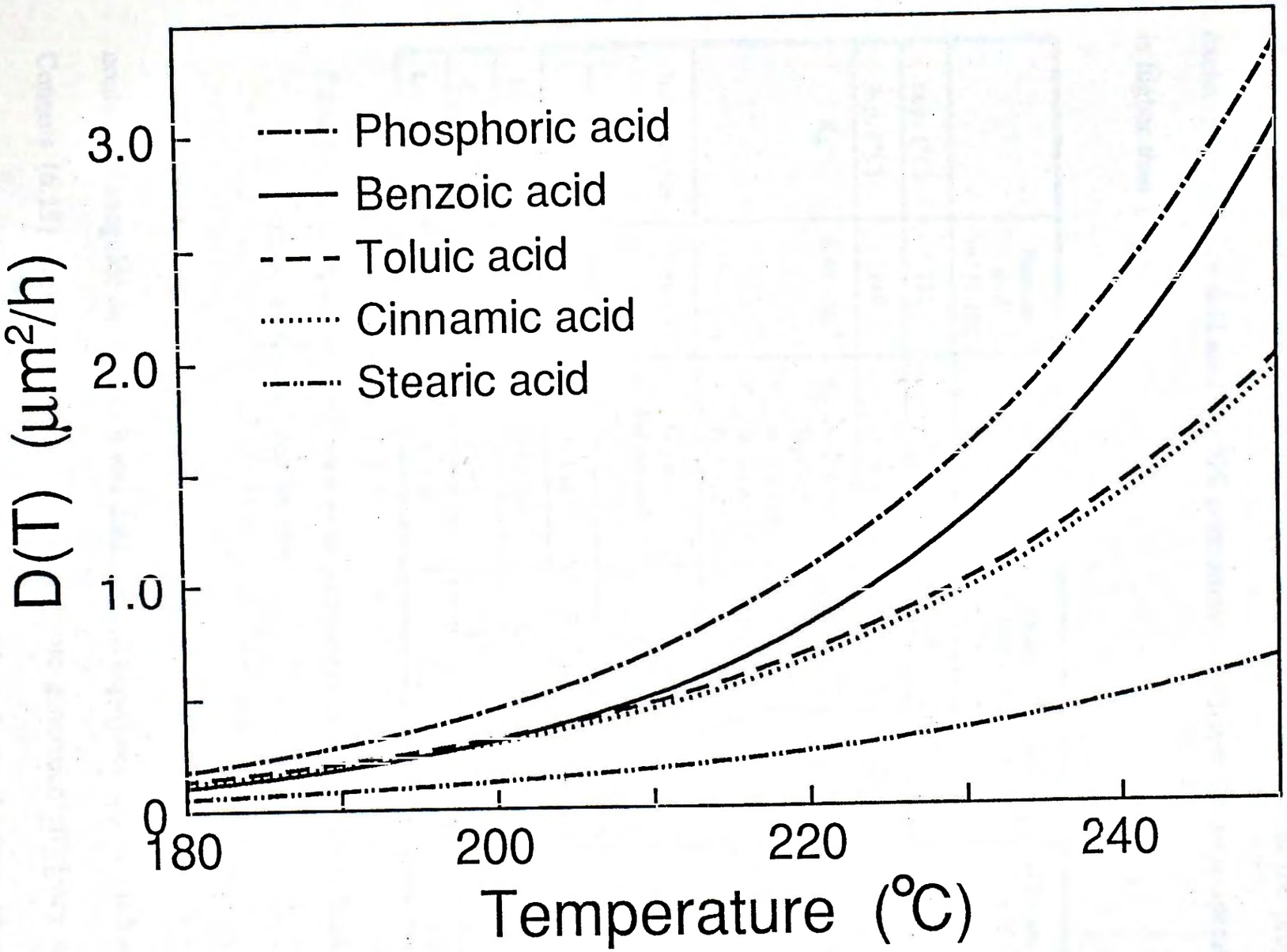

Fig.6.1 Comparison of effective diffusion coefficient D(T) as a function of temperature for different proton sources.

thus K_α could be a measure of the diffusion rate of proton-exchange process. However, the difference in D(T) between any two proton sources cannot be inferred simply from their values of K_α, since K_α is normally used to compare the number of solvated protons in *aqueous solution* at room temperature, and in the proton-exchange process the acid melt is 100% concentrated and the exchange temperature is higher than 150°C.

	Benzoic acid ref.[6.18]	Phosphoric acid	Toluic acid	Stearic acid	Cinnamic acid
m.p. (°C)	122	42.35	109	69.6	133
b.p. (°C)	249	> 300	263	361	300
K_α	6.46×10^{-5}	$K_{\alpha1} = 7.1\times10^{-3}$ (H_3PO_4) $K_{\alpha1} = 1.4\times10^{-1}$ $K_{\alpha2} = 1.1\times10^{-2}$ ($H_4P_2O_7$)	5.62×10^{-5}	1.28×10^{-5}	3.47×10^{-5}
Index profile	Step	Graded: Polynomial	Step	Step	Graded: Truncated-parabolic
Δn_s	0.126	0.145	0.124	0.118	0.141
Do (μm^2h^{-1})	7.36×10^9	6.43×10^8	7.02×10^7	5.0×10^6	9.78×10^7
Q ($kJmol^{-1}$)	94	82.91	75.58	69	77.15
Loss ($dBcm^{-1}$)	2.4	< 1.0	~1.0	~1.0	~1.0

Table 6.1 Comparison of PE waveguide parameters in z-cut $LiNbO_3$ fabricated using different proton sources

A lower rate of diffusion is useful and important in the fabrication of nonlinear waveguide devices, as it was demonstrated experimentally by Sanford and Connors [6.15] that the Cerenkov second-harmonic generation efficiency of PE waveguides using phosphoric acid could be reduced by a factor of 5 for a difference

of 1 minute diffusion time around the optimum time. A better and tighter control over the waveguide parameters could be achieved using toluic, cinnamic or stearic acid as the alternative proton source. From our experimental observation, the stability of cinnamic acid is superior to other organic acids.

At the present stage of our studies the reason for differences in the refractive index profiles obtained using different proton sources is not known. The analyses by other researchers have revealed that the diffusion mechanism of the proton-exchange and annealing process is very complicated [6.19-6.21]. Besides, the PE waveguiding layer $Li_{1-x}H_xNbO_3$ exhibits a complex structure (especially for $x \geq 0.56$) and consists of several (up to six) distinct crystalline phases along with a variety of phase transitions [6.21,6.22]. Further studies correlating the optical properties of the waveguides and structural characteristics of these crystalline phases have to be carried out in order to understand the origin of the differences.

Finally, we conclude that the refractive index profile of PE waveguide is ***not*** necessary a step-index function, and depends on the proton source used. The diffusion rate also depends on the acidity of the proton source.

REFERENCES

Chapter 1

[1.1] I. Hayashi, M. B. Panish, P. W. Foy, and S. Sumski, "Junction lasers which operate continuously at room temperature," *Appl. Phys. Lett.*, vol.17, pp.109-111, 1970.

[1.2] F. P. Kapron, D. B. Keck, and R. D. Maurer, "Radiation losses in glass optical waveguides," *Appl. Phys. Lett.*, vol.17, pp.423-425, 1970.

[1.3] P. K. Tien, "Light waves in thin films and integrated optics," *Appl. Opt.*, vol.10, pp.2395-2413, 1971.

[1.4] S. E. Miller, "A survey of integrated optics," *IEEE J. Quantum Electron.*, vol.8, pp.199-205, 1972.

[1.5] H. Kogelnik, "An introduction to integrated optics," *IEEE Trans. Microwave Theory Tech.*, vol.23, pp.2-16, 1975.

[1.6] S. E. Miller, "Integrated optics: an introduction," *Bell Syst. Tech. J.*, vol.48, pp.2059-2069, 1969.

[1.7] T. Tamir, *Integrated Optics*, Topics Appl. Phys., vol.7, Berlin: Springer-Verlag, 1982.

[1.8] R. G. Hunsperger, *Integrated Optics: Theory and Technology*, Springer Ser. Opt. Sci., vol.33, Berlin: Springer-Verlag, 1984.

[1.9] H. Kogelnik, "Limits in integrated optics," *Proc. IEEE*, vol.69, pp.232-238, 1981.

[1.10] L. D. Hutcheson, *Integrated Optical Circuits and Components*, New York: Marcel Dekker, 1987.

[1.11] M. A. Mentzer, *Principles of Optical Circuit Engineering*, New York:

Marcel Dekker, 1990.

[1.12] I. Andonovic and D. Uttamchandani, *Principles of Modern Optical Systems*, Artech House, 1989.

[1.13] J. Dakin and B. Culshaw, *Optical Fiber Sensors: Principles and Components*, Artech House, 1988.

[1.14] P. Günter, *Electro-optic and Photorefractive Materials*, Berlin: Springer-Verlag, 1986.

[1.15] M. Papuchon, "Integrated optics: $LiNbO_3$ or semiconductors?" *Solid State Devices*, pp.1021-1024, 1988.

[1.16] F. Tosco, *Fiber Optic Communications Handbook*, TAB Books, 1990.

[1.17] E. Voges and A. Neyer, "Integrated-optic devices on $LiNbO_3$ for optical communication," *IEEE J. Lightwave Technol.*, vol.5, pp.1229-1238, 1987.

[1.18] L. Thylén, "Integrated optics in $LiNbO_3$: recent developments in devices for telecommunications," *IEEE J. Lightwave Technol.*, vol.6, pp.847-861, 1988.

[1.19] W. J. Tomlinson and C. A. Brackett, "Telecommunications applications of integrated optics and optoelectronics," *Proc. IEEE*, vol.75, pp.1512-1523, 1987.

[1.20] L. Thylén, "Lithium niobate devices in switching and multiplexing," *Phil. Trans. R. Soc. Lond. A*, vol.329, pp.83-92, 1989.

[1.21] R. C. Booth, "$LiNbO_3$ integrated optic devices for coherent optical fibre systems," *Thin Solid Films*, vol.126, pp.167-176, 1985.

[1.22] W. A. Stallard, A. R. Beaumont, and R. C. Booth, "Integrated optic devices for coherent transmission," *IEEE J. Lightwave Technol.*, vol.4, pp.852-857, 1986.

[1.23] T. Sueta, M. Izutsu, "Integrated optic devices for microwave applications," *IEEE Trans. Microwave Theory Tech.*, vol.38, pp.477-481, 1990.

[1.24] H. F. Taylor, "Application of guided-wave optics in signal processing and sensing," *Proc. IEEE*, vol.75, pp.1524-1535, 1987.

[1.25] R. A. Becker, "Travelling wave electro-optic modulator with maximum bandwidth-length product," *Appl. Phys. Lett.*, vol.45, pp.1168-1170, 1984.

[1.26] S. K. Korotky, G. Eisenstein, R. S. Tucker, J. J. Veselka, G. Raybon, "Optical intensity modulation to 40GHz using a waveguide electro-optic switch," *Appl. Phys. Lett.*, vol.50, pp.1631-1633, 1987.

[1.27] R. C. Alferness, L. L. Buhl, M. D. Divino, S. K. Korotky, L. W. Stulz, "Low-loss broad-band Ti:$LiNbO_3$ waveguide phase modulator for coherent systems," *Electron. Lett.*, vol.22, pp.309-310, 1986.

[1.28] D. W. Dolfi, M. Nazarathy, and R. L. Jungerman, "40GHz electro-optic modulator with 7.5V drive voltage," *Electron. Lett.*, vol.24, pp.528-529, 1988.

[1.29] L. McCaugan and G. A. Bogert, "4×4 Ti:$LiNbO_3$ integrated-optical crossbar switch array," *Appl. Phys. Lett.*, vol.47, pp.348-350, 1985.

[1.30] P. Granestrand, B. Stolz, L Thylén, K. Bervall, D. Döeldissen, H. Heidrich, D. Hoffmann, "Strictly nonblocking 8×8 integrated optical switch matrix," *Electron. Lett.*, vol.22, pp.816-818, 1986.

[1.31] I. Sawaki, T. Shimoe, H. Nakamoto, T. Iwama, T. Yamane, and H. Nakajima, "Rectangularly configured 4×4 Ti:$LiNbO_3$ matrix switch with low drive voltage," *IEEE J. Select. Areas Commun.*, vol.6, pp.1267-1272, 1988.

[1.32] A. Selvarajan and J. E. Midwinter, "Photonic switches and switch arrays on $LiNbO_3$," *Opt. Quantum Electron.*, vol.21, pp.1-15, 1989.

[1.33] H. Heidrich and D. Hoffmann, "Review on integrated-optics switch matrices in $LiNbO_3$," *Trans. IEICE*, vol.E73, pp.94-98, 1990.

[1.34] A. Neyer, "Integrated-optical multichannel wavelength multiplexer for monomode systems," *Electron Lett.*, vol.20, pp.744-746, 1984.

[1.35] H. Haga, M. Izutsu, and T. Sueta, "An integrated 1×4 high speed optical switch and its application to a demultiplexer," *IEEE J. Lightwave Technol.*, vol.3, pp.116-120, 1985.

[1.36] L. M. Johnson, F. J. Leonberger, and G. W. Pratt, Jr., "Integrated optic temperature sensor," *Appl. Phys. Lett.*, vol.41, pp.134-136, 1982.

[1.37] M. Izutsu, A. Enokihara, and T. Sueta, "Integrated optic temperature and humidity sensor," *IEEE J. Lightwave Technol.*, vol.4, pp.828-836, 1986.

[1.38] M. Izutsu, A. Enokihara, and T. Sueta, "Optical-waveguide micro-displacement sensor," *Electron. Lett.*, vol.18, pp.867-868, 1982.

[1.39] C. H. Bulmer and W. K. Burns, "Linear interferometric modulators in Ti:$LiNbO_3$," *IEEE J. Lightwave Technol.*, vol.2, pp.512-521, 1984.

[1.40] R. H. Rediker, T. A. Lind, and F. J. Leonberger, "Integrated optics wave front measurement sensor," *Appl. Phys. Lett.*, vol.42, pp.647-649, 1983.

[1.41] C. H. Bulmer and R. P. Moeller, "Fiber gyroscope with nonreciprocally operated fiber-coupled $LiNbO_3$ phase shifter," *Opt. Lett.*, vol.6, pp.572-574, 1981.

[1.42] R. A. Bergh, H. C. Lefevre, and H. J. Shaw, "An overview of fiber-optic gyroscopes," *IEEE J. Lightwave Technol.*, vol.2, pp.91-107, 1984.

[1.43] W. A. Stallard, T. G. Hodgkinson, K. R. Preston, and R. C. Booth, "A novel $LiNbO_3$-integrated optic component for coherent optical heterodyne detection," *Electron. Lett.*, vol.21, pp.1077-1079, 1985.

[1.44] M. Izutsu, S. Shikama, and T. Sueta, "Integrated optical SSB modulator/frequency shifter," *IEEE J. Quantum Electron.*, vol.17, pp.2225-2227, 1981.

[1.45] K. K. Wong, R. M. De La Rue, and S. Wright, "Electro-optic-waveguide frequency translator in $LiNbO_3$ fabricated by proton exchange," *Opt. Lett.*, vol.7, pp.546-548, 1982.

[1.46] F. Heismann and R. Ulrich, "Integrated-optical frequency translator with strip waveguide," *Appl. Phys. Lett.*, vol.45, pp.490-492, 1984.

[1.47] H. Shimizu, R. Ishikawa, and K. Kaede, "Integrated optical frequency modulator for fiber-optic gyroscope using frequency modulation method," *Electron. Lett.*, vol.22, pp.334-335, 1986.

[1.48] J. Ohya, G. Tohmon, K. Yamamoto, and T. Taniuchi, "Picosecond blue light pulse generation by frequency doubling of a gain-switched GaAlAs laser diode with saturable absorbers," *Appl. Phys. Lett.*, vol.56, pp.2270-2272, 1990.

[1.49] G. Tohmon, J. Ohya, K. Yamamoto, and T. Taniuchi, "Generation of Ultraviolet picosecond pulses by frequency-doubling of laser diode in proton-exchanged MgO:$LiNbO_3$ waveguide," *IEEE Photon. Technol. Lett.*, vol.2, pp.629-631, 1990.

[1.50] H. Nishihara, M. Haruna, and T. Suhara, *Optical Integrated Circuits*, New York: McGraw-Hill, 1989.

[1.51] T. Tamir, *Guided-wave Optoelectronics*, Springer Ser. Electron. & Photon., vol.26, Berlin: Springer-Verlag, 1990.

[1.52] R. G. Hunsperger, *Integrated Optics: Theory and Technology*, Springer Ser. Opt. Sci., vol.33, Berlin: Springer-Verlag, 1991.

[1.53] T. Suhara and H. Nishihara, "Integrated optics components and devices using periodic structures," *IEEE J. Quantum Electron.*, vol.22, pp.845-867, 1986.

[1.54] B. K. Nayar and R. C. Booth, "An introduction to integrated optics," *British Telecom. Technol. J.*, vol.4, pp.5-15, 1986.

[1.55] R. R. A. Symms, "Advances in channel waveguide lithium niobate integrated optics," *Opt. Quantum Electron.*, vol.20, pp.189-213, 1988.

[1.56] W. Sohler, "Integrated optics in $LiNbO_3$," *Thin Solid Films*, vol.175, pp.191-200, 1989.

[1.57] A. Neyer, "Integrated-optic devices in lithium niobate: technology and applications," *Proc. SPIE*, vol.1274, pp.2-17, 1990.

[1.58] H. Nishihara, "Recent advancement on optical integrated circuits," *Proc. IEEE Region 10 Conf. Computer Comm. Syst.*, TENCON'90 (Hong Kong), pp.99-103, 1990.

[1.59] C. H. Bulmer, "Lithium niobate waveguide devices: present performance and future applications," *Proc. SPIE*, vol.1583, pp.176-183, 1991.

[1.60] G. J. Sellers and S. Sriram, "Integrated optical technology-evolving to fill market niches," *Laser Focus*, pp.74-82, Sept. 1986.

Chapter 2

[2.1] D. Marcuse, *Theory of Dielectric Optical Waveguides*, New York: Academic

Press, 1974.

[2.2] M. J. Adams, *An Introduction to Optical Waveguides*, Chichester: Wiley, 1981.

[2.3] M. Born and E. Wolf, *Principles of Optics*, London: Pergamon Press, 1959.

[2.4] R. G. Hunsperger, *Integrated Optics: Theory and Technology*, Springer Ser. Opt. Sci., vol.33, Berlin: Springer-Verlag, 1991.

[2.5] T. Tamir, *Guided-wave Optoelectronics*, Springer Ser. Electron. & Photon., vol.26, Berlin: Springer-Verlag, 1990.

[2.6] L. D. Hutcheson, *Integrated Optical Circuits and Components*, New York: Marcel Dekker, 1987.

[2.7] H. Nishihara, M. Haruna, and T. Suhara, *Optical Integrated Circuits*, New York: McGraw-Hill, 1989.

[2.8] V. Ramaswamy and R. K. Lagu, "Numerical field solution for an arbitrary asymmetrical graded-index planar waveguide," *IEEE J. Lightwave Technol.*, vol.1, pp.408-416, 1983.

[2.9] R. Srivastava, C. K. Kao, and V. Ramaswamy, "WKB analysis of planar surface waveguides with truncated index profiles," *IEEE J. Lightwave Technol.*, vol.5, pp.1605-1608, 1987.

[2.10] G. B. Hocker and W. K. Burns, "Modes in diffused optical waveguides of arbitrary index profile," *IEEE J. Quantum Electron.*, vol.11, pp.270-276, 1975.

[2.11] P. Günter, *Electro-optic and Photorefractive Materials*, Berlin: Springer-Verlag, 1986.

[2.12] J. Dakin and B. Culshaw, *Optical Fiber Sensors: Principles and*

Components, Artech House, 1988.

[2.13] C. S. Tsai, *Guided-Wave Acousto-Optics: Interactions, Devices, and Applications*, Berlin: Springer-Verlag, 1989.

[2.14] F. Tosco, *Fiber Optic Communications Handbook*, TAB Books, 1990.

[2.15] E. A. J. Marcatili, "Dielectric rectangular waveguide and directional coupler for integrated optics," *Bell Syst. Tech. J.*, vol.48, pp.2071-2102, 1969.

[2.16] R. M. Knox and P. P. Toulios, "Integrated circuits for the millimeter through optical frequency range," *Proc. MRI Symposium Submillimeter Waves*, Polytechnic Press, pp.497-516, 1970.

[2.17] T. Tamir, *Integrated Optics*, Topics Appl. Phys., vol.7, Berlin: Springer-Verlag, 1975.

[2.18] K. S. Chiang, "Dual effective-index method for the analysis of rectangular dielectric waveguides," *Appl. Opt.*, vol.25, pp.2169-2174, 1986.

[2.19] E. A. J. Marcatili and A. A. Hardy, "The azimuthal effective-index method," *IEEE J. Quantum Electron.*, vol.24, pp.766-774, 1988.

[2.20] Working Group I, COST 216, "Comparison of different modelling techniques for longitudinally invariant integrated optical waveguides," *IEE Proc.*, pt.J, vol.136, pp.273-280, 1989.

[2.21] G. B. Hocker and W. K. Burns, "Modes dispersion in diffused channel waveguides by the effective index method," *Appl. Opt.*, vol.16, pp.113-118, 1977.

Chapter 3

[3.1] F. Tosco, *Fiber Optic Communications Handbook*, TAB Books, 1990.

[3.2] J. Dakin and B. Culshaw, *Optical Fiber Sensors: Principles and Components*, Artech House, 1988.

[3.3] C. S. Tsai, *Guided-Wave Acousto-Optics: Interactions, Devices, and Applications*, Berlin: Springer-Verlag, 1989.

[3.4] T. Findakly, "Glass waveguides by ion exchange: a review," *Opt. Eng.*, vol.24, pp.244-250, 1985.

[3.5] R. V. Ramaswamy and R. Srivastava, "Ion-exchanged glass waveguides: a review," *IEEE J. Lightwave Technol.*, vol.6, pp.984-1002, 1988.

[3.6] R. Srivastava and R. V. Ramaswamy, "Ion-exchanged waveguides: current status," Proc. SPIE, vol.1583, pp.2-13, 1991.

[3.7] S. I. Najafi, W. J. Wang, J. F. Currie, R. Leonelli, and J. L. Brebner, "Fabrication and characterization of neodymium-doped glass waveguides," *IEEE Photon. Technol. Lett.*, vol.1, pp.109-110, 1989.

[3.8] S. Honkanen, S. I. Najafi, P. Poyhonen, G. Orcel, W. J. Wang, and J. Chrostowski, "Silver-film ion-exchanged singlemode waveguides in Er doped phosphate glass," *Electron. Lett.*, vol.27, pp.2167-2168, 1991.

[3.9] N. A. Sanford, K. J. Malone, and D. R. Larson, "Integrated-optic laser fabricated by field-assisted ion-exchange in neodymium-doped sodalime silicate glass," *Opt. Lett.*, vol.15, pp.366-368, 1990.

[3.10] H. Aoki, O. Maruyama, and Y. Asahara, "Glass waveguide laser," *IEEE Photon. Technol. Lett.*, vol.2, pp.459-460, 1990.

[3.11] E. K. Mwarania, L. Reekie, J. Wang, and J. S. Wilkinson, "Low-threshold monomode ion-exchanged waveguide lasers in neodymium-doped BK-7 glass," *Electron. Lett.*, vol.26, pp.1317-1318, 1990.

[3.12] M. Papuchon, "Integrated optics: $LiNbO_3$ or semiconductors?" *Solid State Devices*, pp.1021-1024, 1988.

[3.13] A. Y. Cho and A. M. Glass, "Photonic materials and processing," *AT&T Tech. J.*, pp.77-91, Nov./Dec. 1990.

[3.14] G. Boyd, R. Miller, K. Nassau, W. Bond, and A. Savage, "$LiNbO_3$: an efficient phase matchable nonlinear optical material," *Appl. Phys. Lett.*, vol.5, pp.234-236, 1964.

[3.15] A. Ballman, "Growth of piezoelectric and ferroelectric materials by the czochralski technique," *J. Am. Ceram. Soc.*, vol.48, pp.112-113, 1965.

[3.16] K. Nassau, H. Levinstein, and G. Loiacono, "Ferroelectric lithium niobate: 2. Preparation of single-domain crystals," *J Phys. Chem. Solids.*, vol.27, pp.989-996, 1966.

[3.17] P. W. Haycock and P. D. Townsend, "A method of poling $LiNbO_3$ and $LiTaO_3$ below T_c," *Appl. Phys. Lett.*, vol.48, pp.698-700, 1986.

[3.18] P. Günter, *Electro-optic and Photorefractive Materials*, Berlin: Springer-Verlag, 1986.

[3.19] G. G. Zhong, J. Jian, and Z. K. Wu, 11th Int. Quantum Electron. Conf., IEEE Cat. No. 80 CH 1561-0, pp.631, 1980.

[3.20] D. A. Bryan, R. Gerson, and H. E. Tomaschke, "Increased optical damage resistance in lithium niobate," *Appl. Phys. Lett.*, vol.44, pp.847-849, 1984.

[3.21] J. L. Jackel, "Proton exchange in MgO-doped $LiNbO_3$," *Electron. Lett.*, vol.21, pp.509-511, 1985.

[3.22] M. Digonnet, M. Fejer, and R. Byer, "Characterization of proton-exchanged waveguides in MgO:$LiNbO_3$," *Opt. Lett.*, vol.10, pp.235-237, 1985.

[3.23] F. Laurell and G. Arvidsson, "Frequency doubling in Ti:MgO:$LiNbO_3$ channel waveguides," *J. Opt. Soc. Am.*, vol.B5, pp.292-300, 1988.

[3.24] T. Y. Fan, A. Cordova-Plaza, M. J. F. Digonnet, R. L. Byer, and H. J. Shaw, "Nd:MgO:$LiNbO_3$ spectroscopy and laser devices," *J. Opt. Soc. Am.*, vol.B5, pp.140-147, 1986.

[3.25] A. Cordova-Plaza, T. Y. Fan, M. J. F. Digonnet, R. L. Byer, and H. J. Shaw, "Nd:MgO:$LiNbO_3$ continuous-wave laser pumped by a laser diode," *Opt. Lett.*, vol.13, pp.209-211, 1988.

[3.26] M. J. Li, M. P. De Micheli, D. B. Ostrowsky, E. Lallier, J. M. Breteau, M. Papuchon, and J. P. Pocholle, "Optical waveguide fabrication in neodymium-doped lithium niobate," *Electron. Lett.*, vol.24, pp.914-915, 1988.

[3.27] E. Lallier, J. P. Pocholle, M. Papuchon, C. Grezes-Besset, E. Pelletier, M. De Micheli, M. J. Li, Q. He, and D. B. Ostrowsky, "Laser oscillation of single-mode channel waveguide in Nd:MgO:$LiNbO_3$," *Electron. Lett.*, vol.25, pp.1491-1492, 1989.

[3.28] E. Lallier, J. P. Pocholle, M. Papuchon, M. De Micheli, M. J. Li, Q. He, D. B. Ostrowsky, C. Grezes-Besset, and E. Pelletier, "Nd:MgO:$LiNbO_3$ waveguide laser and amplifier," *Opt. Lett.*, vol.15, pp.682-684, 1990.

[3.29] M. Gong, G. Xu, K. Han, and G. Zhai, "Nd:MgO:$LiNbO_3$ self-frequency-double laser pumped by a flashlamp at room temperature," *Electron. Lett.*, vol.26, pp.2062-2063, 1990.

[3.30] R. R. A. Syms, "Advances in channel waveguide lithium niobate integrated optics," *Opt. Quantum Electron.*, vol.20, pp.189-213, 1988.

[3.31] M. N. Armenise, "Fabrication techniques of lithium niobate waveguides," *IEE Proc.*, pt.J, vol.135, pp.85-91, 1988.

[3.32] A. Neyer, "Integrated-optic devices in lithium niobate: technology and applications," *Proc. SPIE*, vol.1274, pp.2-17, 1990.

[3.33] G. Götz and H. Karge, "Ion implantation into $LiNbO_3$," *Nucl. Instr. and Meth.*, vol.209/210, pp.1079-1088, 1983.

[3.34] P. D. Townsend, "An overview of ion-implanted optical waveguide profiles," *Nucl. Instr. and Meth.*, vol.B46, pp.18-25, 1990.

[3.35] Ch. Buchal, "Ion beam modification of electro-optical crystals," *Nucl. Instr. and Meth.*, vol.B59/60, pp.1142-1146, 1991.

[3.36] L. Zhang, P. J. Chandler, and P. D. Townsend, "Optical analysis of damage profiles in ion implanted $LiNbO_3$," *Nucl. Instr. and Meth.*, vol.B59/60, pp.1147-1152, 1991.

[3.37] R. V. Schmidt and I. P. Kaminow, "Metal-diffused optical waveguides in $LiNbO_3$," *Appl. Phys. Lett.*, vol.25, pp.458-460, 1974.

[3.38] K. Komatsu, M. Kondo, and Y. Ohta, "Titanium/magnesium double diffusion method for efficient fiber-$LiNbO_3$ waveguide coupling," *Electron. Lett.*, vol.22, pp.881-882, 1986.

[3.39] B. Schüppert, "Reduction of bend losses in Ti:$LiNbO_3$ waveguides through MgO double diffusion," *Electron. Lett.*, vol.23, pp.797-798, 1987.

[3.40] J. L. Jackel, "Suppression of out diffusion in Ti diffused $LiNbO_3$: a review," *J. Opt. Comm.*, vol.3, pp.82-85, 1982.

[3.41] K. S. Buritskii and V. A. Chernykh, "Properties of $LiNbO_3$:Ti waveguides with suppressed outdiffusion of Li_2O," *Sov. J. Quantum Electron.*, vol.16,

pp.1424-1426, 1986.

[3.42] J. L. Jackel, C. E. Rice, and J. J. Veselka, "Proton exchange for high-index waveguides in $LiNbO_3$," *Appl. Phys. Lett.*, vol.41, pp.607-608, 1982.

[3.43] J. L. Jackel, C. E. Rice, and J. J. Veselka, "Proton exchange in $LiNbO_3$," *Ferroelectrics*, vol.50, pp.165-170, 1983.

[3.44] J. L. Jackel, C. E. Rice and J. J. Veselka, "Compositional control in proton-exchanged $LiNbO_3$", *Electron. Lett.*, vol.19, pp.387-388, 1983.

[3.45] M. De Micheli, J. Botineau, S. Neveu, P. Sibillot, D. B. Ostrowsky and M. Papuchon, "Independent control of index and profiles in lithium niobate guides," *Opt. Lett.*, vol.8, pp.114-115, 1983.

[3.46] D. F. Clark, A. C. G. Nutt, K. K. Wong, P. J. R. Laybourn and R. M. De La Rue, "Characterisation of proton-exchange slab optical waveguides in Z-cut $LiNbO_3$," *J. Appl. Phys.*, vol.54, pp.6218-6220, 1983.

[3.47] K. K. Wong, "An experimental study of dilute melt proton exchange waveguides in x- and z-cut lithium niobate," *GEC J. Research*, vol.3, pp.243-250, 1985.

[3.48] K. K. Wong, A, C. G. Nutt, D. F. Clark, J. Winfield, P. J. R. Laybourn, and R. M. De La Rue, "Characterisation of proton-exchange slab optical waveguides in x-cut $LiNbO_3$," *IEE Proc.*, pt.J, vol.133, pp.113-117, 1986.

[3.49] J. L. Jackel, A. M. Glass, G. E. Peterson, C. E. Rice, D. H. Olson, and J. J. Veselka, "Damage-resistant $LiNbO_3$ waveguides," *J. Appl. Phys.*, vol.55, pp.269-270, 1984.

[3.50] M. De Micheli, J. Botineau, S. Neveu, P. Sibillot, D. B. Ostrowsky and M. Papuchon, "Extension of second-harmonic phase-matching range in lithium

niobate guides," *Opt. Lett.*, vol.8, pp.116-118, 1983.

[3.51] N. A. Sanford and W. C. Robinson, "Direct measurement of effective indices of guided modes in $LiNbO_3$ waveguides using the Cerenkov second harmonic," *Opt. Lett.*, vol.12, pp.445-447, 1987.

[3.52] A. Yi-Yan, "Index instabilities in proton-exchanged $LiNbO_3$ waveguides," *Appl. Phys. Lett.*, vol.42, pp.633-635, 1983.

[3.53] R. A. Becker, "Comparison of guided-wave interferometric modulators fabricated on $LiNbO_3$ via Ti indiffusion and proton exchange," *Appl. Phys. Lett.*, vol.43, pp.131-133, 1983.

[3.54] R. L. Davies, "Acousto-optic Bragg diffraction in proton exchanged waveguides," *Proc. SPIE*, vol.517, pp.74-81, 1984.

[3.55] A. Loni, R. M. De La Rue, and J. M. Winfield, "Very low loss proton-exchanged waveguides with a substantially restored electrooptic effect," *Proc. Top. Meet. Integrated & Guided-Wave Optics*, Santa Fe, USA, 1988, paper MD3.

[3.56] P. G. Suchoski, T. K. Findakly, and F. J. Leonberger, "Stable low-loss proton-exchanged $LiNbO_3$ waveguide devices with no electro-optic degradation," *Opt. Lett.*, vol.13, pp.1050-1052, 1988.

[3.57] V. Hinkov and E. Ise, "Control of birefringence in Ti:$LiNbO_3$ optical waveguides by proton exchange of lithium ions," *IEEE J. Lightwave Technol.*, vol.4, pp.444-448, 1986.

[3.58] A. L. Dawar, S. M. Al-Shukri, R. M. De La Rue, A. C. G. Nutt, and G. Stewart, "Fabrication and characterization of titanium-indiffused proton-exchanged optical waveguides in Y-$LiNbO_3$," *Appl. Opt.*, vol.25, pp.1495-

1498, 1986.

[3.59] M. J. Li, M. P. De Micheli, D. B. Ostrowsky, and M. Papuchon, "High index low loss $LiNbO_3$ waveguides," *Opt. Comm.*, vol.62, pp.17-20, 1987.

[3.60] E. Glavas, P. D. Townsend, and M. A. Foad, "Refractive index changes in proton exchange $LiNbO_3$ by ion implantation," *Nucl. Instr. and Meth.*, vol.B46, pp.156-159, 1990.

Chapter 4

[4.1] A. Yi-Yan, "Index instabilities in proton-exchanged $LiNbO_3$ waveguides," *Appl. Phys. Lett.*, vol.42, pp.633-635, 1983.

[4.2] P. K. Tien, R. Ulrich, and R. J. Martin, "Modes of propagating light waves in thin deposited semiconductor films," *Appl. Phys. Lett.*, vol.14, pp.291-294, 1969.

[4.3] P. K. Tien and R. Ulrich, "Theory of prism-film coupler and thin-film light guides," *J. Opt. Soc. Am.*, vol.60, pp.1325-1340, 1970.

[4.4] T. Tamir, *Integrated Optics*, Topics Appl. Phys., vol.7, Berlin: Springer-Verlag, 1982.

[4.5] R. G. Hunsperger, *Integrated Optics: Theory and Technology*, Springer Ser. Opt. Sci., vol.33, Berlin: Springer-Verlag, 1984.

[4.6] W. L. Bond,"Measurement of the refractive indices of several crystals," *J. Appl. Phys.*, vol.36, pp.1674-1677, 1965.

[4.7] J. M. White and P. F. Heidrich, "Optical waveguide refractive index profiles determined from measurement of mode indices: a simple analysis," *Appl. Opt.*, vol.15, pp.151-155, 1976.

[4.8] K. S. Chiang, "Construction of refractive-index profiles of planar dielectric waveguides from the distribution of effective indexes," *IEEE J. Lightwave Technol.*, vol.3, pp.385-391, 1985.

[4.9] Y. Okamura, S. Yoshinaka, and S. Yamamoto, "Measuring mode propagation losses of integrated optical waveguides: a simple method," *Appl. Opt.*, vol.22, pp.3892-3894, 1983.

[4.10] Y. Okamura, A. Miki, and S. Yamamoto, "Observation of wave propagation in integrated optical circuits," *Appl. Opt.*, vol.25, pp.3405-3408, 1986.

[4.11] Y. Okamura, A. Miki, and S. Yamamoto, "Experimental demonstration of optical field evolution in waveguide junctions by using a video camera observing system," *Appl. Opt.*, vol.29, pp.5086-5089, 1990.

Chapter 5

[5.1] J. L. Jackel, C. E. Rice and J. J. Veselka, "Proton exchange for high-index waveguides in $LiNbO_3$," *Appl. Phys. Lett.*, vol.41, pp.607-608, 1982.

[5.2] M. Goodwin and C. Stewart, "Proton-exchanged optical waveguides in Y-cut lithium niobate," *Electron. Lett.*, vol.19, pp.223-225, 1983.

[5.3] D. F. Clark, A. C. G. Nutt, K. K. Wong, P. J. R. Laybourn and R. M. De La Rue, "Characterisation of proton-exchange slab optical waveguides in z-cut $LiNbO_3$," *J. Appl. Phys.*, vol.54, pp.6218-6220, 1983.

[5.4] A. D. F. Toy, *The Chemistry of Phosphorus*, Oxford: Pergamon Press, 1973.

[5.5] D. E. C. Corbridge, *Phosphorus: an outline of its Chemistry, Biochemistry and Technology*, New York: Elsevier Scientific Publishing Co., 1978.

[5.6] K. Yamamoto and T. Taniuchi, "Characteristics of pyrophosphoric acid proton-exchanged waveguides in $LiNbO_3$," *J. Appl. Phys.*, vol.70, pp.6663-6668, 1991.

[5.7] J. M. White and P. F. Heidrich, "Optical waveguide refractive index profiles determined from measurement of mode indices: a simple analysis," *Appl. Opt.*, vol.15, pp.151-155, 1976.

[5.8] K. S. Chiang, "Construction of refractive-index profiles of planar dielectric waveguides from the distribution of effective indexes," *IEEE J. Lightwave Technol.*, vol.3, pp.385-391, 1985.

[5.9] N. Goto and G. L. Yip, "Characterization of proton-exchange and annealed $LiNbO_3$ waveguides with pyrophosphoric acid," *Appl. Opt.*, vol.28, pp.60-65, 1989.

[5.10] M. A. Foad, A. Loni, R. W. Keys, J. M. Winfield and R. M. De La Rue, "Proton-exchanged lithium niobate optical waveguides made from phosphoric acids: detailed studies and comparisons with guides made with benzoic acid," *Proc. SPIE*, vol.1177, pp.31-39, 1989.

[5.11] D. Anderson and M. Lisak, "Approximate solutions of some nonlinear diffusion equations," *Phys. Rev. A*, vol.22, pp.2761-2768, 1980.

[5.12] T. Shiozawa, H. Miyamoto, H. Ohta, M. Yamaguchi and T. Oki, "Determination of two-dimensional optical waveguide index distribution function parameters from effective indexes," *IEEE J. Lightwave Technol.*, vol.8, pp.497-505, 1990.

[5.13] G. B. Hocker and W. K. Burns, "Modes in diffused optical waveguides of arbitrary index profile," *IEEE J. Quantum Electron.*, vol.11, pp.270-276,

1975.

[5.14] T. Taniuchi and K. Yamamoto, "Second harmonic generation using proton-exchanged $LiNbO_3$ waveguides," *Optoelectron. - Devices and Technol.*, vol.2, pp.53-58, 1987.

[5.15] M. De Micheli and P. St. J. Russell, "Anomalous side-shifted multimode spectra in proton-exchanged $LiNbO_3$ waveguides," *Appl. Opt.*, vol.25, pp.3896-3898, 1986.

[5.16] J. Nikolopoulos and G. L. Yip, 'Theoretical modelling and characterization of annealed proton-exchanged planar waveguides in z-cut $LiNbO_3$,' *IEEE J. Lightwave Technol.*, vol.9, pp.864-870, 1991.

[5.17] S. T. Vohra, A. R. Mickelson, and S. E. Asher, "Diffusion characteristics and waveguiding properties of proton-exchanged and annealed $LiNbO_3$ channel waveguides," *J. Appl. Phys.*, vol.66, pp.5161-5174, 1989.

[5.18] C. H. Bulmer, "Characteristics of Ti-indiffused waveguides in MgO-doped $LiNbO_3$," *Electron. Lett.*, vol.20, pp.902-904, 1984.

[5.19] M. De Micheli, J. Botineau, S. Neveu, P. Sibillot, D. B. Ostrowsky, and M. Papuchon, "Independent control of index and profiles in proton-exchanged lithium niobate guides," *Opt. Lett.*, vol.8, pp.114-115, 1983.

[5.20] A. Loni, G. Hay, R. M. De La Rue, and J. M. Winfield, "Proton-exchanged $LiNbO_3$ waveguides: the effects of post-exchange annealing and buffered melts as determined by infrared spectroscopy, optical waveguide measurements, and hydrogen isotopic exchange reactions," *IEEE J. Lightwave Technol.*, vol.7, pp.911-919, 1989.

[5.21] G. B. Hocker and W. K. Burns, "Modes dispersion in diffused channel

waveguides by the effective index method," *Appl. Opt.*, vol.16, pp.113-118, 1977.

[5.22] C. E. Rice and J. L. Jackel, "$HNbO_3$ and $HTaO_3$: new cubic perovskites prepared from $LiNbO_3$ and $LiTaO_3$ via ion exchange," *J. Solid State Chem.*, vol.41, pp.308-314, 1982.

[5.23] C. E. Rice, "The structure and properties of $Li_{1-x}H_xNbO_3$," *J. Solid State Chem.*, vol.64, pp.188-199, 1986.

[5.24] C. Ziling, L. Pokrovskii, N. Terpugov, M. Kuneva, I. Savatinova, and M. Armenise, "H:$LiNbO_3$ optical waveguides made from pyrophosphoric acid," *Proc. SPIE*, vol.1583, pp.90-101, 1991.

[5.25] I. Savatinova, S. Tonchev, E. Popov, E. Liarokapis, and C. Raptis, "Raman scattering of proton exchanged $LiNbO_3$ waveguides," *J. Phys. D*, vol.25, pp.106-112, 1992.

[5.26] C. Canali, A. Carnera, G. Della Mea, P. Mazzoldi, S. M. Al Shukri, A. G. C. Nutt, and R. M. De La Rue, "Structural characterization of proton exchanged $LiNbO_3$ optical waveguides," *J. Appl. Phys.*, vol.59, pp.2643-2649, 1986.

[5.27] I. T. Savatinova, M. Kuneva, B. Jordanov, and D. Kolev, "IR absorbance in proton-exchanged $LiNbO_3$ optical waveguides," *J. Mol. Struct.*, vol.219, pp.165-170, 1990.

[5.28] V. A. Ganshin and Yu. N. Korkishko, "Deformations, stresses and birefringence in proton-exchanged lithium niobate waveguides," *J. Opt. Comm.*, vol.13, pp.2-7, 1991.

[5.29] M. Minakata, K. Kumagai, and S. Kawakami, "Lattice constant changes and

electro-optic effects in proton-exchanged $LiNbO_3$ optical waveguides," *Appl. Phys. Lett.*, vol.49, pp.992-994, 1986.

Chapter 6

[6.1] J. L. Jackel, C. E. Rice and J. J. Veselka, "Proton exchange for high-index waveguides in $LiNbO_3$," *Appl. Phys. Lett.*, vol.41, pp.607-608, 1982.

[6.2] J. L. Jackel, "Proton exchange: past, present, and future," *Proc. SPIE*, vol.1583, pp.54-63, 1991.

[6.3] A. Loni, "Proton-exchanged $LiNbO_3$ waveguides come of age," *Laser Focus World*, pp.183-188, April 1991.

[6.4] J. L. Jackel, A. M. Glass, G. E. Peterson, C. E. Rice, D. H. Olson, and J. J. Veselka, "Damage-resistant $LiNbO_3$ waveguides," *J. Appl. Phys.*, vol.55, pp.269-270, 1984.

[6.5] E. Y. B. Pun, K. K. Wong, I. Andonovic, P. J. R. Laybourn and R. M. De La Rue, "Efficient waveguide Bragg-deflection grating on $LiNbO_3$," *Electron. Lett.*, vol.18, pp.740-742, 1982.

[6.6] K. K. Wong, R. M. De La Rue and S. Wright, "Electro-optic waveguide frequency translator in $LiNbO_3$ fabricated by proton exchange," *Opt. Lett.*, vol.7, pp.546-548, 1982.

[6.7] C. Warren, S. Forouhar, W. S. C. Chang and S. K. Yao, "Double ion exchange chirp grating lens in lithium niobate waveguides," *Appl. Phys. Lett.*, vol.43, pp.424-426, 1983.

[6.8] R. A. Becker, "Comparison of guided-wave interferometric modulators fabricated on $LiNbO_3$ via Ti indiffusion and proton exchange," *Appl. Phys.*

Lett., vol.42, pp.131-133, 1983.

[6.9] G. Tohmon, J. Ohya, K. Yamamoto and T. Taniuchi, "Generation of Ultraviolet Picosecond Pulses by Frequency-Doubling of Laser Diode in Proton-Exchanged MgO:$LiNbO_3$ Waveguide," *IEEE Photon. Technol. Lett.*, vol.2, pp.629-631, 1990.

[6.10] E. Lallier, J. P. Pocholle, M. Papuchon, C. Grezes-Besset, E. Pelletier, M. De Micheli, M. J. Li, Q. He, and D. B. Ostrowsky, "Laser oscillation of single-mode channel waveguide in Nd:MgO:$LiNbO_3$," *Electron. Lett.*, vol.25, pp.1491-1492, 1989.

[6.11] E. Lallier, J. P. Pocholle, M. Papuchon, M. De Micheli, M. J. Li, Q. He, D. B. Ostrowsky, C. Grezes-Besset, and E. Pelletier, "Nd:MgO:$LiNbO_3$ waveguide laser and amplifier," *Opt. Lett.*, vol.15, pp.682-684, 1990.

[6.12] T. Taniuchi and K. Yamamoto, "Second harmonic generation using proton-exchanged $LiNbO_3$ waveguides," *Optoelectron. - Devices and Technol.*, vol.2, pp.53-58, 1987.

[6.13] N. Goto and G. L. Yip, "Characterization of proton-exchange and annealed $LiNbO_3$ waveguides with pyrophosphoric acid," *Appl. Opt.*, vol.28, pp.60-65, 1989.

[6.14] A. Loni, R. W. Keys, R. M. De La Rue, M. A. Foad and J. M. Winfield, "Optical characterisation of z-cut proton-exchanged $LiNbO_3$ waveguides fabricated using orthophosphoric and pyrophosphoric acid," *IEE Proc. J*, vol.136, pp.297-300, 1989.

[6.15] N. A. Sanford and J. M. Connors, "Optimization of the Cerekov sum-frequency generation in proton-exchanged Mg:$LiNbO_3$ channel waveguides,"

J. Appl. Phys., vol.65, pp.1429-1437, 1989.

[6.16] K. Yamamoto and T. Taniuchi, "Characteristics of pyrophosphoric acid proton-exchanged waveguides in $LiNbO_3$," *J. Appl. Phys.*, vol.70, pp.6663-6668, 1991.

[6.17] G. L. Yip and J. Nikolopoulos, "Characterisation of proton-exchanged and annealed proton-exchanged planar waveguides in z-cut $LiNbO_3$," *IEE Proc. J*, vol.138, pp.389-392, 1991.

[6.18] D. F. Clark, A. C. G. Nutt, K. K. Wong, P. J. R. Laybourn and R. M. De La Rue, "Characterisation of proton-exchange slab optical waveguides in z-cut $LiNbO_3$," *J. Appl. Phys.*, vol.54, pp.6218-6220, 1983.

[6.19] A. Loni, R. M. De La Rue, and J. M. Winfield, "Proton-exchanged, lithium niobate planar-optical waveguides: chemical and optical properties and room-temperature hydrogen isotopic exchange reactions," *J. Appl. Phys.*, vol.61, pp.64-67, 1987.

[6.20] M. L. Bortz and M. M. Fejer, "Annealed proton-exchanged $LiNbO_3$ waveguides," *Opt. Lett.*, vol.16, pp.1844-1846, 1991.

[6.21] V. A. Ganshin and Yu. N. Korkishko, "H:$LiNbO_3$ waveguides: effects of annealing," *Opt. Comm.*, vol.86, pp.523-530, 1991.

[6.22] I. Savatinova, S. Tonchev, E. Popov, E. Liarokapis, and C. Raptis, "Raman scattering of proton exchanged $LiNbO_3$ waveguides," *J. Phys. D*, vol.25, pp.106-112, 1992.

Appendix 1 Error Estimations

A1.1 Mode Effective Index

The mode effective index N is given by the relation

$$N = n_p \sin\left[\alpha + \arcsin\left(\frac{\sin\theta}{n_p}\right)\right]$$

where α is the base angle of the rutile prism and θ is the synchronous angle. Taking the first derivatives of N with respect to α and θ, the accuracy ΔN of the mode effective index can then be expressed as

$$\Delta N = \left|\frac{\partial N}{\partial \alpha}\cdot\Delta\alpha\right| + \left|\frac{\partial N}{\partial \theta}\cdot\Delta\theta\right|$$

where

$$\frac{\partial N}{\partial \alpha} = n_p \cos\left[\alpha + \arcsin\left(\frac{\sin\theta}{n_p}\right)\right]$$

$$\frac{\partial N}{\partial \theta} = \frac{\cos\left[\alpha + \arcsin\left(\frac{\sin\theta}{n_p}\right)\right]}{\cos\left[\arcsin\left(\frac{\sin\theta}{n_p}\right)\right]}\cdot\cos\theta$$

In the prism-coupling measurements, the synchronous angle θ is in the range of $\pm 12°$. The uncertainty of the angles measured by the rotating stage is ± 12 arcseconds, i.e. $\Delta\alpha = \Delta\theta = \pm 12$ arcseconds. Hence the accuracy of our measured mode effective indices is found to be $\pm 1.1\times 10^{-4}$.

A1.2 Effective Diffusion Coefficient

The effective diffusion coefficient D_e is calculated using the relation

$$D_e = d^2 / t$$

where d is the waveguide depth and t is the diffusion time. The accuracy ΔD_e of the effective diffusion coefficient can be expressed as

$$\Delta D_e = (\partial D_e/\partial d)\Delta d + (\partial D_e/\partial t)\Delta t$$
$$= (2d/t)\Delta d + (d/t)^2\Delta t$$

In our experiments, the average waveguide depth is 1 μm and the nominal diffusion time is 1 hour. Taking $\Delta d = \pm 0.05$ μm and $\Delta t = \pm 2$ min, ΔD_e is found to be ± 0.133 $\mu m^2 h^{-1}$.

A1.3 Mode Size of Channel Waveguide

The $1/e$ mode size of the channel waveguides is measured from their near-field intensity profiles magnified by a 40× microscope objective lens. The resolution R of a microscope objective lens is given by the relation

$$R = 0.61 \lambda / \text{N.A.}$$

where λ is the wavelength and N.A. is the numerical aperture of the microscope objective lens. In our experiment, λ and N.A. have values of 0.6328μm and 0.65, respectively. Therefore, the accuracy of the measured mode size is $\pm 0.585 \mu$m.

Appendix 2 List of Publications

[1] E. Y. B. Pun, K. K. Loi and P. S. Chung, "Proton-exchanged waveguides in MgO:$LiNbO_3$ using phosphoric acid," *Electron. Lett.*, vol.27, pp.168-170, 1991.

[2] E. Y. B. Pun, K. K. Loi and P. S. Chung, "Index profile of proton-exchanged waveguides in lithium niobate using cinnamic acid," *Electron. Lett.*, vol.27, pp.1282-1283, 1991.

[3] E. Y. B. Pun, K. K. Loi, S. A. Zhao and P. S. Chung, "Experimental studies of proton-exchanged lithium niobate waveguides using cinnamic acid," *Appl. Phys. Lett.*, vol.59, pp.662-664, 1991.

[4] E. Y. B. Pun, S. A. Zhao, K. K. Loi and P. S. Chung, "Proton-exchanged $LiNbO_3$ optical waveguides using stearic acid," *IEEE Photon. Technol. Lett.*, vol.3, pp.1006-1008, 1991.

[5] K. K. Loi, E. Y. B. Pun and P. S. Chung, "Proton-exchanged optical waveguides in z-cut $LiNbO_3$ using toluic acid," *Electron. Lett.*, vol.28, pp.546-548, 1992.

[6] E. Y. B. Pun, P. S. Chung and K. K. Loi, "Annealing effects on proton-exchanged $LiNbO_3$ optical waveguides using stearic acid," *Microwave Opt. Technol. Lett.*, accepted for publication.

[7] E. Y. B. Pun, K. K. Loi and P. S. Chung, "Experimental studies of proton-exchanged waveguides in lithium niobate using toluic acid," Proceeding of SPIE OE/FIBERS'91 (Boston, U.S.A.), vol.1583, pp.64-70, 1991.

[8] E. Y. B. Pun, K. K. Loi, S. A. Zhao and P. S. Chung, "Annealing

properties of proton-exchanged waveguides in $LiNbO_3$ using stearic acid," Proceeding of SPIE OE/FIBERS'91 (Boston, U.S.A.), vol.1583, pp.102-108, 1991.

[9] E. Y. B. Pun, K. K. Loi and C. F. Mak, "Optical waveguides in MgO:$LiNbO_3$ by H^+/Li^+ exchange using a new proton source: adipic acid," Proceeding of ECOC/IOOC'91 (Paris, France), paper WeB6-4, pp.421-424, 1991.

[10] E. Y. B. Pun, Y. O. Tse, K. K. Loi and P. S. Chung, "Effect of annealing on proton-exchanged $LiNbO_3$ waveguide fabricated using octanoic acid," Technical Digest of MOC'91 (Yokohama, Japan), pp.46-49, 1991.

[11] E. Y. B. Pun, K. K. Loi and P. S. Chung, "Proton-exchanged optical waveguides in z-cut $LiNbO_3$ using phosphoric acid," *IEEE J. Lightwave Technol.*, submitted for publication.

[12] K. K. Loi, E. Y. B. Pun and P. S. Chung, "Characterization of annealed proton-exchanged $LiNbO_3$ waveguides fabricated using toluic acid," *Appl. Opt.*, submitted for publication.

[13] K. K. Loi, C. F. Mak, E. Y. B. Pun and P. S. Chung, "Experimental studies of proton-exchanged $LiNbO_3$ waveguides using adipic acid," in preparation.